ACE

Applied and Computational Engineering

The 2nd International Conference
on Functional Materials and Civil Engineering

Eskişehir, Turkey

August 23 - August 30, 2024

EWA Publishing

Volume 91

Editor
Ömer Burak İSTANBULLU
Eskişehir Osmangazi University

ISSN: 2755-2721
ISSN: 2755-273X (eBook)

ISBN: 978-1-83558-619-8
ISBN: 978-1-83558-620-4 (eBook)

Publication of record for individual papers is online:
https://www.ewadirect.com/proceedings/ace/home/index

This imprint is published by **EWA Publishing**
Address: John Eccles House, Robert Robinson Avenue, Oxford, England, OX4 4GP
Email: info@ewapublishing.org

Committee Members

CONF-FMCE 2024

General Chairs

Ömer Burak İSTANBULLU, *Eskişehir Osmangazi University*

Organizing Chair

Sajjad Seifi Mofarah, *UNSW Sydney*

Organizing Committee

Marwan Omar, *Illinois Institute of Technology*
Sharidya Rahman, *Monash University*
Selda Kapan Ulusoy, *Erciyes University*
Ming Fang, *Chinese Academy of Agricultural Sciences*
Linyan Han, *University of Leeds*
Javier Cifuentes-Faura, *University of Murcia*

Technical Program Chair

Niaz Ahmed, *FAST NUCES Islamabad*

Technical Program Committee

Achintya Haldar, *University of Arizona*
Ioannis Spanopoulos, *University of South Florida*
Farzaneh Tahmoorian, *CQUniversity Australia*
Alan Wang, *University of Auckland*
Festus Adedoyin, *Bournemouth University*
Jamarosliza binti Jamaluddin, *Universiti Teknologi Malaysia*
Nadia Adrus, *Universiti Teknologi Malaysia*
Funlola Famuyiwa, *Oxford Brookes University*
Jiajie Wang, *Tohoku University*
Vijay Varadan, *Pennsylvania State University*

Publicity Committee

Toqeer Mahmood, *National Textile University*

Preface

The 2nd International Conference on Functional Materials and Civil Engineering (CONF-FMCE 2024) is an annual conference focusing on research areas including functional materials, civil engineering, transportation engineering, and energy engineering. It aims to establish a broad and interdisciplinary platform for experts, researchers, and students worldwide to present, exchange, and discuss the latest advance and development in functional materials, civil engineering, transportation engineering, and energy engineering.

This volume contains the papers of the 2nd International Conference on Functional Materials and Civil Engineering (CONF-FMCE 2024). Each of these papers has gained a comprehensive review by the editorial team and professional reviewers. Each paper has been examined and evaluated for its theme, structure, method, content, language, and format.

Cooperating with prestigious universities, CONF-FMCE 2024 organized three workshops in Eskişehir, Chicago and Auckland. Dr. Ömer Burak İSTANBULLU chaired the workshop “Patient- and Tissue-Specific Approaches in Implantable Biomaterial Design, Development and Production”, which was held at Eskişehir Osmangazi University. Dr. Marwan Omar chaired the workshop “Nanotechnology in Computer Science: Pioneering the Future of Computing”, which was held at Illinois Institute of Technology. Dr. Alan Wang chaired the workshop “Workshop on Advanced Nanotechnology and Computational Modelling 2024 (WANCM 2024)”, which was held at University of Auckland.

Besides these workshops, CONF-FMCE 2024 also held an online session. Eminent professors from top universities worldwide were invited to deliver keynote speeches in this online session, such as Dr. Ömer Burak İSTANBULLU from Eskişehir Osmangazi University and Dr. Marwan Omar from Illinois Institute of Technology. They have given keynote speeches on related topics of functional materials, civil engineering, transportation engineering, and energy engineering.

On behalf of the committee, we would like to give sincere gratitude to all authors and speakers who have made their contributions to CONF-FMCE 2024, editors and reviewers who have guaranteed the quality of papers with their expertise, and the committee members who have devoted themselves to the success of CONF- FMCE 2024.

Dr. Ömer Burak İSTANBULLU

General Chair of Conference Committee

Workshops

Workshop – Eskişehir: Patient- and Tissue-Specific Approaches in Implantable Biomaterial Design, Development and Production

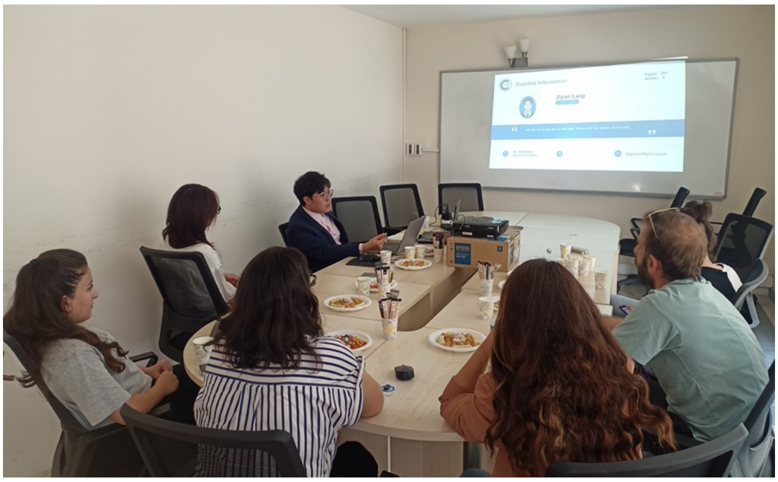

August 23rd, 2024 (GMT+3)

Biomedical Engineering Department, Eskişehir Osmangazi University

Workshop Chair: Dr. Ömer Burak İSTANBULLU, Assistant Professor in Eskişehir Osmangazi University

Workshop – Chicago: Nanotechnology in Computer Science: Pioneering the Future of Computing

August 16th, 2024 (UTC-5)

ITM Department, Illinois Institute of Technology, USA

Workshop Chair: Dr. Marwan Omar, Associate Professor in Illinois Institute of Technology

Workshop – Auckland: Workshop on Advanced Nanotechnology and Computational Modelling 2024 (WANCM 2024)

September 27th, 2024 (UTC +13)

Faculty of Medical and Health Sciences and Bioengineering Institute, University of Auckland

Workshop Chair: Dr. Alan Wang, Associate Professor in University of Auckland

The 2nd International Conference on Functional Materials and Civil Engineering

CONF-FMCE 2024

Table of Contents

Proceedings of the 2nd International Conference on Functional Materials and Civil Engineering
DOI: 10.54254/2755-2721/91/20241106

Research on the application of the construction technology of the residential exterior wall thermal insulation structure

Ziyu Lu

College of Resources, Shandong University of Science and Technology, Tai'an, 271000, China

ziyuziyu4u@163.com

Abstract. The energy problem has become the main factor restricting the sustainable development of society and protecting the ecological environment. China's vast territory, changeable climate and environment increase the difficulty of building energy conservation and emission reduction, and restrict China's sustainable development strategy. It is urgent to reduce building energy consumption and improve energy utilization. The external wall insulation can effectively reduce the energy consumption of buildings. Through the analysis of the current situation of civil building wall insulation and energy-saving system, it is found that there are many problems in the construction, management and material application of external wall insulation; According to the concept of energy conservation, environmental protection and sustainable development, this paper puts forward countermeasures, hoping to have a certain reference significance for the external wall insulation construction of other similar projects.

Keywords: exterior wall insulation, Energy saving, Construction technology.

1. Introduction

Construction industry is a consuming industry that consumes a large amount of resources and affects the natural environment. With the continuous rapid increase of China's resident population and the continuous improvement of people's living quality, the comprehensive energy consumption of civil buildings is increasing [1], and it is urgent to solve the problem of shortage of civil building resources. The energy-saving development of the construction industry is an inevitable requirement of today's society. Energy-saving and thermal insulation building technology is to improve the housing conditions of the people in China and reduce the energy problems caused by building heating and cooling in winter and summer [2]. The development and use of building energy saving and thermal insulation technology is the basic means to realize building energy saving in China. The innovation of technological means is an important method to improve the production technology level and the comprehensive competitiveness of enterprises in the construction market. In this case, based on the external wall energy saving renovation project of A project community, based on the analysis and summary of the significance of external wall insulation in building energy saving and the current application situation, discuss the problems and solutions in the construction, so as to achieve the purpose of accelerating the development of external wall insulation construction technology [3].

Since the 1990s, the problem of building energy consumption has become highly valued in China. The central government and local people's governments at all levels have formulated and introduced a series of policies and regulations, to promote the development of building energy saving to a certain extent and thermal insulation technology. However, due to the influence of different factors such as climatic conditions and regional characteristics [4], the promotion and application of many energy saving technologies are often greatly restricted, which increases the difficulty of the relevant government departments; mainly reflected in the following main aspects: first, the huge management system of building energy saving technology, which increases the difficulty of construction technology application and management to some extent; second [5],the lack of necessary understanding of the applicable conditions of green energy-saving construction technology in some areas, leads to blindness in the selection of building energy saving technology. Through the analysis of external wall insulation construction technology analysis of project A, combined with the actual situation of the energy saving construction technology suitable for the promotion of the region, so as to promote the further development of the building external wall insulation industry.

2. Overview of construction technology of building exterior wall insulation

2.1. Exterior wall insulation

Exterior wall insulation is a composite wall with heat insulation function composed of polymer modified mortar, flame retardant polystyrene board, extrusion polystyrene board and other materials. The energy saving insulation project integrating building insulation, exterior wall waterproof and finish decoration, can not only improve the building energy efficiency, reduce the construction cost, but also meet the requirements of energy saving insulation of modern buildings [6]. Exterior wall insulation technology uses polymer modified mortar and other adhesives to cement polystyrene foam or extrusion board and other polymer materials with low density and high thermal resistance on the building exterior wall, and then lay decorative and protective decorative layer, give the building additional thermal insulation performance. In high latitude and cold areas, external wall insulation can prevent or delay the heat loss in the building at low temperature, stabilize the internal temperature; or in low latitude hot areas, exterior wall insulation can also prevent the influence of environmental temperature on the indoor temperature, isolate the heat outside the exterior wall of the building, and achieve the effect of heat insulation. Whether it is heat insulation or heat insulation, the external wall insulation system is to stabilize the internal temperature of the building within an appropriate range, and reduce the energy consumption caused by regulating the internal temperature of the building, so as to achieve the purpose of energy saving and emission reduction [7].

2.2. Exterior wall thermal insulation materials

The building materials used for external wall insulation are called external wall insulation materials, mainly including the following categories:

2.2.1. Extruded polystyrene plate (XPS)

Extruded polystyrene board is the earliest application, the most mature technology, the market share of the highest energy-saving insulation material. Because of the high closure rate of its internal structure, it has good water resistance and low water absorption rate, and also avoids the energy loss due to airflow convection. The extruded polystyrene plate has low thermal conductivity and high adiabatic performance, its chemical performance is relatively stable, can deal with all kinds of harsh climate conditions, and in a variety of high temperature and high humidity environment may still maintain excellent heat resistance for a long time. However, it has poor air permeability due to its high closure rate. When the temperature and humidity change greatly, the internal stress caused by its deformation is also relatively large, which is easy to produce local stress damage. In practical engineering, the external insulation system of extruded polystyrene board is prone to hollow, cracking and falling off.

DOI: 10.54254/2755-2721/91/20241106

2.2.2. Foamed polystyrene plate (EPS)

Under the same thickness, the heat insulation effect of foamed polystyrene board is weaker than that of extruded polystyrene board, and its tensile strength and thermal conductivity are smaller than that of extruded polystyrene board, and its weather resistance is poor. But the foaming polystyrene board has good air permeability, high ductility and high bonding strength, so the construction difficulty is relatively low, and the construction speed is fast.

2.2.3. Phenolic plates

Phenolic plates have very small thermal conductivity, have good heat insulation, excellent fire resistance, and will not release highly toxic substances in the fire. The phenolic plates have a low density and a light weight. When the temperature varies greatly, it does not produce great stress, and it has good durability. But its water absorption rate is high, the water absorption is easy to crush after drying, low strength, poor impact resistance, small bending deformation, easy to crack and fall off under the action of external force.

2.2.4. Foamed polystyrene board

Foamed polystyrene plates are heat insulation and sound insulation material with the highest fire grade. It has low thermal resistance coefficient, good air permeability, stable chemical performance, not easy to be corrosion and pollution mildew, in the fire will not release toxic gas. But its low tensile strength, high water absorption rate, easy to deformation.

3. Case Analysis of the construction technology of residential exterior wall thermal insulation

3.1. Residential Project Overview

The total building area of Phase II of Project A is 13,894 square meters, and the unit building height is eight floors, with six floors and the first floor belongs to the semi-underground warehouse and storage room. The seismic fortification intensity is 7 degrees, the seismic performance grade is Grade 2, and the actual service life of the building can reach 70 years. The main body of the building adopts the mixed foundation of pile foundation-raft plate, and the superstructure of the building adopts reinforced concrete frame shear wall. The internal partition wall is filled with hollow aerated concrete block, the external wall filling is filled with aerated fly ash block, and the external wall of the building is decorated with water-proof and moisture-proof plastering [8].

The second phase of project A has 112 residential units, and since 2015, about 86 households have occupied it, accounting for 77% of the total. Since the first half of 2017, some residents have reported that the indoor temperature is low in winter, which can only be maintained at about 14 degrees Celsius, which cannot reach the 16 degrees Celsius stipulated by the national standard, and is far from meeting the comfort requirements of living. The heating pipeline used in the building complex is central heating, and the residential boiler room is secondary heating into the house, but the effect still cannot meet the heating needs of residents. In 2018, XX Municipal Government issued the special Regulations on building energy conservation, which made clear requirements for the heating and energy conservation of buildings, and set up special subsidies to ensure the smooth implementation of energy conservation renovation projects. After the relevant government departments decided that in order to meet the needs of residents in winter, the construction of the second phase of A project was carried out in September 2018. The external wall insulation project belongs to the energy saving renovation project of the existing buildings, and the most widely used construction technology in the building insulation technology has become the best choice of the project.

3.2. Construction scheme of external wall insulation of the project

A project phase ii external wall insulation structure construction mainly by the surface processing (basic processing, measuring line), insulation layer construction (paste anchor EPS, ESP polystyrene board grinding), protective layer construction (daub surface mortar, alkali grid cloth lattice cloth, daub surface paste) and decorative surface construction (coating water resistant elastic putty, surface coating or face brick construction) composed of four parts.

3.2.1. Wall base surface treatment and measurement and laying out

Clean up the surface of the external wall of the original building, eradicate the peeling, hollow drum, foaming and other defects that affect the construction, ensure the leveling and stability of the wall, remove the external wall hanging equipment, and ensure the safety of the construction personnel. Test the local flatness and vertical degree of the wall, and pop the horizontal and vertical control lines on the outer wall at a certain distance to ensure the straight and stability of the insulation material.

In the process of handling the base of Project A, since the building complex is not built long, it is not necessary to deal with the base too much, and most residents have installed air conditioning and some low-level households have installed stainless steel anti-theft isolation window, which brought great constant to the construction. Therefore, after consultation with the residents committee, the construction team decided to remove part of the air conditioning machine and anti-theft Windows that affect the construction, and install them again after the construction, so as to minimize the impact of the construction on the residents' lives. After the external wall equipment is removed, the base leveling treatment is carried out, the surface is coated with 5mm thick waterproof mortar mixed with 1% water reducing agent, and the first waterproof and impermeable treatment is carried out while leveling the base level.

3.2.2. Install the ESP thermal insulation board

ESP board paving follows the construction method of top-down, dislocation lap. The construction personnel use the crane to start the construction from the upper part of the building. The insulation board is 1 / 2 of the length of the insulation board, and the cutting length of the sporadic plate at the corner (see Figure 3.3) and the hole should not be less than 1 / 3 of the plate length. From top to bottom, the plate can reduce the influence of gravity on the plate bonding, and prevent the overall strength of the stress caused by the sliding of the bonding place on the upper plate and the plate weight on the lower wall. The construction method of misjoint and the bonding anchor can maximize the insulation plate into a whole, and the upper and lower joints between the plates often become a weak point in the structure. In order to ensure the bonding strength, the laying of the board should not exceed 2 layers to the anchorage, and the board should be anchored after suspending the construction. It is strictly prohibited to hang the empty board empty.

The bonding of ESP plate and the bonding of steel plate anchor bolt are combined. The main feature of this anchoring method is that on the basis of the traditional bonding anchoring method, an ESP insulation plate is directly fixed by resetting several new anchor positions. The head of the anchor bolt is made of high-strength nylon fiber and plastic composite, and the tail anchor bolt is made of rotary screw type expansion bolt. The limit value of the overall tensile force and bearing capacity strength of a single link bolt should be greater than 1.5 kn. It is suitable for the decoration construction of the building exterior wall and wall insulation layer mainly made of the building exterior wall envelope decoration, as well as the energy saving transformation of the large building exterior wall envelope structure with weak building base attachment protection ability. Although the construction of this process is more complex, the weight of the insulation wall is divided in the whole wall structure, and is fixed in the structural layer of the building through the anchor bolt, which greatly improves the overall strength of the insulation system and effectively improves the overall service life of the insulation layer.

3.2.3. EPS board grinding

EPS steel plate must be kept continuously for at least 24h before or after fixation, so as not to affect the overall strength of EPS steel plate. In the process of grinding the insulation board, you can use special friction agent or hand rub to polish the surface and the edge of the board thoroughly, eliminating the difference between the thickness between the floor and the edge, and in the use of the EPS debris

DOI: 10.54254/2755-2721/91/20241106

scattered on the board should be cleaned at any time. If the joint is large, more than 50mm should be bonded with mortar grid strip, layered filling; less than 50mm can be directly filled with mortar.

3.2.4. Laying of grid cloth

The laying of the grid cloth uses the two-channel mortar plaster laying method. That is, apply a layer of bonding mortar slightly larger than the size of the mesh cloth on the surface of the EPS composite plate, then press the mesh cloth into the bonding mortar with a spatula, and then apply a layer of mortar evenly. The two lines of mortar clamp the mesh cloth in the middle, the curing time is not less than 72H, and the maintenance time should be moderately extended after precipitation. The next construction process can be carried out before the layer of mortar is evenly dried.

3.2.5. Selection of the finish layer

EPS composite external wall thermal insulation layer is a kind of light and flexible thermal insulation structure decoration surface material, which can be matched with flexible wall coating. The veneer foundation layer of the exterior wall insulation layer of EPS insulation board should give priority to the elastic coating to ensure the descriptive nature of the insulation structure and extend the service life of the structure. In the construction scheme of project A, the exterior wall insulation finish is covered with waterproof wall paint to enhance the waterproof coefficient of the structure and laid at a height of 1.5 m to prevent the erosion of surface water on the wall and improve the strength of external force during use.

4. Problems in the construction of energy saving and insulation of 4 A project

4.1. Construction environment problems

The total building area of Phase II of Project A is 13,894 square meters, and the unit building height is eight floors, with six floors and the first floor belongs to the semi-underground warehouse and storage room. The seismic fortification intensity is 7 degrees, the seismic performance grade is Grade 2, and the actual service life of the building can reach 70 years. The main body of the building adopts the mixed foundation of pile foundation-raft plate, and the superstructure of the building adopts reinforced concrete frame shear wall. The internal partition wall is filled with hollow aerated concrete block, the external wall filling is filled with aerated fly ash block, and the external wall of the building is decorated with water-proof and moisture-proof plastering.

The building is in line with the overall layout of the northern building facing south, and the overall layout of the “convex” room layout. Among them, the balcony of the south living room and the large area of floor-to-ceiling glass Windows, in order to meet the living requirements of room lighting, ventilation and beauty, the area of doors and Windows in the external wall accounts for 21% of the total area, and the proportion of doors and Windows is higher, and the energy consumption in the process of building use is also increased accordingly.

The area where the residential project of Project A is located belongs to monsoon climate. According to the temperature in winter is often below zero in the past 20 years, and is often accompanied by gale weather of 3~7; the daytime temperature in summer is higher than 25 degrees Celsius, often accompanied by precipitation above 100 mm, and the temperature difference between day and night is large. In order to ensure the heating and cooling demand of the residents, the embedded water circulation temperature control facilities are adopted. It is a typical northern building with cold in winter and has heating demand. Meanwhile, in order to reduce the high temperature in summer and improve living comfort, each household has 1-3 air conditioning equipment, which brings great challenge to the energy consumption of the building complex [9].

The second phase of project A has 112 residential units, and since 2015, about 86 households have occupied it, accounting for 77% of the total. Since the first half of 2017, some residents have reported that the indoor temperature is low in winter, which can only be maintained at about 14 degrees Celsius, which cannot reach the 16 degrees Celsius stipulated by the national standard, and is far from meeting the comfort requirements of living. The heating pipeline used in the building complex is central heating,

DOI: 10.54254/2755-2721/91/20241106

and the residential boiler room is secondary heating into the house, but the effect still cannot meet the heating needs of residents. In 2018, XX Municipal Government issued the special Regulations on building energy conservation, which made clear requirements for the heating and energy conservation of buildings, and set up special subsidies to ensure the smooth implementation of energy conservation renovation projects. After the relevant government departments decided that in order to meet the needs of residents in winter, the construction of the second phase of A project was carried out in September 2018. The external wall insulation project belongs to the energy saving renovation project of the existing buildings, and the most widely used construction technology in the building insulation technology has become the best choice of the project.

4.2. Construction quality problems

4.2.1. Immature technology leads to inadequate base treatment

Empty drum and foaming occur on the original base wall of Project A, with wall peeling occasionally; After removing the problem wall according to the construction technology, the flatness of the external wall cannot meet the construction requirements, so the problem wall must be repaired. The flatness of the base wall can directly affect the final construction effect of the whole external wall insulation system. The size deviation between the surface layer and the modified surface layer is largely due to the flatness treatment of the wall base is not in place, and the base treatment is not in place will lead to the large bonding between the insulation layer and the base is not firm, which is easy to produce empty drum and cause serious construction quality problems such as inter-layer condensation and insulation layer peeling. Therefore, the base treatment size deviation of the external insulation system must also meet the requirements.

4.2.2. Technical defect The waterproof layer has poor water insulation effect

The waterproof construction effect of some floors of the external wall insulation structure of Project A is not good, resulting in the condensation phenomenon in the insulation structure and returning to the wall surface after the condensation of the wall vapor in the wall and the condensation affect the lives of the wall, forming a heat bridge damaging the insulation layer and expanding at the low temperature in winter,[9] destroying the safety of the insulation layer structure. The poor water-separation effect mainly consists of several aspects:

First, the waterproof treatment of the insulation layer is not in place, the base treatment mortar is not mixed with water admixture, resulting in the water inside the building and residential water from the wall into the insulation structure, the temperature decreases in the insulation layer condensation to form water droplets.

Second, the insulation structure construction, occasional precipitation, and plaster and bonding mortar not reduce water agent, the material itself water content is too large, and material moisture without full evaporation drying after two construction, the moisture enclosed inside the insulation structure, as the temperature changes, material internal moisture evaporation precipitation, and condensation inside the insulation structure.

Third, the construction treatment of the insulation layer is mixed with the water separation admixture, but affected by the low temperature climate in winter, the local condensate water inside the structure produces freezing and thawing cycle, seriously damaging the strength of the structure, resulting in the surface layer under the internal stress cracks, lost the original water separation effect.

4.2.3. The treatment loophole causes the cracking and shedding of the insulation layer

The external wall insulation system is composed of surface layer, bonding layer, insulation block layer and base layer, and each part may occur in different degrees of cracking problems and affect each other.

The external cause of the insulation layer cracking is the temperature difference causing uneven cracks in the overall structure; it is also possible that the thermal expansion coefficient between the insulation layer and the building destroys the integrity of the insulation layer by the thermal expansion

DOI: 10.54254/2755-2721/91/20241106

of the original building and the shrinkage rate of the insulation system produces large-scale stripping between the building and the insulation layer, seriously reducing the bonding strength of the insulation layer, resulting in cracking and peeling. Affected by the climate [10], rain and snow erosion, wind also lead to problems such as insulation cracking, especially in the wall of the wind, affected by wind negative pressure, insulation layer will be affected by an outward suction, once the wind or insulation structure itself has cracking, quality problems such as adhesion, is easy to lead to insulation whole peeling. In addition, the stability change of the building caused by the geological influence of foundation settlement and earthquake will also seriously affect the overall strength and bonding strength of the insulation layer, leading to the cracking and peeling of the insulation layer.

There are also many internal factors affecting insulation layer cracking and peeling, such as: the base treatment is not in place, the base flatness tolerance is too large, so that the subsequent construction of material bonding is not in place, resulting in empty drum cracking and other phenomena. When the insulation block is anchored, the wrong seam is not laid according to the requirements of the construction plan, and the block produces long distance cracks, and the structural integrity of the reduction produces cracks. During the construction of the blocks, the construction is not carried out from top to bottom, until the internal stress between the blocks occurs due to gravity and material expansion and other factors [11], which destroys the structure from the inside out. The condensation problems caused by various reasons will also lead to the cracking of the insulation structure under the action of frost swelling factors. After the development and accumulation of cracking and adhesive problems, there will be more serious denation damage under their own action.

4.3. Construction material problems

4.3.1. Poor material quality and poor insulation effect of local wall
The quality of construction materials directly affects the quality and service life of the engineering.

After the renovation of the external wall of Project A, the overall room temperature of the community has been improved after energy saving insulation renovation; however, some residents complained that the heating room temperature did not meet the comfortable living requirements. After the property personnel counted the owners, these residents are concentrated in A concentrated range. After testing by a third party professional thermal testing personnel, a large area of heat source leakage was found in the southwest side of the 2-3 floor wall of no [12]. 13 building. After the professional thermal testing team analyzes the cause of the poor insulation effect in the area, 13 residential building belongs to the late stage of the construction plan, in the construction process of 13 material scheduling problems, temporary construction group purchased a batch of untested material construction, and use the rest after the cutting sporadic block material, and do not strengthen processing, directly led to the structure of the area integrity greatly reduced, the insulation effect appear obvious difference.

4.3.2. The first layer surface brick is not laid according to the design drawing, and the surface layer is seriously damaged
After 15 months of construction and renovation, different degrees of dirt occurred within 1.5 meters above the floor of external wall energy saving and insulation project in project A; 12 wall cracks, 8 damaged wall corners, and 3 serious wall depressions. According to the investigation of construction drawings and community residents, the wall cracks and damage are mostly caused by external force collision and accidental collision of vehicles; but the decorative protection blocks of the insulation layer on the construction drawing are not laid, but directly decorated. This directly leads to the strength of the external wall is insufficient, resulting in the wall in a short period of damage.

5. Measures to deal with the external wall insulation construction problems of the 5 A project

5.1. Adjust the construction plan to avoid environmental impact

The construction of external wall insulation structure is strictly prohibited in winter, and low temperature and precipitation are the biggest factors affecting the construction. When construction temperature may not be lower than 5°C, 5 level of natural wind and fog climate conditions shall not be the construction work, otherwise not only affect the material maintenance time, material is frozen will destroy the product quality, thus cracking, water resistance, seriously affect the overall quality of the thermal insulation system. When the construction average air temperature is low, the appropriate amount of polymer adhesive or water reducing agent can be mixed into the bonding mortar to change the overall nature of the bonding mortar or reduce the bubbles in the mortar, so as to resist the influence of low temperature on the bonding curing.

It is forbidden to conduct construction in rainy days. Before the insulation structure is formed, the high water content of the material is too easy to lead to quality defects such as frost and condensation in the insulation system. When the rain and snow weather occurs in the construction process, the construction should be stopped in time to protect the construction working face, the curing time of the bonding layer mortar should be appropriately extended, and the construction can be carried out only after the surface is completely dry.

5.2. Optimize the construction technology of external wall thermal insulation

5.2.1. Base treatment of building exterior wall

Exterior wall insulation construction of the basic surface should not be too dry, before the construction of oil, release agent hinder bonding adhesion, raised, empty drum and loose parts should be made one by one and leveling, the basic surface shall not be layer, empty drum, cracks, basic surface shall not have powder, peeling, ash, alkali phenomenon. In the construction and transformation of the external insulation of the original building, the surface coating of the original wall should be completely removed, the empty and hollow part of the original veneer brick should be removed, and the too smooth parts should be polished to ensure that the insulation structure is closely bonded to the original wall to ensure the stable and reliable project quality.

The service cycle of project A building complex is short, most of the exterior walls are in good condition, and some of the cracked empty walls can be constructed directly on the surface of the exterior wall after foundation treatment. Part of the empty drum and powder wall are cleaned manually and cut around the treatment surface to ensure the bonding strength between the leveling layer and the wall; mechanically clean the wall within 1-2 meters of the open air duct to avoid the influence of oil pollution on the adhesion. After the problem wall is cleaned, the chisel wall is leveled with the waterproof bonding mortar to ensure the flatness of the base wall, and the construction of the next process can be carried out with the mortar hardening.

5.2.2. Application of composite thermal insulation materials

The use of composite materials in the external wall insulation construction can effectively improve the engineering quality and reduce the construction cost.

In this project, The base treatment plaster of the insulation wall and the bonding mortar are mixed with 15 mm long polymerization material short fiber, The incorporation of this fibrous material creates the fibrous skeleton in the mortar, Greatly improve the mortar bonding properties and tensile strength, Can resist the influence of mortar shrinkage and external impact on the adhesive layer, Effectively reduce the production of mortar dry crack; At the same time, the mortar with equal proportion of 20% mortar cement agent, The incorporation of the cementing agent can significantly improve the mechanical properties of the mortar, Reduce the amount of water used in the mortar, Improve the bonding strength of bonding mortar, Also greatly enhance the waterproof and impermeability of the base mortar, Can Have better bonding and impermeability ability under the same base treatment condition.

Select 15% granular expanded verdellite in the selection of expanded polystyrene board (EPS). Compared with the general insulation block, the unit quality of this block has increased by 10%, but the insulation effect, strength, wear resistance and fire retardant have been improved to a certain extent.

5.2.3. Laying of surface layer mesh cloth

The surface mesh cloth is sandwiched between the two bonding mortar, forming a high strength overall structure with the mortar, which can effectively resist the impact of external factors, and the mesh cloth pulls the insulation block into a whole, to prevent the large area of stripping damage during the mild cracking and weak bonding.

The laying of the grid cloth should be made by two plastering methods. First, apply a layer of plaster paste with an area larger than the mesh cloth, and then press the grid cloth into the wet plaster paste. When the plaster paste is slightly dry and hard to touch, the second plaster paste should be applied. The door and window opening must be strengthened network processing, along the mouth corner to do the package processing. After the net cloth is stuck to prevent rain erosion or collision, easy to collide with the Yang Angle, doors and Windows should take protective measures, the feeding mouth part to take pollution prevention measures, surface damage or pollution should be treated immediately. After construction, the wall surface shall be protected from the collision of other objects within 5 hours, and the protective layer shall not be rained within 8 hours. After the protective layer is finally set, water shall be sprayed in time. When the average temperature is higher than 12℃, it shall not be less than 50 hours, and it shall not be less than 70 hours when lower than 10℃.

5.3. Strict control of material quality

5.3.1. Standardize the material procurement process

The procurement of construction materials should follow the following principles:

First, on the basis of fully ensuring the quality, we should buy the necessary materials at the most economical price. Two is to each kind of raw material price (goods) more than three, the best of the best. Third, the on-site supervisor, the on-site representative of Party B and the project department personnel shall be informed in advance of the admission of the materials before the construction. Fourth, the supervisor, the resident representative of Party B and the project department shall check and accept the incoming raw materials according to the sample materials submitted by the supplier. If neither party has any objection, the custodian shall be responsible for checking all the original materials entering the site and handling the corresponding warehousing procedures on the site. Fifth, the custodian personnel is responsible for receiving all the entry data with the qualification certificate, inspection result report and relevant data.

5.3.2. Strengthen the site management of materials

First of all, it is necessary to establish and improve the stacking management system and material stacking responsibility system of the site construction materials. The site construction materials should be carried out in strict accordance with the requirements of the site plan following the overall site planning, and the site staff is responsible for the specific responsibility. For inflammable, explosive and light materials, the corresponding site should be arranged for stacking, and the incoming quantity and the stacking density should be strictly controlled to ensure the safety of materials and personnel.

Secondly, it is necessary to further strengthen the management of the overall layout of the site. According to different construction stages, the changes of materials and materials, design changes and other actual conditions, timely adjust the stacking position on the site, keep the path smooth, and reduce the secondary tilt and reverse transportation. Understand and accurately grasp all the material construction progress and engineering materials related information anytime and anywhere, do a good job of balancing the material adjustment, correctly and reasonably organize the construction of all materials. The detailed preparation of the material preparation scheme must be strict and reliable, and

DOI: 10.54254/2755-2721/91/20241106

ensure that it can be timely and accurately used to ensure the actual construction technology requirements.

In addition, the construction site must be responsible for the supervision and management of all materials and materials, the materials must be qualified; the number and configuration of material personnel shall be able to promote the normal production and processing. The construction operation management personnel shall also be responsible for the communication and coordination of the construction site to meet the smooth progress of the construction progress.

6. Conclusion

The application of external wall energy saving insulation technology can not only provide people with more comfortable production and living environment and good living environment, but also solve the problem of energy restriction of China's economic development "bottleneck" fundamental way, and energy saving construction technology is the basic technology of building energy saving, is an important way to enhance the technical level of construction industry, the sustainable development of China plays an important role.

Building energy saving heat preservation technology has great potential, but due to the heat preservation technology development time is relatively short, lead to the current building insulation technology in our country there are a lot of problems to be solved, this not only need the architects 'hard work, but also need the joint efforts of the social from all walks of life, believe that as long as we with scientific vision, realistic attitude, down-to-earth style of work together, China's building energy saving heat preservation technology can be faster and better development.

References

[1] Shen Yandi. Study on the energy saving effect of external insulation wall in residential buildings in hot summer and cold winter [D]. Zhejiang University, 2017.
[2] Bi Daiyou. Research on the quality control of external insulation system of building exterior wall [D]. Harbin Engineering University, 2017.
[3] week practice. Research on the application of thermal insulation materials in external wall insulation [D]. Xihua University, 2017.
[4] Yang Shaowei, Zhang Weijie. Research on the impact of external wall thermal insulation on building energy conservation in hot summer and cold winter areas [J]. Building energy efficiency, 2020,48 (11): 102-105.
[5] Wang Shaowei. Construction technology of building exterior wall insulation and energy-saving materials analysis [J]. Green and environmental protection building materials, 2020 (11): 114-115.
[6] Ma Xing, Guo Jie, Zhang Xiaojun. Discussion on the construction technology of external insulation and energy saving in construction engineering [J]. Residential and Real Estate, 2020 (30): 44 + 46.
[7] Wang Wei. Research on construction technology and construction technology of residential engineering [J]. Engineering construction and Design, 2020 (19): 209-210 + 213.
[8] Jin Jiasheng. The application of external wall thermal insulation technology in construction engineering construction [J]. Ceramics, 2020 (09): 108-109.
[9] Wang Longlong. Study on the durability of external insulation system of thin plastering exterior wall in cold areas [D]. Xi'an University of Architecture and Technology, 2020.
[10] Hua Xue. Study on the thermal adaptability of external wall insulation system in cold and cold areas [D]. Shenyang Jianzhu University, 2018.
[11] Yin sound. Application of the external insulation system in the reconstruction project of old residential area [N]. China Building Materials News, 2019-09-09 (004).
[12] In the association. Eight advantages of the application of external wall insulation technology [N]. China Building Materials News, 2019-02-26 (004).

DOI: 10.54254/2755-2721/91/20241067

Truss structural damage identification based on Bayesian probabilistic inference

Peiyang Song

School of Civil Engineering, Southwest Jiaotong University, Chengdu, China

1811030417@stu.hrbust.edu.cn

Abstract. A truss is a common structure in structural engineering, but it will inevitably be damaged when used. It is necessary to establish a reasonable and accurate structural damage identification method to effectively detect the damage and ensure the safe state of the structure. This paper uses a Monte Carlo sampling algorithm for modeling programming based on Bayesian theory for damage identification of statically indeterminate truss structures. By comparing different loading schemes and monitoring node measurement schemes, this paper derives the law of truss optimization. It obtains the optimal posterior distribution of damaged members to find the optimal identification scheme. In addition, using the displacement calculation formula of the truss, this paper gives the optimization direction of the damage identification monitoring scheme. The results show that when the axial force of the damaged member is larger than that of other members, the updating effect of the damaged member is better . And the feasibility of the method is verified by using the actual displacement value and damage value. The method proposed in this paper can effectively update the damage values of bars using known displacement information. However, the method in this paper also has the deficiency of not considering the iterative use of data, and it needs to be improved with the idea of combining the information.

Keywords: Structural Damage Identification, Bayesian Inference, Bayesian Updating, Structural Health Monitoring.

1. Introduction

In recent years, significant progress has been made in the development of structural engineering. However, the structure is inevitably affected by factors such as loads and environmental changes during the service stage, leading to internal defects or reduced structure performance. The safety problems of the structure are constantly highlighted. To ensure the safety and durability of structures, engineering refers to the process of exploring the damage state of a structure as structural damage identification. Since structural damage on engineering is generally difficult to detect, the structure only shows obvious abnormal reaction when the damage is serious, when the structure's performance will be significantly reduced, and even jeopardize the safe use of the structure. In order to ensure the use of the structure in a safe condition, it is necessary to establish a reasonable and accurate method for identifying structural damage in existing structures.

The current system identification methods can be categorized into deterministic and uncertainty methods depending on the deterministic nature of damage identification[1]. Traditional deterministic methods are simple and easy to apply, but the actual damage problems of engineering structures have huge uncertainties, and the actual situation of the structure needs to be examined. Probability-based uncertainty methods can rationally apply established information to implement more accurate evaluations[2],which are currently the main research direction in this field. The Bayesian method is one such approach, which posits that the parameter to be updated is a random variable whose prior distribution is known[3]. In this context, other relevant known conditions can be employed to infer the parameter, establish the likelihood function, derive the posterior distribution of the variable, and subsequently analyze the parameter quantitatively in accordance with the numerical characteristics of the distribution. This method can effectively utilize the actual data and reduce the uncertainty of the a priori model, thereby enhancing the accuracy of the prediction. It is capable of identifying whether a structure is damaged and quantifying the extent and location of such damage. This has led to its widespread adoption in the engineering field.

This paper primarily analyze the damage of statically indeterminate truss structures based on Bayesian updating theory and Monte Carlo sampling algorithm. Provided that the stiffness of all the members and the prior distribution of the stiffness of the damaged member are known, the stiffness (cross-sectional area) of the damaged member is sampled in large quantities so as to update the stiffness of the damaged member. By means of a continuous process of optimization, both the loading scheme and the structural response value measurement scheme are refined. This enables the optimal posterior distribution of the target member to be identified, thus formulating the optimal monitoring scheme. The relationship between the posterior distribution and the actual values is verified using the real displacement values. In conclusion, the law of truss damage identification is succinctly summarized.

2. Research Methodology

2.1. Bayesian Inference

Bayesian inference establishes the posterior joint probability distribution function of the desired random variable and applies a reasonable sampling method to obtain the marginal probability of each parameter variable. After obtaining the sampling distribution of a random variable, the probability distribution of the parameters of the random variable is appraised based on the characteristics of the mean and standard deviation of the distribution. In structural analysis applications, the random variable can be the stiffness, mass, cross-sectional area, and other relevant structural parameters[4]. Furthermore, Bayesian inference can be employed in an iterative manner. The updated posterior distribution can be utilized as a new prior, and a new posterior distribution can be derived according to the new information. This process is referred to as a Bayesian update.

In the context of structural engineering, events A and B can be conceptualized as random variables, designated as x and y, respectively. The Bayesian formulation[5] can be expressed through the following conditional probability distribution: assuming that the displacement value Y of a structure can be expressed as a function of the load value P and the structural parameter X

$$Y = (X, P) \tag{1}$$

In the event that the prior probability density distribution function $f_X(x)$ of a random variable x is known, then the joint probability density function of X and Y is:

$$f_{XY}(x, y) = f_Y(y|x) \cdot f_X(x) = f_X(x|y) \cdot f_Y(y) \tag{2}$$

The prior probability distribution function of y, a standardized constant, is denoted by $f_Y(y)$. This distribution does not contain any information about x. Consequently, a constant can be used to replace it. Consequently, the posterior distribution of x is given by[6-8]

$$f_X(x|y) = \frac{f_Y(y|x) \cdot f_X(x)}{f_Y(y)} = \frac{1}{c} f_Y(y|x) \cdot f_X(x) \tag{3}$$

DOI: 10.54254/2755-2721/91/20241067

In essence, Bayesian inference is the process by which subjective predictions (prior distribution) are continually corrected (conditional distribution) by real situations to implement more accurate information (posterior distribution).

2.2. Monte Carlo system of sampling

In the Bayesian updating process, solving equation (3) yields the posterior probability distribution of the parameters, enabling the structure's analysis. However, the form of this mathematical model is complex and difficult to solve. In order to obtain the form of the probability density distribution of a parameter, it is often necessary to solve it using sampling techniques. Consequently, in recent years, there has been a growing tendency to employ probabilistic sampling simulations to address such issues. The most frequently utilized method in this regard is the Monte Carlo sampling approach[9-11].

Monte Carlo methods are based on probabilistic and statistical theoretical approaches that utilize random numbers to solve computational problems. This is achieved by modelling the problem being solved in terms of corresponding probabilities, with computers then employed to implement statistical simulations or sampling in order to obtain an approximate solution to the problem. The fundamental concept is to obtain a substantial number of samples from a specified distribution and employ these samples to examine the characteristics of the distribution in question. The method circumvents the mathematical complexities inherent to structural reliability analysis by procuring a more precise a posterior probability, irrespective of whether the state function is nonlinear or not, and whether the random variable is non-normal or not, provided that the number of simulations is sufficiently large.

The particular sampling method employed was that of acceptance-rejection sampling[12]. The fundamental idea of this algorithm is that when sampling a complex distribution $f(y)$, which is difficult to solve, by considering samples from another distribution$g\ (y)$, which is straightforward to sample. Then a mechanism is employed to remove some samples, thereby ensuring that the remaining samples are drawn from the same distribution as the desired distribution $f(y)$. This method permits the sampling of complex probability distributions, obviating the necessity for the calculation of the objective function. The specific implementation steps are as follows:

- A sample y_i is taken from $g\ (y)$.
- A random number, u_i, is sampled from the uniform distribution, $U(0,1)$.
- If the equation $u_i \leq \frac{f\,(y)}{cg\ (y)}$ holds, the sample y_i is deemed acceptable, otherwise rejected.

2.3. The principle of virtual work

Given that the criteria for acceptance of sampling is based on the displacement value, the optimal direction can be identified by calculating the displacement of the truss. The virtual work principle of force can be defined as follows: The total virtual work done by the external force equals the total virtual work done by the internal force on each microsegment in its corresponding deformation. In other words, the virtual work of the external force is equal to the virtual work of deformation[13]. This results in the truss displacement formula, which can be expressed as follows:

$$\Delta = \sum \left(\frac{N_p \cdot \overline{N}}{EA} l \right)_i \tag{4}$$

3. Research findings and discussion

3.1. The object of study

This paper presents a damage analysis of a statically indeterminate truss structure under ideal conditions. In light of the statically indeterminate truss's structural configuration and the stiffness of all its members, it is assumed that damage exists in two of the truss members and that the prior distribution of two members is known. The specific values are shown in Figure 1 and Table 1.

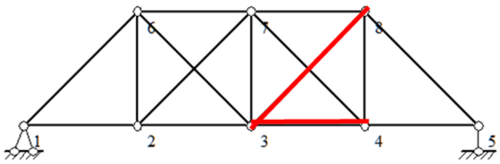

Figure 1. Research objects truss.

In Figure 1, the red color represents the damaged members, and the distance and height between the two nodes of the transverse truss are 15 metres. The distribution of damaged members before the implementation of the proposed solution is as follows:

The prior distribution of member 3-4 obeys the uniform distribution U(0.56,1.54).

The prior distribution of member 3-8 obeys the uniform distribution U(0.28,1.26).

Table 1. Stiffness of other members

Member	1-2	2-3	4-5	1-6	6-7	7-8	2-7
EA($10^5 kN/m$)	1.4	1.33	1.4	1.54	1.47	1.47	1.25
Member	8-5	2-6	3-6	3-7	4-8	4-7	
EA($10^5 kN/m$)	1.54	1.26	1.12	1.12	1.26	1.05	

In this study, the trusses were assumed to be linearly elastic, with a certain degree of measurement error. It was assumed that the modulus of elasticity E was constant and identical for all data set members presented in Table 1. Subsequently, each item in the table was divided by E to conduct the cross-sectional area sampling. The proposed methodology for modifying the loading points and monitoring the displacement points is constrained by the following parameters: the maximum load that can be applied at each node is limited to 100kN (either vertically or horizontally), and each node can be monitored for x- and y-direction displacements.

3.2. Research process

Specifically, the aforementioned process was achieved through the utilization of Opensees modelling and Excel to plot histograms in the following steps:

- A truss model is constructed, the value of the damaged stiffness of the target member is posited within the a priori distribution, and then the displacement values are output and recorded.
- A truss model with the same structural characteristics is created anew, selected at random from the prior distribution, and the randomly generated values are assigned to the stiffness of the member, thereby producing the corresponding displacement values.
- A comparison of the displacement values generated from the models constructed in the initial two steps is next, with particular attention paid to the error. Acceptance-rejection sampling should then be employed to determine whether the sampled data should be accepted, with the resulting stiffness outputted if so.
- A substantial number of repetitive samples must be performed in order to generate a collection of samples, thus obtaining the posterior distribution.
- The obtained posterior distribution was plotted as a histogram in Excel, and the mean value and standard deviation of the data should be calculated to observe the optimization situation.
- Steps 2 to 5 were repeated, with both the loading node and the monitoring displacement node undergoing alteration until the optimal posterior distribution was achieved.
- Once the optimal solution has been identified, the damaged member is updated according to the true displacement values calculated from the optimal solution. Subsequently, the results are compared with the true damage values in order to verify the conclusions drawn.

DOI: 10.54254/2755-2721/91/20241067

A discussion of the results will now be presented.

3.3. Preliminary study

The preliminary study was predominantly informed by the exhaustive method. The control variable method was employed to implement this process. This entailed fixing the loading node and changing the monitoring displacement node, as well as fixing the monitoring displacement node and changing the loading node. Finally, the corresponding histograms were plotted based on the data output from each scheme.

3.3.1. Influence of load magnitude

The first objective is to investigate the impact of load magnitude by modifying solely the load magnitude while maintaining the loading and monitoring scheme. Given that the impact of load magnitude on displacement is negligible under relative error, the absolute error is employed for execution.

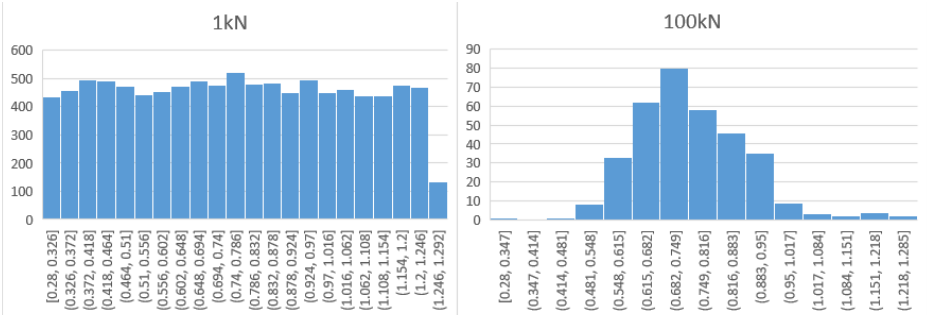

Figure 2. Updating effects with different loads under absolute error

As illustrated in Figure 2, the member exhibits minor updating effects when the load is relatively low, due to the inability to produce more pronounced displacement. However, a pronounced updating effect is observed when the load reaches 100kN. It can be concluded that the greater the load, the more pronounced the updating effect. The following analysis will be applied using a load of 100kN. The damaged members 3-4 and 3-8 have been subjected to a considerable axial force, while the remaining members have experienced either a minimal or negligible axial force.

3.3.2. Stage of exhaustive enumeration of all node schemes

At this stage, it was first observed that the updating results were poor for both target members when loads were applied at the 2-node or the 6-node. Figure 3 illustrates one such case, wherein the vast majority of displacement nodes exhibit an insignificant distribution. Furthermore, the histograms generated when nodes 2 and 6 are employed as monitoring displacement node exhibit a similar pattern to those previously described. This indicates that the information provided by these two nodes is not deemed to be significant and will not be considered in subsequent analyses.

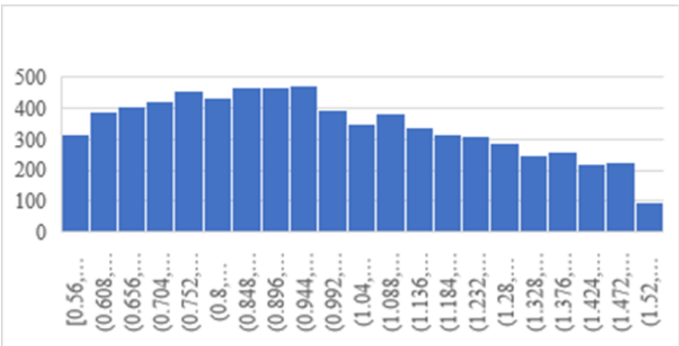

Figure 3. Histogram of the displacement of node 2 monitored with load acting on node 7

DOI: 10.54254/2755-2721/91/20241067

It was additionally determined that when monitoring the 4 node displacements, good updating effects on members 3-4 could be observed with loads acting on any of the nodes. Conversely, a significant updating effect on the 3-8 member was only discernible when monitoring the 8 node displacements. Figure 4 illustrates that even the 2-node loads, subject to poor updating as previously described, can be updated with reasonable accuracy when monitoring 4-node displacements. The findings indicate that monitoring displacement schemes exert a more pronounced influence on the updating effect than loading schemes.

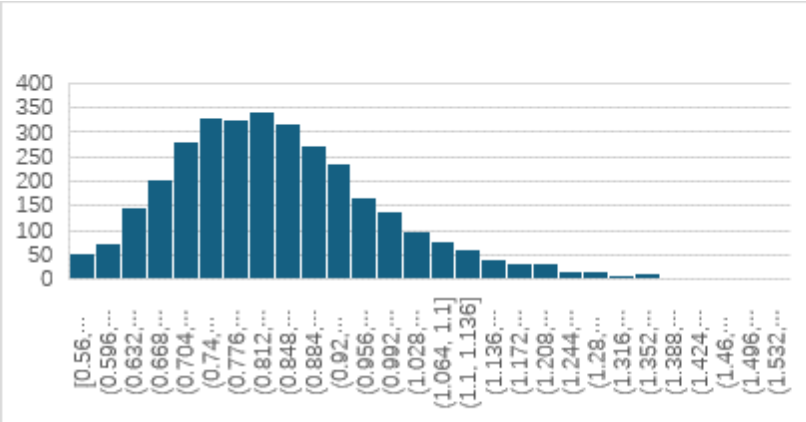

Figure 4. Histogram of 3-4 member with monitoring 4-node displacements and 2-node loading

Given the rather large sample size and the amount of redundant information obtained through the exhaustive method, only a few representative graphs have been selected for presentation. The following is a summary of the initial analysis:

- The greater the load, the more effective the updating.
- The update of nodes 2 and 6 is inadequate, and subsequent optimizations primarily focus on four other nodes.
- Monitoring displacement schemes exerts a more pronounced influence on the updating effect than loading schemes.
- It is not necessary to update both members simultaneously; their respective optimizations should be discussed separately, given the markedly disparate stress conditions under which they operate.

3.4. Deep optimization

Since the samples are judged acceptable or unacceptable by their deviation from the true displacement values, the effect of truss displacement is considered to be analyzed. Given that the displacement formula (4) is a sum formula, if there is a strong correlation between the displacement value and the damaged member, an effective updating effect can be obtained if the term representing the damaged member is larger than the other terms. The only thing that is relevant to the variation scheme in the equation is the axial force. It is therefore necessary to ensure that the value of $\square_{\square} \cdot \bar{\square}$ is large compared to the other members. That is, the axial force on the damaged member reaches its maximum value in both the actual loading case and the virtual force case. The former depends on the loading node, while the latter depends on the monitoring displacement node. The objective of the optimization is to identify a suitable loading node and monitoring displacement node, with the aim of ensuring that the axial force of members 3-4 and 3-8 is greater than that of the other members in both the real and virtual cases.

3.4.1. Optimization of loading schemes

In order to identify the optimal loading scheme for maximizing the axial forces in members 3-4 and 3-8, it is first necessary to consider the application of applying two opposite loads along the direction of

DOI: 10.54254/2755-2721/91/20241067

the parallel member at both ends of the member. This approach can potentially subject the members to significant axial forces, thereby enhancing the scheme's effectiveness. Nevertheless, applying diagonal loads to diagonal brace 3-8 in practice is challenging, which has led to the continued use of the vertical loading scheme.

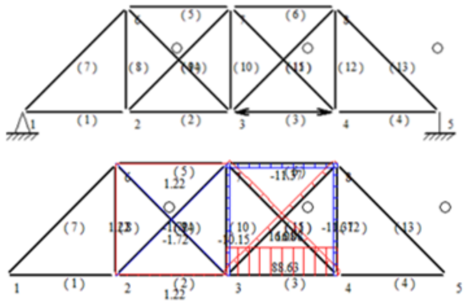

Figure 5. 3-4 Member loading scheme and its axial force diagram

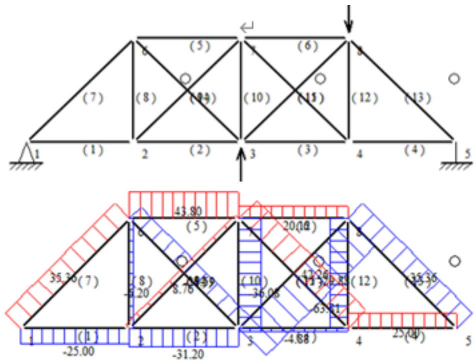

Figure 6. 3-8 Member loading scheme and its axial force diagram

As illustrated in Figure 5 and Figure 6, the damaged members 3-4 and 3-8 have been subjected to a considerable axial force, while the remaining members have experienced either a minimal or negligible axial force.

3.4.2. Optimization of the monitoring node schemes

The preceding theory posits that the optimal monitoring displacement points are also situated at the two nodes which applied loads. Nevertheless, in order to minimize the cost, it is anticipated that only one monitoring node will be selected. Optimization aims to apply a load at a single node and identify the scheme that exhibits the highest axial force in the target member.

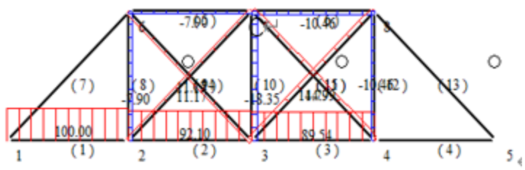

Figure 7. Axial force diagram with horizontal rightward load applied at 4 node only.

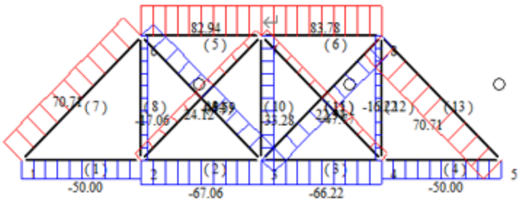

Figure 8. Axial force diagram with vertical upward load applied at 3 node only.

The final selection resulted in node 4 being designated as the monitoring displacement node for rods 3-4, while node 3 was designated as the monitoring displacement point for rods 3-8. The corresponding axial force diagrams are presented in Figure 7 and Figure 8.

3.4.3. Final optimization scheme

The final optimization scheme for the 3-4 member is as follows: in terms of the loading scheme, 100KN is loaded horizontally to the left at the 3 node and 100KN horizontally to the right at the 4 node. Regarding the monitoring node displacement scheme, the 4 node x- and y-direction displacements are monitored concurrently. For this analysis, it is assumed that the absolute error is 0.5mm and the measurement error is 0.5m standard deviation.

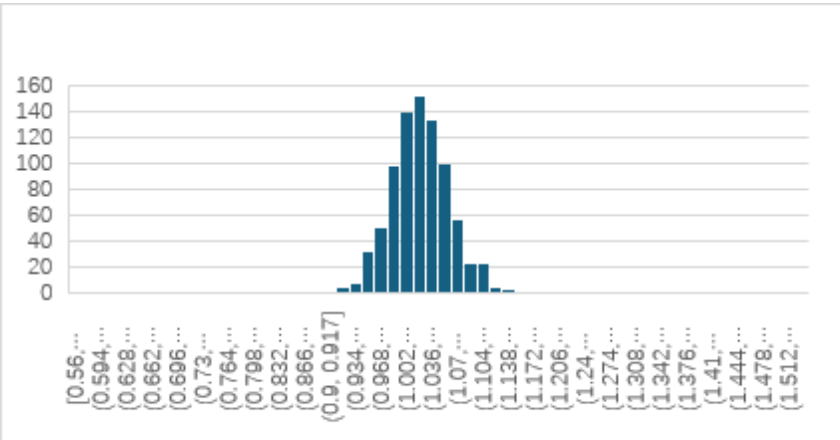

Figure 9. Histogram of the final optimized scheme for member 3-4

The true value of the displacement calculated by modelling is used as the update information: the displacement of 4 node in y and x direction is -0.007746m,0.013214 m, respectively. A histogram is drawn based on the sampled data, as shown in figure. 9. The Figure 9 illustrates that the parameter effectively converges to a concentrated region following a series of transition stages from a uniform initial distribution. The posterior distribution exhibits minimal dispersion, enhancing the optimization's effectiveness. The mean and standard deviation of the sampling data were calculated as 1.029542 and 0.038805, respectively. The true value of the damaged member was determined to be 1.00800, and the difference value between the mean value of the update result and the true value was found to be Δ=1.029542-1.00800=0.021542. This indicates that the updating effect is satisfactory.

The final optimization scheme for the 3-8 member is as follows: in terms of the loading scheme, 100KN is loaded vertically upward at the 3 node and 100KN vertically downward at load 8 node. In terms of the monitoring node displacement scheme, the 3 node x- and y-direction displacements are monitored concurrently. For this analysis, it is assumed that the absolute error is 0.5mm and the measurement error is 0.5m standard deviation. For the purposes of this analysis, it is assumed that the absolute error of the measurement error is 0.5mm and the standard deviation is 0.5m.

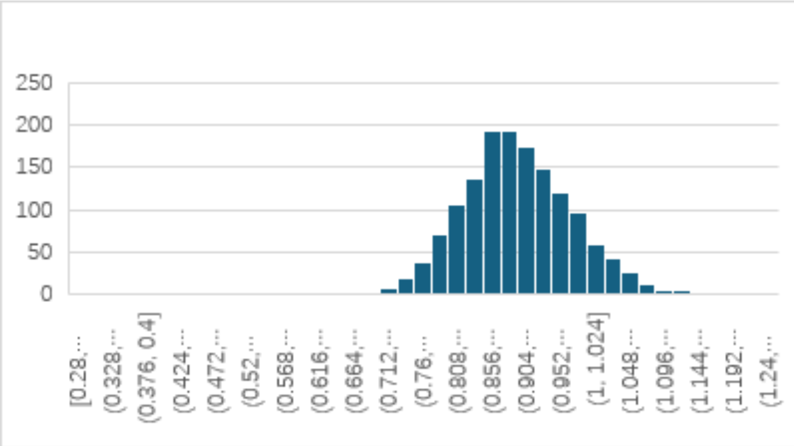

Figure 10. Histogram of the final optimized scheme for member 3-8

The true value of the displacement calculated by modelling is used as the update information: the displacement of node 3 in y and x direction is 0.022509m, -0.005883m respectively. A histogram is drawn based on the sampled data, as shown in Figure. 10. The figure illustrates that the parameter effectively converges to a concentrated region following a series of transition stages from a uniform initial distribution. The posterior distribution exhibits minimal dispersion, enhancing the optimization's effectiveness. The mean and standard deviation of the sampling data were calculated as 0.90361 and 0.074351, respectively. The true value of the damaged member was determined to be 0.87800, and the difference value between the mean value of the update result and the true value was found to be Δ=00.90361-00.87800=0.02561. This indicates that the updating effect is satisfactory.

The above two figures demonstrate the efficacy of the optimization direction proposed in this paper.

4. Conclusion

This paper presents an update of two of the damaged members of the statically indeterminate truss. In the event that the extent of damage to the members is known, the posterior distribution of the stiffness of the damaged members is updated continuously through sampling, thereby realizing an update that is very close to the true value. Concurrently, the optimal monitoring scheme for damage identification of truss members was identified through a process of continuously changing the loading and monitoring displacement node schemes, as well as the principle of virtual work. The following conclusions were then drawn:

1) The greater the magnitude of the load, the more pronounced the beneficial effect of the damaged member's updating. This is due to the fact that larger loads can result in more discernible displacement.
2) The direction of truss damage identification is to adjust the scheme to ensure the axial force of the target member is significantly greater than that of the other members.
3) Although this paper is primarily concerned with statically indeterminate trusses, this law can also be extended to determinate trusses and all trusses statically. The objective of the optimization scheme is to subject the diagonals to shear and the chords to bending moments or direct tension.

Nevertheless, there are some limitations in the methodology employed in this study. For instance, the displacement was not monitored in a single direction, and a step-by-step loading scheme was not attempted. These shortcomings may result in the optimization results not reaching an optimal state. It is proposed that future studies should consider the correlation or overlap between the information provided by the loading and displacement nodes schemes. The combination of two pieces of information that are highly correlated and contain a large amount of similar information will result in a weak boost, which may lead to inefficiency. Conversely, if the two pieces of information do not contain significant overlapping content, they can be considered complementary, which may result in more effective updates. Subsequently, the objective of the future truss optimization scheme will be to determine the most appropriate methodology for selecting the loading nodes and monitoring displacement nodes, to ensure that the information provided by these nodes is complementary.

References

[1] Li X H 2009 *A Bayesian Probabilistic Approach to Structural Parameter Identification and Application* Institute of Engineering Mechanics, China Earthquake Administration
[2] Zhong Z H, Niu J and Wang H 2012 *China Civil Engineering Journal* 45(08) pp 121-130
[3] Feng X, Li G Q and Zhou J 2005 *Earthquake Engineering and Engineering Vibration* (02) pp 105-113
[4] Shen J L 2015 *Structural damage identification based on advanced Bayesian probabilistic inference sampling approach and application in truss structures* Hefei University of Technology
[5] Bernardo J M and Smith A F M 2002 *Bayesian Theory* (New York : John Wiley and Sons Inc)
[6] Beck J L 1989 *American Society of Civil Engineers*
[7] Beck J L and Katafygiotis L S 1991 *Updating of a model and its uncertainties utilizing dynamic test data* Proc. 1st Int. Conf. on Computational Stochastic Mechanics (Boston: Computational Mechanics Publications) pp 125–136
[8] Beck J L and Katafygiotis L S 1998 *Journal Of Engineering Mechanics* 124(4) pp 455-461
[9] Fishman G S 1996 *Monte Carlo: Concepts, Algorithms, and Applications* (Berlin: Springer)
[10] Yuen K V 2010 *Bayesian methods for structural dynamics and civil engineering* (New York : John Wiley and Sons Inc)
[11] Yuen K V and Katafygiotis L S 2005 *Earthquake Engineering & Structural Dynamics* 34(2) pp 167-187
[12] Hastings W K 1970 *Biometrika* 57(1) pp 97-109
[13] Zhou X Z, Lin J H, Hu Z W and Zheng J J 2020 *Journal of Zhejiang University of Technology* 48(02) pp 212-216

Proceedings of the 2nd International Conference on Functional Materials and Civil Engineering
DOI: 10.54254/2755-2721/91/20241107

Advances and Prospects of 3D Semiconductor Nanocomposite Materials for Solar Cells in Renewable Energy

Boyang Sun

Taiyuan University of Technology, School of Materials Science and Engineering, Taiyuan, 030000, China

18630257623@163.com

Abstract. With the escalating environmental pressures, the multifaceted characteristics of 3D materials in terms of energy utilization and stability have attracted widespread attention. This paper employs literature research, surveys, and descriptive research methods to discuss how 3D composite nanomaterials promote further innovation in new solar cells and their application in practical situations. The article mainly focuses on 2D/3D perovskite solar cells, multi-walled carbon nanomaterials, and three-dimensional ordered macroporous materials (3DOM) and deeply explores their roles in various battery frameworks. The research finds that the incorporation of 3D composite nanomaterials has promoted progress in solar cells in terms of conversion efficiency and high transmission speed, but there are still great challenges in terms of popularization and stability. It also emphasizes their far-reaching impact on promoting sustainable energy development. This paper not only provides insights into cutting-edge research but also highlights the profound impact that the development of 3D nanomaterials has on advancing sustainable energy development options. Unlocking the full potential of three-dimensional nanomaterials through interdisciplinary cooperation holds great promise for solving energy problems and creating new fields.

Keywords: 3D Nanomaterials, Dye-Sensitized Solar Cells, 3D Ordered Materials, Perovskite Solar Cells, Multi-carbon wall nanotube materials.

1. Introduction

Based on the major strategic goal of “dual carbon” proposed in China, there is a high national focus on new energy, sustainable, clean, and low-cost nanomaterials for solar cell applications. The development of 3D materials has emerged as a prominent issue, and 3D nanomaterial batteries are a new type of battery structure. Among them, 2D and 3D perovskite batteries have attracted widespread attention due to their high efficiency and low cost. In order to find more efficient materials, this article summarizes a method to merge 2D perovskite layers into 3D structures, and with continuous investment, this field has achieved great success. In addition, through in-depth research and application of 3D large-pore ordered materials, their advantages such as high surface area, rich porosity, and promotion of substance and light interaction have been discovered, and their application in battery electrodes such as 3DOM has been found. In addition, there are still some research gaps, such as three-dimensional nanomaterials in the preparation of new solar cell equipment and higher performance research, that need to be further overcome, discovered and studied with methods with higher efficiency and better preparation processes.

DOI: 10.54254/2755-2721/91/20241107

Research on 3D nanomaterials could help develop low-cost, environmentally friendly batteries, improve energy efficiency, and open up new avenues for future energy development, This review also discusses the prospects and challenges of the development of 3D nanomaterials in solar cells.

2. The application of different nanomaterials in batteries

The application of 3D nanomaterials in solar cells primarily involves the formation of composite material structures to improve the photoelectric conversion efficiency, reduce costs, and increase stability of solar cells through the special properties of their composite material structures. The followings are the applications of different nanomaterials in solar cells.

3D nanomaterial batteries represent a new type of battery structure. 3D nanomaterials, with their excellent performance and wide range of applications, have become popular materials in the field of solar energy. These three-dimensional composite materials, formed by the combination of zero-dimensional particles, one-dimensional nanomaterials, and two-dimensional nanomaterials, offer remarkable advantages in terms of stability, environmental friendliness, and sustainability. Notably, three-dimensional nanomaterials such as 3DOM, three-dimensional carbon nanotube composites, and composite structures in 2D/3D perovskite soar cells all exhibit promising potential for enhancing the performance of solar cells.

The 3D large-pore ordered materials have a larger surface area, unique optical properties, and excellent mass transfer performance, which can improve the adsorption of dye molecules and capture rate. Moreover, they promote the interaction between materials and light, thus exhibiting significant potential in the realm of solar cell applications. For example, in dye-sensitized solar cells (DSSCs), 3DOM TiO_2 thin films serve as photoelectric anodes. Their large-pore structure with a large surface area, good light response, and high conductivity, facilitate the promotion of redox reactions in the electrolyte. Due to the good three-dimensional interwoven, ordered large-pore structure, it can reduce the penetration resistance, improve the diffusion and electron migration efficiency of the electrolyte, and significantly increase the photovoltaic efficiency.

As one of the important components of dye-sensitized batteries, the photoanode not only acts as a channel for the transmission of photogenerated electrons to the transparent conductive oxide substrate but also allows for efficient diffusion of the electrolyte to the anchored dye molecules. It can be said that the photoanode is an important part of ensuring the high power conversion rate and the stability of the related period of DSSCs [1]. According to previous studies, short circuit current (*Jsc*) of the devices is related to electron transfer efficiency, light scattering, and dye absorption, while the open circuit voltage (*Voc*) is mainly determined by the energy difference between the material's Fermi level and the Nernst potential of the redox pair [2-3].

The layered three-dimensional ordered structure in 3D ordered macro/mesoporous TiO_2 (3DOM/m TiO_2) can mitigate electron recombination to some extent, thereby accelerating efficient electron to the electron collector and increasing electron mobility. At the same time, the increased porosity and specific surface area of electrons promote the amount of dye absorption, and through the porous structure, it becomes a light scattering center that is conducive to light collection. The application of this three-dimensional hierarchical macro/meso-TiO_2 structure holds great promise for advancing novel electrode materials with high conversion efficiency and excellent stability.

3. Battery architecture using 3D nanomaterials

The development of solar cells is closely tied to the choice of materials, as different materials give arise to special structures with different characteristics. Among these, the utilization of 3D nanomaterials in battery architecture has emerged as a prominent research area. 3D nanocomposite materials are inseparable from practical applications. 3D nanostructures need to ensure the stability of the structural framework while maintaining the original characteristics of nanomaterials. Notable current architectural approaches encompass three-dimensional network structures in organic solar cell acceptor materials, mixed 2D and 3D perovskite heterostructures in perovskite solar cells, the layered three-dimensional

DOI: 10.54254/2755-2721/91/20241107

ordered structure in the aforementioned 3DOM/m TiO_2, etc [4]. The following takes dye-sensitized batteries and 2D/3D perovskite solar cells as examples.

3.1. Dye-Sensitized batteries

Dye-sensitized batteries possess the advantages of convenient assembly, high cost-effectiveness, a high power conversion rate, relatively stable performance. As an ideal new energy renewable energy source, their success lies in the introduction of nanomaterials as battery electrodes [5].

Among them, three-dimensional multi-walled carbon nanomaterials are quite special. Their bamboo-like structure has rich edge defects, which can overcome the disadvantage of absorbing a small amount of sunlight by absorbing a dye monolayer, and then produce a larger photocurrent by continuous reflection within the film [6]. It promotes the electron transfer dynamics at the electrode- electrolyte interface and greatly improves the energy conversion efficiency.

Zheng Wei, Tao Qi and others conducted research on the preparation and characterization of multi-walled carbon nanotube materials in the electrodes of dye-sensitized batteries. They successfully developed a counter electrode (CE) for dye-sensitized solar cells (DSSCs) [7]. Due to the excellent conductivity and mechanical properties of carbon nanomaterials, graphene CEs have been extensively used to improve their performance in DSSCs. CE materials are all three-dimensional (3D) materials, and can be divided into two types. Dr. Xue Yuhua prepared N-doped graphene foam on a piece of graphene paper and Dr. Li Shuxian manufactured carbon nanotubes as CEs to improve their catalytic activity [8]. The main approach involves using multi-walled carbon nanotube (MWCNTs) as the 3D matrix with nano graphite powder serving as a filler to create CE films on fluorine tin oxide glass. By placing MWCNTs in a strong acid environment to reduce aggregation and using nano graphite powder to increase conductivity, Figure 1 illustrates the working principle of DSSCs with CEs applied to electrodes in the laboratory settings. The composite 3D structure in this device is conducive to accelerating the rate of electron transfer channels between MWCNTs and fluorine tin oxide (FTO) [7].

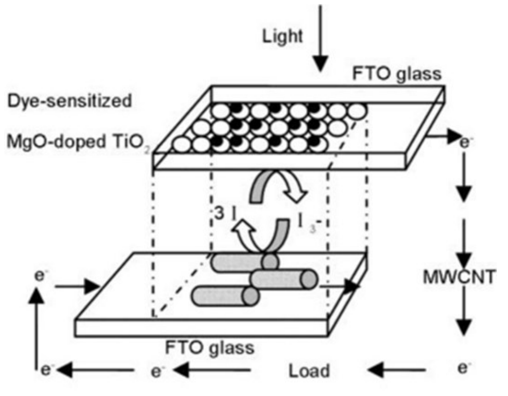

Figure 1. Schematic representation of a DSSC with MWCNTs as the counter-electrode [7]

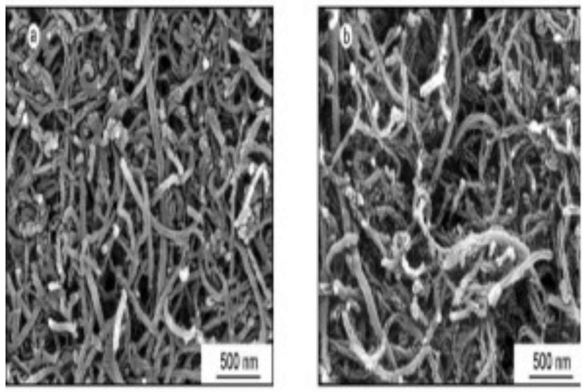

Figure 2. SEM images of the counter-electrodes (a) before and (b) after the acid oxidition [7]

The performance of MWCNTs is characterized by the electrochemical impedance spectra (EIS), Cyclic voltammetry curve (CV), and Volt-ampere characteristic curve (I-V) analysis of the photoelectric properties of DSSCs. Figure 2 illustrates this characterization, where panel (a) and (b) depict high magnification images of MWCNTs on the substrate before and after acid oxidation, respectively. The three-dimensional meso-porous network is formed by multi-walled carbon nanotubes. From this, the characteristics of MWCNTs can be analyzed with a rough surface and a higher specific surface area, which is conducive to the catalysis of CEs. After acid oxidation treatment, the contact between the electrode and the electrolyte is increased. The increase in surface defects and porosity of MWCNTs promotes an increase in specific surface area and catalytic activity. The nano graphite material will enter the pores to form a porous network structure with excellent electrical conductivity, improving the conductivity of the electrode. At the same time, CE materials have good reversibility and stability.

In addition, the research also shows that acid oxidation and nanographite are beneficial to improve conductivity and the photoelectric properties of the battery. However, MWCNTs may weaken the adhesion of the bottom plate, eventually leading to detachment during operation. Research by Tong Jiawei and others has shown that the ionic liquid modification of MWCNTs has maintained good wettability and enhanced thermal conductivity, which can effectively improve the dispersibility and adhesion of MWCNTs in the liquid. This solves the hidden danger of the problem [9].

3.2. Perovskite solar cells (PSCs)

Carrier transport is an important step in promoting the efficiency of the formation of more efficient and stable perovskite solar cells. In their reseach, Saba Rasheed et al. demonstrated the utilization of a new electron transport layer (ETL) comprising tin oxide, graphene nanoribbons (GNRs), nitrogen-doped GNRs(N.GNRs), and gold nanoparticles(Au-NPs). They also proposed three 2D/3D perovskite solar cell architecture as well as the impact on solar cells. These advancements greatly improve the photovoltaic conversion efficiency (PCE) of solar cells.

Although two-dimensional nanomaterials show good characteristics in solar cells, their limited carrier transport rate and narrower absorption range hinder satisfactory PCE results. To address this issue, 2D/3D perovskite batteries have attracted attention. The 2D layer can act as a moisture-proof protective cover safeguarding the 3D layer from degradation. The selection of suitable ETL materials is critical for PSCs performance; among them, metal oxides such as tin oxide (SnO_2) and titanium dioxide (TiO_2) are commonly employed as ETL materials in perovskite solar cells (PSCs) due to their stability and electron conductivity and other advantages. The three structures are TiO_2/SnO_2/GNRs/PSC, c. TiO_2/SnO_2/GNRs/N.GNRs/Au-NPs/PSC, and c. TiO_2/SnO_2/GNRs/N.GNRs/PSC.

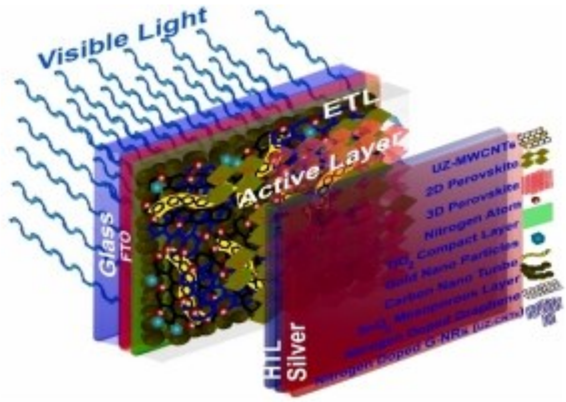

Figure 3. Schematic diagram of c. TiO_2/SnO_2/GNRs/N.GNRs/Au-NPs/Perovskite/PEDOT: PSS/Ag Perovskite Solar Cell [10]

As shown in Figure 3, the three perovskite structures are all composed of FTO glass, which should be cleaned following the standard procedure. After air-drying at room temperature, the pristine FTO glass can exhibit enhanced performance. The second step is to deposit a dense TiO_2 layer. The third step shows different constructions for the three structures. The first sample uses deionized water to make a graphene nanoribbon solution by ultrasonic treatment. In the second sample, nitrogen-doped graphene nanoribbons are formed via probe ultrasonication. And in the third structure, additional components such as gold nanoparticles are incorporated. Subsequently, analysis methods such as ultraviolet-visible spectroscopy were used to detect that the third structure had a smaller band gap and smaller interface resistance with the addition of gold nanoparticles, which is conducive to carrier transport. It also indicates the resonance characteristics of plasmonic nanomaterials, which can better promote charge transfer and achieve higher efficiency [10].

4. Challenges and development trends of solar cells based on 3D nanomaterials

Due to the defects in two-dimensional nanomaterial solar cells, the development of three-dimensional nanomaterials is being focused on [11]. For 3D large-pore ordered materials, the large pore morphology may lead to structural instability and photocatalytic performance is far from ideal in practical application. There are not many types of materials that can be coupled, which is an important problem to be solved for large-scale applications [12]. At the same time, 3D nanomaterials in solar cells, taking 3D perovskite batteries as an example, reduce interface recombination, which also causes the loss of charge transfer, and the extraction and transmission efficiency issues in the three-dimensional grid holes still need to be further improved, and a subsequent study of 2D/3D heterostructures showed higher photoelectric performance and stability [13-14]. And multi-walled composite carbon nanotubes in the application process will also be affected by the solvent environment for a long time. Corrosion impacts long-term performance, and how to balance their own characteristics to adapt to different scenes is still a big challenge.

5. Conclusion

It can be seen that the use of three-dimensional nanomaterials in solar cells can increase the efficiency of light capture and collection capacity of the cell due to its large specific surface area. The three-dimensional spatial grid structure with multi-stage pore structure, porous, large pore, and multi-layer can increase the ability of light reflection and scattering, the light utilization efficiency, and the space utilization rate of materials to a certain extent. It also has the characteristics of an optimized charge transfer path and can freely design a unique charge transfer channel, which can reduce the recombination rate of three-dimensional material space so as to better improve the photoelectric conversion efficiency. At the same time, perovskite solar cells and dye-sensitized cells composed of three-dimensional materials have made progress in stability and light utilization, and the three-dimensional heterogeneous structure in perovskite solar cells better changes the interface quality, reduces the resistance between the electron/hole transport layer, reduces the energy loss during charge transfer, and also improves the environmental adaptability of the battery.

In addition, dye-sensitized battery CE materials improve the stability and activity of the battery, but the adhesion problem also leads to certain hidden dangers, and the ionic liquid modification just solves this problem. Therefore, three-dimensional nanomaterials play an important role in sustainable development and are widely used in solar cells, and their new structural design, material synthesis, photovoltaic conversion, and other characteristics are of great significance for battery research. With the deepening of research, some new three-dimensional nanomaterials in the preparation of photovoltaic cells and performance research gaps and problems will be solved, while there will be more new materials and structures to further improve the photoelectric conversion rate, promote the development of existing technologies, and provide a new path for future sustainable development.

References

[1] Hao, Li, et al., Self-assembled 3DOM macro/mesoporous TiO_2 photoanodes for dye-sensitized solar cells, Applied Surface Science, 2018(439): 1026–33. https://doi.org/10.1016/j.apsusc.2017.12.221

[2] Liang, Chen, et al., Enhanced Photovoltaic Performance of a Dye-Sensitized Solar Cell Using Graphene–TiO_2 Photoanode Prepared by a Novel in Situ Simultaneous Reduction-Hydrolysis Technique, Nanoscale 5, 2013(08): 3481–85, https://doi.org/10.1039/C3NR34059G

[3] Nailiang, Yang, et al., Two-Dimensional Graphene Bridges Enhanced Photoinduced Charge Transport in Dye-Sensitized Solar Cells, ACS Nano 4, 2010(03): 887–94, https://doi.org/10.1021/nn901660v

[4] Xin, Li, et al., Advances in Mixed 2D and 3D Perovskite Heterostructure Solar Cells: A Comprehensive Review, Nano Energy, 2023(118): 108979. https://doi.org/10.1016/j.nanoen.2023.108979

DOI: 10.54254/2755-2721/91/20241107

[5] Prem, Singh, Saud, et al., Dye-Sensitized Solar Cells: Fundamentals, Recent Progress, and Optoelectrical Properties Improvement Strategies, Optical Materials 2024(150): 115242. https://doi.org/10.1016/j.optmat.2024.115242

[6] Won, Jae, Lee, et al., Efficient Dye-Sensitized Solar Cells with Catalytic Multiwall Carbon Nanotube Counter Electrodes, ACS Applied Materials & Interfaces 1, 2009(06): 1145–49. https://doi.org/10.1021/am800249k

[7] Wei, Zheng, et al., Fabrication and Characterization of a Multi-Walled Carbon Nanotube-Based Counter Electrode for Dye-Sensitized Solar Cells, New Carbon Materials 30, 2015(05): 391–96. https://doi.org/10.1016/S1872-5805(15)60198-6

[8] Yuhua, Xue, et al., Nitrogen-Doped Graphene Foams as Metal-Free Counter Electrodes in High-Performance Dye-Sensitized Solar Cells, 2024. https://doi.org/10.1002/anie.201207277

[9] Jiawei, Tong, et al., Tribological properties of ionic liquid modified MWCNTs, MoS_2 and their composite nanofluids, Journal of Engineering science 45, 2023(02): 286–94. https://doi.org/10.13374/j.issn2095-9389.2021.08.05.004

[10] Saba, Rasheed, et al., Comparative Study of 2D/3D Hybrid Perovskite Solar Cell Containing Different Modified Carbon Nanomaterials Based Electron Transport Layers (ETL), Optical Materials, 2023(144): 114364. https://doi.org/10.1016/j.optmat.2023.114364

[11] Shreya, et al., Emerging Advances and Future Prospects of Two Dimensional Nanomaterials Based Solar Cells, Journal of Alloys and Compounds, 2024(1001): 175063. https://doi.org/10.1016/j.jallcom.2024.175063

[12] R, Guo, et al., Recent Progress of Three-dimensionally Ordered Macroporous (3DOM) Materials in Photocatalytic Applications: A Review, Wiley Online Library, 2024. https://onlinelibrary.wiley.com/doi/full/10.1002/smll.202207767

[13] R, Lin, et al., All-Perovskite Tandem Solar Cells with 3D/3D Bilayer Perovskite Heterojunction, Nature, 2023. https://www.nature.com/articles/s41586-023-06278-z?utm_source=xmol&utm_medium=affiliate&utm_content=meta&utm_campaign=DDCN_1_GL01_metadata.

[14] Pengwei, Li, et al., Phase Pure 2D Perovskite for High-Performance 2D–3D Heterostructured Perovskite Solar Cells, Advanced Materials 30, 2018(52): 1805323. https://doi.org/10.1002/adma.201805323

Proceedings of the 2nd International Conference on Functional Materials and Civil Engineering
DOI: 10.54254/2755-2721/91/20241104

Design of an Intelligent Pen Based on Vector Magnetic Sensing

Keyi Ding

School of Electronic Information and Communication, Huazhong University of Science and Technology, Wuhan, Hubei Province, China

18806856991@163.com

Abstract. In the era of interconnected devices, as the intelligence of equipment deepens, human-computer interaction models are continually evolving. People are no longer satisfied with traditional pen-and-paper methods and seek ways to take notes that can be saved and accessed in the cloud at any time. Among smart writing devices, smart pens are critical components. Most current smart pens utilize infrared cameras to capture high-frequency images, recording the coordinates of strokes as they traverse specific coded points. This positioning method requires special paper and has drawbacks such as high costs and low sensitivity. Addressing the shortcomings of common positioning methods, this paper proposes a magnetic positioning method. By establishing an array of magnetic sensors, it aims to achieve precise tracking of the smart pen's tip. The paper first explores the basic magnetic field theory of permanent magnets and introduces the fundamental theory of magnetic dipoles, followed by a discussion on classical magnetic positioning theory. Additionally, the paper analyzes the sources of error in magnetic sensors. Finally, it describes the use of MATLAB to design an app for the real-time calculation and display of handwriting.

Keywords: magnetic sensor array, magnetic field measurement system, localization algorithm.

1. Introduction

With the rapid development of information technology and the widespread use of smart devices, smart pens have emerged as a convenient and efficient input tool, gradually demonstrating their unique advantages in fields such as education, office work, and artistic creation. Smart pens not only fulfill the functions of traditional writing instruments but also utilize digital methods to record, store, and transmit written content, significantly enhancing users' writing experience and data processing capabilities.

Currently, smart pens on the market primarily rely on technologies such as camara [1,2], pressure sensing [3], capacitive sensing, and optical recognition. Although these technologies have achieved some success in practical applications, they also have limitations. For instance, pressure sensors can wear out after prolonged use, leading to decreased measurement accuracy; capacitive sensing technology struggles with multi-touch and complex gesture recognition; and optical recognition technology is easily affected by external lighting, impacting recognition performance. Therefore, finding a more stable and efficient smart pen design has become a focal point of research.

Vector magnetic sensing technology, as an emerging sensing technology, has shown promising application prospects in the field of smart devices in recent years. In 2010, Yang et al. combined particle swarm optimization with the Levenberg-Marquardt (LM) algorithm to achieve the positioning and tracking of three magnetic dipole targets [4]. In 2018, Gao *et al*. applied the LM algorithm for locating moving magnetic targets [5]. Vector magnetic sensors can detect the strength and direction of magnetic fields and convert this information into precise spatial position and orientation data through algorithms. Compared to traditional sensing technologies, vector magnetic sensing offers high sensitivity, strong anti-interference capability, and good stability, making it particularly suitable for application in smart pen design.

This paper aims to explore the design of smart pens based on vector magnetic sensing technology. By analyzing its working principles, key technologies, and application scenarios, we will verify its feasibility and advantages in practical applications. First, we will introduce the basic principles and characteristics of vector magnetic sensors; then, we will detail the system design and hardware implementation of the smart pen; next, we will analyze the software algorithms and data processing methods; finally, we will validate the performance of the smart pen through experiments and practical applications, while also looking ahead to its future development directions.

2. Mathematical Model of Magnetic Positioning Methods

Between 1820 and 1821, J. B. Biot and F. Savart conducted experiments on straight electric currents and electromagnetic forces. They concluded that the electromagnetic force exerted on a point at a distance d from a straight conductor is directly proportional to the current intensity I and inversely proportional to the distance d. This is known as the Biot-Savart Law, and the magnetic positioning studied in this article is based on this principle.

2.1. Biot-Savart Law

As shown in Figure 1, the current element d$\boldsymbol{l}$ has a current intensity of I, point P is any observation point, $\boldsymbol{r}$ is the distance between the current element and point P, and θ is the angle between the line connecting the current element to observation point P and the current element itself. The direction of the magnetic flux density d$\boldsymbol{B}$ generated by the current element at point P can be determined using the right-hand rule of Ampère; at point P, the magnetic flux density direction is perpendicular to the paper and directed inward. The magnitude of the magnetic flux density d$\boldsymbol{B}$ can be obtained using the Biot-Savart law, as indicated in equation (1). The vector form of the Biot-Savart law can be found in equation (2). μ_0 is the magnetic permeability of free space.

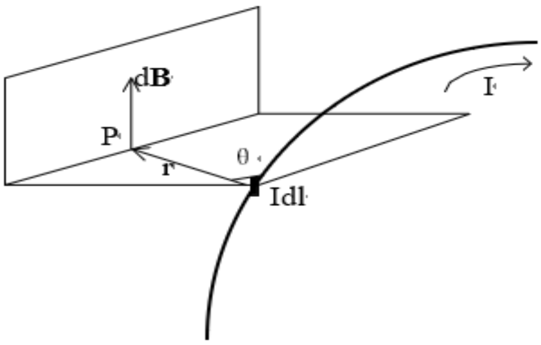

Figure 1. Schematic diagram of the magnetic field generated by a current element at a point in space.

$$|\mathrm{d}\boldsymbol{B}| = \frac{\mu_0}{4\pi}\frac{I|\mathrm{d}\boldsymbol{l}|\sin\theta}{|\boldsymbol{r}|^2} \tag{1}$$

$$\mathrm{d}\boldsymbol{B} = \frac{\mu_0}{4\pi}\frac{I\mathrm{d}\boldsymbol{l}\times\boldsymbol{r}}{|\boldsymbol{r}|^3} \tag{2}$$

DOI: 10.54254/2755-2721/91/20241104

2.2. Magnetic Dipole Localization Model

The magnetic field generated around ferromagnetic targets, together with the background magnetic field, causes a distortion in the surrounding magnetic field, known as magnetic anomaly. When the detection distance exceeds three times the size of the target, it can be treated as a magnetic dipole, with its vector magnetic field represented by Equation (3), where $\boldsymbol{m}$ denotes the target's magnetic moment.

$$\boldsymbol{B}(\boldsymbol{m},\boldsymbol{r}) = \frac{\mu_0}{4\pi}\left[\frac{3(\boldsymbol{m}\cdot\boldsymbol{r})\boldsymbol{r}}{|\boldsymbol{r}|^5} - \frac{\boldsymbol{m}}{|\boldsymbol{r}|^3}\right] \tag{3}$$

2.3. Application of the L-M Algorithm to Solve the Magnetic Dipole Model

The mathematical expression for a magnetic dipole is a high-order nonlinear equation with a very complex form. Although there are currently many optimization algorithms available for solving high-order nonlinear equations, such as Powell's method [6], Downhill Simplex [7], DIRECT [8], and multipole coordinate search methods [9], we ultimately chose the L-M (Levenberg-Marquardt) algorithm [10] as the primary method for solving the magnetic dipole model.

The L-M algorithm is an iterative method used to find the minimum of nonlinear multivariable real functions in the form of sums of squares. It has become a standard solution for nonlinear least squares problems, combining both the gradient descent method and the Gauss-Newton method. The algorithm inherits the local convergence properties of the Gauss-Newton method while also retaining the global characteristics of gradient descent. Because the L-M algorithm utilizes approximations of second-order derivative information, it is significantly faster than gradient-based methods. Essentially, it functions as a second-order gradient method, offering rapid convergence that meets real-time requirements. When the solution obtained using the L-M algorithm differs greatly from the correct solution, the algorithm behaves similarly to gradient descent, resulting in slow convergence but ensuring eventual convergence. Conversely, when the solution is close to the correct answer, the L-M algorithm operates as the Gauss-Newton method.

If m groups of magnetic field data are collected, substituting them into equation (3) will yield a nonlinear system of equations consisting of m equations, as shown in equation (4).

$$\begin{gathered}
\cdots \\
\boldsymbol{f}_i(\boldsymbol{P}) = \boldsymbol{B}_i - \frac{\mu_0}{4\pi}\left\{\frac{3(\boldsymbol{m}\cdot\boldsymbol{r})\boldsymbol{r}}{|\boldsymbol{r}|^5} - \frac{\boldsymbol{m}}{|\boldsymbol{r}|^3}\right\} = \boldsymbol{0} \\
\boldsymbol{f}_{i+1}(\boldsymbol{P}) = \boldsymbol{B}_{i+1} - \frac{\mu_0}{4\pi}\left\{\frac{3(\boldsymbol{m}\cdot\boldsymbol{r})\boldsymbol{r}}{|\boldsymbol{r}|^5} - \frac{\boldsymbol{m}}{|\boldsymbol{r}|^3}\right\} = \boldsymbol{0} \\
\boldsymbol{f}_{i+2}(\boldsymbol{P}) = \boldsymbol{B}_{i+2} - \frac{\mu_0}{4\pi}\left\{\frac{3(\boldsymbol{m}\cdot\boldsymbol{r})\boldsymbol{r}}{|\boldsymbol{r}|^5} - \frac{\boldsymbol{m}}{|\boldsymbol{r}|^3}\right\} = \boldsymbol{0} \\
\cdots
\end{gathered} \tag{4}$$

In Equation (4), $\boldsymbol{r} = (x-a)\boldsymbol{i} + (y-b)\boldsymbol{j} + (z-c)\boldsymbol{k}$ represents the displacement vector between the permanent magnet and observation point P, while $\boldsymbol{m} = n\boldsymbol{i} + p\boldsymbol{j} + q\boldsymbol{k}$ denotes the magnetic moment of the permanent magnet. $\boldsymbol{B}_i$ indicates the magnetic field strength data collected during the i-th measurement. Equation (4) can be succinctly expressed as Equation (5).

$$\boldsymbol{f}_i(\boldsymbol{P}) = \boldsymbol{0}, i = 1,2,\ldots,m \tag{5}$$

In equation (5), $\boldsymbol{P} = (a,b,c,n,p,q)^{\mathrm{T}}$ represents the unknown parameters, which include the position of the permanent magnet (a,b,c) and the magnetic dipole moment (n,p,q).

Solving a system of nonlinear equations can be equivalent to an unconstrained optimization problem, where a target function is constructed to find its optimal solution (or minimum point) within the domain of the independent variables. If the target function consists of the sum of squares of several functions, then the problem of finding its minimum value is referred to as a nonlinear least squares problem.

From equation (5), it can be seen that $\boldsymbol{f}: D \subset R^6 \to R^m$, $\boldsymbol{f} = (f_1, f_2, \ldots, f_m)^T$. The definition of the objective function is provided in equation (6).

DOI: 10.54254/2755-2721/91/20241104

$$\varphi(\boldsymbol{P}) = \frac{1}{2}\boldsymbol{f}(\boldsymbol{P})^T\boldsymbol{f}(\boldsymbol{P}) \tag{6}$$

Clearly, if $\varphi : D \subset R^6 \to R^1$, solving the system of equations (5) is transformed into the problem of finding the optimal solution (or minimum point) for expression (6). This is a nonlinear least squares problem, as indicated in expression (7). We will solve this problem with the L-M algorithm.

$$\min_{x\in D}\varphi(\boldsymbol{P}) = \min_{x\in D}\frac{1}{2}\boldsymbol{f}(\boldsymbol{P})^T\boldsymbol{f}(\boldsymbol{P}) \tag{7}$$

3. Magnetic Sensor Error Analysis

In an ideal scenario, the measurements from the magnetic sensor are completely accurate. Depending on the position of the magnetic sensor, the three-axis readings reflect the projection of the geomagnetic field strength across the three axes, satisfying equations (8) and (9):

$$\boldsymbol{h} = [h_x, h_y, h_z] \tag{8}$$

$$h_x^2 + h_y^2 + h_z^2 = |\boldsymbol{B}|^2 \tag{9}$$

$\boldsymbol{B}$ is the geomagnetic induction intensity vector, and $\boldsymbol{h}$ represents its three components.

For magnetic sensors, errors can be divided into two parts. One part originates from internal factors, including variations in three-axis sensitivity, non-orthogonality of the three axes, and zero bias. The other part comes from external sources, namely hard magnetic interference and soft magnetic interference.

The internal errors are illustrated in the figure below. Hard magnetic interference is caused by permanent magnets near the sensor, while soft magnetic interference affects both the strength and direction of the original magnetic field.

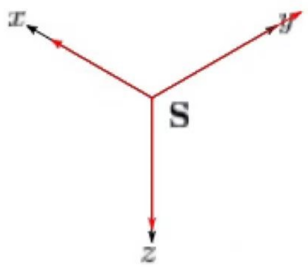

(a). variations in three-axis sensitivity.

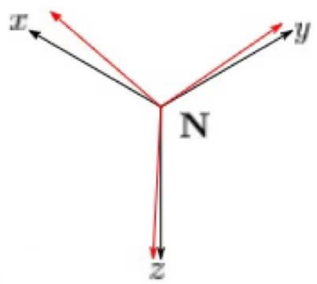

(b). non-orthogonality of the three axes.

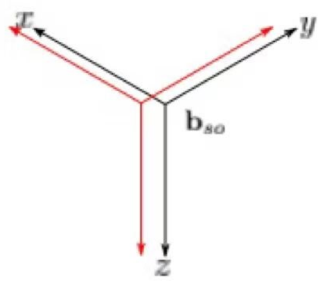

(c). zero bias.

Figure 2. The internal errors.

First, the external magnetic field has been altered due to interference from both soft and hard magnetism. Consider the external interference as shown in Equation (10)

$$\boldsymbol{h_m} = \boldsymbol{I}_{3\times3}\boldsymbol{h}_0 + \boldsymbol{F_h} \tag{10}$$

$\boldsymbol{h}_0$ is the ideal measurement result, $\boldsymbol{I_{3\times3}}$ is a 3×3 matrix representing soft magnetic interference, and $\boldsymbol{F_h}$ is a *3 × 1* vector representing hard magnetic interference. After considering the internal errors, we arrive at Equation (11).

$$\boldsymbol{h} = \boldsymbol{S_{3\times3}N_{3\times3}h_m} + \boldsymbol{F}_{\mathrm{os}} = \boldsymbol{S_{3\times3}N_{3\times3}}(\boldsymbol{I_{3\times3}h_0} + \boldsymbol{F_h}) + \boldsymbol{F}_{\mathrm{os}} \tag{11}$$

In the equation, $\boldsymbol{S_{3\times3}}$ and $\boldsymbol{N_{3\times3}}$ are both *3 × 3* matrices representing sensitivity differences and non-orthogonal effects, while $\boldsymbol{F}_{\mathrm{os}}$ is a *3 × 1* vector indicating zero offset.

The simplification yields the relationship between the true value and the measured value (12).

$$\boldsymbol{h}_0 = \boldsymbol{W}^{-1}(\boldsymbol{h} - \boldsymbol{V}) \tag{12}$$

$\boldsymbol{W}$ is a 3×3 matrix and is symmetric, resulting in only 6 coefficients. $\boldsymbol{V}$ is a 3×1 vector, which has a total of 9 coefficients. If we only consider hard magnetic interference, then we have $\boldsymbol{h}_0 = \boldsymbol{h} - \boldsymbol{V}$. Since $\boldsymbol{h}_0$ lies on the sphere, there is equation (13).

$$\boldsymbol{h}_0{}^{\mathrm{T}}\boldsymbol{h}_0 = (\boldsymbol{h} - \boldsymbol{V})^{\mathrm{T}}(\boldsymbol{h} - \boldsymbol{V}) = |\boldsymbol{B}|^2 \tag{13}$$

Both $\boldsymbol{h}$ and $\boldsymbol{V}$ can be expressed in the form of 3×1 vectors, leading to equation (14).

$$\left[{h_x}^2 + {h_y}^2 + {h_z}^2\right] - \left[h_x\ h_y\ h_z\ 1\right]\begin{bmatrix} 2V_x \\ 2V_y \\ 2V_z \\ B^2 - ({V_x}^2 + {V_y}^2 + {V_z}^2) \end{bmatrix} \tag{14}$$

For the above equation, we can use the least squares method to determine the bias value.

4. Smart Pen Assistant App Design

We have obtained the equations regarding magnetic moment, coordinates, and magnetic induction intensity (4). Using the L-M algorithm API in MATLAB, we solved this equation and applied the least squares method to (14) to determine the bias error. Finally, we plotted the trajectory of the pen.

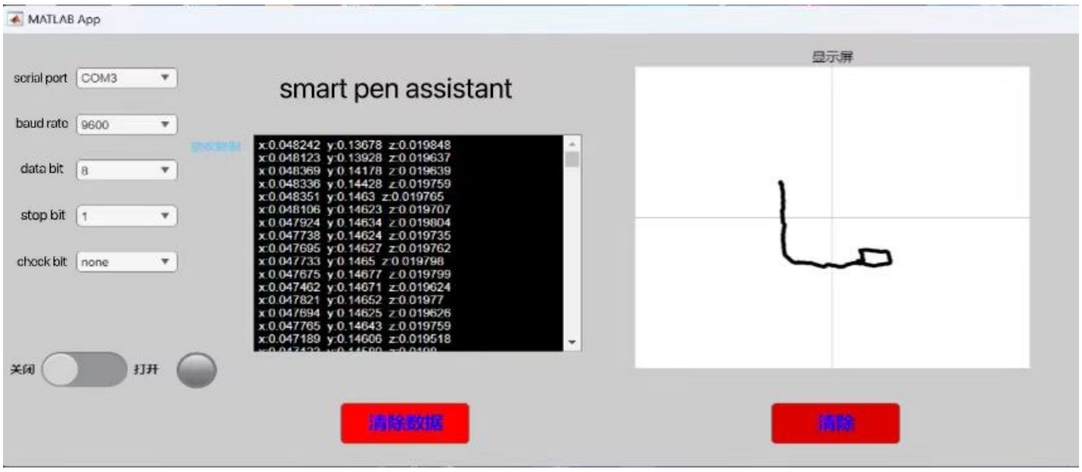

Figure 3. Smart Pen Assistant

In the above figure, the left is the serial port information, the middle is the real-time three-axis magnetic induction intensity of the magnetic sensor array, and the right is the real-time handwriting display.

We designed and built a magnetic sensing array with a cylindrical magnet in a pen, and Figure 4 is a photograph of the real thing.

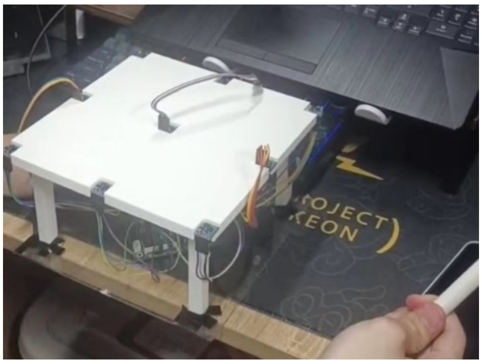

Figure 4. photograph of magnetic sensor arrays and pen

5. Conclusion

In this paper, the algorithm of magnetic sensor array positioning is discussed, the L-M algorithm is used to solve the equations, and the error causes of the magnetic sensor are discussed to improve the positioning accuracy. Finally, MATLAB was used to design an app to solve the uploaded data in real time and display handwriting. We have built the real thing, and the real thing has been tested to have good positioning accuracy, which can display handwriting in real time.

References

[1] Thienen, Dieter Van et al. 2015. Smart Study: Pen and Paper-Based E-Learning.

[2] Siddiqui, A. T., & Muntjir, M. 2017. An Approach to Smart Study using Pen and Paper Learnin g. *International Journal of Emerging Technologies in Learning*, 12(05), 117–27. https://doi.o rg/10.3991/ijet.v12i05.6798.

[3] Tapia-Jaya, Ojeda-Zamalloa, *et al.* 2018. An Intelligent Pen to Assess Anxiety Levels Through Pressure Sensors and Fuzzy Logic. In: Ahram, T., Falcão, C. (eds) *Advances in Human Facto rs in Wearable Technologies and Game Design*. *AHFE 2017. Advances in Intelligent Systems and Computing*, vol 608. Springer, Cham. https://doi.org/10.1007/978-3-319-60639-2_7.

[4] Wan'an Yang, Chao Hu, *et al.* 2010. A New Tracking System for Three Magnetic Objectives. *IE EE Transactions on Magnetics*, 46, 4023-29. https://doi.org/10.1109/TMAG.2010.2076823.

[5] Gao Xiang, Shenggang Yan and Bin Li. 2017. A Novel Method of Localization for Moving Obj ects with an Alternating Magnetic Field. *Sensors*, 17, 923(1–12). https://doi.org/10.3390/s17 040923.

[6] Ding Haiyong, Bian Zhengfu. 2009. A Sub-pixel Registration Approach Based on Powell Algor ithm. *ACTA PHOTONICA SINICA*, 38(12), 3322-27.

[7] J. A. Nelder, R. Mead. 1965. A Simplex Method for Function Minimization. *The Computer Journal*, 7, 308-13.

[8] Mattias Bjorkman, Kenneth Holmstrom. 1999. Global Optimization Using the DIRECT Algorit hm in Matlab. *Advanced Modeling and Optimization*, 1(2), 17-29.

[9] Waltraud Huyer, Arnold Neumaier. 1999. Global Optimization by Multilevel Coordinate Search. *Journal of Global Optimization*, 14, 331-55.

[10] Lourakis. 2005. A Brief Description of the Levenberg-Marquardt Algorithm Implemened by levmar.

Proceedings of the 2nd International Conference on Functional Materials and Civil Engineering
DOI: 10.54254/2755-2721/91/20241071

Bayesian updating of truss structures using OpenSees

Zixuan Wang

School of Construction Engineering, Dalian University of Technology, China

wzx20020122@mail.dlut.edu.cn

Abstract. The study of Bayesian updating of truss structures using The Open System for Earthquake Engineering Simulation (OpenSees) can not only promote the application of Bayesian methods in structural engineering, but also provide a strong support for structural health monitoring in practical engineering. This paper proposes a method of Bayesian updating of truss structures using OpenSees to improve the accuracy of structural analysis and prediction. Based on OpenSees, a finite element model with a truss structure as an example is established, the basic parameters such as nodes, units, material properties and boundary conditions are defined, and the prior distributions of the initial parameters are set by empirical judgment. After collecting observational data such as structural response, Bayes' theorem is utilized to combine the a priori distribution with the observational data to update the parameter estimates. The posterior estimates of the parameters are obtained by constructing the likelihood function and applying the Monte Carlo method to sample from the posterior distribution. Numerical simulations are performed using the updated parameters, and the simulation results are compared with the observed data to verify the accuracy and reliability of the model. Finally, structural damage identification is performed based on the updated model. The methodology in this paper provides a systematic framework to dynamically update and optimize the truss structural model by continuously incorporating new data, significantly improving the prediction's accuracy and reliability.

Keywords: OpenSees, Truss structure, Bayesian updates, Structural damage identification.

1. Introduction

As a common form of engineering structure, truss structure is widely used in bridges, buildings, towers and other fields. It has the advantages of light structure, clear force and convenient construction. However, with the increase of service life and the change of external environment, truss structure will inevitably be damaged and degraded. The reliability of the project is crucial, and it is of great significance to protect people's lives and properties and improve the quality of construction. Over the years, numerous major accidents have been caused by structural damage at home and abroad. For example, in 2018, the Morandi Bridge located in Genoa, Italy, collapsed during a rainstorm, resulting in multiple deaths and injuries [1]; in 2013, the Rana Plaza building in Bangladesh suddenly collapsed during its construction, resulting in the deaths of more than 1,100 people [2]; and in 2020, a residential building located in Tongling, Anhui Province, suddenly collapsed, resulting in the deaths of seven people [3]. All these accidents show that structural deterioration and inadequate maintenance are one of the major causes of building damage. Therefore, timely and accurate assessment of the health status of truss structures is of great significance to ensure structural safety and prolong service life.

DOI: 10.54254/2755-2721/91/20241071

In recent years, with the development of computer technology and sensor technology, Structural Health Monitoring (SHM) technology has been widely applied and studied [4]. By monitoring and analyzing the dynamic response of the structure, the location and degree of damage of the structure can be identified. The Bayesian updating method in the SHM technique has gradually attracted the attention of researchers because of its ability to effectively combine the a priori information and the new observation data to improve the accuracy of parameter estimation [5]. For example, Song Chaolin proposed a Bayesian updating method for probabilistic models in the optimization study of large-span cable-stayed bridges, where random variables are defined based on a priori knowledge, and the posterior updating of the variables is continuously performed to grasp the structural state more accurately [6]. Bayesian updating of structures is beneficial for improving the reliability and safety of engineering.

Meanwhile, the Open System for Earthquake Engineering Simulation (OpenSees) as an open source finite element analysis software, is widely used in civil engineering [7]. Its powerful modeling and analysis functions provide a powerful tool for health monitoring and assessment of truss structures. By using OpenSees for finite element modeling of truss structures, the response of the structure under different loading conditions can be simulated, thus providing the necessary data support for Bayesian updating.

This study will take a case study of a super-static structure as an example, aiming to combine the OpenSees finite element analysis software and Bayesian updating method for damage identification of truss structures. A simple regularity investigation is carried out by establishing a finite element model of the truss structure, simulating its dynamic response under different loading conditions, and updating and identifying the structural parameters by combining with the Bayesian updating method in order to explore a more optimal solution for optimizing the truss.

2. Methodologies

2.1. Bayesian update

The research background of Bayesian updating stems from Bayesian statistics, which is a statistical inference method based on Bayes' theorem [8]. Its core principle i.e. we combine a priori probabilities with observed data in order to compute a posteriori probabilities. Nowadays, Bayesian updating can be used to monitor the system state in real time, adjust the control parameters, and predict the future system behavior, which is important for monitoring engineering structures and so on.

And the application of Bayesian updating in engineering structures has significant value, which can be used to combine sensor data and prior knowledge to monitor the health state of the structure in real time and predict possible damage. By continuously updating the estimation of structural health state, abnormal behavior of the structure can be detected in time and corresponding maintenance measures can be taken to prolong the service life of the structure and reduce the maintenance cost, which helps to more accurately assess the reliability level of the structure. At the same time, it helps to find more economical, safe and reliable structural solutions in the design stage, and to improve the efficiency and quality of the design.

2.2. Likelihood function

Likelihood Function is a fundamental concept in statistical inference used to measure the likelihood of an observation occurring for a given parameter value [9]. The likelihood function plays a central role in parameter estimation and model selection. For a parameterized statistical model, the likelihood function is a function of the observed data as a parameter, reflecting the relative likelihood of different parameter values given the observed data.

Formally, if we have a set of observations $D = \{x_1, x_2, \dots, x_n\}$, and a parameter vector θ, the likelihood function $L(\theta; D)$ is defined as:

$$L(\theta; D) = P(D|\theta) = P(x_1, x_2, \dots, x_n|\theta) \tag{1}$$

In this expression, it is the observations' joint probability or probability density given the parameters. Importantly, although is called a "likelihood function", it is not really a probability distribution, but rather a function of the parameters .

2.3. Monte Carlo

In Bayesian updating, the computation of posterior distributions of parameters often involves complex integrals and exploration of multidimensional spaces. The Monte Carlo method is an effective numerical computation technique that utilizes random sampling to approximate complex integrals and probability distributions [10]. The method estimates the probability distribution of parameters by simulating a large number of random samples. In Bayesian updating, Monte Carlo methods are commonly used to sample from the posterior distribution to characterize the parameters' uncertainty. This paper explores the kernel of the methodology i.e., Bayesian updating of hyperstatic truss structures using Monte Carlo methods via OpenSees. This study entails specifying the structure to be studied, converting the actual structure of the truss into a mathematical model using OpenSees, defining the damage scenarios that need to be estimated, and generating a large number of random samples based on the probability distribution of the problem, which are generated using a normal distribution. Then, each random sample is simulated to obtain the corresponding results, the results are statistically analyzed, and the acceptance of new samples is considered based on the response of the true values.

3. Experimental results and discussion

3.1. Research Objects and Overview

In this paper, the case selected for the research object is shown in Figure 1, which consists of 8 nodes and 15 rods, and the member numbers are all reflected in Figure 1 . Define the damaged rod stiffness, rod 3 and rod 13 obey the uniform distribution U (0.56,1.54) and U (0.28,1.26), respectively, and the known stiffness of each rod is shown in Table 1.

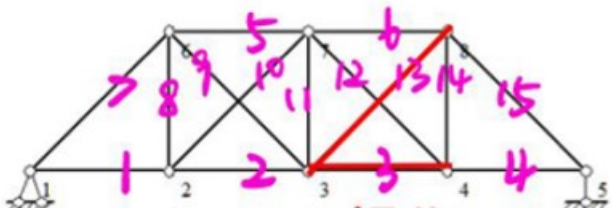

Figure 1. Subjects of experimental study

Table 1. Stiffness of each rod

rod	1	2	4	5	6	7	8	9	10	11	12	14	15
EA/10^5kN·m^2	1.4	1.33	1.4	1.47	1.47	1.54	1.26	1.12	1.05	1.12	1.05	1.26	1.54

3.2. Finite Element Modeling of Truss Structures Based on OpenSees

(1)model

The model data were processed using OpenSees software, and the truss structure's node coordinates, boundary conditions, material properties, and applied loads were defined by Tcl script. Loads were applied to different locations of the truss structure, and different loads were applied to the same locations to monitor the Bayesian updating of the damaged bars at different points under the loads.

(2)Correlate parameters and point displacements

The parameters of the truss structure model are updated and calibrated by the observed measurement point displacement data, thus improving the accuracy and reliability of the model. By continuously collecting and analyzing the measurement point displacement data, possible damage or deterioration of

DOI: 10.54254/2755-2721/91/20241071

the structure during use can be detected, so that timely maintenance measures can be taken to extend the structure's service life.

(3)Updating parameters

Updating the parameters can help identify the actual performance of the structure, including material properties, member stiffness, etc.

(4)Creating models that simulate real-life situations

In the modeling and analysis of truss structures, there may be uncertainties in parameters such as material properties, geometric dimensions, and boundary conditions. Through Monte Carlo method, a large number of random samples can be generated to model these uncertainties, thus reflecting the actual structure more comprehensively.

3.3. Research Methodology Processes and Laws

Loads were applied to different locations of the truss structure and different loads were applied to the same locations to monitor the Bayesian updating of the damaged bars at different points under load. The collected data samples were then counted using excel and histograms were created to observe the data samples more clearly.

This investigation did not obtain a clear pattern gap when different loads were applied at member node 8 under relative error. Thus, it was changed to absolute error by varying the load size, and it was seen that the larger the value of load adopted, the better the optimization effect. As shown in Figure 2 , Figure 3 , Figure 4 , the displacement effect is shown for the cases of 100kN, 10kN and 1kN vertical force applied respectively. Comparing with the 10kN and 1kN cases, the optimization effect is better in the 100kN case, not only in terms of the acceptance rate but also in terms of the statistics such as the mean value of the histogram.

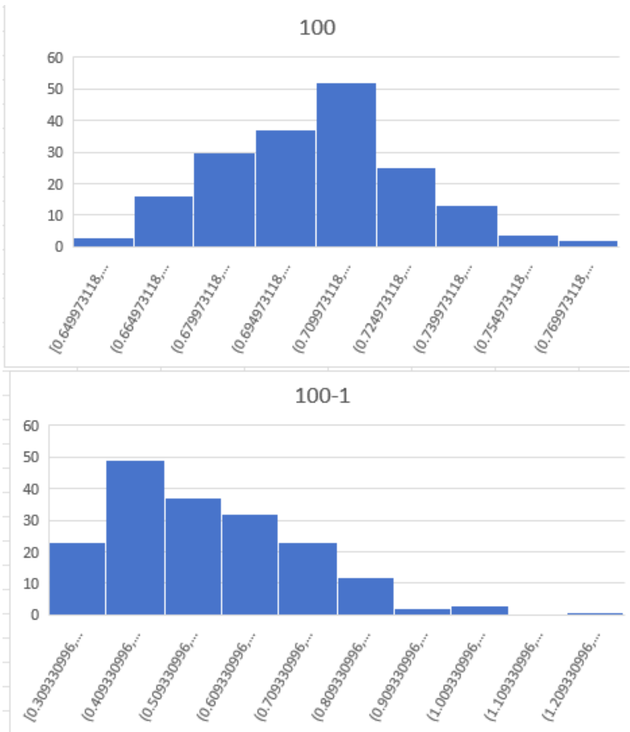

Figure 2. Optimization effect under 100kN load

DOI: 10.54254/2755-2721/91/20241071

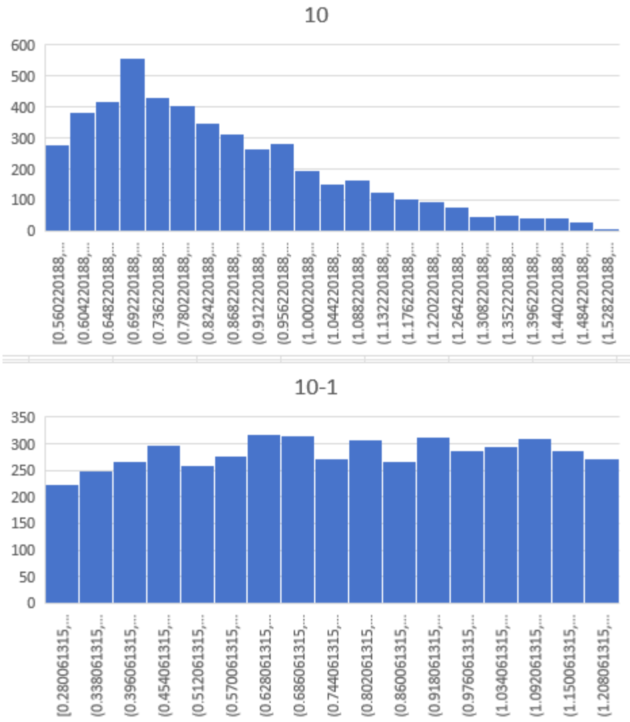

Figure 3. Optimization effect under 10kN load

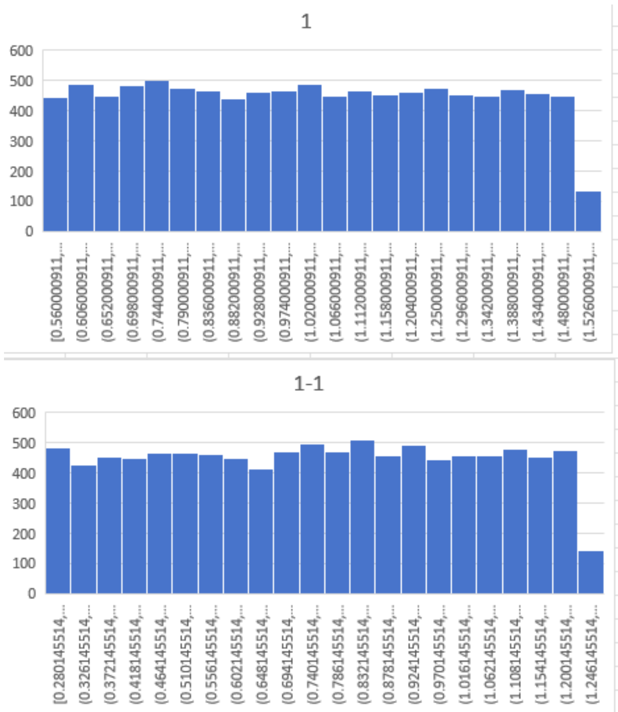

Figure 4. Optimization effect under 1kN load

DOI: 10.54254/2755-2721/91/20241071

Following the application of 100kN vertical force at node 8, comparing the other updates of different node displacements on the damaged rods, it is found that node 4 of this component is optimized best for both rods 3 and 13. As shown in Figure 5 , Figure 6 , Figure 7 , the optimization effect of nodes 3, 4 and 6 on two rods respectively.

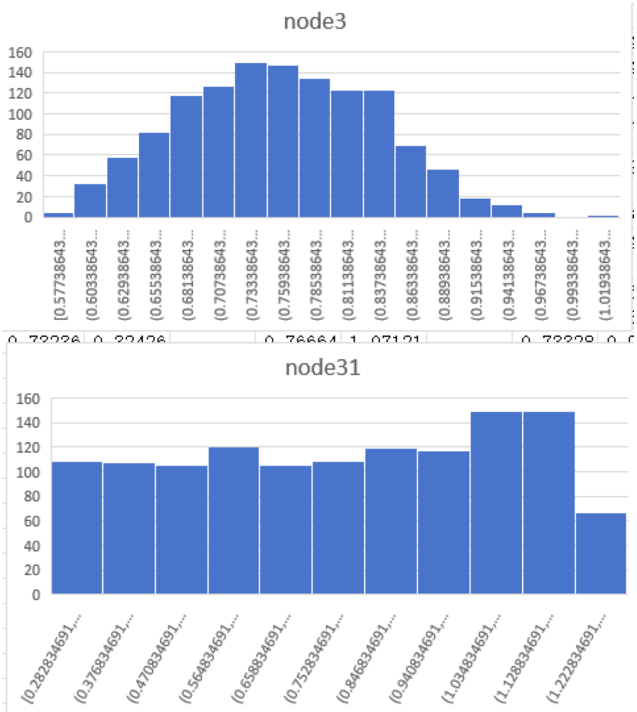

Figure 5. Effect of node 3 on two-rod optimization

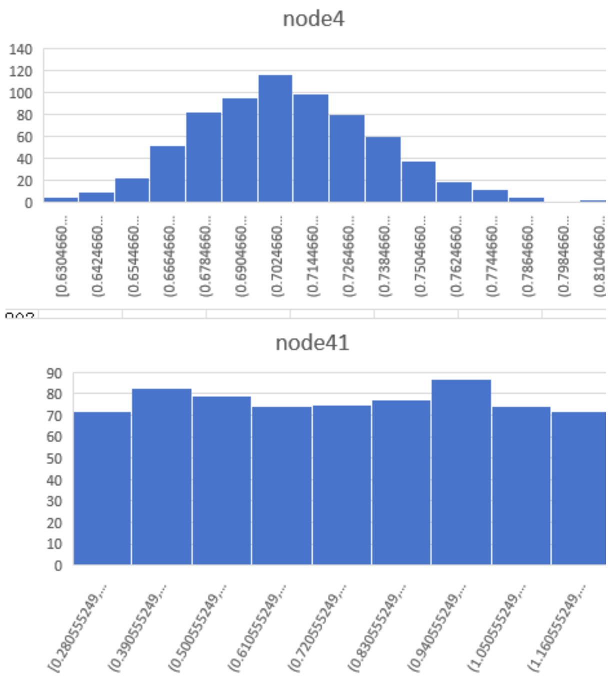

Figure 6. Effect of node 4 on two-rod optimization

DOI: 10.54254/2755-2721/91/20241071

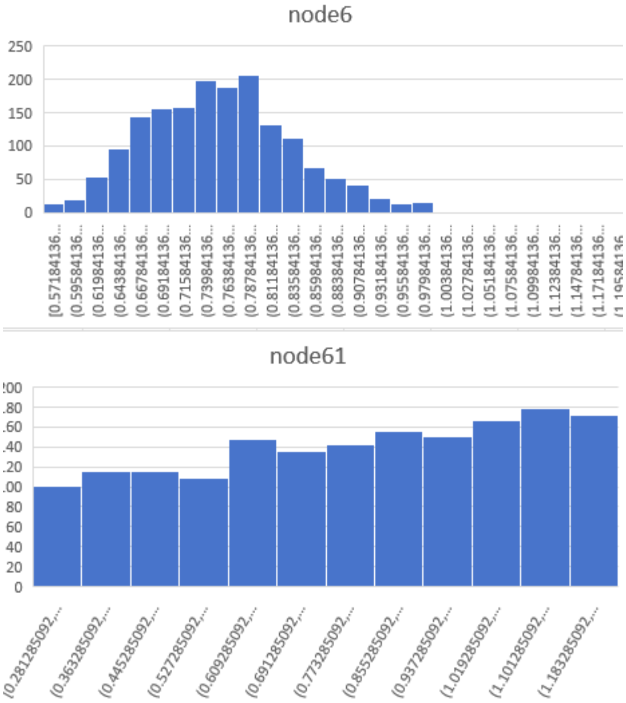

Figure 7. Effect of node 6 on two-rod optimization

Finally, under the absolute error to replace the load added to the node location, monitoring node 4, found that loading at node 3 for a more optimal solution.

Therefore, this investigation adopts loading 100kN vertical force to node 3 and monitoring node 4 as an example to monitor the updating effect on the two rods, and using OpenSees to run again to provide the update of the real displacement situation of the relevant nodes through actual testing, comparing the sample mean and standard deviation, it is obvious to find that this solution has a better updating effect on the lower chord rod 3, while the updating effect on the inclined rod 13 is not good, and the subsequent should be replaced. Other loading schemes, such as applying loads in different directions, should be used to seek a better updating effect on the inclined rods. Meanwhile, the deeper investigation can be combined with the structural mechanics solver, and the principle of virtual work can be applied to better understand the internal force and displacement of the truss.

4. Conclusion

The Bayesian updating method can effectively utilize the observation data to update the parameters of the truss structure model and improve the accuracy of the model. This helps structural health monitoring and damage identification, and provides an important reference for structural design and maintenance.

This paper shows how to build a truss structure model in OpenSees and optimize the model parameters by combining the Bayesian updating method. It also shows the process of exploring the Bayesian updating of more optimal solutions and discovering the simple law with a truss structure as an example, mainly with the loading to node 8 scheme. In the relative error case, the vertical load is defined at node 8 and the load size is changed, and no obvious difference is found; in the absolute error case, the vertical load is defined at node 8 and the load size is changed, and it can be seen that the larger the value of the load is adopted, the better the optimization effect is. Absolute error case, the 100kN vertical load is defined at node 8, monitoring different points displacement, can be found in which node 4 on the optimization of the two rods is the best; 100kN vertical load is defined at different nodes, monitoring point 4, can be found that the load acts on node 3, point 4 displacement on the two rods displacement optimization is the best; loading 100kN vertical load to node 3, monitoring node 4,3 rods optimization better.

DOI: 10.54254/2755-2721/91/20241071

This investigation process can be extended to future work on more complex structural systems and a wider range of application scenarios.

References

[1] Wang X 2018 Modern shift (11) pp 25.
[2] Huang Z 2022 Human Rights Research (04) pp 65-92.
[3] Xiang J 2024 China Real Estate News (004).
[4] Wang N R 2023 Construction Technology (in English) 52(21) pp 33-40.
[5] Tan J L, Fang S E and Jiang X 2023 Building Structure 53(16) pp 91-97.
[6] Song C L 2022 Tongji University.
[7] Fu Z Y, Yin X Q and Wang G X 2023 Journal of Disaster Prevention and Mitigation Engineering 43(06) PP 1463-1475.
[8] Xiao X, Wang Z Y and Li Q W, et al 2022 Engineering Mechanics 39(S1) pp 336-341.
[9] Liang F Z, Song Z J and Zhang Y H 2004 Tianjin:Tianjin University Press.
[10] Jiu Z T and Wang J C 2024 Urban Roads and Bridges and Flood Control (04) pp 228-233+25.

Proceedings of the 2nd International Conference on Functional Materials and Civil Engineering
DOI: 10.54254/2755-2721/91/20241101

Future development trend of batteries for electric vehicles

Zhihan Liao

School of Automobile and Transportation, Tianjin University of Technology and Education, Tianjin, China

0502220210@tute.edu.cn

Abstract. Environmental pollution and energy crisis have become the focus of global attention and urgent issues to be solved. To address these challenges, electric vehicles have emerged. Nowadays, some studies has gradually solved the problem of environmental pollution. However, these studies not note the performance issues with batteries. This article note the cruising range, the charging time and the Battery recycling and reuse technology. Thus the development of batteries will lead to a bright future.

Keywords: Electric vehicle, Energy system technology, Battery development.

1. Introduction

Nowadays, environmental pollution and energy crisis has become the focus of attention and urgent problems to be solved around the world. To deal with these two thorny problems, electric vehicles were appeared. Electric vehicles are environmentally friendly and energy efficient, with no exhaust emissions and reduced consumption of traditional fossil fuels. Battery technology is one of the core technologies of electric vehicles. The battery of an electric vehicle plays a decisive role in the powertrain and safety system of the entire vehicle. The developments of battery status and future trend are of great significance for the wide application of electric vehicles. Currently, the most widely used battery for electric vehicles is the chemical battery. Chemical batteries can be divided into two categories: storage batteries and fuel cells [1].

Hassoun professor studies the sustainable energy storage systems to improve the performance and sustainability of electrochemical energy storage. Dr. Yaxiang Lu proved that layered O3-type NaNi0.12Cu0.12Mg0.12Fe0.15Co0.15Mn0.1Ti0.1Sn0.1Sb0.04O2 have the longer cycling stability and the outstanding rate capability. This material may become the mainstream of battery materials in the future.

2. Electric vehicle battery types and characteristics

2.1. Lead-acid battery

Lead-acid battery is a type of battery with a long history of development, which is low cost, mature technology and high safety. At present, the types of batteries in China are divided according to the positive and negative electrode materials, mainly including VRLA batteries, nickel-cadmium batteries and zinc-manganese batteries, among which VRLABs are widely used in aerospace, communications, transportation and other fields due to the advantages of good sealing, low price, high stability and mature

DOI: 10.54254/2755-2721/91/20241101

regeneration technology [2]. The lead-acid battery is composed of a positive plate, a negative plate, an electrolyte, a separator, an outer shell, a pole, a tab, a busbar and a safety valve (Figure 1). These materials containing lead elements give them extremely high chemical stability, making them highly safe. However, with the increasing demand for power in electric vehicles, the low energy density of lead-acid batteries restricts the trend of lead-acid batteries to become mainstream batteries.

Figure 1. Lead-acid battery discharging.

2.2. Fuel cells

Fuel cell is a power generation device that directly converts the chemical energy of fuel into electrical energy, which has the advantages of high power generation efficiency and less environmental pollution. The main ones that are widely used in the household market are proton exchange membrane fuel cells (PEMFC) and solid oxide fuel batteries (SOFC) [3]. The working principle of fuel cells is the reverse process of water electrolysis, that is, the conversion of fuel and oxidant into electricity, water, and heat through electrodes [4]. Proton exchange membrane fuel cells (PEMFC) are widely recognized for their low operating temperature, fast start-up, high specific power, and easy operation, and are regarded as the preferred energy source for powered vehicles.

Proton exchange membrane fuel cells (PEMFC) are widely recognized for their low operating temperature, fast start-up, high specific power, simple structure, and easy operation, and are regarded as the preferred energy source for powered vehicles. The working principle is shown in Figure 2, hydrogen enters the anode and is decomposed into hydrogen ions and electrons by the anode catalyst on the anode, and then the electrons form an electric current in the external circuit. Hydrogen ions travel through the proton exchange membrane to the cathode. Oxygen enters the cathode and passes through the cathode catalyst on the cathode to form water with the hydrogen ions produced by the anode, while releasing heat. The chemical equation [5] is:

Anode reaction equation $H_2 \rightarrow 2H^+ + 2e^-$

The cathode reaction equation is $\frac{1}{2}O_2 + 2H^+ + 2e^- \rightarrow H_2O$

The total reaction equation $H_2 + \frac{1}{2}O_2 \rightarrow H_2O$

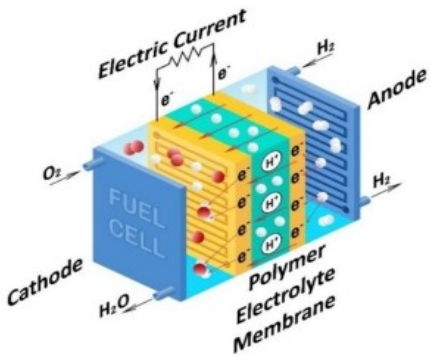

Figure 2. Fuel cell circuit diagram.

2.3. Lithium-ion batteries

Lithium-ion batteries are currently one of the most commonly used battery types in electric vehicles. It has the advantages of high energy density, long service life, and no memory effect, and is widely used in various electronic products and electric vehicles [6]. The reduction potential of lithium metal is extremely low, and the theoretical specific energy can be greater than 3800 mAh/g, far exceeding that of conventional carbon materials. This shows that lithium-ion batteries have a very high ceiling, even though they are currently prone to fire. The main components of lithium-ion batteries are cathode materials, anode materials, exchange membranes, electrolytes, shells, etc [7]. At present, commercial lithium-ion batteries use graphite as the negative electrode, which is difficult to meet the high demand for energy storage characteristics in today's era,so, the key to improving the energy storage of lithium-ion batteries currently lies in finding electrode materials with high energy density.For example, vanadium disulfide (VS2) and silicon germanium composite materials are very suitable negative electrode materials for this requirement. Of course, in addition to alloy materials that can be used as negative electrode materials for lithium-ion batteries, carbon based materials are also very suitable as negative electrode materials. The advantage of this carbon based composite material is minimal pollution during production and low cost. As the largest component in terms of weight and cost in LIBs, positive electrode materials are still one of the main bottlenecks in achieving high performance of LIBs.

2.4. Nickel metal battery

Nickel metal batteries can be divided into nickel-chromium batteries and nickel-metal hydride batteries. The energy density and charging times of nickel-chromium batteries have certain advantages, but their pollution to the environment does not conform to the original design intention of electric vehicles, which restricts its development. Currently, 99% of the market share of hybrid power batteries belongs to nickel-metal hydride batteries , and 99% of the existing market share of hybrid batteries is NiMH power batteries [8]. The anode material of nickel-metal hydride batteries is a hydrogen storage alloy. The types of hydrogen storage alloys include AB5 hydrogen storage alloys, superlattice hydrogen storage alloys, etc. A typical representative of AB5 hydrogen storage alloy is LaNi5 intermetallic compound. The advantages of the AB5 alloy electrode are good cycling stability and rate performance [9]. In pursuit of higher density batteries, AB5 hydrogen storage alloys began to become AB3 unidirectional superlattice alloys. In addition to the AB5 hydrogen storage battery, researchers also studied A2B7 single-phase superlattice alloys, A5B19 and AB4 single-phase superlattice alloys.

3. The future development trend of new energy vehicle batteries

With the continuous progress of electric vehicle technology and decreasing costs, the price of electric vehicle batteries is gradually decreasing, enabling more consumers to buy EVs. Recently, China’s electric vehicle industry has experienced rapid growth due to strong government support and promotion. The number of new energy vehicles has increased from under 10,000 in 2011 to 6.03 million in 2021 [10]. Currently, research and development efforts in new EV battery technology primarily focus on lithium-ion batteries which offer high energy density and low self-discharge rates. In the future, advancements in battery technology will be a key driving force for EV development.

3.1. Increase cruising range

The problem of short cruising range faced by new energy vehicle battery technology is mainly due to the limitation of the energy density of the battery itself and the reduced efficiency under actual use conditions. In other words, increasing the energy density can greatly increase the cruising range. The gap in energy density compared with fossil fuels has significantly limited the range of new energy vehicles.

The weight of the battery has an important impact on the performance and range of new energy vehicles. In new energy vehicles, batteries usually account for a considerable part of the vehicle's weight. Therefore, the development of lightweight battery technology is of great significance for improving the performance and mileage of new energy vehicles. At present, some new lightweight battery technologies

DOI: 10.54254/2755-2721/91/20241101

are constantly developing, such as: lithium-sulfur batteries, solid-state batteries, etc. These new battery technologies have higher energy density and lower weight, which can further improve the performance and range of new energy vehicles. At the same time, it can not only reduce the internal weight of the battery, but also reduce the weight of the outer packaging of the battery, that is, the battery pack shell.

3.2. Shorten the charging time

Shorter charging times are another important trend in the development of battery technology. In order to accelerate the charging efficiency of the battery, it is adjusted according to the fast charging theory. Fast charging methods can be roughly divided into three categories: segmented constant current charging method, pulse charging method, and intermittent fast charging method [11]. The focus here is on segmented constant current charging. Segmented constant current charging, as the name suggests, refers to the process of charging an electric vehicle by keeping the input current constant in stages. The flowchart is shown below.

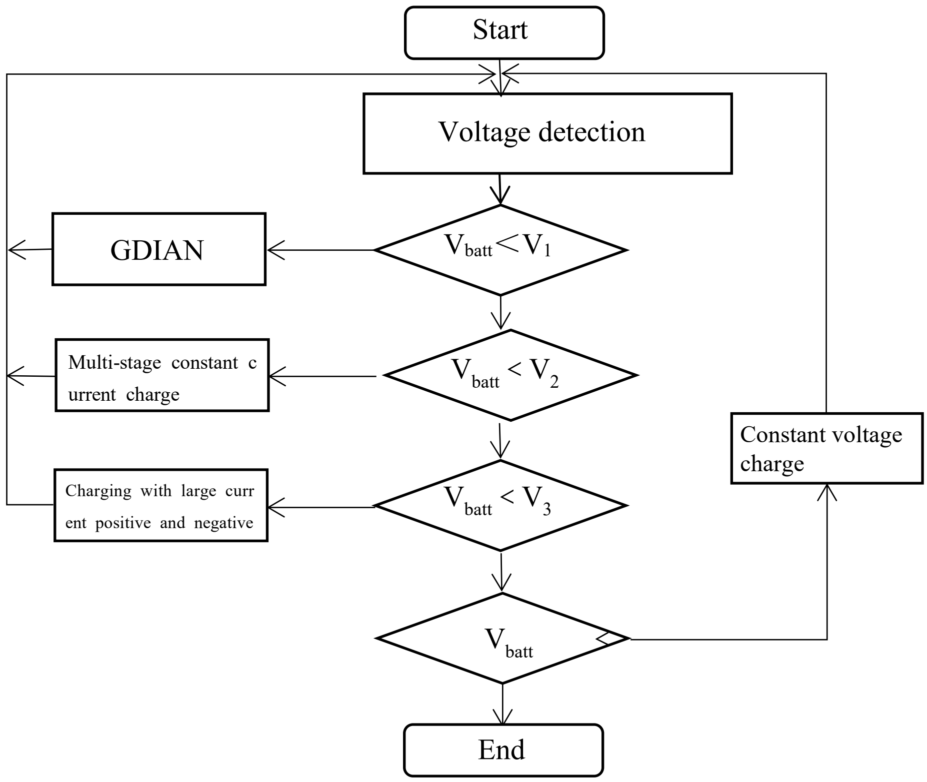

Figure 3. Segmented constant current charging process diagram.

Discharge the power battery; Check the terminal voltage of the battery to determine if it is less than V1 (V1=2.55V). If it is less than V1, proceed to the next step of low current (1/10C) pre charging; When the voltage exceeds V1, check if its voltage is less than V2 (V2=3.0V). If it is less than V2, perform segmented constant current charging. Once the terminal voltage of the battery exceeds the set value V3 (V3=3.3V), it is necessary to check whether the value is lower than the actual measured voltage. If this is indeed the case, high current forward and reverse pulse charging should be adopted. If the battery voltage has reached the preset 3.3V, it indicates that the battery is fully charged. To prevent excessive polarization reactions in power batteries, it is necessary to use high current forward pulse charging. Pulse charging is to solve the problem of the maximum charging current that the battery can accept gradually decreasing with time during the charging process. By introducing discharge, efficiently improving the performance of the battery and delaying its effective working life. Intermittent charging is divided into two forms: current intermittent charging and voltage intermittent charging. Taking intermittent current charging as an example, in the initial stage of battery charging, a larger current is usually selected for rapid charging. When the voltage at both ends of the battery reaches the preset value, and then the current value will be reduced repeatedly until charging is completed. The same applies to intermittent voltage charging.

Lacking of charge device is also one of the factors that lead to long charging times. In order to realize the popularization of new energy vehicles, the construction of a large number of charging piles needs to be carried out, and these charging piles need to have high-power charging capacity to meet the user's fast charging needs.

3.3. Battery recycling and reuse technology

The purpose of new energy vehicles is to protect the environment, which requires electric vehicle batteries to be environmentally friendly. At present, except for fuel cells that can achieve near zero pollution throughout the entire process, all other batteries have a certain impact on the environment. The ore raw materials used to produce these batteries also have significant pollution, indicating an urgent need for battery recycling and reuse technology.

4. Conclusion

In the field of new energy vehicles, the advancement of battery technology is a key factor driving the development of the entire industry. There are still many difficulties in batteries, such as the impact of energy density, battery life, safety, cost, and other aspects. The research and commercial application of new battery technology will also inject new vitality into the development of the new energy vehicle industry. The battery technology of future electric vehicles will inevitably break through the shortcomings of short range, long charging time, and high battery pollution.

References

[1] Yan Guo. Can the recycling of power batteries open the "Blue Ocean" while the new regulations are officially announced, Resource regenerating, 2018(7): 16-23.
[2] Chengzhong Kuang, Shifeng Ou. Overview of Valve-Regulated Lead Acid Battery Online Monitoring and Health Assessment Technologies. Mechanical and Electrical Information, 2024(04): 1-11.
[3] Jiajun Zhao,Peihong Wang. The Present Situation and Trend of Mainstream Fuel Cell Technologies. Shanghai Energy Conservation, 2015(04): 199-203.
[4] Shengtao, Zhang and Yan, Wen. Development and Application of Fuel Cells. World Science and Technology Research and Development, 2003(3): 57-66
[5] Bei, Gou, Woon, Ki, Na, and Bill, Diong. Fuel Cell-Modeling, Control, and Application. CRC Press, 2010
[6] Huiren, Liang. Current Status and Trends of Electric Vehicle Battery Technology Development. Automotive Test Report, 2023(23): 149-51.
[7] Hengyi Jia Research and application of materials for lithium-ion batteries. power technology, 2011(07): 869-71.
[8] Sihui, Zeng. Analysis of Power Battery Recycling of New Energy Vehicles from the Perspective of Circular Economy.China Resources Comprehensive Utilization, 2022(12): 94-96.
[9] Fengxia, Zhang, and Cheng, Tan. Research Progress of Advanced Cathode Electrode Materials for Nickel-Metal Hydride Battery. Materials Reports, 2023(02): 18-26.
[10] Zhen, Bao. Exploration of Optimization Strategies for New Energy Vehicle Battery Technology. Automotive Test Report, 2023(23): 67-69.
[11] Tiezhou, Wu, Chengdong, Lu, and Zhuyue, Huang. A method to improve energy utilization of lithium battery pulsecharging. Power technology, 2020(12): 5.

DOI: 10.54254/2755-2721/91/20241099

Adding Yaw System to Improve Wind Energy Utilization of Offshore Wind Turbines

Hangcheng Wu

Tianjin University of Technology Mechanical Engineering Tianjin, 300384, China

2360423192@stud.tjut.edu.cn

Abstract. In wind power generation, the wind energy loss caused by yaw and other factors is as high as 50%, which directly leads to the difficulty of greatly improving The efficiency of wind power generating in producing electricity. The development of yaw control system restricts the progress of wind energy utilization, The purpose of this study is to investigate the application and influence of automatic steering of offshore wind turbines in practice. This paper proposes that the automatic yaw system of offshore wind turbine can improve the efficiency of wind power generation. The outcomes of the experiment demonstrate that the wind resources can be fully utilized and the power generation efficiency of the offshore fan can be improved by enabling the offshore fan to automatically turn according to the wind direction. The research has a certain value for the development of new energy power generation technology. In this paper, the method of Simulink simulation experiment is used to demonstrate that the yaw system can improve the wind energy utilization coefficient of offshore fan.

Keywords: offshore fan, automatic yaw system, optimal control, optimal adaptive design.

1. Introduction

The topic of reaching the carbon peak has gained increasing attention from the scholarly community as well as the general public in recent years, and it has had a major impact on The Times' evolution. The use of new energy generation has gradually become the mainstream of the world. The utilization rate of wind power generation is increasing, and by the end of 2023, the total global wind power generation has reached 1,021GW, of which offshore wind power is 75GW and continues to rise. Analysis of wind resources, wind farm layout, wind turbine design, control technology, and wind farm siting are all included in wind energy technology. The wind turbine control system has grown in importance as a means of ensuring the wind energy conversion system's stability and effectiveness, and control technology is essential to the wind turbine's overall stable and effective functioning [1].

2. Analysis

2.1. Basic principle of offshore fan

Typically, an offshore wind farm has a specific quantity of wind turbines and transmission equipment.. Wind turbines convert wind energy into electricity, and transmission systems deliver electricity to substations. Wind turbine is a power generation device of wind farm. A single wind turbine includes blades, fans, tower and foundation parts. The working principle of the fan is the principle of aerodynamics [2]. The lift force generated by the pressure difference between the front and back sides of the blades is used to rotate the fan and pass through the gearbox to drive the wind turbine rotor, transforming wind energy into the rotor's kinetic energy in the generator, and finally transforming the rotor's kinetic energy into electrical energy output.

2.2. Wind energy theory

According to the expression of wind energy:

$$E = \frac{1}{2}\rho A v^3 \tag{1}$$

Where, V is the wind speed, ρ is the air density, and A is the swept area of the wind wheel.

It can be seen that the size of the wind energy and the airflow density is proportional to the cube of the swept area through the wind wheel and the airflow velocity. ρ and v are correlated with altitude, geomorphic conditions, geographical location and other factors.

2.3. Wind wheel theory

According to the Bates limit [3], the energy that the wind turbine absorbs from the surrounding air has a limit, and the power consumption part is the kinetic energy of rotation retained in the wake portion. The power reduction is mainly caused by energy conversion, and the specific value depends on the model of the wind turbine and generator used, so the wind energy utilization coefficient of the wind turbine in practical applications is $C_P<0.593$

2.4. Characteristic coefficient of the fan

Wind energy utilization coefficient C_P: the degree of energy that The wind energy efficiency coefficient expresses how much power a wind turbine can produce from the natural wind.

Blade tip speed ratio λ: In order to represent the state of the wind wheel under varying wind velocities, the ratio of the PI speed of the blade tip to the wind speed is measured, which is called the blade tip speed ratio.

Torque coefficient C_T and thrust coefficient C_T: In order to easily compare the torque and thrust generated by the wind turbine under the action of the air flow, the variable λ is generally made into a curve of torque and thrust.

2.5. Leaf element momentum theory

Leaf element momentum theory is composed of two parts, specifically, momentum theory and leaf element theory. The leaf element is divided into many micro segments along the wind turbine blade. It is assumed that the mutual flow on each blade element is independent, that is, the blade element can be regarded as a two-dimensional airfoil. In this case, the aerodynamic characteristics acting on each blade element can be integrated along the radial direction to obtain the aerodynamic characteristics of the entire wind turbine [4].

3. Control theory and model

3.1. Fan yaw control principle

Making sure the wind wheel is correctly aligned with the direction of the wind is the function of yaw in the wind system, the most basic component is the yaw bearing connecting the main frame and the tower barrel, the active yaw drive is usually used in the upwind wind turbine, sometimes also used in the downwind wind generator, it is equipped with a number of yaw motors, each of which is used to drive a tiny gear that is meshing with a large gear, which is attached to the yaw bearing. An active yaw system, which is frequently employed in downwind wind turbines, controls this process with a wind direction monitor installed on the wind turbine nacelle [5].

3.1.1. Adaptive control

Because the speed of the wind, wind turbine acceleration, and paddle angle have a nonlinear relationship, the dynamic performance of wind turbine depends on wind speed to a large extent. The controller is designed with the lowest sensitivity to these parameter changes so that it can adapt to system parameter changes. Systems with fluctuating characteristics, particularly those with rapid or broad fluctuations, can also benefit from these adaptive control approaches. The Adaptive management scheme ongoing measures the values of the system parameters and then changes the dynamic characteristics of the control system to ensure that the desired performance standards are always met.

3.1.2. Optimal control

Changes in the input signal balance variations in the system output in an optimal control system, which operates in the temporal domain. Optimal control is originally a multi-variable method, which makes it suitable for the control design of variable speed wind turbines. The control problem has been defined by optimal control theory. according to the performance metric, which is usually a result of the mistake between the control command and the actual response of the system, and then uses mature mathematical methods to determine the values of the design parameters, so that the value of the performance index is maximum or minimum. The optimal control algorithm usually needs to detect the state variables of the system or the state observer based on the machine model.

3.2. Power control of wind turbine

3.2.1. Generator model

The wind power producing the system's power management component generally includes: wind speed model, pneumatic model, generator part, gearbox part and frequency converter part.

The wind turbine studied in this paper is an asynchronous generator, whose output power varies according to the slip rate, and the slip rate is controlled by adjusting the frequency converter, so as to achieve variable speed constant frequency [6].

Coordinate transformation: Both the stator and three windings can be compared to the rotor of a three-phase asynchronous motor, and After coordinate transformation, the two-phase stationary coordinate system and the three-phase stationary coordinate system can be equivalent., and then the two-phase stationary coordinate system is equivalent to the rotating two-phase coordinate system with rotation speed $\omega_1 = 0$ [7].

Mathematical model of asynchronous generator:

$$\begin{cases} \dfrac{d_\omega}{dt} = \dfrac{n_p^2 L_m}{J_G Lr}\left(i_{sq}\Psi_{rd} - i_{sd}\Psi_{rq}\right) - \dfrac{n_p}{J_G}T_L \\ \dfrac{d\Psi_{rd}}{d_t} = -\dfrac{1}{T_r}\Psi_{rd} + (\omega_1 - \omega)\Psi_{rq} + \dfrac{L_m}{T_r}i_{sd} \\ \dfrac{d\Psi_{rq}}{d_t} = -\dfrac{1}{T_r}\Psi_{rq} + (\omega_1 - \omega)\Psi_{rd} + \dfrac{L_m}{T_r}i_{sq} \\ \dfrac{di_{sd}}{dt} = \dfrac{L_m}{\sigma L_r L_s T_r}\Psi_{rd} + \dfrac{L_m}{\sigma L_r L_s}\Psi_{rq}\omega - \dfrac{R_s L_r^2 + R_r L_m^2}{\sigma L_s L_r^2}i_{sd} + \omega_1 i_{sq} + \dfrac{u_{sd}}{\sigma L_s} \\ \dfrac{di_{sq}}{dt} = \dfrac{L_m}{\sigma L_r L_s T_r}\Psi_{rq} + \dfrac{L_m}{\sigma L_r L_s}\Psi_{rd}\omega - \dfrac{R_s L_r^2 + R_r L_m^2}{\sigma L_s L_r^2}i_{sq} + \omega_1 i_{sd} + \dfrac{u_{sq}}{\sigma L_s} \end{cases} \tag{2}$$

Where: u_{sd}, u_{sq} are the stator voltage at coordinate d_q, i_{sd} and i_{sq} are the stator current, ω_1 is the rotation speed at coordinate d_q, ω is the asynchronous motor speed, T_L is the load torque, R_s is the stator winding resistance, Ψ_{rd} and Ψ_{rq} are the rotor flux, L_m is the mutual inductance between the stator and the rotor equivalent winding, L_s is the self-inductance of the stator equivalent two-phase winding. L_r is the self-inductance of the equivalent two-phase winding of the rotor, n_p is the pole number, T_r is the electromagnetic time constant of the rotor, $T_r = L_r/R_r$ is the equation of state, and J_G is the moment of inertia of the asynchronous motor unit.

3.2.2. Gearbox system

The simplified model of the gearbox system is shown in the figure. The wind turbine shaft and generator shaft are respectively installed on the left and right sides of the gear, and the tooth ratio is the speed ratio of the left and right sides of the gear [8]. The simulation model is simplified, ignoring the energy consumption in the transmission process of the actual operation of the gearbox.

Gearbox drive system dynamic model:

$$\left(J_{rot} + N_{gear}^2 J_G\right)\frac{dw_{rot}}{dt} = T_{at} - N_{gear}T_G \tag{3}$$

Where w_{rot} is the speed of the wind wheel, J_G is the moment of inertia of the generator, J_{rot} is the moment of inertia of the wind wheel, and T_G is the load torque.

3.2.3. Motor side inverter control model

Since the collector ring connects the motor side frequency converter with the winding asynchronous motor, the model of the motor side frequency converter in the dq coordinate system is:

$$\begin{cases} u_{rd} = i_{rd}R_r + \sigma L_r \dfrac{di_{rd}}{d_t} - \omega_s\left(-\dfrac{L_m}{\omega_1 L_s}U_G + \omega_s \sigma L_s i_{rd}\right) \\ u_{rq} = i_{rq}R_r + \sigma L_r \dfrac{di_{rq}}{d_t} + \sigma\omega_s L_r i_{gd} i_{rq} \end{cases} \tag{4}$$

Where, U_G is the power grid voltage.

If the load remains constant, the rotor current does not change. When the additional electromotive force is added to the circuit, the synthetic electromotive force of the rotor loop is reduced, so the rotor current and electromagnetic torque are correspondingly reduced, the load torque remains unchanged, and the motor speed is reduced.

The ideal electromagnetic power is:

$$P_{em} = sP_{em} + (1 - s)P_{em} \tag{5}$$

Where, P_{em} is electromagnetic power; sP_{em} is the slip power.

3.3. Side wind and yaw error

Side wind V_0 is perpendicular to the wheel shaft and perpendicular to the surface. It occurs because of yaw errors or sudden changes in wind direction. For the forward blade, it increases the tangential velocity. The speed of the tangential of the receding blade decreases. Note that tangential velocity is mostly affected by the cosine period disturbance that is responsible for yaw inaccuracy [9].

3.4. Yaw motion

In addition to causing the turning moment, yaw motion also affects the blade speed. If the position of the blade is vertical and there is a yaw rate, The blade will support the speed. qd_{yaw} due to yaw rotation (d_{yaw} is the distance from the tower shaft to the center of the wind turbine). The speed will rise by $rqsin(\beta)$ if the flapping angle causes the blade to tilt away from the axis of revolution. This impact is absent when the blade is in the horizontal position and is strongest when the blade is upright, up, or down.

3.5. Yaw stability

Any pure sinusoidal response results in a net torque around the yaw axis. The sinusoidal periodic response is affected by rotational motion, yaw error, wind shear and gravity. First of all, it should be pointed out that both vertical wind shear and gravity on the curved blade tend to cause the wind wheel

DOI: 10.54254/2755-2721/91/20241099

to deviate from the wind in the same direction [10]. That means the wind wheel will be subjected to the side wind from the negative direction. The sideways wind caused by the yaw error attempts to turn the wind wheel back in the other direction.

3.6. Output power prediction

The output power of wind turbines varies with the wind speed, and each wind turbine has its own unique power curve. This curve can be used to predict power generation without taking into account the specific technicalities of other parts. The power output at the hub height as a function of wind speed is displayed on the power curve.

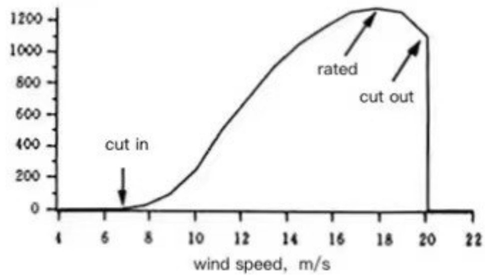

Figure 1. Classical curvature curve of wind turbine

3.7. Turbine power control: stall, variable pitch or pneumatic surface

At high wind speeds, stall control takes advantage of aerodynamic lift reduction at high angles of attack to reduce torque. For the stall to work, the rotor speed must be independently controlled. The stall-controlled wind turbine blades are fastened to the hub to form a simple connection. However, stall control is characterized by a relatively large wind speed to achieve maximum power. Stall-controlled wind turbines always use a separate braking system to ensure that the fan can be shut down when various conditions occur.

The blade of a variable blade wind turbine can rotate around its long axis and change its paddle Angle. Changing the paddle Angle also changes the Angle of attack relative to the wind and the torque generated. However, the wheels become more complex and need to be equipped with variable pitch bearings. In addition, a variable pitch execution system must be used.

Yaw control makes the wind wheel deviate from the wind direction to reduce the power, and the wheel hub must be able to withstand the rotating load caused by the yaw movement, but its structure is relatively simple.

4. Simulation analysis

In order to verify the control strategy proposed in this paper, a simulation model is built in Matlab/Simulink, and the rated power of the wind turbine is 1.8MW. Figure 1 shows the real wind speed during a certain period of time.

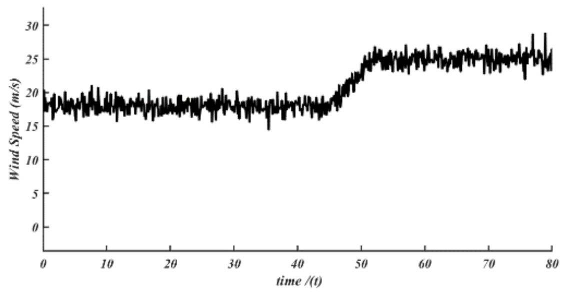

Figure 2. Real wind speed during a certain period of time

Figure 3.(a) shows the speed waveform of the fan under different wind speeds. In the figure, waveform A is the speed waveform under maximum power tracking control method, and waveform B is the speed waveform under wide speed operation control. Figure 3. (b) is the steering Angle waveform, and the waveform in the figure is the steering Angle waveform under the tracking control approach with greatest power; Figure 3.(c) is the output power waveform of the wind turbine, waveform A is the power waveform under the maximum power tracking control method, waveform B is the power waveform under the wide speed operation control. Figure 4. shows the working state of the fan at different wind speeds.

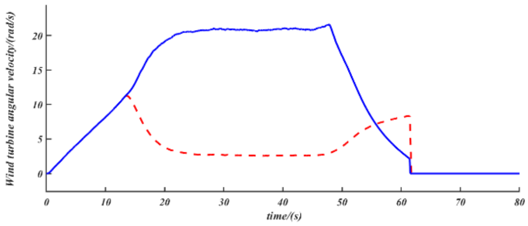

(a) Fan speed waveform at different wind speeds

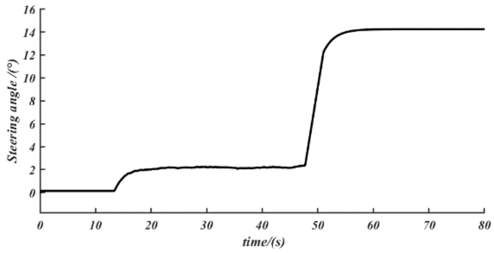

(b) Turning Angle waveform

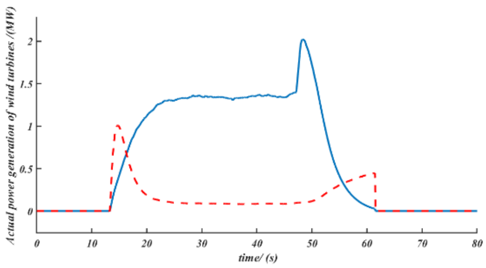

(c) Wind turbine output power waveform

Figure3. Wave form

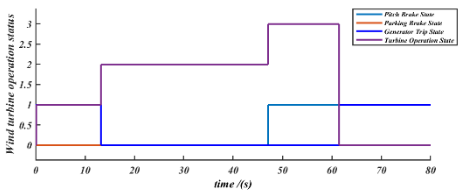

Figure 4. Fan working state

It can be seen from Figure 3.and Figure 4. that, compared with no steering Angle control, under the steering Angle control of maximum power point tracking, the steering Angle adjustment is gentle and the generating power is higher, which is due to the coordinated control of steering Angle and generator speed under this method. Between the cut wind speed and cut wind speed, the control of the maximum power point tracking steering Angle ensures that the fan is automatically aligned to the wind direction, minimizes wind turbine deterioration and keeps efficiency at its highest level across a broad range of wind speeds to maximize wind energy harvesting.

5. Conclusion

An adaptive control strategy of steering angle-speed coordination based on optimal control is proposed for offshore wind turbines. This strategy does not rely on the mathematical model of the offshore fan, and effectively avoids the bad influence of modeling errors and unmodeled dynamics on the control. By improving the adaptive control method of optimal control, the multi-input and multi-output controller is designed to smooth the output power, reduce the steering Angle regulation frequency, and relieve the operating pressure of the steering mechanism. Finally, based on Matlab/Simulink simulation, a 1.8MW fan is simulated under the actual wind conditions. The effectiveness of improving the adaptive control method by integrated iterative learning control is verified by comparison. The design of steering Angle - speed coordinated control strategy controller has better performance of power regulation.

The actual fan operation is more complex and more factors need to be considered. Therefore, there are still many aspects to be further studied, and the follow-up work can be improved from the following aspects: In the design of the controller for the control range below the rated wind speed, only the full power output of the fan is considered, and the lower limit power output of the rated wind speed is not considered. Further research on the fan power limited control strategy is needed.

In the design of the controller, this paper only pays attention to the fluctuation of power, the change of speed and steering Angle, and does not consider the load of the mechanical parts of the fan and the fatigue load of the transmission system tower. In the actual operation of the fan, the influence of all aspects should be considered comprehensively, and the overall optimal control objective should be established to achieve the overall optimal control of speed, power, mechanical load, etc.

The output power fluctuations generated during the operation of wind turbines can also be suppressed by energy storage devices such as wind turbines and batteries, and the energy storage system can also be applied to the frequency regulation of wind power systems and the compensation of active power, which will also be an aspect worth studying in the future.

References

[1] Pan Xueping,Guo Jinpeng,Sun Xiaorong,etc.Frequency domain equivalent modeling method for frequency response characteristics of doubly-fed wind farms[J/OL]. Power grid technology,1-13[2024-07-04].https://doi.org/10.13335/j.1000-3673.pst.2024.0248.pp.1-9

[2] Cai Yunxiu.Working principle and aerodynamic theoretical calculation of wind turbine[J]. Scientific and technological information, 2012, (17):103-104+167. pp.104-105

[3] Jiang Haibo,Cao Shuliang,Yang Ping.The power limits of horizontal axis wind turbines[J].Journal of Mechanical Engineering,2011,47(10):113-118.pp.113-114

[4] Wang Qi. Optimization design of wind turbine blade shape based on multi-island genetic algorithm and momentum leaf element theory[J].Mechanical design and manufacturing engineering,2024,53(06):29-33.pp.29-30

[5] Liu Yang. Analysis of the influence of improving wind measurement accuracy of wind vane on power generation [J]. Electric power survey and design 2018, (06):73-76.DOI:10.13500/j.cnki.11-4908/tk.2018.06.015.PP.73-76

[6] Gao Fuwei. Research on maximum wind energy tracking control for variable speed constant frequency wind power system[J].Electronic fabrication, 2022, 30(02):90-92.DOI:10.16589/j.cnki.cn11-3571/tn.2022.02.024.pp.90-92

[7] Li Jinchun. Research on real-time model predictive control for three-phase induction motor[D].Dalian University of Technology,2014.pp.29-40

[8] Guo Guanghua, Chen Xuan, Guan Yingchun, etc. Design of vibration signal acquisition system for fan gear box[J].Electrical technology, 2023, (08):62-65.DOI:10.19768/j.cnki.dgjs.2023.08.016.pp.62-65

DOI: 10.54254/2755-2721/91/20241099

[9] Hu Qiankun, Guo Peng, Dong Ketao, etc.Research on static yaw error diagnosis method of wind turbine based on distribution hypothesis testing[J].Electric power science and Engineering, 2024, 40(03):52-60.pp.53-54
[10] Cheng Lifeng. Research on error and control strategy of wind turbine yaw system[D]. North China Electric Power University (Beijing),2017.PP.41-43

DOI: 10.54254/2755-2721/91/20241088

Design of urban low-carbon green transportation demonstration area in the context of "dual carbon" -- Taking Wuhua District of Kunming City (Zhengyi Road and Sanshi Street area) as an example

Jingfei Yan

Kunming University of Science and Technology Oxbridge College, Kunming, 650211, China

Songtian818@163.com

Abstract. In the context of "dual-carbon", by reconstructing the relationship between people and vehicles, optimizing spatial quality, and taking street space renovation as a starting point, we can continuously improve the travel experience of human-centered neighborhoods, build a higher-quality living environment, and guide green travel. Under this context, this study takes Wuhua District, Kunming, Zhengyi Road and Sanshi Street as a case to explore the design of urban low-carbon green transportation demonstration area under the background of "dual-carbon". By analyzing the "dual-carbon" strategy and related policies, and taking into account the current transportation situation in Wuhua District, Kunming, it is found that there are problems such as traffic congestion, chaotic parking, and poor bus routes in this area. To address these challenges, this study proposes a series of optimization measures based on successful cases at home and abroad, including improving the transportation network, strengthening non-motorized parking management, introducing intelligent traffic management systems, and optimizing the connection between bus routes and rail transit. These measures will help improve transportation efficiency, reduce congestion, promote green travel, and provide useful lessons and references for the construction of low-carbon transportation demonstration zones in other cities.

Keywords: low carbon transportation, green mobility, transportation planning, green cities.

1. Introduction

The development of green and low-carbon transportation is an important measure for the transportation industry to strengthen the construction of ecological civilization, serve the national goal of carbon peak and carbon neutrality, and fight the battle of pollution prevention and control. In order to implement Xi Jinping's thought on ecological civilization as well as the "Opinions of the Central Committee of the Communist Party of China and the State Council on the complete and accurate implementation of the new development concept to do a good job of carbon peak carbon neutral work [1]. Opinions of the CPC Central Committee and State Council on Deepening the Battle Against Pollution Prevention and Control Outline for the Construction of a Stronger Transportation State [2]. The Ministry of Transportation and Communications (MOTC) has issued the Green Transportation Standard System [3] and the Green Transportation Standard System (2022) [4]. It aims to further promote energy saving and carbon

DOI: 10.54254/2755-2721/91/20241088

reduction, pollution prevention and control, ecological environment protection and restoration, and resource saving and intensive utilization in the field of transportation to make up for the shortcomings, strengthen the weaknesses, and promote enhancement, accelerate the formation of green and low-carbon modes of transportation, promote the harmonious development of transportation and nature, and provide a strong support for the promotion of sustainable development of the city and the acceleration of the construction of a strong nation of transportation.

On September 22, 2020, president Xi Jinping announced during the general debate of the 75th United Nations General Assembly that China's carbon dioxide emissions are striving to peak by 2030, and to achieve carbon neutrality by 2060 [4]. The transportation industry is one of the major industries in energy consumption and greenhouse gas emissions, and is an important area to improve air quality, achieve greenhouse gas emission reduction and mitigate climate change, as well as a key and difficult area to influence the city's carbon peaking and transportation pollution reduction.

The above provides an urgent background and demand for promoting the construction of low-carbon green transportation demonstration zones. Kunming, as one of the first batch of "National Bus City Construction Demonstration Cities", "National Low-Carbon Transportation Pilot Cities", "Pilot Cities of Green Travel Creation" and "National Smart Bus Demonstration Cities", has basically established the main position of green travel in urban transportation. As the first batch of "National Bus City Construction Demonstration City", "National Low Carbon Transportation Pilot City", "Pilot City of Green Travel Creation" and "National Intelligent Public Transportation Demonstration City", the city has basically established the main position of green travel in urban transportation, and possesses a good foundation for low-carbon transportation development. As transportation hubs and commercial centers in Kunming, Wuhua District's Zhengyi Road area and Sanshi Street area have become important bottlenecks restricting the sustainable development of the city. This study aims to propose innovative solutions to the transportation problems in the core area of Wuhua District, with the goal of building a low-carbon green transportation demonstration area.

2. The current situation in the area of Zhengyifang and Sanshi Street in Wuhua District, Kunming

2.1. Description of the area

Located in the center of Kunming City, the Zhengyifang and Sanshi Street areas are important commercial and cultural gathering areas in the city, with high daily pedestrian flow and significant traffic pressure. At the same time, the traffic problems in this area are typical, and the study of its traffic status and improvement measures has a strong demonstration and promotion value.

2.2. Current situation

(1) Problems of public transportation, such as Figure 1, conventional bus, site coverage, walking the main street and auxiliary street neighborhoods around the bus stops densely, Nanping Pedestrian Street, the entire line are in the conventional bus stops within 300 meters of the coverage, but the bus service is inefficient.

Initial formation of networked operation of the rail: 5 rail transit lines have been opened for operation (including 1 branch), the initial formation of networked operation, Line 3 Wuyi Road Station site 500m can fully cover Zhengyi Road Pedestrian Street and Nanping Street Pedestrian Street.

DOI: 10.54254/2755-2721/91/20241088

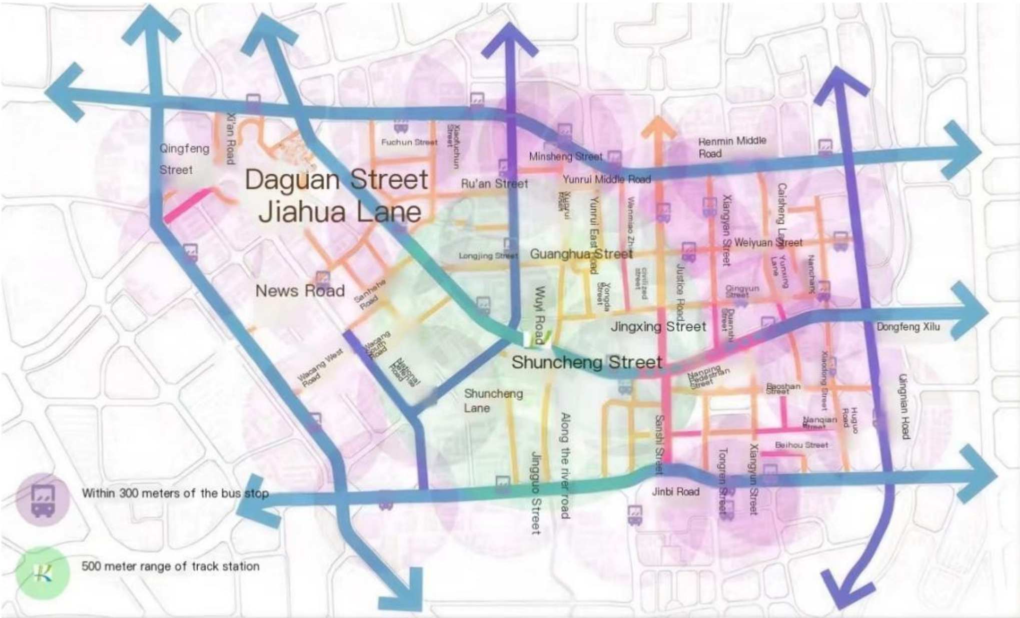

Figure 1. Map of rail and bus coverage

(2) The characteristics of the pedestrian street, with obvious boundaries and discontinuous. Pedestrian street and the surrounding road slow moving articulation facilities are perfect: pedestrian street and the surrounding motor vehicle operation section of the current situation to pedestrian crosswalks, overpasses, underpasses and other slow moving facilities articulation, better to meet the needs of pedestrians to cross the street, to ensure the continuity between the slow moving facilities.

There are clear management boundaries, motorized isolation facilities, and manual management of the road sections with surrounding motor vehicles to ensure the safety and comfort of the pedestrian zone. There are comprehensive signage at the entrances and exits of the pedestrian street (see Figure 2 and Figure 3).

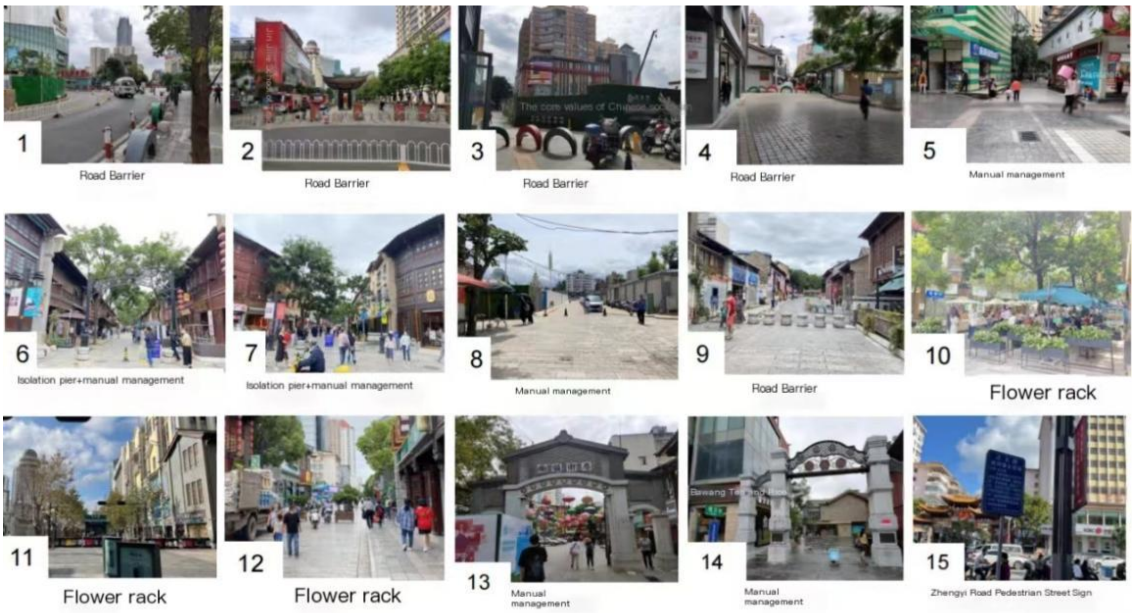

Figure 2. Management measure

Figure 3. Corresponding position

(3) Non-motorized parking is a problem, chaotic and unorganized, encroaching on the slow-moving space. All motorized and non-motorized vehicles are prohibited within Nanping Pedestrian Street, and there are segregation facilities and management personnel to maintain the entrances and exits.

Mainly concentrated in the vicinity of commercial and office buildings, most of the parking spots are located on the sidewalks, seriously encroaching on the sidewalks, and are managed and charged for. A small portion of the use of the front area of the building is designated as a parking area, belonging to the self-parking, and has a person to manage. Some parking is primarily in front of commercial and restaurant establishments along the street. Parking order is average, but encroachment on the sidewalk is serious.

(4) Motorized vehicle parking problems, occupying non-motorized space, and parking in the front area of the building concentrated around commercial and office buildings, seriously occupying public space (Figure 4).

Figure 4. Motor vehicle parking situation

3. Design Principle

3.1. Design thinking

Firstly, this study analyzes and summarizes the traffic characteristics and problems through field investigation of the current situation of the area, public transportation resources, public transportation coverage, non-motorized parking spots, motorized vehicle parking information, pedestrian entrances and exits, signage information, and the slow-moving system.

Then, combined with the famous foreign pedestrian street area Oxford Street in London, Hong Kong Mongkok district traffic planning and traffic organization and management experience, put forward the pedestrian street upgrading and transformation objectives, "individual motorization reduction + green travel increase + pedestrian street increase + non-motorized parking space specific" as the core, from the integration of the district traffic organization. It proposes planning strategies, detailed planning schemes and specific implementation measures in four aspects, such as integrating district traffic organization, public transportation services, upgrading the spatial quality of streets and building intelligent transportation.

Finally, slow traffic, public transport, non-motor vehicles, street space quality, and other systems are coordinated to promote the integration of the three networks of "rail transit network + conventional bus network + slow traffic network", establish a "bus + walking" travel system, and guide the public to give priority to choosing The public will be guided to give priority to public transportation, walking and cycling as green modes of transportation. During the implementation process, the "people-oriented" planning concept is maintained, the street space is purified, and the quality of the street space is comprehensively upgraded, which has a demonstration and leading role in creating "green mobility" in the core area of Kunming City. The design concept is shown in Figure 5.

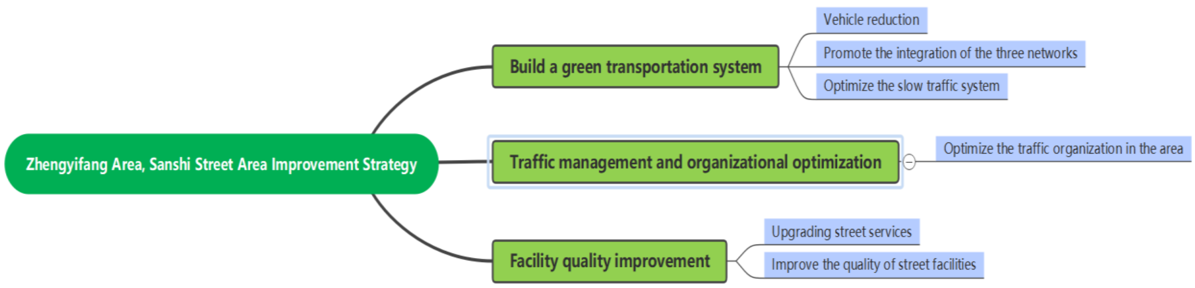

Figure 5. Design ideas

3.2. Wuhua District Zhengyi Road Area and Sanshi Street Area Improvements

3.2.1. Field survey and status analysis. Conducted a field survey of the Zhengyi Road and Sanshi Street areas in the core area of Wuhua District, Kunming, to obtain detailed data on public transportation resources, completion of the road network and level of service, non-motorized parking locations, motorized vehicle parking information, information on pedestrian entrances and exits and signage, and slow-moving systems.

Relevant traffic characteristics and issues, such as traffic congestion, parking difficulty, and pedestrian access, are collected through field observations.

Analyze the traffic planning and management experience of famous pedestrian street areas at home and abroad, explore their successful practice cases, and gain a deeper understanding of their traffic organization, public transport services, street space quality and other characteristics.

Draw lessons from the traffic management experience of advanced foreign cities and understand their implementation strategies and technical means for pedestrian street upgrading and transformation. Such as adopting differentiated, flexible traffic management methods by mode and time, congestion charging and other measures.

DOI: 10.54254/2755-2721/91/20241088

(1) Take Oxford Street in London as an example, such as in Figure 6 and Figure 7. According to the characteristics of the pedestrian flow in the neighborhood, it has adopted a differentiated and flexible traffic management approach in both the main street and the secondary street in terms of modes and time periods, effectively expanding the pedestrian priority area in the hot spot concentration area, maximizing the protection of the right of way for pedestrians, and at the same time, trying to make it possible to facilitate the passage of public transport and bicycle traffic, combining with Each intersection and road section is upgraded to provide a safe and comfortable street walking environment.

Congestion Charging Zone According to Transport for London, vehicles traveling in the Congestion Charging Zone pay £15 per day from 7a.m, to 6p.m. on weekdays and from 12p.m. to 6p.m. on weekends and bank holidays, except on Christmas Day and New Year's Day. Residents within the congestion zone who are 17 years of age or older are entitled to a 90% congestion discount. In addition, vehicles with more than nine seats, urban cleaning vehicles, small tricycles, roadside assistance vehicles, ambulances and fire engines, and vehicles used by disabled people are exempt from the Congestion Charge [5].

Figure 6. London Congestion Zone logo

Figure 7. London Congestion Zone logo

(2) Build the integration of rail and bus, optimize the direction of bus routes, increase the connection between bus routes and rail, and increase the connection between bus stops and rail.

Impact site: Zhengyi Road Pedestrian Station, Weiyuan Street Station, 6 bus routes, peak hourly bus traffic of 180 passengers; to solve the problem, the bus can be reached as the focus, and to ensure the level of public transport services, the original Zhengyi Road south to north bus service lines are evacuated to the youth road for the organization, such as Figure 8, Figure 9.

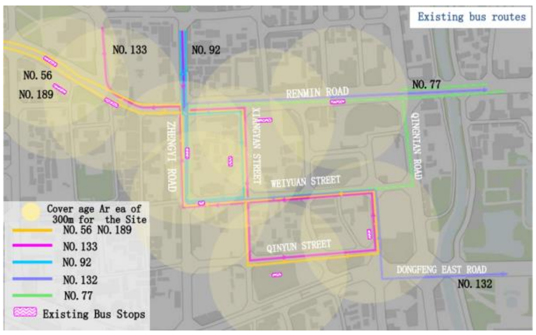

Figure 8. Zhengyi Road: the original north-south bus service line

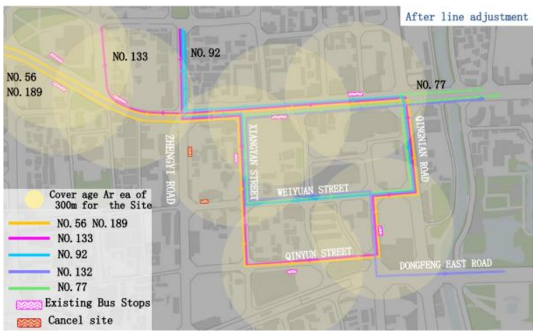

Figure 9. Optimized line.

(3) Create characteristic slow-travel routes: create a high-quality walking environment in the area, with Nanping Street and Zhengyi Road Pedestrian Street as the skeleton, and transform Zhengyi Road into a pedestrian street, to set up removable flower boxes, shown in Figure 10 and Figure 11. Implement a differentiated traffic organization for time periods, with parking or loading/unloading of passengers

DOI: 10.54254/2755-2721/91/20241088

and goods prohibited during the business hours of 7 a.m. to 12 a.m. Combine the peripheral pedestrian corridors to connect cultural attractions, commercial centers, and recreational parks to create distinctive pedestrian routes that reflect the atmosphere of the historic district. Due to the addition of a new pedestrian street, local adjustments to the traffic organization are required. Solutions involving motorized entrances and exits of buildings along the route.

	The serial number	Locations	Management measures
add new	1	Intersection of Zhengyi Road - Renmin Road	portable flower box
	2	East of Guanghua Street entrance of zhengyifang Undergroun Parking lot	portable flower box
	3	State Administration of Foreign Exchange Yunnan Branch (Weiyuan Street)	portable flower box
	4	West side of qinyunStreet Car Park	portable flower box
cancel	5	Fire Brigade dormitory entrance	Cancel the flower box
	6	Intersection of Zhengyi Road - Qingyun Street	Cancel the flower box

Figure 10. Pedestrian traffic organization optimization measures

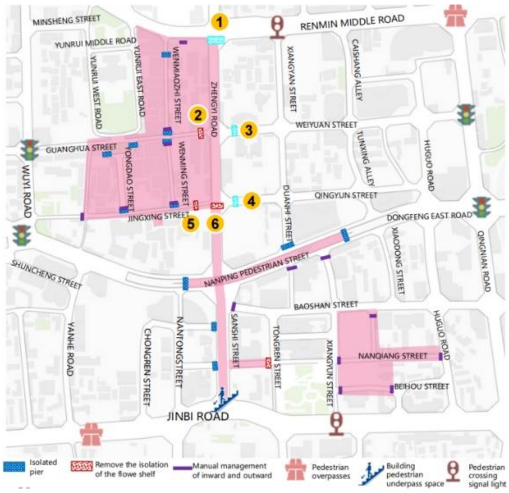

Figure 11. Corresponding position

Close the Xiangyan Street pedestrian crossing: Detour through the Zhengyi Road intersection, cancel the signal lights, and reduce the impact on the main line of Renmin Road traffic.

Enhance parking enforcement, for this micro-circulation road; illegal parking behavior and violations of retrograde behavior will be severely punished. Installation of directional signs: upgrade the installation of directional signs at the intersection of Weiyuan Street-Elephant Eye Street and Qingyun Street-Elephant Eye Street, reminding vehicles that Zhengyi Road is a pedestrian street in front of them, which is prohibited for motorized vehicles, and requesting them to make detours in advance.

(4) Strengthen the management of non-motorized on-street parking. To first delineate the no-traffic area, the demonstration area is divided into the core walking area and the demonstration of the peripheral area. The core walking area to create a "public transportation+ walking" travel system, prohibit non-motorized vehicles into. The peripheral areas of the demonstration zone will be divided into the core pedestrian zone and the peripheral areas of the demonstration zone.

Control the total amount of placement: strengthen the limitations on the number of shared bicycles placed in the area, and control it within 3,000.

Delineation of no-traffic zones: The demonstration area is divided into the core pedestrian zone and the peripheral zone of the demonstration area. The core pedestrian zone will be divided into the core pedestrian zone and the peripheral zone. The peripheral area of the demonstration zone will create a "public transportation + bicycle + walking" travel system, with electronic fences and a "parking in the fence" parking layout for bicycles.

Regulate parking spaces: 52 non-motorized parking frames are set up around the sub-branch road road side facilities belt and the main road subway station, with a total parking area of about 3,900 square meters, which can meet the parking demand of 1,900 electric bicycles (or 5,200 shared bicycles). According to the non-motorized travel sharing ratio of the area, 1,250 electric bicycles + 1,870 shared bicycles can be parked. The rest of the e-bikes are parked in the plot-allocated e-bike parking spaces.

Increase penalties: strengthen the shared bicycle, private non-motorized vehicle indiscriminate parking penalties, in the integrity file.

(5)Improvement of irregular parking, introduction of intelligent traffic management, intelligent parking, and improvement of traffic efficiency [6]. The establishment of parking guidance, parking berth sharing system, improve the utilization rate of parking spaces in the area. In the key units (into the bank, school, market, etc.) to set up a small number of harbor type temporary parking spaces with limited parking, building front area public space optimization.

(6)Expansion of the pedestrian zone: adding "three horizontal and one vertical" pedestrian streets.

Adjust Zhengyi Road (Qingyun Street-People's Road), the whole line of Jingxing Street, Nanqiang Street, and Fulin Plaza as pedestrian streets, totaling 1.6km, and the size of the pedestrian street in the area after adjustment reaches 3.9km.

4. Innovative features

(1) Helping to create a low-carbon green transportation demonstration area, innovative establishment of the "current situation survey - traffic characteristics and problems - case studies - planning strategies - program measures" technical line of work.

(2) For the first time in Kunming, a core green and low-carbon demonstration zone has been created in the city's core area, with "individual motorization reduction + green increment" as its core. By coordinating multiple systems such as slow-moving transportation, public transportation, non-motorized vehicles, motorized vehicles, and street space quality, the city promotes the integration of three networks, namely, "rail transportation network, conventional bus network, and slow-moving transportation network" [7]. To establish a "public transportation + slow-moving" travel system, and guide the public to give priority to public transportation, walking, cycling and other green travel modes [8]. The project is a demonstration of "green mobility" in the core area of Kunming.

(3) Adhering to the concept of "people-oriented" planning, purifying street space and comprehensively upgrading the quality of street space. Following the idea of changing from "car-oriented" to "people-oriented", this paper proposes a strategy that is compatible with the commercial, historical and cultural neighborhoods in the district. First, through the addition of "three horizontal and one vertical" pedestrian streets, to "line" connect "piece" to create a core pedestrian street area, improve the carrying capacity of pedestrian street traffic. Secondly, optimize the connection between the pedestrian street and the surrounding road slow-moving system, so as to realize the separation of pedestrian and vehicular traffic. Third, comprehensively clean up the front area of the building and the road surface of the illegal parking of motor vehicles, standardize the management of non-motorized vehicles, purify the street space walking quality, and so on.

5. Conclusion

This study explores the design and implementation strategies of an urban low-carbon transportation demonstration zone in the Wuhua District of Kunming, in the context of "dual-carbon", in the area of Zhengyi Road and Sanshi Street. Through a detailed analysis of the current traffic situation in the area, and combining successful cases at home and abroad, this paper proposes a series of innovative and operable low-carbon transportation improvement measures. (1) By optimizing public transport services, it aims to improve the coverage and convenience of bus routes and increase the seamless connection between public transport and rail transit in order to reduce the frequency of private car use, thereby reducing traffic congestion and carbon emissions. (2) With regard to the improvement of pedestrian precincts, emphasis has been placed on installing more slow-moving facilities, optimizing the walking environment, ensuring pedestrian safety, and enhancing the comfort and attractiveness of walking. This not only helps reduce carbon emissions, but also enhances the livability of the city. (3) A strategy for regulating and managing non-motorized vehicles is proposed to ensure the reasonable use of slow-moving space through the designation of special non-motorized parking areas and the strict management of non-motorized parking behaviors, so as to create an orderly and safe traffic environment. (4) Introducing an intelligent traffic management system, utilizing advanced technological means for dynamic traffic management, establishing an intelligent parking system, and improving the efficiency of traffic management. This will not only effectively alleviate traffic congestion, but also provide the public with a more convenient traveling experience. (5) By enhancing policy support and public participation, we hope to raise the public's awareness of green mobility and encourage the public to

DOI: 10.54254/2755-2721/91/20241088

actively participate in the construction and maintenance of the low-carbon transportation demonstration zone. This strategy requires not only the guidance and support of the government, but also extensive public participation and cooperation.

Although this study proposes a series of specific implementation measures, it still faces many challenges in its actual operation. Future research should further explore issues in terms of policy support and implementation pathways, public participation and behavioral guidance, technological innovation and application, as well as long-term effect evaluation and feedback.

References

[1] Opinions of the Central Committee of the Communist Party of China and the State Council on Complete and Accurate Comprehensive Implementation of the New Development Idea and Doing a Good Job in Carbon Peak and Carbon Neutrality[C]// Blue Book of China Enterprise Reform and Development 2021. [Publisher unknown], 2021:6.

[2] Opinions of the CPC Central Committee and State Council on deepening the battle against pollution [N]. People's Daily,2021-11-08(001). DOI:10.28655/n.cnki.nrmrb.2021.011759.

[3] Yin Fou, Mei Shen. Green transportation standard system release system planning transportation green low-carbon standardization development[J]. Waterways and Ports,2022,43(04):560.

[4] Zicheng Li, Jue Wang. Green Transportation and Urban Sustainable Development-An Assessment of the Policy Effect of Low-Carbon Transportation System Pilot Based on Spatial Double Difference [J/OL]. Journal of Lanzhou University of Finance and Economics:1-16 [2024-07-05]. http://kns.cnki.net/kcms/detail/62.1213.f.20240315.1611.016.html.

[5] Song Gao, Dong Wang, Xiaoli Sun, et al. Traffic Environment Improvement of Commercial Pedestrian Street in Historical Neighborhoods--Taking Jianghan Road Pedestrian Street in Wuhan as an Example [C]// Academic Committee of Urban Transportation Planning, China Society of Urban Planning. Wuhan Institute of Transportation Development Strategy, 2022:17. DOI:10.26914/c.cnkihy.2022.059256.

[6] Zhirong Ye. Organic Regeneration of Transportation in the Context of Urban Renewal in Core Areas [J]. Shanghai Highway, 2024(02):215-220+260.

[7] Xuedan Zhang, Lizhen Li, Xinhui Wang, et al. Spatial Planning Research on Slow Traffic on Urban Branch Roads Based on Dense Road Network [C]// 2022 Annual Conference on Urban Transportation Planning in China. [Publisher unknown], 2022:16.DOI:10.26914/c.cnkihy. 2022.059205.

[8] Guan Zhen. Research on Rail Transit Interchange Planning Based on "Three-Network Integration" [C]//The Annual Conference on Urban Transportation Planning in China 2021/2022. [Publisher unknown], 2022:9. DOI:10.26914/c.cnkihy.2022.059162.

Proceedings of the 2nd International Conference on Functional Materials and Civil Engineering
DOI: 10.54254/2755-2721/91/20241086

Advancements in shape-memory alloys: Properties, applications, challenges, and future prospects

Rong Gao

Shanghai Pinghe School, Shanghai, China

ronggao2007@outlook.com

Abstract. Shape-memory alloys (SMAs) are advanced engineering materials that have gained significant attention in recent years due to their unique properties and potential applications. SMAs have the remarkable ability to recover their original shape after deformation, making them invaluable in various fields, from biomedical devices to aerospace engineering. Despite their many advantages, SMAs also face several challenges, including the need for improved processing techniques and the development of more efficient actuation systems. To address these challenges, researchers have adopted various approaches, including using advanced fabrication methods and developing novel actuation systems. Recent research has yielded several notable achievements in the field of SMAs. For example, researchers have developed new processing techniques that allow the production of SMAs with improved properties, such as higher strength and better fatigue resistance. Additionally, researchers have developed new actuation systems that allow for more precise and efficient control of SMA behavior. Looking ahead, the future of SMAs looks promising. With continued research and development, SMAs have the potential to revolutionize various fields, from aerospace engineering to biomedical devices. However, further work is needed to overcome the remaining challenges and fully realize the potential of these remarkable materials. This article provides a comprehensive overview of SMAs, including their properties, fabrication methods, and various applications. It also discusses the challenges facing the field, the approaches to address them, and recent achievements.

Keywords: Shape-memory alloys, advanced engineering materials.

1. Introduction

Shape-memory alloys (SMAs) operate on the fundamental principle of the Shape Memory Effect (SME). SME involves a temperature-induced phase transformation that reverses deformation. The martensitic phase in SMAs, typically monoclinic or orthorhombic in structure, undergoes this transformation. Interestingly, martensite lacks sufficient slip systems for easy dislocation motion and deforms through detwinning. Thermodynamically, martensite is favored at lower temperatures, while austenite is favored at higher temperatures. When cooling austenite into martensite, internal strain energy is introduced, leading to the formation of many twins, a process known as self-accommodating twinning.[1] SMAs primarily utilize the martensitic phase at their operating temperatures to exploit the shape memory effect, and it's worth noting that no atomic bonds are broken or reformed during this process.

Additionally, geometrically necessary dislocations, a type of dislocation in crystalline materials, play a role in plastic deformation. Pseudo elasticity, also known as super-elasticity, is another crucial phenomenon in SMAs, characterized by the reversible response to applied stress via phase transformations between austenitic and martensitic phases.[2] SMAs exhibit various types of pseudo elasticity, with the main pseudo elasticity occurring during the stress-inducement phase transformation process. This behavior is illustrated graphically, where stresses above the martensitic stress induce austenite-to-martensite transformation, resulting in large macroscopic strains until no austenite remains (C). Upon unloading, martensite reverts to the austenite phase below the austenitic stress (D), allowing strain recovery until the material is fully austenitic and minimal deformation persists.

Shape Memory Alloys (SMAs) have garnered considerable significance and attention in recent years. These alloys possess the remarkable ability to deform when subjected to a changed temperature and spontaneously revert to their original shape when the temperature changes again.

2. Applications of Shape-memory Alloys

In materials science, Shape-memory Alloys (SMAs) have garnered considerable attention and significance. These alloys can deform when subjected to cold temperatures and then effortlessly revert to their original shape upon heating, a phenomenon referred to as the Shape Memory Effect (SME). This unique behavior has opened doors to many practical applications, including biomedical devices, aerospace engineering, etc.

This section provides several introductions of its real-life applications, along with the possible limitations and their possible drawbacks.

2.1. Biomedical Applications

SMAs can be used in biomedical applications. Most shape-memory alloys used in medical devices are Nitinol (NiTi) due to its good workability in the martensite phase and good resistance to corrosion and fatigue.

2.1.1. Orthodontics. Archwires and palatal expanders are the most significant orthodontic devices. They take advantage of superelasticity. Because of bone remodeling, SMA materials can apply almost constant force to the teeth during dental repositioning.[3] The almost constant oral cavity temperature helps SMAs produce proper constant spring-back forces over various deformations. This makes SMAs more effective than classical alloys since traditional materials have a more rigid shape.

2.1.2. General Surgery. In general surgery, SMAs can be used in minimally invasive surgery (MIS) since surgical endoscopic procedures require devices to access and operate into intricate regions. SMAs benefit from stainless and other conventional materials since they provide higher flexibility and improve effectiveness in narrow cavities. This fits the requirements of low-sized components. Furthermore, super-elasticity provides high strain recovery and a wide, constant stress plateau over many strains. These unique SMA characteristics led to the designing and manufacturing novel optimized instruments, which are especially favorable for MIS.[4]

2.1.3. Neurosurgery. In neurosurgery, NiTi micro guidewires can also be used. Aneurysm treatments and angioplasty require flexible NiTi micro guidewires which are smaller than 0.5mm to form a guide for the advancement and positioning of other devices, such as angioplasty balloons, stents, and filters, by following tortuous paths without kinking.[5] Since they have the qualities of high steerability and torquability, high strain recovery, and resistance to torsion and kinking, NiTi wires could cause fewer problems in bending than conventional materials, reducing the operation time and improving the surgeon's ease.

SMAs can also be used in orthopedics, otolaryngology, urology, physical therapy, etc.[6] However, the transformation between the martensitic and austenitic phases in SMAs can be relatively slow, leading to delays in actuation or response time, which could not be favorable in critical medical procedures. Meanwhile, the high-quality SMAs can be expensive. This could restrict their use in cost-sensitive medical applications and limit further development.

DOI: 10.54254/2755-2721/91/20241086

2.2. Aerospace Engineering

Notably, shape-memory alloys have the potential to realize adaptive flaps according to two different architectures: compliant and kinematic.

Owing to their distinctive attributes, particularly the NiTi variety, Shape Memory Alloys (SMAs) hold significant potential for application in aerospace contexts, including tasks like wing morphing, propulsion systems enhancement, and noise mitigation.[7] These attributes encompass considerable recoverable strains, substantial stress generation, extensive hysteresis loops within the stress-strain relationship, and variable electrical properties. By harnessing these unique characteristics, SMA components can fulfill multifunctional roles as structural elements, serving as actuators, dampers, or sensors.[8] This multifunctional capacity enables the streamlining of systems, reducing the number of components and complexity, a particularly appealing prospect within the aerospace engineering sector. In this demanding field, marked by stringent requirements for low weight and exceptional reliability, SMAs emerge as an attractive and versatile asset.

2.2.1. Bray foil Morphing Wing System. The Bray foil morphing wing system is designed to automatically set the attack angle on a freely rotating wing, using a single uninterrupted shell of composite or similar stiff sheet material. The wing changes camber and thickness while setting an increasingly variable reflex to match the angle of attack with the change in lift characteristics of the morphing section. Simplicity is the advantage. It has far fewer moving parts, less maintenance, and a lower cost than other typologies. It has no sliding joints or hinged panels, common in other morphing typologies. The wings' ability to set attack angles by the reflex section eliminates the need for the tailplane moment, thus reducing airframe drag by some 20% or more from a normal aircraft.

The Bray foil system is an ideal application for SMA actuators.[9] The SMA wires can be embedded into the skin or used to actuate structural mechanisms linked to the flexible skin to realize optimized airfoil shapes. As the pressure bubble, controlling the transition between laminar and turbulent flow is strongly related to the curvature of the airfoil shape; drag reduction resulting from a delay in the laminar-to-turbulent flow transition can be realized by changing adaptively airfoil camber and moving the morphed airfoil to the optimized position.

2.2.2. Variable Geometry Jet Engine Nozzle. Another example is the variable geometry of jet engine nozzles. The nozzles are meticulously engineered to modulate the exhaust flow area of jet engines, a measure that holds the potential to enhance fuel efficiency and curtail emissions significantly. However, conventional variable geometry nozzles are characterized by sophistication and substantial weight, factors that can exert adverse effects on the overall aircraft performance. SMAs represent an appealing, lightweight, and dependable alternative that can streamline the design of such nozzles. In manufacturing a variable geometry jet engine nozzle, SMAs can be effectively employed as actuators to regulate the position of the nozzle flaps. Upon heating, the SMA wires contract, exerting tension on the flaps, thus inducing closure. Therefore, the exhaust flow area can be reduced. Conversely, during the cooling phase, the SMA wires would expand. This allows the flaps to revert to an open config, enlarging the exhaust flow area. This operational sequence can be repetitively executed without any discernable degradation in performance, rendering SMA an exceptionally well-suited material for this application.[10]

2.2.3. Hinge and Deployment System for Solar Array. The last example of the application of SMAs in aerospace engineering is in developing hinge and deployment systems for solar arrays on satellites. This system is designed to deploy the solar arrays once the satellite is in orbit, which can provide power to the satellites' systems. Nonetheless, traditional hinge and deployment systems are complex and can be prone to failure, which could jeopardize the mission of the satellite launch. SMAs can offer a lightweight and reliable alternative that could simplify the design of these systems.[11] In a hinge and deployment system for a solar array, SMAs can be used as actuators to control the position of the hinges. When heated, the SMA wires contract and pull the hinges into a closed position, therefore securing the solar array. When cooled, the wires expand and allow the hinges to open, deploying the solar array. This

DOI: 10.54254/2755-2721/91/20241086

process can be repeated many times without any degradation in performance. This makes SMA an ideal material for this application. Additionally, SMAs can be used as sensors to detect the position of the hinges and ensure that they are in the correct position before each deployment. This could, hence, improve the reliability of the system and further reduce the risk of failure.

3. The solution to cutting challenges

3.1. Overview of Cutting Challenges

Shape-memory alloys (SMA), especially NiTi, are difficult to cut due to their unique mechanical properties, shape-memory effect (SME), and pseudo elasticity. These properties make NiTi SMAs ideal for various applications, including aerospace and medical fields.[12] However, these alloys are more challenging to cut than other advanced engineering materials due to their high ductility, crystal-oriented and stress-oriented mechanical properties. Waterjet technology is a non-conventional machining process that uses a high-pressure jet of water to cut a wide range of materials. The waterjet is typically pressurized to between 30,000 and 90,000 psi and forced through a small orifice, which creates a high-velocity jet of water that can cut through materials with high precision.

In some cases, abrasive particles, such as garnet, can be added to the water jet to increase its cutting power. One of the main advantages is its ability to cut a wide range of materials. It can cut metals, composites, ceramics, and plastics without generating heat or mechanical stresses that would damage the workpiece. This makes it an ideal cutting approach for materials that are difficult to cut using conventional methods. It also has high precision and accuracy, which makes it suitable for applications that require tight tolerances and high-quality cuts. Additionally, waterjet technology is environmentally friendly since it does not generate hazardous waste or emit harmful fumes.[12]

Subsequently, researchers propose the utilization of waterjet technology as a prospective approach for the difficulties associated with the cutting of NiTi SMAs. Waterjet technology can effectively cut materials that are difficult to cut because it has benefits, such as minimizing both mechanical and thermal damage to the surfaces of the workpiece and, therefore, widely gaining recognition.

3.2. Approaches

Researchers conducted several experimental approaches using a commercial waterjet machine to investigate the feasibility of using waterjet technology to mill NiTi SMAs. Their methodologies included water pressure, traverse speed, and standoff distance.[13] They also used a high-speed camera to capture images of the cutting process and analyzed the images to determine the quality of the cut.[14]

As a result, waterjet technology was able to successfully mill NiTi SMAs, but the quality of the cut was highly dependent on the cutting parameters. Specifically, researchers found that the increase in the water pressure and the decrease in the traverse speed can result in higher-quality cuts. The standoff distance also significantly affects the quality of the cut, with a shorter standoff distance coming with a higher quality cut. Subsequently, researchers conducted a series of controlled depth milling experiments. In these experiments, researchers used a custom-built fixture to control the depth of the cut and varied the cutting parameters to determine their effects on the quality of the cut. As a result, the cutting parameters significantly impact the cutting qualities, with the water pressure and traverse speed the most.

Increasing the water pressure and decreasing the traverse speed resulted in a higher quality cut; specifically, a water pressure of 400 MPa and a traverse speed of 0.5 mm/s resulted in the highest quality cut. The effects of the cutting parameters on the surface roughness of the cut are also analyzed. Researchers found that increasing the water pressure and decreasing the traverse speed can result in a smoother surface finish. The standoff distance also has a significant effect on the surface roughness, with a shorter standoff distance resulting in a smoother surface finish.

3.3. Strengths and Weakness

Waterjet technology is known for its ability to cut advanced difficult-to-cut materials with minimal mechanical and thermal damage to the workpiece surfaces.[15] This is particularly important for NiTi

SMAs, which are highly ductile and have unique mechanical properties that make them difficult to cut using conventional methods. Secondly, this technology is capable of producing high-precision cuts with minimal kerf width, which is vital for applications that require high accuracy and precision.[16] Meanwhile, it can be used to cut a wide range of materials, not only SMAs but also metals, composites, ceramics, and plastics, which makes it a versatile cutting approach.[17]

Nevertheless, limitations still exist in waterjet technology. Firstly, it could be expensive to implement, especially for small-scale applications. The equipment's cost and maintenance can make it prohibitive and be a limiting factor for some applications. Secondly, waterjet technology is generally slower than other cutting approaches, such as laser cutting or plasma cutting. This could be a limitation for applications that require high speed and high production rates or when the products are vulnerable. Thirdly, while waterjet technology can produce high-quality cuts, the surface finish may not be as smooth as other cutting methods. This could be another limitation for applications that require a high-quality surface finish.

In conclusion, researchers solved the problem of cutting NiTi shape memory alloys by exploiting the waterjet technology. Through a series of experiments, the optimal cutting parameters for waterjet milling of NiTi SMAs were determined, which resulted in high-quality cuts with minimal mechanical and thermal damage to the workpiece surfaces. Further research is needed to optimize the cutting parameters for specific applications, such as medical applications requiring high-quality cuts.

4. The solution to long cycle time

Another major challenge in the practical applications of shape memory alloy actuators is their long cycle time. Cycle time refers to the time required for the SMA actuators to complete one cycle of operation, which includes both heating and cooling phases.[18] In the procedures, the cooling process could be slow, making the cycle long. For example, a typical NiTi alloy with a diameter of 0.25mm takes about 5.4 seconds to cool off.[19] Adding one second for heating, the actuator could take approximately 6.4 seconds to complete one cycle of operation. This drawback results in a very low cyclic frequency of roughly 0.056 hertz, which may not be suitable for many applications, especially unsuitable for fast cyclic applications.[20] This limitation poses constraints in domains such as robotics and aerospace engineering. Hence, devising a solution to diminish the cooling time of SMA actuators is imperative for advancing SMA technology.

4.1. Forced Air Cooling

Forced air cooling is a cooling technique that involves directing a stream of air over the SMA actuator to expedite heat transfer and reduce the cooling period. It is commonly used in applications such as robotics and automation, where the actuators are exposed to the air. This approach could increase the heat transfer coefficient and allow for faster cooling of the SMA actuators. Nonetheless, it is worth noting that while forced air cooling can significantly diminish cooling times, it demands a substantial energy input and may not be universally applicable. The energy input required for forced air cooling can be huge, and it would limit its use in applications where energy consumption is a concern and also increase the expenses. Additionally, forced air cooling may not be suitable for applications where the actuator is enclosed or where additional energy is of no feasibility. Despite these limitations, forced air cooling can effectively undermine the cooling duration of SMA actuators in more applications.[21]

4.2. Water Cooling

Water cooling involves circulating water around the SMA actuators to enhance heat dissipation and curtail cooling intervals. Water has a higher heat capacity than air, so it can absorb more heat energy from the SMA actuator, resulting in faster cooling.[22] Water cooling has been observed to be more effective than forced air cooling in reducing cooling times. However, it necessitates access to a water source and may not be appropriate for all scenarios. It is commonly used in applications where the actuator is enclosed or where additional energy is of no feasibility.[23] Therefore, water cooling may not be suitable for applications where the actuator is exposed to the water or where the use of additional equipment is of no feasibility.

4.3. Fluidic Cooling

Internal fluidic cooling encompasses fluid circulation through the SMA actuator to expedite cooling, such as a refrigerant or coolant. The fluid absorbs heat from the SMA actuator, which results in faster cooling.[24] This method has proven highly effective in curtailing cooling times but involves the requirement of a fluid source and may entail more intricate implementation than forced air or water cooling methods. Fluidic cooling is commonly used in applications where the actuator is enclosed or where the use of additional energy is not feasible. Therefore, it may not be suitable for applications where the actuator is exposed to fluids or where the use of additional equipment is not feasible.

4.4. Strategies Design

In addition to cooling techniques, various design strategies have been explored to decrease the cooling duration of SMA actuators.[23] These strategies encompass reducing the size of the SMA wire, augmenting the surface area of the SMA wire, and employing multiple SMA wires in parallel or series configs.[25] A reduction in the size of the SAM wire has shown the potential to significantly decrease cooling times, albeit potentially diminishing the actuators' force outputs.[26] Meanwhile, increasing the surface area of the SMA wires can also expedite cooling but may necessitate more convoluted designs. Employing multiple SMA wires in parallel or series can enhance the actuators' force output without substantially elongating cooling durations.

Furthermore, researchers have examined the application of pre-strain to diminish cooling durations. Pre-strain involves applying slight deformation to the SMA wire before heating, reducing the strain required to reset the actuator. Pre-strain may decrease the actuator's force output and entail a more intricate design.

4.5. Elastic Compensation

The principle of elastic compensation in shape memory actuators has been introduced to maximize the overall stroke and the useful output force.[27] The elastic compensation system adds a conventional spring to the shape memory actuator, which is mounted with preload and acts transversely to the wires. The compensation system is designed to have specific elastic stiffness and compensation force at the position of minimum net force, which is calculated from the design data of the actuator.[28] Researchers show that the elastic compensation system can increase the stroke or useful force of the actuator by more than 2.5 times compared to the actuator without compensation while maintaining the same level of performance.

Overall, the choice of SMA alloy can exert a discernible impact on the cooling duration of the actuator. Some SMA alloys exhibit faster cooling rates than others, thereby making the overall cycle time shorter than before. Nevertheless, this alloy choice may influence other actuator properties, including force outputs and durability. In conclusion, researchers have explored various approaches to alleviate the cooling time associated with the SMA actuators. These approaches encompass cooling methodologies such as forced air, water, and internal fluidic cooling, as well as design modifications like altering wire size, enhancing surface area, and employing multiple wires in parallel or series. The selection of the SMAs itself can also influence cooling times. Mitigating the cooling duration, therefore the cycle time, of the SMA actuators can help researchers surmount a principal hurdle in the practical application and broaden the utilization of SMAs across diverse domains.

5. The solution to difficult control

Another major challenge associated with the practical application of shape memory alloy (SMA) actuators is their difficult control. SMA actuators exhibit highly nonlinear behavior, making them difficult to control using traditional methods. In addition, SMA actuators have a slow response time and a hysteresis effect, which further complicates their control. The nonlinear behavior of SMA actuators arises from the complex relationship between the input, the current or voltage, and the actuator's output, the displacement or force.[29] The relationship is highly dependent on the SMA wire's temperature and strain state. As a result, traditional control methods, such as proportional-integral-derivative (PID) control, may not effectively control SMA actuators.[30] The slow response time of SMA actuators is due to their long cycle time, as discussed in the previous section. The hysteresis effect of SMA actuators is that the actuator does not return to its original shape immediately after cooling. Instead, it requires applying a certain amount of strain before it returns to its original shape. This hysteresis effect can make it difficult to control the position or force output of the actuator accurately.

5.1. Model-based Control

Model-based control is a control technique that involves developing a mathematical model of the SMA actuator and using this model to design a control system.[31] The authors note that model-based control can effectively control SMA actuators, allowing for precise control of the actuator's behavior.[32] Nevertheless, it requires a good understanding of the behavior of the actuator and may be difficult to implement in practice.[33] The accuracy in the whole process of operating the model is crucial to the success of the control system. Any errors in the model could lead to poor actuator performance.[34] Model-based control is commonly used in applications where the precise control of the actuator is required, such as robotics and automation. However, model-based control may not be suitable for applications where the actuator's behavior is highly nonlinear, it is difficult to estimate, or additional equipment is not feasible.

5.2. Adaptive Control

Adaptive control involves adjusting the system's control parameters in real-time based on the actuator's behavior.[35] It is a control technique distinguished by its capacity to dynamically modify system control parameters in response to the actuator's evolving behavior. This approach can be effective when the actuator's behavior remains uncertain or undergoes variations over time.

Additionally, adaptive control can exhibit sensitivity to external disturbances and uncertainties, potentially impacting the control system's performance.[36] This approach has already found practical applications in the control of SMA actuators. For instance, a Generalized Predictive Control system was employed to address the nonlinear behavior of an SMA spring-based linear motion actuator in 2010. Likewise, adaptive PID controllers, combined with an inverse hysteresis model, are investigated to actuate an SMA-based robotic hand, demonstrating the capability to mitigate overshooting and achieve effective tracking control.

5.3. Sliding Mode Control

Sliding mode control involves designing a control system that forces the actuator's output to follow a sliding surface. The sliding surface is a function of the system's state variables, designed to ensure that the actuator's output converges to a desired value.[37] According to the researchers, the sliding mode control can effectively control SMA actuators, especially in the presence of disturbances and uncertainties.[38] This is because sliding mode control is designed to be robust to disturbances and uncertainties, and it can ensure that the actuator's output converges to the desired value even in the presence of these disturbances.

However, sliding mode control can be sensitive to noise and may require a more complex design because it involves designing a sliding surface that is sensitive to the system's state variables.[37] Additionally, sliding mode control can require a more complex design than other control techniques, making it more difficult to implement in practice.

Overall, researchers have examined many strategies to enhance the control of SMA actuators. These approaches encompass model-based control, adaptive control, sliding mode control, etc. By refining the control mechanisms governing SMA actuators, researchers can effectively address a significant obstacle hindering their practical application, expanding the scope of SMA utilization across a broader spectrum of applications.

DOI: 10.54254/2755-2721/91/20241086

6. Conclusion

In conclusion, Shape-Memory Alloys (SMAs) are advanced engineering materials that have gained significant attention in recent years due to their unique properties and potential applications. SMAs can recover their original shape after deformation, making them invaluable in various fields, from biomedical devices to aerospace engineering. This paper has provided a comprehensive overview of SMAs, including their properties, fabrication methods, and various applications. It has also discussed the challenges facing the field, the approaches to address them, and recent achievements. Despite the many advantages of SMAs, several challenges remain, including the need for improved processing techniques and the development of more efficient actuation systems. However, with continued research and development, SMAs have the potential to revolutionize various fields, from aerospace engineering to biomedical devices. Using SMAs in biomedical applications shows great promise, with the development of new SMA-based devices and implants that can improve patient outcomes and quality of life. Additionally, the use of SMAs in aerospace engineering has the potential to reduce weight and improve fuel efficiency, leading to significant cost savings and environmental benefits. Overall, the future of SMAs looks promising, and continued research and development in this field will undoubtedly yield many exciting discoveries and applications.

References

[1] U. Dahmen, "Phase Transformations, Crystallographic Aspects," in *Encyclopedia of Physical Science and Technology*, 2003. doi: 10.1016/b0-12-227410-5/00560-3.

[2] K. K. Alaneme and E. A. Okotete, "Reconciling viability and cost-effective shape memory alloy options – A review of copper and iron based shape memory metallic systems," 2016. doi: 10.1016/j.jestch.2016.05.010.

[3] D. J. Fernandes, R. V. Peres, A. M. Mendes, and C. N. Elias, "Understanding the Shape-Memory Alloys Used in Orthodontics," *ISRN Dent*, vol. 2011, 2011, doi: 10.5402/2011/132408.

[4] C. Song, "History and Current Situation of Shape Memory Alloys Devices for Minimally Invasive Surgery," *The Open Medical Devices Journal*, vol. 2, no. 2, 2010, doi: 10.2174/1875181401002020024.

[5] D. J. Hoh, B. L. Hoh, A. P. Amar, and M. Y. Wang, "Shape memory alloys: Metallurgy, biocompatibility, and biomechanics for neurosurgical applications," *Neurosurgery*, vol. 64, no. SUPPL. 5, 2009, doi: 10.1227/01.NEU.0000330392.09889.99.

[6] L. Petrini and F. Migliavacca, "Biomedical Applications of Shape Memory Alloys," *Journal of Metallurgy*, vol. 2011, 2011, doi: 10.1155/2011/501483.

[7] R. Pecora, I. Dimino, M. Bray, and R. Bray, "SMA for aeronautics," in *Shape Memory Alloy Engineering: For Aerospace, Structural, and Biomedical Applications*, 2021. doi: 10.1016/B978-0-12-819264-1.00015-7.

[8] L. Janke, C. Czaderski, M. Motavalli, and J. Ruth, "Applications of shape memory alloys in civil engineering structures - Overview, limits and new ideas," *Materials and Structures/Materiaux et Constructions*, vol. 38, no. 279, 2005, doi: 10.1617/14323.

[9] A. Concilio, V. Antonucci, F. Auricchio, L. Lecce, and E. Sacco, *Shape Memory Alloy Engineering: For Aerospace, Structural, and Biomedical Applications*. 2021. doi: 10.1016/B978-0-12-819264-1.01001-3.

[10] G. Song and N. Ma, "Shape memory alloy actuated adaptive exhaust nozzle for jet engine," 2009

[11] A. Guzik and O. Benafan, "Design and Development of CubeSat Solar Array Deployment Mechanisms Using Shape Memory Alloys," in *44th Aerospace Mechanisms Symposium*, 2018.

[12] J. M. Llanto, M. Tolouei-Rad, A. Vafadar, and M. Aamir, "Recent progress trend on abrasive waterjet cutting of metallic materials: A review," 2021. doi: 10.3390/app11083344.

[13] M. Muniraju and G. Talla, "Exploring sustainable machining processes for nitinol shape memory alloy: a review of eco-friendly EDM and other techniques," 2024. doi: 10.1007/s40430-023-04642-8.

[14] M. C. Kong, D. Axinte, and W. Voice, "Challenges in using waterjet machining of NiTi shape memory alloys: An analysis of controlled-depth milling," *J Mater Process Technol*, vol. 211, no. 6, 2011, doi: 10.1016/j.jmatprotec.2010.12.015.

[15] X. Liu, Z. Liang, G. Wen, and X. Yuan, "Waterjet machining and research developments: a review," 2019. doi: 10.1007/s00170-018-3094-3.

[16] P. Thakur, D. N. Raut, and F. Siddiqui, "Recent Applications, Developments and Challenges in Waterjet Technology," in *Lecture Notes in Mechanical Engineering*, 2022. doi: 10.1007/978-981-16-9236-9_14.

[17] H. T. P. Liu, "Advanced waterjet technology for machining curved and layered structures," *Curved and Layered Structures*, vol. 6, no. 1, 2019, doi: 10.1515/cls-2019-0004.

[18] J. W. Sohn, J. S. Ruth, D. G. Yuk, and S. B. Choi, "Application of Shape Memory Alloy Actuators to Vibration and Motion Control of Structural Systems: A Review," 2023. doi: 10.3390/app13020995.

[19] A. Dana, S. Vollach, and D. Shilo, "Use the force: review of high-rate actuation of shape memory alloys," 2021. doi: 10.3390/act10070140.

[20] S. Jayachandran, N. Yashwanth, H. F. Hussain, and I. A. Palani, "Investigation on Actuation Performance of Shape Memory Alloy Actuator for Robotics Application," in *Lecture Notes in Mechanical Engineering*, 2023. doi: 10.1007/978-981-19-3866-5_45.

[21] F. Taylor and C. K. Au, "Forced Air Cooling of Shape-Memory Alloy Actuators for a Prosthetic Hand," *J Comput Inf Sci Eng*, vol. 16, no. 4, 2016, doi: 10.1115/1.4033233.

[22] A. Osorio Salazar, Y. Sugahara, D. Matsuura, and Y. Takeda, "A Novel, Scalable Shape Memory Alloy Actuator Controlled by Fluid Temperature," in *Mechanisms and Machine Science*, 2021. doi: 10.1007/978-3-030-55807-9_69.

[23] S. Lederlé, "Issues in the design of shape memory alloy actuators," *Aeronatics and astronautics*, 2002.

[24] I. Y. Paez-Pidiache, A. Luviano-Juárez, N. Lozada-Castillo, E. Castillo-Castañeda, and H. Reyes-Torres, "Design, characterization and construction of an actuator based on shape memory alloys," *MRS Adv*, vol. 6, no. 39–40, 2021, doi: 10.1557/s43580-021-00158-2.

[25] R. W. Wheeler *et al.*, "Engineering design tools for shape memory alloy actuators: CASMART collaborative best practices and case studies," *J Intell Mater Syst Struct*, vol. 30, no. 18–19, 2019, doi: 10.1177/1045389X19873390.

[26] J. S. Koh, "Design of shape memory alloy coil spring actuator for improving performance in cyclic actuation," *Materials*, vol. 11, no. 11, 2018, doi: 10.3390/ma11112324.

[27] G. Scirè Mammano and E. Dragoni, "Elastic compensation of linear shape memory alloy actuators using compliant mechanisms," in *Journal of Intelligent Material Systems and Structures*, 2014. doi: 10.1177/1045389X13488253.

[28] S. Saito, S. Oka, and R. Onodera, "Modelling of a shape memory alloy actuator for feedforward hysteresis compensator considering load fluctuation," *CAAI Trans Intell Technol*, vol. 7, no. 4, 2022, doi: 10.1049/cit2.12129.

[29] E. A. Williams, G. Shaw, and M. Elahinia, "Control of an automotive shape memory alloy mirror actuator," *Mechatronics*, vol. 20, no. 5, 2010, doi: 10.1016/j.mechatronics.2010.04.002.

[30] H. F. M. Ali, Y. Kim, Q. H. Le, and B. Shin, "Modeling and control of two DOF shape memory alloy actuators with applications," *Microsystem Technologies*, vol. 28, no. 10, 2022, doi: 10.1007/s00542-022-05301-z.

[31] E. J. Abdullah, J. Soriano, I. Fernández de Bastida Garrido, and D. L. Abdul Majid, "Accurate position control of shape memory alloy actuation using displacement feedback and self-sensing system," *Microsystem Technologies*, vol. 27, no. 7, 2021, doi: 10.1007/s00542-020-05085-0.

[32] R. Neugebauer, K. Pagel, A. Bucht, and W. G. Drossel, "Model-based position control of Shape memory alloy actuators," *International Journal of Mechatronics and Manufacturing Systems*, vol. 5, no. 2, 2012, doi: 10.1504/IJMMS.2012.046521.

[33] A. Kumagai, T. I. Liu, and P. Hozian, “Control of shape memory alloy actuators with a neuro-fuzzy feedforward model element,” *J Intell Manuf*, vol. 17, no. 1, 2006, doi: 10.1007/s10845-005-5512-2.

[34] N. T. Tai, N. B. Kha, and K. K. Ahn, “Predictive position and force control for shape memory alloy cylinders,” *Journal of Mechanical Science and Technology*, vol. 24, no. 8, 2010, doi: 10.1007/s12206-010-0504-3.

[35] E. Shi, X. Zhong, T. Wang, X. Li, C. Bu, and X. Zhao, “Adaptive control for shape memory alloy actuated systems with applications to human–robot interaction,” *Front Neurosci*, vol. 18, 2024, doi: 10.3389/fnins.2024.1337580.

[36] P. Senthilkumar, G. N. Dayananda, M. Umapathy, and V. Shankar, “Experimental evaluation of a shape memory alloy wire actuator with a modulated adaptive controller for position control,” *Smart Mater Struct*, vol. 21, no. 1, 2012, doi: 10.1088/0964-1726/21/1/015015.

[37] H. Ashrafiuon and V. R. Jala, “Sliding mode control of mechanical systems actuated by shape memory alloy,” *Journal of Dynamic Systems, Measurement and Control, Transactions of the ASME*, vol. 131, no. 1, 2009, doi: 10.1115/1.3023121.

[38] N. T. Tai and K. K. Ahn, “Adaptive proportional-integral-derivative tuning sliding mode control for a shape memory alloy actuator,” *Smart Mater Struct*, vol. 20, no. 5, 2011, doi: 10.1088/0964-1726/20/5/055010

Proceedings of the 2nd International Conference on Functional Materials and Civil Engineering
DOI: 10.54254/2755-2721/91/20241084

Research on electric heating green snow melting and anti-icing technology for tunnel, bridge, and culvert entrances

Xingsen Du[1,2], Kepeng Zong[1,3], Chunyu Ma[1,4], Jizeng Li[1,5], Chaolong Qi[1,6,*]

[1]Linyi University, Linyi, Shandong Province, Industrial Avenue North Section, West Side, Lanshan District, 276000, China

[2]550997491@qq.com
[3]1097957914@qq.com
[4]1224746270@qq.com
[5]1784404425@qq.com
[6]qichaolong@lyu.edu.cn
[*]corresponding author

Abstract. This paper addresses the issue of electric heating snow melting at tunnel, bridge, and culvert entrances. It explores a novel carpet-style electric heating snow melting and anti-icing system for these areas. The study analyzes the shortcomings of existing electric heating snow melting methods and proposes effective measures for improvement. To accurately assess the characteristics of current snow melting techniques, the research considers the damage caused by traditional snow melting methods to road structures and subsequent maintenance issues, while emphasizing energy-saving and environmentally friendly technologies. The snow melting process was simulated using Star-CCM+. The results show that the new carpet-style electric heating elements significantly improve snow melting efficiency. Preheating the road surface before snow accumulation greatly reduces snow retention time, enabling timely snow and ice removal. Typically, electric heating elements in snow melting systems are installed beneath the road surface at tunnel entrances. After installation, to protect the elements and ensure smoothness, a layer of cement or another suitable material is poured over them. However, these heating elements require regular inspection or replacement, which necessitates breaking up the road surface, increasing maintenance costs, and disrupting normal traffic operations. This study overcomes these challenges by providing significant convenience for installation and maintenance work, reducing costs, and minimizing the impact on traffic operations.

Keywords: Bridges and culverts, Tunnels, Traffic, Snow melting and anti-icing, Snow melting strategies.

1. Introduction

Accumulation of Snow at Tunnel and Bridge Entrances: The accumulation of snow at tunnel and bridge entrances is an issue that requires attention. Snow can have multiple adverse effects on traffic. Firstly, it reduces the width of the road, affecting the normal trajectory of vehicles. Secondly, snow can melt and refreeze, forming ice layers that lower the friction coefficient of the road surface and increase the risk of vehicle skidding.

DOI: 10.54254/2755-2721/91/20241084

Current Road De-icing Technologies: Currently, various de-icing technologies coexist. A common method is passive de-icing, which primarily involves removing snow after it has fallen. This includes mechanical methods and chemical de-icing, using pre-application and dynamic spreading of de-icing agents [1], and manual clearing to remove snow and ice from the road surface. However, this approach requires lane closures or traffic blockages and can be inefficient, especially in very low temperatures or with thick snow accumulation.

Active de-icing technologies involve altering the composition and structure of the road surface so that it can actively melt snow and ice during snowfall. These include self-stress elastic pavements [2], low-freezing-point pavements, and energy-converting pavements. For example, self-stress elastic pavements [3] use elastic materials with high deformation characteristics to break up the ice and snow layer under vehicle load. Low-freezing-point pavements [4] incorporate additives into the asphalt mixture that gradually leach out to melt snow and ice. Energy-converting pavements use embedded heat transfer pipes or conductive elements to convert external energy into heat, including fluid-heated, heat pipe-heated, and electrically heated pavements.

Self-Deicing Pavement Technology [5]: Self-deicing pavement technology involves adding antifreeze and de-icing chemicals to the pavement materials without changing the construction process or difficulty. Through capillary action, these chemicals are slowly released to prevent snow accumulation and inhibit ice formation without affecting the performance of the pavement or polluting the environment. This technology is easy to operate, has low corrosiveness to roads and bridges, can prevent icing for many years, and reduces maintenance costs. For instance, in Changchun, roads with self-deicing asphalt pavements that contain high-performance composite antifreeze additives can actively melt snow without forming ice during small snowfalls in winter. Even in heavy snowfall, the roads do not accumulate ice and are easy to clear, thus providing safety. Although the material cost of this technology is relatively high, its application is still limited. However, with increased promotion and usage, costs may decrease, making it feasible for wider application in the future.

Challenges in Snow and Ice Removal in Cold Regions: In cold regions or under special weather conditions, the accumulation of snow and ice on the road surface is a significant challenge, requiring attention to key areas such as road sections, bridges, and tunnels [6]. For instance, the G356 highway in Meihuashan, managed by the Shuicheng Highway Administration, is a critical section for frost and slip prevention in winter. The administration activates emergency response, implements a 24-hour duty system, strengthens hazard inspections, and road monitoring, and provides timely rescue to stranded drivers and passengers.

2. Analysis of Domestic Cases and Technologies

Road electrical heating for snow and ice removal is a technology that uses electrical heating to melt snow and ice on roads. Some common systems include:

1. Intelligent Electrical Heating De-icing Technology [7]: Developed by the research team led by Professor Xiao Henglin from the School of Civil Engineering and Environmental Engineering at Hubei University of Technology, this technology consists of a monitoring system, heating system, and power supply system. It uses high-strength, high-efficiency carbon fiber heating modules installed at a certain depth in the road or bridge surface. When activated, these modules heat up and melt the snow and ice. The advantages include remote control, low energy consumption, quick heating, and smart remote control. This technology has been successfully applied to projects such as the G59 Hu-Bai Expressway and the Bai Sangguan Bridge.

2. Intelligent Loop Heat Pipe De-icing System [8]: Developed by Sichuan Highway Planning, Survey, and Design Institute Co., Ltd., this system uses 4mm diameter heat pipes buried 5cm below the road surface. It ensures safe passage on 2.2m wide roads during winter and uses an air source heat pump with an efficiency ratio of over 3.0 at low temperatures as the heat source. The system includes a weather monitoring station and sensors to control heating based on real-time data, minimizing maintenance needs.

3. Heating Cable Snow and Ice Removal System [9]: This system embeds heating cables in asphalt concrete to transfer heat through conduction, radiation, and convection, effectively melting snow and

DOI: 10.54254/2755-2721/91/20241084

ice. The heating cables are safe, durable, and environmentally friendly, and can be used in a variety of outdoor facilities, including roads, bridges, and airport runways.

4. Self-regulating Heating Tape Snow Removal System [10]: For example, self-regulating heating tapes can adjust their output power based on environmental temperature changes, increasing power when the temperature is low and decreasing it when the temperature rises. They are suitable for various concrete surfaces and can be cut to length and easily installed.

These technologies effectively address snow and ice accumulation on roadways, enhancing winter road safety and reducing traffic accidents. However, their installation and maintenance costs are relatively high, requiring careful consideration of practicality and economic benefits. Moreover, using cleaner and more energy-efficient sources can help reduce operational costs and environmental impact.

In the electric snow melting technology, heating elements are often installed under the pavement at tunnel entrances [11]. Typically, after installation, a layer of cement or other suitable material is poured over the heating elements to protect them and ensure a smooth road surface. However, these heating elements require regular inspection or replacement, which necessitates digging up the pavement. This not only increases maintenance costs but also disrupts normal road traffic.

Therefore, to address these issues, a new type of electric heating element for the snow melting system at tunnel entrances is proposed.

3. Snow Melting System for Tunnel Entrances

The tunnel entrance is a necessary passage for vehicles entering and exiting the tunnel. In winter, if the snow at the tunnel entrance is not cleared in time, it may gradually accumulate, blocking the tunnel entrance and affecting normal traffic flow. Current technology often involves installing a snow-melting system beneath the pavement at some tunnel entrances. This system is used to heat the pavement in cold weather conditions, melting the snow and ice in the tunnel entrance area and its vicinity. The electric heating elements used in the snow-melting system are typically made of high-efficiency, durable materials capable of generating sufficient heat at low voltages to effectively melt ice and snow. These heating elements can be heating pipes, heating cables, or heating plates [7].

Accumulation of snow and ice on road surfaces is common in most parts of China. Timely and effective removal of snow and ice from road surfaces is crucial for ensuring traffic safety and improving road traffic capacity. Fluid heating road snow-melting systems are favored by road workers worldwide for their strong controllability, wide range of heat energy sources, and green, pollution-free characteristics.

This solution establishes an electric heating element for a tunnel entrance snow-melting system, belonging to the field of road snow-melting technology. The electric heating element for the tunnel entrance snow-melting system includes an installation box, multiple heating pipes, and multiple placement components. One end of the installation box is open, and a placement groove is provided at the upper end near the open side of the installation box. The inner wall bottom end of the installation box is fixedly connected with a pair of symmetrical positioning blocks. The placement components include a placement box that matches the heating pipes. In this solution, when installing and removing multiple heating pipes, the user only needs to turn on the road switch located next to the road. This will use the drive component to place multiple placement components from the placement groove into the installation box's inner cavity or remove them all from the placement groove, without the need to excavate the road surface at the tunnel entrance. This does not affect the normal operation of road traffic, greatly facilitating installation and maintenance work, reducing maintenance costs, and minimizing the impact on traffic flow.

3.1. Electric Heating Elements for Tunnel Entrance Snow-Melting Systems

Description of the numbering in the figures:

1.Installation box;

2.Placement groove;

3.Positioning block;

4.Positioning groove;
5.Cable storage compartment;
6.Drive component; 601. Servo motor; 602. Chain; 603. Positioning rod;
7.Heating pipe;
8.Placement component; 801. Placement box; 802. Roller; 803. Rack; 804. Cable slot.

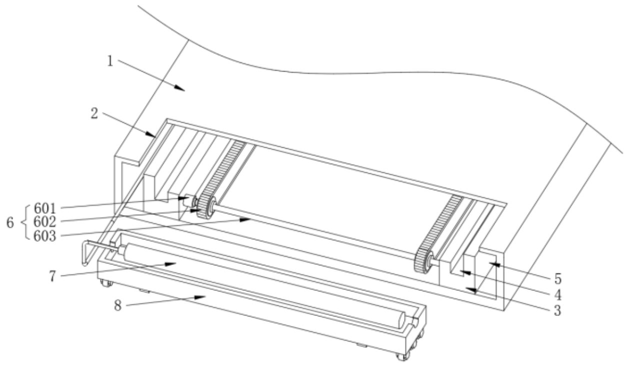

Figure 1. Installation Component Assembly Diagram

The system includes an installation box (1), multiple heating tubes (7), and multiple placement components (8). It is characterized in that: one end of the installation box (1) is open, and a placement slot (2) is located at the upper end near the open side of the installation box (1). The bottom end of the inner wall of the installation box (1) is fixedly connected to a pair of symmetrically positioned limiting blocks (3). The placement components (8) include a placement box (801), which matches the heating tubes (7). A driving component (6) is positioned between the pair of limiting blocks (3).

3.2. Electric Heating Elements for Tunnel Entrance Snow-Melting Systems - Placement Components

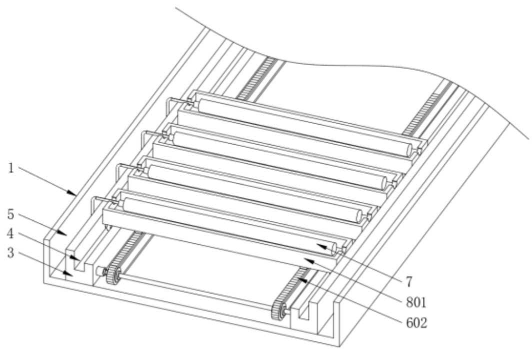

Figure 2. Placement Component Diagram

Referring to Figure 2, a pair of symmetrical rollers (802) is fixedly connected to the bottom end of the placement box (801). The upper end of the positioning block (3) has a positioning groove (4) that matches the rollers (802). A cable storage compartment (5) is formed between the end of the positioning block (3) away from the other and the inner wall of the installation box (1). A pair of cable slots (804) that match the heating pipes (7) is provided at the top end of the placement box (801).

3.3. Electric Heating Elements for Tunnel Entrance Snow-Melting Systems - Drive Components

Referring to Figure 3, the drive component (6) includes a servo motor (601) and a pair of positioning rods (603). The servo motor (601) is mounted at one end of the positioning block (3), and a pair of positioning rods (603) is set on both sides of the installation box (1) cavity. One end of one of the positioning rods (603) is fixedly connected to the output end of the servo motor (601), while the other end is rotatably connected to the positioning block (3). The other positioning rod (603) has both ends rotatably connected to the pair of positioning blocks (3). A pair of sprockets is fixedly connected to the outer ends of the pair of positioning rods (603). A chain (602) is installed at the outer end of the sprockets. Multiple sprockets are connected through the chain (602), and the bottom end of the placement box (801) is fixedly connected with a rack (803) that matches the chain (602).

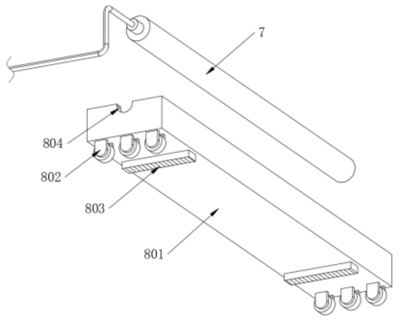

Figure 3. Drive Component Diagram

3.4. Electric Heating Elements for Tunnel Entrance Snow-Melting Systems - Working Principle

The working principle of the electric heating road snow-melting technology involves installing heating elements, such as carbon fiber heating wires, beneath or inside the road surface. These heating elements convert electrical energy into thermal energy, increasing the road surface temperature to melt ice and snow. During construction or renovation, special carbon fiber heating wires are embedded between the upper and lower layers of the asphalt road surface. When in operation, electrical energy is converted into thermal energy, raising the temperature of the equipment. The ice and snow melt as the road surface temperature increases, forming liquid water that flows into side ditches or gutters along the equipment's slope, thus reducing snow and ice accumulation on the road surface. An intelligent control system is employed to achieve energy-saving and efficient snow melting, automatically adjusting the heating power and duration based on snow accumulation on the road and weather conditions. Compared to traditional methods like manual ice and snow removal or the application of snow-melting agents, this technology offers certain advantages, including better snow and ice removal effectiveness, proactive snow melting, and savings in manpower and resources.

This device includes an installation box, multiple heating pipes, and multiple placement components. One end of the installation box is open, and a placement groove is provided at the upper end near the open side of the installation box. The inner wall bottom end of the installation box is fixedly connected with a pair of symmetrical positioning blocks. The placement components include a placement box that matches the heating pipes, with a drive component set between a pair of positioning blocks.

At the bottom end of the placement box, a pair of symmetrical rollers is fixedly connected. The upper end of the positioning block has a positioning groove that matches the rollers. A cable storage compartment is formed between the end of the positioning block away from the other and the inner wall of the installation box. A pair of cable slots that match the heating pipes is provided at the top end of the placement box.

The drive component includes a servo motor and a pair of positioning rods. The servo motor is mounted at one end of the positioning block, and the pair of positioning rods is set on both sides of the installation box cavity. One end of one of the positioning rods is fixedly connected to the output end of the servo motor, while the other end is rotatably connected to the positioning block. The other positioning rod has both ends rotatably connected to the pair of positioning blocks.

A pair of sprockets is fixedly connected to the outer ends of the pair of positioning rods. A chain is installed at the outer end of the sprockets. Multiple sprockets are connected through the chain, and the bottom end of the placement box is fixedly connected with a rack that matches the chain.

DOI: 10.54254/2755-2721/91/20241084

3.5. Benefits

Compared to existing technologies, the advantages of this technical solution are as follows:

In this solution, when installing and removing multiple heating pipes, the user only needs to turn on the road switch located next to the road. This allows the drive component to place multiple placement components from the placement groove into the installation box's inner cavity or remove them all from the placement groove. There is no need to excavate the road surface at the tunnel entrance, and it does not affect normal road traffic operations. This greatly facilitates installation and maintenance work, reduces maintenance costs, and minimizes the impact on traffic flow.

4. Specific Implementation

Below, with reference to the accompanying drawings in the embodiment of this technical solution, the technical solution of this embodiment will be described clearly and completely. It is apparent that the described technical solution is only one of the embodiments, and not all of the embodiments based on this technical solution.

In the description of this technical solution, it should be noted that terms such as "upper," "lower," "inner," "outer," "top/bottom end," etc., refer to positional or orientation relationships based on the orientations or positions shown in the drawings, and are only for convenience in describing the present invention and simplifying the description. They do not indicate or imply that the described device or component must have a specific orientation or be constructed and operated in a specific orientation. Additionally, terms such as "first," "second," etc., are used merely for descriptive purposes and should not be understood as indicating or implying relative importance.

In the description of this technical solution, unless explicitly specified and limited otherwise, terms such as "install," "provided with," "mounted on/connected to," etc., should be understood broadly. For example, "connected" can mean fixed connection, detachable connection, or integral connection; it can be mechanical or electrical; it can be direct or indirect through intermediate media, or it can be internal communication between two components. For those skilled in the art, the specific meaning of these terms in this invention can be understood based on the context.

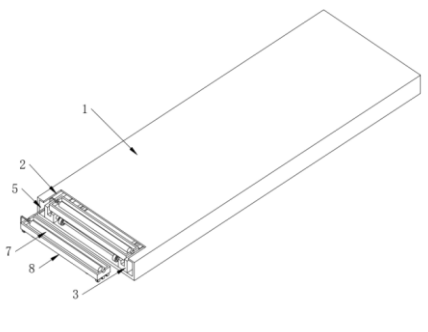

Figure 4. Main Structure Schematic Diagram

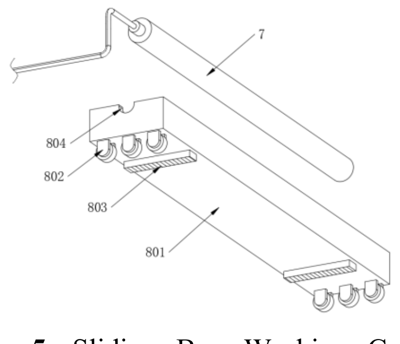

Figure 5. Sliding Box Working Component Schematic Diagram

Referring to Figure 5, a tunnel mouth snow-melting system electric heating element includes an installation box (1), multiple heating tubes (7), and multiple placement components (8). One end of the installation box (1) is open, and a placement slot (2) is provided at the upper end near the open side of the installation box (1). The bottom end of the inner wall of the installation box (1) is fixedly connected to a pair of symmetrically positioned limiting blocks (3). The placement components (8) include a placement box (801), and the heating tubes (7) are matched with the placement box (801). A driving component (6) is positioned between the pair of limiting blocks (3).

Referring to Figure 4, the user can first horizontally embed the installation box (1) under the road surface at the tunnel mouth. An openable road surface switch that matches the placement slot (2) is set above the placement slot (2). The user then installs multiple heating tubes (7) onto multiple placement components (8), and subsequently places the placement components (8) one by one into the installation

DOI: 10.54254/2755-2721/91/20241084

box (1) from the placement slot (2). During the process of placing the components (8), the driving component (6) moves the placement components (8) further into the interior of the installation box (1) until the heating tubes (7) are closely arranged inside the installation box (1). With this arrangement, when multiple heating tubes (7) are activated simultaneously, the heat emitted can be conducted to the upper end of the installation box (1) and then to the road surface above, thereby heating and accelerating the melting of snow on the road surface. The user can install and remove multiple heating tubes (7) simply by opening the road surface switch located beside the road. This allows the driving component (6) to move the placement components (8) into the interior of the installation box (1) from the placement slot (2) or remove them entirely without needing to excavate the road surface at the tunnel mouth, thus not affecting the normal operation of road traffic.

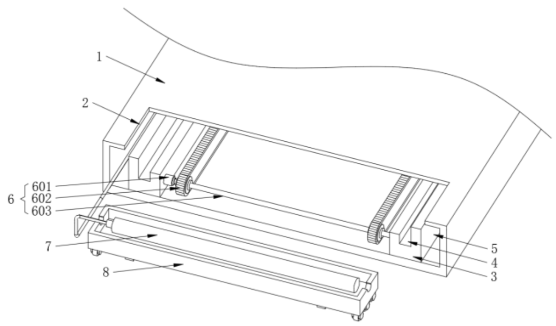

Figure 6. Partial Structure Schematic Diagram

Referring to Figure 6, the bottom end of the placement box (801) is fixedly connected to a pair of symmetrically positioned rollers (802). The upper end of the limiting block (3) is provided with a limiting slot (4) that matches the rollers (802). A pair of limiting blocks (3) forms a wire storage chamber (5) between their mutually distant ends and the inner wall of the installation box (1). The top end of the placement box (801) is provided with a pair of wire placement grooves (804) that match the heating tubes (7).

When installing multiple heating tubes (7), the user first places the heating tubes (7) inside the placement box (801). The placement box (801) is then inserted into the interior of the installation box (1) from the placement slot (2), causing the pair of rollers (802) at the bottom end of the placement box (801) to enter the pair of limiting slots (4). This allows the placement box (801) to slide on the limiting blocks (3) via the rollers (802). At the same time, the user can place the cables connected to the heating tubes (7) in the wire placement grooves (804) and then insert the cables into the wire storage chamber (5). With this setup, when the placement box (801) moves into the deeper part of the installation box (1), the cables connected to the heating tubes (7) remain in the wire storage chamber (5), avoiding direct contact between the cables and the heating tubes (7), thus preventing damage to the cables from the heat of the heating tubes (7).

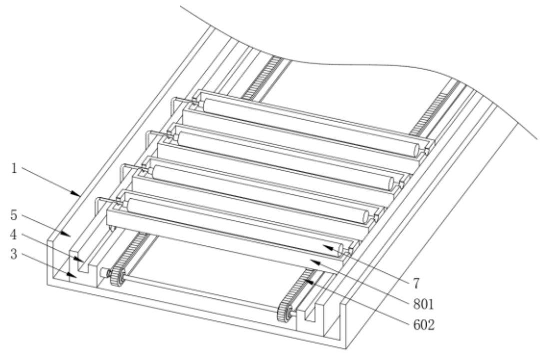

Figure 7. Internal Structure Schematic Diagram

DOI: 10.54254/2755-2721/91/20241084

Referring to Figure 7, the driving component (6) includes a servo motor (601) and a pair of limiting rods (603). The servo motor (601) is mounted at one end of the limiting block (3). The pair of limiting rods (603) are positioned on both sides of the inner cavity of the installation box (1). One limiting rod (603) is fixedly connected to the output end of the servo motor (601), and the end of the limiting rod (603) away from the servo motor (601) is rotatably connected to the limiting block (3). The other limiting rod (603) is rotatably connected at both ends to the pair of limiting blocks (3). Each external end of the pair of limiting rods (603) is fixedly connected to a pair of sprockets. A chain (602) is mounted on the external end of each sprocket, and multiple sprockets are connected by the chain (602). The bottom end of the placement box (801) is fixedly connected to a rack (803) that matches the chain (602).

When the user places the placement box (801) on the pair of limiting blocks (3), the pair of racks (803) at the bottom end of the placement box (801) engages with the pair of chains (602). At this point, the user activates the servo motor (601) to drive the limiting rods (603) to rotate, which in turn rotates the pair of sprockets. With the cooperation of the other limiting rod (603) and another pair of sprockets above it, the chains (602) are driven to move. The movement of the chains (602) drives the racks (803) to move, thereby causing the placement box (801) to slide on the limiting blocks (3) via the rollers (802) and move deeper into the installation box (1). The user then sequentially places additional placement boxes (801) closely behind the previous one into the installation box (1). This allows multiple placement boxes (801) carrying heating tubes (7) to be delivered into the interior of the installation box (1), completing the installation of the heating tubes (7). Similarly, by reversing the direction of rotation of the servo motor (601), the user can remove the multiple placement boxes (801) one by one from the placement slot (2).

5. Working Principle

When in use, the user can first horizontally embed the installation box (1) under the road surface at the tunnel mouth. An openable road surface switch that matches the placement slot (2) is set above the placement slot (2). After opening the road surface switch, the user places multiple heating tubes (7) in the interior of multiple placement boxes (801), then inserts the placement boxes (801) into the interior of the installation box (1) from the placement slot (2). The rollers (802) at the bottom end of the placement boxes (801) will enter the limiting slots (4). At the same time, the cables connected to the heating tubes (7) are placed in the wire placement grooves (804) and then inserted into the wire storage chamber (5). After placing the placement box (801) on the limiting blocks (3), the racks (803) at the bottom end of the placement box (801) will engage with the chains (602). The user then activates the servo motor (601), which drives the limiting rods (603) to rotate and in turn rotates the sprockets, causing the chains (602) to move. The movement of the chains (602) drives the racks (803) and causes the placement box (801) to slide via the rollers (802) on the limiting blocks (3) and move deeper into the installation box (1). The user continues to place additional placement boxes (801) into the installation box (1), thereby completely installing the heating tubes (7). Conversely, by reversing the direction of the servo motor (601), the user can remove the placement boxes (801) from the placement slot (2). The user then closes the road surface switch and activates the heating tubes (7). The heat emitted is conducted to the upper end of the installation box (1) and then to the road surface above, thereby heating and accelerating the melting of snow on the road surface.

The above describes the preferred embodiment.

6. Conclusion

This paper introduces the de-icing and snow melting technology for tunnel and bridge openings based on the existing electric heating snow melting and de-icing technology, proposing the energy requirements and corresponding methods for de-icing and snow melting at tunnel and bridge openings [7]. Based on case studies [12], the feasibility and rationality of the power supply operation of carpet-style electric heating elements have been preliminarily concluded as follows:

1. Maturity of the Technology: The electric heating road snow melting technology has already been applied in some practical projects and has achieved good results. This project adjusts and optimizes the

existing technology based on actual engineering applications, effectively solving the problem of road surface icing when installed at highway tunnel and bridge locations. The control system is precise: it includes a complete and mature precise control system [13], ensuring uniformity and stability in road surface temperature. The project uses an intelligent control system, based on the Internet of Things, to achieve remote monitoring and control [14].

2. Stable Energy Supply: This technology requires electricity as an energy source. The power supply is relatively stable and can be supplemented by renewable energy sources such as solar energy, so the energy supply issue will not become a bottleneck for this technology.

3. Cost-Effectiveness: Although the initial investment for electric heating road snow melting technology is relatively high, its maintenance costs and labor operation costs are relatively low. It can effectively reduce traffic accidents and improve road capacity. Therefore, from a long-term perspective, this technology has certain cost-effectiveness.

4. Energy Saving and Environmental Protection: Compared with traditional snow melting methods, this technology does not require the use of chemical de-icing agents, which would not pollute the environment. It can also save energy and reduce the emission of greenhouse gases such as carbon dioxide.

5. Extension of Road Surface Lifespan: Chemical de-icing agents can corrode the road surface, shortening its lifespan. In contrast, the electric heating road snow melting technology does not damage the road surface but reduces the freeze-thaw cycle, extending the road surface's lifespan. Once installed, it forms an integrated structure with the road surface and does not require further excavation for maintenance, avoiding damage.

6. Improved Road Capacity and Safety: Road surface icing can lead to decreased road capacity. Using this technology can quickly eliminate road surface icing, improving road capacity and reducing traffic congestion. Icy road surfaces are a major cause of traffic accidents. By using this snow melting and de-icing technology, road surface icing can be effectively eliminated, enhancing road safety and reducing traffic accidents.

7. In Summary, this technology has significant snow melting capability and timeliness. It can be installed during the construction process based on actual road conditions and does not require further damage to the road surface during future use and maintenance. It does not affect normal traffic capacity. Further experimental research is needed on the temperature distribution and heat effectiveness of carpet-style snow melting and de-icing devices under different burial depths and road surface material conditions.

References

[1] Zhou Xiaopeng. Study on the Ice Melting Efficiency of Road Deicing Agents and the Law of Secondary Freezing [D]. Supervisor: Guo Dedong; Wei Jincheng. Shandong Jiaotong University, 2020. DOI: 10.27864/d.cnki.gsjtd.2020.000019

[2] Tan Yiqiu, Zhang Chi, Xu Huining, Tian Dong. Review of Active Snow and Ice Removal Pavement Snow Melting and Ice Melting Characteristics and Road Performance [J]. China Journal of Highway and Transport, 2019, 32 (04): 1-17.

[3] Cao Haibo, Chen Tuanjie, Lu Jingjing, Chen Shi. Feasibility Study on Pavement Self-Stress Ice-Breaking Paving Structure [J]. Modern Transportation Technology, 2011, 8 (02): 16-18+33.

[4] Qiao Shizhe, Qin Hao, Huang Wanqing, Cao Mingming. Evaluation of Ice Melting Performance of Low Freezing Point Asphalt Concrete Pavement Based on Machine Vision [A]. China Association for Science and Technology, Ministry of Transport, Chinese Academy of Engineering, Hubei Provincial People's Government, 2022 World Transport Conference (WTC2022) Proceedings (Highway Engineering Section) [C]. Xihua University School of Energy and Power Engineering; Sichuan Provincial Traffic Survey and Design Institute Co., Ltd.; 2022: 172-179.

[5] Liu Zhuangzhuang, Zhang Youwei, Ji Pengyu, Hao Yazhen, Li Lin. Review of Electric Heating Snow Melting Pavement Technology [J]. Journal of Chang'an University (Natural Science Edition), 2022, 42 (03): 14-25.

[6] Huaihua City Transportation Bureau. Ensure Smooth Traffic with Deicing and Snow Melting in Huaihua, 2023-12-22.
[7] Nagai N, Miyamoto S, NishiwaKi M, et al. Numerical Simulation of Snow Melting on Pavement Surface with Heat Dissipation Pipe Embedded [J]. Transactions of the Japan Society of Mechanical Engineers. B, 2008, 74(3): 640-647.
[8] Han Ming. Optimization Study on the Design Scheme of Electric Heating Method for Road Snow Melting and Ice Melting [D]. Supervisor: Xiao Henglin. Hubei University of Technology, 2020.
[9] Zhou Shuiwen, Pan Song, Zhang Rong. Application Practice of Intelligent Loop Heat Pipe Snow Melting on Sichuan-Jiuzhaigou Road [J]. Shanghai Highway, 2023, (04): 1-6+207.
[10] Lu Guoju, Zhang Zherui, Zhao Yongfang, Zhang Meihong. Experimental Study on Snow Melting and Ice Melting with Carbon Fiber Heating Cable in Asphalt Concrete Surface Layer [J]. Scientific and Technological Innovation, 2023, (02): 196-200.
[11] Chen Weijian. Brief Analysis of the Application of Electric Heat Tracing in Snow Melting of Marine Step Modules [J]. Mechatronics Information, 2019, (06): 5-6.
[12] Ming Ruitao. Study on the Migration and Accumulation of Deicing Agents at Ski Resorts Based on SWAT Model [D]. Beijing University of Civil Engineering and Architecture, 2021. DOI: 10.26943/d.cnki.gbjzc.2021.000250.
[13] Du Xingsen. Road and Bridge Maintenance System V1.0 [P] China Patent: 2024SR03128274, 2024-02-26.
[14] Du Xingsen. Highway and Bridge Inspection System [Abbreviation: Highway and Bridge Inspection] V1.0 [P] China Patent: 2022SR0951652, 2022-07-20.

DOI: 10.54254/2755-2721/91/20241080

The working principles of canard wings and its aerodynamic advantages and effects on aircraft

Wenduo Lai

Whartonn School, Chengdu, Sichuan, 610093, China

26676825601@gmail.com

Abstract. Canard wings have gradually become more and more popular since the advent of the supersonic jet era, and research on the subject has become more detailed in order to be able to manoeuvre this pair of small wings more perfectly and effectively. This paper mainly studies the aerodynamic principle of the canard wings and the impact of its aerodynamic advantages on the efficacy and stealth performance of the aircraft under different aerodynamic stability and makes a comparative analysis with the horizontal tail. Through literature analysis and review as well as a small number of comparative analyses, this paper concludes that although canard wings can provide many aerodynamic advantages, they also have their limitations. Canards can only be effectively coupled when they are close to the main wing and longitudinally higher than or equal to the height of the main wings. The radar cross-section (RCS) characteristic of the canard wings will increase with the angle of its deflection.

Keywords: Close-coupling, Static stability, Pitching moment coefficient, Radar cross-section (RCS), anti-gravity.

1. Introduction

The canard wings are a pair of small wings in front of the main wings on both sides of the aircraft cockpit, it is similar to placing the horizontal tails that are usually located on the two sides of the engine at the rear of the fuselage in a conventional layout, at the front. In the current canard wings research context, there are only several studies that discuss canard wings alone or compare horizontal tails with them, most of them are related to the combination with other layouts. This paper first analyzes the working principles of the canard wings, including the fundamentals of the canard wings and the realization of the effective canard wings, then this paper analyzes the influence of the deflection angle of the wing of the canard layout aircraft on its own lift and the effect of the pitching angle formed by the deflection of the canard wings in three circumstances. On this basis, this paper discusses the aerodynamic advantages and effects of canard wings on aircraft, and by comparing the literature related to another existence that is similar to canard wings on aircraft - the horizontal tails, it is concluded that the lifting effect of the canard wings is better than the horizontal tails. This paper can provide some reference value for scholars who study aircraft aerodynamics as well as those who study canard wings or horizontal tails.

DOI: 10.54254/2755-2721/91/20241080

2. Working principle of canard wings

2.1. The fundamentals of canards and the realization of effective canards

The center of gravity and aerodynamic focus of the aircraft are both located between the canard and the main wing, while the canard is a pair of small wings placed in front of the main wing. It provides positive lift to balance the aerodynamic center of gravity while the aircraft is in flight [1]. As the speed and pitching angle of the aircraft change, the aerodynamic centre moves backwards. The aerodynamic centre of an aircraft shifts backward significantly when it is traveling at supersonic speed, and as a result, the nose-down moment will considerably increase as well. Any airflow passing over the wing will be pulled out into a vortex. As shown in Figure 1, the vortex had been pulled out by the canard and strake wings of a Su-30sm, when it was in a circulating flight state. The vortices generated by the canard will affect the generation of vortices on the main wing surface due to downwash, resulting in a reduction in lift. When the distance between the canard and the main wing is far, the vortices of the canard are almost exhausted when it reaches the main wing, and the main wing is attenuated by the disturbance from the canard again [2]. When the distance between the canard and the main wing is shortened, a similar leading edge slit wing will be formed, the effective chord length and lift of the wing will be increased equivalently, and a high-pressure zone will be generated at the leading edge of the main wing; then the interference between the canard vortices and the main wing vortices will be beneficial, the lift coefficient and lift-to-drag ratio will be improved, and the stall angle of attack will also increase, which is known as the close coupling [1-2].

The canard location should be placed at a height that is at least not lower than the height of the main wing, because in that case the vorteices of the canard will not interfere with the vorteices on the main wing, and will be rapidly exhausted during transmission. Only when the height is greater than or equal to this position will the canard make a fierce downwash effect on the main wing, thus reducing the effective angle of attack and increasing the induced drag and lift simultaneously [2].

Figure 1. Su-30SM in a circulating flight state.

2.2. The influence of the wing deflection angle on lift of the canard aircraft

Angle of attack(AOA), as the name implies, is the angle formed by the chord of the aircraft wing and the laminar flow passing through it. From the above analysis, it can be seen that the canard will generate vortices, so the vortices will manifest as two types of disturbances under the two ranges of attack angle of the aircraft deflection separately. When the aircraft is in a small to medium AOA, the lost main wing lift is compensated by the canard lift, and its overall lift will not be affected. Because the vortex pulled out by the canard will produce a downwash effect, thereby restricting the formation of the main wing vortex, and through calculation it can be concluded that the generation of the leading edge vortex on the main wing will be disturbed; at the same time, adverse separation vortices will also form on the lower wing surface, but the lift loss in this part will be compensated by the lift generated by the canard [1].

DOI: 10.54254/2755-2721/91/20241080

Therefore, there is almost no unfavorable impact on the overall lift situation in the range of small and medium angles of attack.

When a canard aircraft at a large AOA range flight, or when the AOA of its canard increases, the effective AOA of the main wing(The angle between the velocity line synthesised by the disturbance and the chord line on the wing or the axis line on the fuselage)will decrease, the induced drag will increase, and the lift will increase significantly, but the lift-to-drag ratio will decrease; this is because the canard will still produce a downwash effect on the main wing in this case, which is similar to the small and medium AOA disturbances above [1-2]. But more importantly, the low-pressure vortex pulled out by the canard will compel the leading edge separation vortex on the main wing to form a stronger leading edge concentrated vortex so that the flow field is changed, which is the reason why the lift of the canard aircraft is increased. [1]. For example, at a large angle of attack of 20°, the pressure on the upper surface of the main wing increases because the vortex of the main wing is destroyed by the downwash of the canard, and the vortex lift is reduced [1]. However, since the pressure on the upper wing surface increases, the corresponding vortex lift of the canard also increases accordingly, so overall the lift generated by vortex does not change too much.

2.3. The effects of canard deflecting pitching angles in three cases

The nose-up moment is the ratio of the positive pitching moment coefficient C_m to the angle of attack Incidence α, while the nose-down moment is a negative ratio, and the pitching moment balance Cm equals 0. Figure 2. shows how the three static stability of the aircraft in the longitudinal directions varies with changes in the angle of attack α and the pitch moment coefficient C_m.

2.3.1. Static stability. For the static stability curve, shown in Figure 2, the slope is negative. When Cm is 0 , the angle of attack α_e is the pitching moment equilibrium, on that occasion aircraft will neither nose down nor up; when the pitching moment coefficient decreases as the angle of attack α increases, the aircraft is in a state of nose-down moment. The aircraft then has a tendency to return to the α_e pitching moment equilibrium [3]. For a statically stable aircraft with a positive canard deflection, the curve Cm-α will translate upward in the coordinate system of Figure 2, and the angle of attack at its α_e pitching moment equilibrium will increase as well [3]. The new pitching moment balance of the angle of attack is $\alpha_e+\alpha$.

2.3.2. Neutral static stability. This neutral static stability curve is shown in Figure 2 as a horizontal straight line with the same slope as the x-axis of the angle of attack α which is 0; regardless of how the angle of attack α increases, it is still in a state of pitch moment balance, so the aircraft will produce neither nose-down nor nose-up moment. For a neutral statically stable canard aircraft, a positive upward deflection of the canard will cause the curve to translate upwards and parallel to the x-axis, so that in this case, the aircraft is still in a nose-up moment at the new angle of attack; therefore, in order to avoid a stall, the canard only can be straightened to a deflection angle of 0° at the corresponding angle of attack, so that the aircraft can re-achieve pitching moment equilibrium at the new angle of attack [3]. At that time, Cm equals 0, and the new pitching moment balance of the angle of attack is also $\alpha_e+\alpha$.

2.3.3. Static instability. Figure 2 shows that for this graph, the slope of the static instability curve is positive, showing a gradually improving trend. When the angle of attack Incidence α increases, the pitching moment increases at the same time, because Cm also increases, so the aircraft will present a state of continuous nose-up; the nose-up moment simultaneously continues to increase, causing the aircraft to stall [3]. For a statically unstable canard aircraft, the canards do not actually need to be deflected significantly; a slight deflection of the canard will result in the aircraft continuously raising its head [3]. At this moment, the canard will deflect negatively downward, and this curve will translate downward in the coordinate system, allowing the canard aircraft to re-balance the pitching moment at the new angle of attack. $\alpha_e+\alpha$ is likewise the new pitching moment equilibrium angle of attack, while C_m is naught.

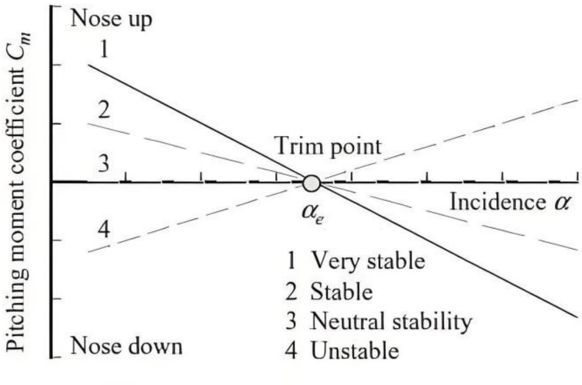

Figure 2. The linear equation graph of the degree of longitudinal static stability.

2.4. Analysis of effects on airframe stealth

RCS (Radar Cross Section) is a physical quantity that is the intensity of the echo received after the electromagnetic wave emitted by the radar is reflected by the target object [4]. The impact of canard on the overall RCS must be analyzed from the following two aspects: Supersonic cruise and a certain flight attitude including take off, landing, close combat or perform large maneuvers. Regarding the first aspect, when the aircraft is in a cruising state, the canard of an aircraft with canards will usually only deflect slightly and maintain a negative deflection angle, and the canard will not deflect positively [5]. Therefore, the frontal RCS of a canard aircraft will not be negatively affected when it is exposed to radar waves. As for the second aspect, the canard sometimes needs to be deflected significantly to perform certain special maneuvers, which will further damage the RCS of the entire fuselage and increase its RCS signature on the radar [5].

3. The aerodynamic advantages and effects of canards on aircraft

The advantages of aircraft using canard layouts are as follows: First, the aircraft has excellent nose-down control and recovery capabilities, especially at large angles of attack [1,6]. Second, in terms of vector thrust, when the direction of the canard balancing moment is the same as the direction of the vector thrust, they are superposed to form a resultant force. Third, the size and volume of the canard can be reduced, because the pitching angle control of the canard aircraft does not necessarily rely solely on the canard, but can also be assisted by the ailerons at the trailing edge of the main wing [1]. Fourth, when the canard aircraft accelerating in supersonic flight, the distance that the aerodynamic center moves backward to the aircraft fuselage is shortened, makes it easier to balance the moment in the supersonic flight, the canard is positively deflected simultaneously, and the balancing resistance of the canard aircraft is significantly reduced; The positive lift is generated by the canard trim moment, and the vortex lift generated by the changes in speed and angle of attack is derived from the favorable interference of the vortex coupling between the canard and the main wing, so the overall lift-drag ratio is expanded [1,6]. Finally, as to the advantages of canard deflection, canard aircraft experience an increase in lift when positive deflection occurs; as for negative deflection, it will be helpful to correct the aircraft from dangerous situations (such as stall or spin).

4. Comparison between the canards and horizontal tails

Regarding the aerodynamic layout of the two currently mainstream fighter jets, their advantages will also be compared next. According to Figure 3, the schematic diagram of lift for conventional and canard layout aircraft represents that the horizontal tails provide negative lifts, while the canards provide positive lifts. Therefore, it is usually simply considered that the canard wings are just the horizontal tails placed in front of the main wings, but this tacitly acknowledges that their respective contributions to the aircraft are concurrent. Through all the previous analyses of canards, its advantages are not only just the augment in the lift of the main wing vortex in the close coupling but also in its nose-down control ability, lift-to-drag ratio under supersonic endurance, vector thrust superposition and small canard surface. Compared with the conventional layout where the horizontal tail is placed at the rear, the canard is installed in front of the main wing, which is like installing a huge horn headlight and is easily noticed in dark and open areas. This is because, for the movable canard, the gap caused by the movement between it and the fuselage is directly exposed to the radar detection in front of the aircraft, increasing the possibility that the RCS characteristics of the fuselage are detected simultaneously [5]. But for the horizontal tail, which is located behind the main wings, the main wing blocks approximately most of the gaps that are prone to exposure risks when the horizontal tail moves, which greatly reduces the possibility of being detected by radar from the front. Therefore, conventional layout aircraft are ahead of canard layout aircraft in stealth.

Figure 3. Schematic diagram of lift for conventional and canard layout aircraft

5. Conclusion

This paper mainly discusses the principle of effective lift increase of canards, using its aerodynamic advantages as well as the effect and influence of canard deflection angle on the aircraft under different conditions, and compares it with a horizontal tail. To sum up, there is no doubt that canards have an aerodynamic lift effect on an aircraft. Canards can only be effectively coupled when they are close to the main wing and longitudinally higher than or equal to the height of the main wings. Although the canard affects the lift of the main wing to a certain extent, it can also serve as a substitute and supply more lifts. In terms of stealth performance RCS compared with the horizontal tail, is like a tractor, large and loud, easier to be detected on the radar. This paper could add specific data and calculations for analysis and comparison in three aspects: the influence of the wing deflection angle of the canard aircraft on its own lift, the analysis of the effect of the fuselage's stealth, and the comparison between the canards and the horizontal tails. Future research could focus more on how aircraft can truly overcome gravity and implement anti-gravity technology.

References

[1] Ma Baofeng, Liu Peiqing, Deng Xueying. Advances in aerodynamic research on close-coupled canard configuration[J]. Acta Aerodynamica Sinica, 2003(03):320-329.
[2] Li Yulong, Yang Wei, Yang Zhigang. Numerical study of canard layout ground effect wing [J]. Aeronautical Computing Technology, 2010, 40(04): 27-30+34.
[3] Fang Xiangduoduojigai. Why does the J-20's canard deflect in the opposite direction. 2022,12.www.bilibili.com/video/BV1cW4y1T768/?spm_id_from=333.788&vd_source=0310bce15ba005d6fac5e6050a08ef46
[4] Jia Jianwei, Wang Cong, Zhang Yu, et al. Calculation of radar scattering cross section of aircraft coated with dielectric coatings[C]//Microwave Branch of China Electronics Society, Key

DOI: 10.54254/2755-2721/91/20241080

Laboratory of Antenna and Microwave Technology. Proceedings of the 2016 National Conference on Military Microwave, Terahertz and Electromagnetic Compatibility Technology. 2016:3.

[5] Guo Zhanzhi, Chen Yingwen, Ma Lianfeng. Research on the influence of radar scattering cross section of canard wings [J]. Acta Aeronautica Sinica, 2020, 41(06): 266-276.

[6] Zhang Jigao. Aerodynamic layout division of fighter jets[J]. Acta Aerodynamica Sinica, 2009, 27(05): 616-622.

DOI: 10.54254/2755-2721/91/20241079

Research progress on improving ionic conductivity of NZSP solid electrolyte

Boyan Tang

School of Materials Science and Engineering, Hefei University of Technology, Hefei, China

waxyxy9903@163.com

Abstract. Due to the limited resources of lithium batteries, and the safety of liquid electrolytes, and the working principle of sodium batteries and lithium batteries are similar, and the cost is relatively low, so the development of sodium ion solid state batteries has its feasibility and necessity. Among them, NASICON solid electrolyte with its unique three-dimensional structure, and good thermoelectric performance has been widely concerned, in order to better understand the development of such materials and the latest developments, this paper reviews the crystal structure of NZSP solid electrolyte, conductive mechanism, preparation methods of research progress. NZSP solid electrolyte with its room temperature asymmetric monoclinic phase and large grain boundary resistance, resulting in ionic conductivity is not enough to meet the application needs, on the basis of the above content, for the existence of NZSP ionic conductivity low problem, related discussions were carried out. The research progress of improving the ionic conductivity of NZSP based on preparation technology, grain control and grain boundary control is discussed. And in the end, the possible future development trend of NZSP material is summarized and prospected, which will play a certain reference and promotion role for the future research on NASICON solid electrolyte.

Keywords: NASICON, Ionic conductivity, NZSP, Solid electrolyte, Ion doping, sintering.

1. Introduction

Energy is the core element of modern social operation and human civilization progress. Fossil energy has a long history, but its non-renewability and pollution limit its application. In the new energy industry, lithium battery with its high energy density, high power and other advantages occupy a very important position.

However, some elements in lithium batteries are low in abundance in the Earth's crust and unevenly distributed around the world [1, 2]. Sodium and lithium are in the same family, the properties of the two are very similar, and sodium resources are distributed around the world, which can avoid development constraints caused by resource shortages [3]. The structure and working principle of the two batteries are similar (as shown in Figure 1), so sodium-ion batteries can be a perfect substitute for lithium-ion batteries.

Sodium-ion liquid batteries have the disadvantages of low safety, flammability and volatility. In contrast, solid-state batteries have good safety, good thermal stability and high energy density [4]. The oxide solid electrolyte in the inorganic solid electrolyte has good comprehensive performance, among which the NASICON solid electrolyte has a stable three-dimensional frame structure and shows excellent electric heating performance. However, its ionic conductivity is still not enough to meet the requirements of practical applications. Tsai et al. [5] prepared a solid electrolyte with $5\times10^{-3}S\cdot cm^{-1}$ ionic conductivity, which verified the potential of improving NASICON ionic conductivity. Zahra [6] found through research that doped ions and process conditions would affect the ionic conductivity of NASICO, thus confirming the feasibility of ion doping to improve the ionic conductivity. In this paper, the current research on improving the ionic conductivity of NASICON solid electrolyte is reviewed, with the purpose of understanding the development direction and advantages of different relevant research, and the existing problems in the research, the preliminary solution and prospect are put forward.

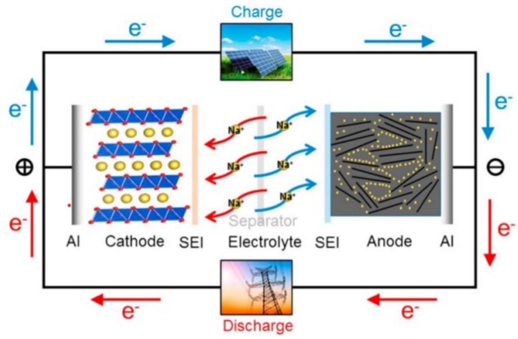

Figure 1. Schematic diagram of the operation of a NASICON ion battery [7]

2. NASICON's conductive mechanism

2.1. NASICON's crystal structure

The general formula of the NASICON type electrolyte is $Na_{3+x}Zr_{2-x}Si_xP_{3-x}O_{12}$ ($0 \le x\le 3$), which can be seen as a solid solution of $NaZr_2P3O_{12}$ and $Na_4ZrSi_3O_{12}$. As can be seen from the figure, the crystal configuration of $Na_{3+x}Zr_{2-x}Si_xP_{3-x}O_{12}$ includes the SiO_4/PO_4 tetrahedron, the ZrO_6 octahedron and the three structural units of Na+ ions. By sharing oxygen atoms with the apex angles of the SiO_4/PO_4 tetrahedron and the ZrO_6 octahedron, a three-dimensional rigid skeleton is constructed, that is, each SiO_4/PO_4 tetrahedron and four ZrO_6 octahedra coordination, and a single ZrO_6 octahedron is connected to the surrounding six SiO_4/PO_4 tetrahedra.

Because of the difference in Si content, $Na_{3+x}Zr_{2-x}Si_xP_{3-x}O_{12}$ can be divided into monoclinic crystal and rhombohedral crystal in general. When $x < 2.8$ and $x > 3.2$, $Na_{3+x}Zr_{2-x}Si_xP_{3-x}O_{12}$ is rhombic phase. In the Rhombohedral phase, each ZrO_6 octahedron is connected with six $(P/Si)O_4$ via the form of common vertices to form a three-dimensional skeleton, Na+ is located in the skeleton gap, and the rhombohedral structure has two Na^+ sites, Na1 and Na2, i.e. only one ion transport path, Na1-Na2. When $1.8 \le x \le 2.2$, these compounds belong to the monoclinic phase and are stable at room temperature. Monoclinic phase is the rotation deformation of rhomboid phase, in which the original Na2 site splits into new Na2 and Na3 sites [8]. There are three sites in NZSP: Na1, Na2 and Na3. The increase of sites makes Na1-Na2 and Na1-Na3 have transport paths at the same time. The monoclinic phase and rhombic phase can be transformed into each other at a certain temperature. Compared with the rhombohedral phase, the monoclinic phase has a relatively wide Na^+ conduction path, resulting in higher ionic conductivity. While monoclinic phase is asymmetric phase, rhombic phase is symmetric phase, and its activation energy is lower than monoclinic phase, while rhombic phase is stable at high temperature and difficult to stabilize at lower temperature, which hinders the development of rhombic phase to improve ionic conductivity [9].

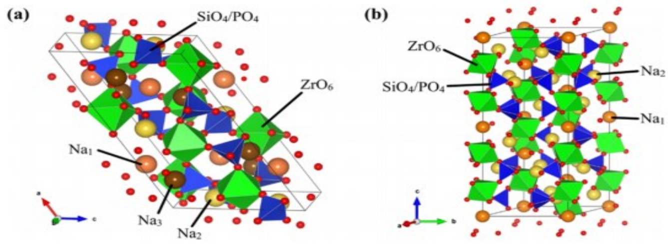

Figure 2. Crystal structure of NASICON electrolyte. (a) monoclinic crystal (b) rhombic crystal [10]

2.2. Ion transport mechanism of NASICON

The conduction mechanism of ions in solid electrolyte depends on the type of electrolyte. NASICON solid electrolyte is a kind of ionic electrolyte, while the ion transport in inorganic electrolyte is related to its vacancy and defect, as shown in FIG. 3. It mainly includes (1) the transport mechanism in the vacancy, (2) the transport mechanism in the gap, and (3) the co-transport mechanism between the vacancy and gap. This classical model of ion transport believes that a single ion jumps from one lattice site to another adjacent lattice site through the ion transport channel inside the crystal, so as to achieve ion transport. The ionic conductivity of inorganic solid electrolyte conforms to Arrhenius formula:

$$\sigma = \sigma_0 e^{-\frac{E_A}{K_B T}} \tag{1}$$

Where σ_0 refers to the pre-factor, E_A is the diffusion activation energy, k_B is the Boltzmann constant, and T is the absolute temperature. It can be seen that the ionic conductivity is related to the pre-factor, the diffusion activation energy and the temperature. In the actual reference research, the ionic conductivity can be optimized by adjusting the above several parameters. In addition, there are other mechanisms related to ion transport mechanisms. For example, He et al [11]., through AIMD simulation study, found that rapid diffusion in superionic conductors is not simply through the typical isolated ion jump in solid, but through the cooperative migration of multiple ions with low energy barrier. This provides theoretical support for ion doping to improve the conductivity; Wang et al [12]. revealed how non-Arrhenius transport in ion transport is caused by classical MD model simulation. This transport mechanism further modified the ion diffusion activation transport model and can be widely applied to superionic conductors.

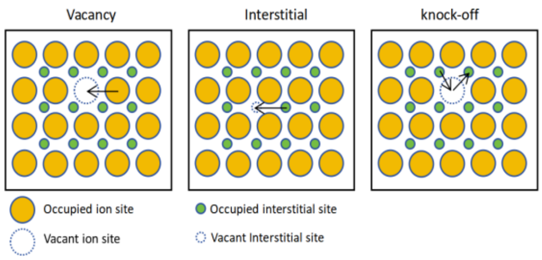

Figure 3. Schematic diagram of ion transport mechanism in inorganic solid electrolyte [13]

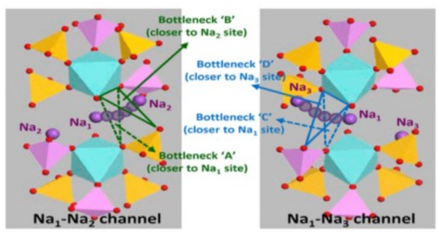

Figure 4. Four different types of bottlenecks in the monoclinic Nasicon structure [14]

For the NASICON solid electrolyte, in the monoclinic structure of the NZSP electrolyte, sodium ions are transported through a triangular bottleneck area. This bottleneck region is formed by oxygen atoms that share angles in the octahedral (ZrO_6) and tetrahedral structures (SiO_4/ PO_4). The diffusion of Na ions is closely related to the bottleneck area. Anurag Tiwari et al [15]. used VESTA software to measure the crystal structure of NZSP sintered at 1250°C and found that the shortest distances between Na1-Na2, Na1-Na3 and Na2-Na3 sites were 3.5 Å, 3.0 Å and 4.4 Å, respectively. The shortest distance between Na1 and Na3 sites indicates that the most efficient transport route of Na ions is through the Na1-Na3-

DOI: 10.54254/2755-2721/91/20241079

Na1 pathway [16], which means that the transport between Na1-na2 is the limiting factor of ionic conductivity.

Furthermore, in the two transport paths of the monoclinic phase structure mentioned above, there will be four different bottleneck regions A- bottleneck region D. As can be seen from the figure, regions A and B are located at the NA1-NA2 transport channel, regions C and D are located at the NA1-NA3 transport channel, the centers of regions A and C are located near the Na1 site, and the centers of regions B and D are located near the Na2 and Na3 sites respectively. The area of bottleneck region A to bottleneck region D is 6.2719, 5.0648, 5.9995, and 5.6488Å^2, respectively. Since Ea is mainly determined by the smallest bottleneck, bottleneck region B in the NA1-NA2 transport path may be a limiting factor for Na^+ conduction.

3. Preparation process of NASICON

3.1. Solid State reaction method

Solid phase reaction method is a traditional and simple method to synthesize Nasicon type solid electrolyte, its general process is: batching → ball milling → pre-firing → molding → sintering. In the sintering process, the choice of sintering temperature and sintering time is an important factor affecting the density of the material, and the density is an important factor [17] affecting the conductivity of NASICON ion. For the sintering of NZSP generally choose 1100℃, because it can be melted [18] at such a temperature, in addition to its pre-sintering and ball milling, the purpose of pre-burning is to obtain a relatively high purity of the sintering phase, the purpose of ball milling is to mix raw materials evenly and the pre-sintered particles fine.

In addition to the classical solid-phase sintering method, other solid-phase sintering methods in recent years have also been applied to the preparation of NZSP, Basitti Hitesh [19] use SPS method to prepare NZSP solid electrolyte, and annealing treatment. The traditional sintering of materials requires a temperature of up to 1225℃; However, SPS requires temperatures as low as 1050C. In addition, the relative density of the sample prepared by conventional sintering can reach 91%, while the maximum density of the sample prepared by SPS and annealed is about 98%, allowing the ionic conductivity to reach $3.5\times10^{-4}S\cdot cm^{-1}$. Ren et al. [20]. use instantaneous sintering method to further reduce the sintering temperature and time relative to SPS, so as to avoid Na, P evaporation and secondary phase precipitation due to high temperature and sintering time is too long, and the conductivity can reach 10^{-4}-10^{-3} $S\cdot cm^{-1}$. In addition, Sahir Naqash et al. [21]. adopted liquid-phase assisted solid phase sintering, and finally obtained a total conductivity of up to $1\times10^{-3}S\cdot cm^{-1}$, which shows that the development prospect of this method is very broad.

3.2. Sol-gel method

Compared with the traditional solid phase method, the sol-gel method can achieve the atomic-level mixing of raw materials, shorten the mass transfer process, and produce more uniform products. At the same time, the temperature required for densification can be effectively reduced to avoid the generation of impurity phase. The sol-gel method is first to form a colloidal solution, and then heated to form a gel network, after drying for heat treatment crystallization, and then sintering. The process flow is shown in Figure 5. Among them, the crystallization of $Na_3Zr_2Si_2PO_{12}$-based material usually starts at 600℃and is completedbetween 750 ℃ and 900℃ [22].

Jin Xiaojian et al. [23] prepared NASICON powder with different proportions by sol-gel method, and characterized it by XRD, SEM and Agilent test equipment. It was found that when the P source is excessive by 10%, the formation of ZrO_2 can be inhibited, and new impurity phosphates will not be generated due to the excess of P source. At this time, the ionic conductivity can reach 3.87×10^{-3} $S\cdot cm.^{-1}$

DOI: 10.54254/2755-2721/91/20241079

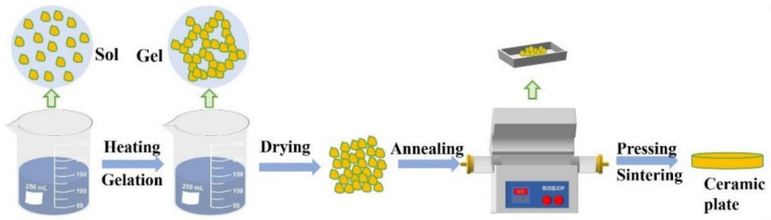

Figure 5. Process flow chart of sol-gel method [24]

3.3. Other preparation methods

In addition to the above, there are many other methods for the preparation of NZSP solid electrolytes, each of which presents its own unique advantages. For example, Liu et al. [25] used the LF-FSP method to produce NASICON nano powder, thus eliminating many steps necessary in the traditional solid-state process. Nanoscale final grains and higher sintering properties are achieved, and better performance is obtained at lower sintering temperatures. D. N. Grishchenko et al. synthesized NASICON with composition $Na_3Zr_2Si_2PO_{12}$ by pyrolysis of organic solution mixture [26]. The composition and morphology of the compound were confirmed by X-ray diffraction analysis and scanning electron microscopy. The synthesis of NASICON took an average of nine hours, the shortest time of all known methods for preparing the material.

Different preparation methods and process parameters will have a great impact on the ionic conductivity of NZSP materials, and the ionic conductivity of NZSP solid electrolytes can be controlled by controlling the preparation method and process.

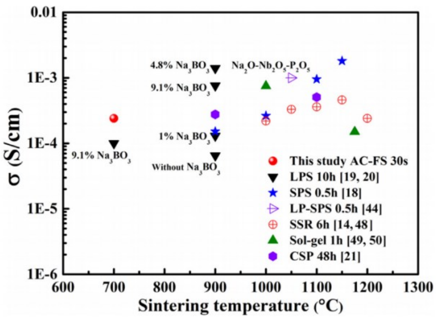

Figure 6. Relation between room temperature conductivity of NASICON ceramics and sintering temperature under different conditions [20]

4. Methods for increasing the ionic conductivity of NASICON solid electrolyte

4.1. Improving ion conductivity based on the preparation process

According to the second part above, it can be seen that for NZSP materials, different process parameters of the same process and different synthesis processes will affect the density, grain growth, impurities and other factors in the preparation, and then make the final ionic conductivity of NZSP materials change, so the first aspect is to regulate the process parameters and change the process. To achieve the improvement of ionic conductivity.

4.1.1. Process parameters

Therefore, the optimization effect of the change of process parameters on the ionic conductivity in sintering is discussed. The two important parameters in sintering are heating temperature and holding time. And often high heating temperature and long holding time there is a synergistic effect.

Through the comprehensive comparative analysis of electrochemical impedance spectroscopy at normal temperature, Chen Dan [27] explored the influence of different sintering temperature and holding time on density and conductivity. The analysis showed that the conductivity first increased with the increase of sintering temperature, and then decreased. With the extension of holding time, the conductance rises first and then becomes stable. Mihaela Iordache et al. [28] measured the particle size of NASICON powder sintered at different temperatures by dynamic light scattering (DLS) particle size: About 1000 nm at 1100°C, between 618.6 and 1315.4 nm at 1150°C and between 500.6 and 1008 nm at 1175°C. And found that sintering at 1175 ° C, the highest ionic conductivity.

In addition to the parameters in sintering, the optimization of process parameters in forming can also optimize the ionic conductivity of NASICON solid electrolyte. Man Kit Chong et [29] al. found that different grinding times lead to the formation of different types of ZrO_2, which is the reason for the different ionic conductivity. The NZSP milling for 24 h obtained the highest total ionic conductivity (9.66×10^{-4} S·cm^{-1}) at room temperature.

4.1.2. Preparation method

It can be seen from the second part of the preparation method that there are many different preparation methods for the preparation of NZSP, and different preparation methods have different effects on the ionic conductivity of NZSP materials due to their different characteristics.

The cold sintering, LF-FSP method and pyrolysis method mentioned above can respectively shorten the preparation time, save work steps, and reduce the sintering temperature and other needs. This section will introduce some of them and other related preparation methods on the basis of improving the ionic conductivity.

By fitting the composite impedance data with equivalent circuits, Diksha N. Karmalkar et [30] al. found that the grain and grain boundary total resistance of materials prepared by HT-SSR method were smaller than those prepared directly by SSR, except the parent phase. The basic principle of hydrothermal solid phase combination (HT-SSR) is that HT method can produce nanoparticles from a uniform water-based cationic mixture. This is expected to increase the density and thus reduce the grain boundary resistance of the sintered pellets. Li Zhi [31] made a comparative analysis of NZSP prepared by conventional sintering method and spray drying method, and found that the room temperature ionic conductivity of the material obtained by spray drying method was significantly higher than that obtained by conventional sintering method through the analysis of the EIS fitting data.

Table 1. Room temperature ionic conductivity of CS-NZSP and SD-CS-NZSP [31]

Sample	σ_b	σ_{gb}	σ_t	E_a/eV
CS-NZSP	1.28×10^{-3}	8.03×10^{-4}	4.94×10^{-4}	0.34
SD-CS-NZSP	1.664×10^{-3}	1.21×10^{-3}	6.96×10^{-4}	0.32

4.2. Improvement of ionic conductivity based on grain regulation

For Nasicon type ion conductors, the conduction mechanism of Na+ within the grain and at the grain boundary is different. Therefore, the improvement of its ion conductivity can be considered [32, 33] from the two aspects of grain and grain boundary respectively. For grains, according to the first part of the preceding description, in addition to the concentration of Na+ in sodium superionic conductors, the bottleneck area of the Na site transport path is also a factor limiting the improvement of ionic conductivity, so the next will be discussed from this aspect and the synergistic co-doping of the two.

4.2.1. Improving Na^+ concentration

The concentration of sodium ions is directly related to the number of sodium ions to participate in the transport, obviously the more sodium ions to participate in the transport of its higher conductivity, low ion doping is commonly used to increase the concentration of Na+ a way, its principle only according to the charge balance principle that can be seen, doping is equivalent to low ion instead of Zr^{4+} site, in order to balance the positive charge, The concentration of sodium ions in the crystal cell will be increased, so the ionic conductivity will be increased accordingly. Adam G. Jolley et [34] al. doped a variety of trivalent (Al^{3+}, Fe^{3+}, Y^{3+}) and divalent cations (Co^{2+}, Ni^{2+}, Zn^{2+}) respectively, and found that

DOI: 10.54254/2755-2721/91/20241079

the ionic conductivity was higher than that of undoped at room temperature. Luo et al. [35] found that the ionic conductivity of NZSP doped transition metal elements (Fe, Co, Ni) was also improved.

4.2.2. Enlarge the size of Na+ transport bottleneck area

As discussed in the previous part, the size of the bottleneck region will affect the size of the activation energy, and the increase of the diffusion bottleneck will lead to the increase of the ionic conductivity. According to Arrhenius formula, it can be found that it will further affect the ionic conductivity. To enlarge the bottleneck size, ions with larger radius are usually doped at the Zr site [24].

Liu et [25] al. substituted Zr4+ by Ce4+ and found that the Na+ diffusion "bottleneck" expanded sharply from 5.4 to 5.6 A2, resulting in a very high ionic conductivity of $2.4 \times 10^{-2} S \cdot cm^{-1}$ at 140°C. In addition, by doping Ca^{2+} in the system, the size of the sodium ion migration channel is effectively regulated, and the ionic conductivity of the solid electrolyte at room temperature is greater than $10^{-3} S \cdot cm^{-1}$ [36]. As for Ga doping, the triangular bottleneck area of the original sample is 5.234Å^2, but the triangular bottleneck area is increased by gallium substitution. When replaced by Ga0.1, the area can reach 6.165Å^2. The material has a superior total conductivity [37] of 1.06×10^{-3} S cm^{-1} at 25°C.

4.2.3. Co-doping

In addition to the above two methods carried out independently, there are also relevant studies on co-doping methods to improve ionic conductivity. Co-doping technology refers to adding another ion while adding a low-priced state ion, which can increase the Na+ concentration, and other ions can choose ions with larger radius, expand the size of the bottleneck area or assist sintering. Reduce the resistance of the grain boundary and improve the ionic conductivity. Luo et al. [35] co-doped transition metals to obtain NZSP with $5.03 \times 10^{-6} S \cdot cm^{-1}$ electronic conductivity. Omar et al. [38] synthesized NZSP co-doped with Sc/Yb. Sc^{3+} doping increased the carrier content in the system, while Yb with larger ionic radius expanded the size of Na+ transport channel. The synergistic effect of the two made the optimal ionic conductivity of the synthesized material $1.62\times10^{-3} S \cdot cm^{-1}$.

4.3. Improvement of ionic conductivity based on grain boundary regulation

The last aspect of this paper to improve the ionic conductivity is based on grain boundary regulation. Compared with the ion transport within the grain, the ion transport at the grain boundary is more difficult [24], so the ionic conductivity at the grain boundary is often lower than the ion conductivity in the grain. In this paper, the improvement of phase purity and the modification of grain boundaries are discussed.

4.3.1. Improving phase purity

In the preparation process, sometimes due to high temperature, element volatilization will cause the formation of impurity phase, and the formation of impurity phase will sometimes increase the grain boundary resistance, causing a very adverse effect on the grain boundary conductivity. The impurity phase can be avoided by the change of the aforementioned process parameters to adjust, in sintering usually occurs when the expected NASICON phase rises to a certain sintering temperature, and the impurity phase gradually decreases with the increase of sintering temperature, but sometimes if the sintering temperature is too high, it may reappear such as $Na_2ZrSi_2O_7$ and ZrO_2 impurity phase [39]. Increase the grain boundary resistance, resulting in a decrease in ionic conductivity. And often for the sintering of NZSP need a certain high temperature, so try to reduce the sintering temperature and time, reduce volatilization to avoid the formation of impurity phase is an important idea here. Jin An Sam Oh et al. [10] used the method of adding sintering agent Na_2SiO_3 to reduce the sintering temperature and sintering time of NZSP electrolyte, and provide the liquid phase for the sintering process. The highest ionic conductivity at room temperature is 1.45 mS·cm^{-1}. In addition, the above improvements [29, 40] in process parameters and different processes such as SPS, instantaneous sintering, pyrolysis of organic solution mixture, etc. [19, 20, 26], have respectively reduced the sintering temperature or sintering time and avoided the formation of impurity phase.

4.3.2. Grain boundary modification

Grain boundary modification is the method of introducing certain elements or phases into the grain boundary to regulate the electrical conductivity at the grain boundary. By changing the structure and chemical composition of the grain boundary, the properties of the material can be changed. When synthesizing NZSP, Zhang et al. [41] introduced a certain amount of La into the system. It was found by XRD pattern that the presence of La would cause $Na_3La(PO_4)_2$ phase to form at the grain boundary and fill the grain boundary, increasing the relative density of the ceramic sheet from 87.6% to 99.6%. The room temperature ionic conductivity of the obtained $Na_{3.3}Zr_{1.7}La_{0.3}Si_2PO_{12}$ electrolyte reached $3.4\times10_{-3}S\cdot cm_{-1}$. Shao et al. [42] added NaF to the precursor when synthesizing NZSP. Through SEM observation, it is found that the amorphous phase containing fluorine is formed around the grain, this amorphous phase modifies the grain boundary, making the density increase, the obtained solid electrolyte room temperature ionic conductivity up to $3.6\times10^{-3}S\cdot cm^{-1}$. In addition, a new preparation method can be used, such as the Si/P ratio in NASICON structure can be adjusted by the phosphate grain boundary phase formed by rare earth oxide assisted sintering method, so as to improve the ionic conductivity of the electrolyte [43].

5. Summary and Prospect

solid electrolyte was first proposed in 1976 and has made great progress in recent years. However, the current practical application of NZSP is still facing many problems and challenges, among which the ionic conductivity is low and does not meet the application needs of the problem remains to be solved. To this end, this paper first reviewed the crystal structure of the material, ion transport mechanism, preparation process, intended to fundamentally understand the NZSP in different factors on the ionic conductivity of the influence of the situation, on this basis, from the preparation process, grain control and grain boundary control of three aspects of the promotion of ionic conductivity methods. Through the ion transport mechanism found, based on Arrhenius equation, found that sodium ion concentration and bottleneck area size affect the grain conductivity, mainly through the optimization of process parameters, the development of new preparation process, ion doping, avoid impurity phase generation and grain boundary modification several aspects to improve the ionic conductivity. At present, good progress has been made in all aspects of research. However, for NASICON solid electrolyte, there are still some other problems, such as dendrite growth, electrode volume change, etc. For solid electrolyte, this is also an aspect that must be improved, so it also needs to be further studied. Based on these, In the future, the research focus of NASICON solid electrolyte should be focused on improving the ionic conductivity at the same time, ensuring the flexibility of its solid state interface, so as to reduce the interface problem, which can be improved by introducing a film or adding sintering additives.

References

[1] SAWICKI M, SHAW L L. Advances and challenges of sodium ion batteries as post lithium ion batteries [J]. RSC Advances, 2015, 5(65): 53129-54.
[2] HUANG Y, CHEN P, SHU X, et al. Extraction and recycling technologies of cobalt from primary and secondary resources: A comprehensive review [J]. International Journal of Minerals, Metallurgy and Materials, 2024, 31(4): 628-49.
[3] YU T, LI G, DUAN Y, et al. The research and industrialization progress and prospects of sodium ion battery [J]. Journal of Alloys and Compounds, 2023, 958.
[4] MA M, ZHANG M, JIANG B, et al. A review of all-solid-state electrolytes for lithium batteries: high-voltage cathode materials, solid-state electrolytes and electrode–electrolyte interfaces [J]. Materials Chemistry Frontiers, 2023, 7(7): 1268-97.
[5] MA Q, TSAI C-L, WEI X-K, et al. Room temperature demonstration of a sodium superionic conductor with grain conductivity in excess of 0.01 S cm−1 and its primary applications in symmetric battery cells [J]. Journal of Materials Chemistry A, 2019, 7(13): 7766-76.

[6] KHAKPOUR Z. Influence of M: Ce4+, Gd3+ and Yb3+ substituted Na3+xZr2-xMxSi2PO12 solid NASICON electrolytes on sintering, microstructure and conductivity [J]. Electrochimica Acta, 2016, 196: 337-47.
[7] LI Y L Y, ZHAO C, ET AL. Recent advances of electrode materials for low-cost sodium-ion batteries towards practical application for grid energy storage [J]. Energy Storage Materials, 2017, 7: 130-51.
[8] WANG H, ZHAO G, WANG S, et al. Enhanced ionic conductivity of a Na3Zr2Si2PO12 solid electrolyte with Na2SiO3 obtained by liquid phase sintering for solid-state Na+ batteries [J]. Nanoscale, 2022, 14(3): 823-32.
[9] U J, LIU L, ZHOU X., et al. Research Progress of NASICON type sodium ion Conductor solid lectrolyte [J]. Journal of the Chinese Academy of Ceramics, 2023, 51(06): 1611-25
[10] OH J A S, HE L, PLEWA A, et al. Composite NASICON (Na3Zr2Si2PO12) Solid-State Electrolyte with Enhanced Na+ Ionic Conductivity: Effect of Liquid Phase Sintering [J]. ACS Applied Materials & Interfaces, 2019, 11(43): 40125-33.
[11] HE X, ZHU Y, MO Y. Origin of fast ion diffusion in super-ionic conductors [J]. Nature Communications, 2017, 8(1).
[12] WANG J, DING J, DELAIRE O, et al. Atomistic Mechanisms Underlying Non-Arrhenius Ion Transport in Superionic Conductor AgCrSe2 [J]. ACS Applied Energy Materials, 2021, 4(7): 7157-67.
[13] ZHANG B, TAN R, YANG L, et al. Mechanisms and properties of ion-transport in inorganic solid electrolytes [J]. Energy Storage Materials, 2018, 10: 139-59.
[14] PARK H J K, NEZAFATI M, ET AL. Sodium ion diffusion inNasicon (Na3Zr2Si2PO12) solid electrolytes:Effects of excess sodium [J]. ACS Appl Mater Interfaces, 2016: 8(41): 27814–24.
[15] TIWARI A, MEGHNANI D, MISHRA R, et al. Impact of sintering temperature and ascertaining hopping bottlenecks for ions in sodium superionic conducting electrolyte for sodium-ion batteries [J]. Journal of Power Sources, 2023, 580.
[16] WANG S, FU J, LIU Y, et al. Design principles for sodium superionic conductors [J]. Nature Communications, 2023, 14(1).
[17] WEN C, LUO Z, LIU X, et al. Enhanced electrochemical properties of NASICON-type Na3Zr2Si2PO12 solid electrolytes with Tb3+-ions-assisted sintering [J]. Solid State Ionics, 2023, 393.
[18] JHA P K, PANDEY O P, SINGH K. Optimization of High Conducting Na3Zr2Si2PO12 Phase by new Phosphate Salt for Solid Electrolyte [J]. Silicon, 2016, 9(3): 411-9.
[19] HITESH B, SIL A. Effect of sintering and annealing on electrochemical and mechanical characteristics of Na3Zr2Si2PO12 solid electrolyte [J]. Journal of the American Ceramic Society, 2023, 106(11): 6743-54.
[20] REN K, CAO Y, CHEN Y, et al. Flash sintering of Na3Zr2(SiO4)2(PO4) solid-state electrolyte at furnace temperature of 700 °C [J]. Scripta Materialia, 2020, 187: 384-9.
[21] NAQASH S, MA Q, TIETZ F, et al. Na 3 Zr 2 (SiO 4) 2 (PO 4) prepared by a solution-assisted solid state reaction [J]. Solid State Ionics, 2017, 302: 83-91.
[22] O. SCHAF A W, 1 P.L. LLEWELLYN,1 P. KNAUTH,1,∗ N. KAABBUATHONG,2 M.L. DI VONA,2, TRAVERSA2 S L E. Preparation and Electrical Properties of Dense Ceramics with NASICON Composition Sintered at Reduced Temperatures [J]. Journal of Electroceramics, 2004: 13, 817–23.
[23] IN X, LIU D, WANG J. Preparation and Conductivity of Nanoscale NASICON fast ionic onductor [J]. Shandong Chemical Industry, 2023, 52(04): 26-8.
[24] Wang Q. Structural modification of Nasicon Na_3Zr_2Si_2PO_(12) solid electrolyte and properties of all-solid-state batteries [D], 2023.
[25] LIU S, ZHOU C, WANG Y, et al. Ce-Substituted Nanograin Na3Zr2Si2PO12 Prepared by LF-FSP as Sodium-Ion Conductors [J]. ACS Applied Materials & Interfaces, 2019, 12(3): 3502-9.

DOI: 10.54254/2755-2721/91/20241079

[26] GRISHCHENKO D N, DMITRIEVA, E.E. & MEDKOV, M.A. New Method for the Preparation of NASICON (Na3Zr2Si2PO12) by Pyrolysis of Organic Solutions [J]. Theor Found Chem Eng, 2023: 57, 1034–8

[27] Chen D. Preparation and Electrical Properties of Na_3Zr_2Si_2PO_(12) ceramics [D], 2019.

[28] IORDACHE M, OUBRAHAM A, PETREANU I, et al. NASICON Membrane with High Ionic Conductivity Synthesized by High-Temperature Solid-State Reaction [J]. Materials, 2024, 17(4).

[29] CHONG M K, ZAINUDDIN Z, OMAR F S, et al. Na3Zr2(SiO4)2PO4 NASICON-type solid electrolyte: Influence of milling duration on microstructure and ionic conductivity mechanism [J]. Ceramics International, 2022, 48(15): 22106-13.

[30] KARMALKAR D N, DUTTA D, BERA A K, et al. Synthesis of High Na+ Ion-Conducting NASICON-Based Electrolytes and Insights from Diffraction and Positron Annihilation Lifetime Spectroscopy Studies [J]. The Journal of Physical Chemistry C, 2024, 128(2): 768-77.

[31] Li W. Preparation and performance optimization of sodium superionic conductive solid lectrolyte Na_3Zr_2Si_2PO_(12) [D], 2022.

[32] ORTIZ-MOSQUERA J F, NIETO-MUñOZ A M, RODRIGUES A C M. New Na1+xGe2(SiO4)x(PO4)3–x NASICON Series with Improved Grain and Grain Boundary Conductivities [J]. ACS Applied Materials & Interfaces, 2020, 12(12): 13914-22.

[33] PARK H, JUNG K, NEZAFATI M, et al. Sodium Ion Diffusion in Nasicon (Na3Zr2Si2PO12) Solid Electrolytes: Effects of Excess Sodium [J]. ACS Applied Materials & Interfaces, 2016, 8(41): 27814-24.

[34] JOLLEY A G, COHN G, HITZ G T, et al. Improving the ionic conductivity of NASICON through aliovalent cation substitution of Na3Zr2Si2PO12 [J]. Ionics, 2015, 21(11): 3031-8.

[35] LUO J, ZHAO G, QIANG W, et al. Synthesis of Na ion-electron mixed conductor Na3Zr2Si2PO12 by doping with transition metal elements (Co, Fe, Ni) [J]. Journal of the American Ceramic Society, 2022, 105(5): 3428-37.

[36] LU Y, ALONSO J A, YI Q, et al. A High-Performance Monolithic Solid-State Sodium Battery with Ca2+ Doped Na3Zr2Si2PO12 Electrolyte [J]. Advanced Energy Materials, 2019, 9(28).

[37] HUANG C, YANG G, YU W, et al. Gallium-substituted Nasicon Na3Zr2Si2PO12 solid electrolytes [J]. Journal of Alloys and Compounds, 2021, 855.

[38] PAL S K, SAHA R, KUMAR G V, et al. Designing High Ionic Conducting NASICON-type Na3Zr2Si2PO12 Solid-Electrolytes for Na-Ion Batteries [J]. The Journal of Physical Chemistry C, 2020, 124(17): 9161-9.

[39] LIU Y, LIU L, PENG J, et al. A niobium-substituted sodium superionic conductor with conductivity higher than 5.5 mS cm−1 prepared by solution-assisted solid-state reaction method [J]. Journal of Power Sources, 2022, 518.

[40] XING Y, LI Y, ZHANG C. Low temperature preparation of dense and highly conductive NASICON electrolyte by solid-state reactive sintering [J]. Solid State Ionics, 2021, 373.

[41] ZHANG Z, ZHANG Q, SHI J, et al. A Self-Forming Composite Electrolyte for Solid-State Sodium Battery with Ultralong Cycle Life [J]. Advanced Energy Materials, 2016, 7(4).

[42] SHAO Y, ZHONG G, LU Y, et al. A novel NASICON-based glass-ceramic composite electrolyte with enhanced Na-ion conductivity [J]. Energy Storage Materials, 2019, 23: 514-21.

[43] WANG X, MEI W, CHEN J, et al. Rare Earth Oxide-Assisted Sintered NASICON Electrolyte Composed of a Phosphate Grain Boundary Phase with Low Electronic Conductivity [J]. ACS Applied Energy Materials, 2022, 5(1): 777-83.

DOI: 10.54254/2755-2721/91/20241073

The ways and mechanisms of using CFRP materials to strengthen the flexural performance of reinforced concrete beams

Junyi Zhang

Department of engineering and technology, China University of Geosciences Beijing, Beijing, China

13012719621@163.com

Abstract. Due to the increasing demand for structural strengthening and retrofitting solutions, Fiber-reinforced plastic (FRP) materials has emerged as a promising technology to improve the performance of existing structures. FRP material is a composite material composed of fiber-reinforced plastics, known for its excellent strength and resistance to corrosion. The primary components of this material consists of various fibers, such as glass fiber, carbon fiber, or aramid fiber, along with a resin matrix, such as epoxy resin, polyester resin. FRP materials are commonly employed in construction engineering to enhance the flexural strength of concrete structures. This paper, through methods of literature review and building physical models, investigates the effectiveness of Carbon Fiber Reinforced Polymer (CFRP) materials in enhancing the bending strength of reinforced concrete beams. This study aims to examine the impact of carbon fiber reinforced polymer (CFRP) sheets on the flexural strength of reinforced concrete beams, which aims to establish calculation formulas based on the specific impacts observed. The findings of this study demonstrate the capacity of FRP materials, specifically CFRP materials, to improve the bending strength of reinforced concrete beams. The usage of FRP materials for structural reinforcement offers a durable, corrosion-resistant, and lightweight solution that can prolong the lifespan and improve the structural efficacy of existing infrastructure.

Keywords: CFRP materials, reinforced concrete beams, flexural strength.

1. Introduction

Reinforced concrete structures are widely used in the construction due to their exceptional strength and durability. However, the deterioration of infrastructure due to the passage of time and the increased demands placed on it have necessitated the implementation of effective strengthening techniques to enhance the performance and safety of existing structures. Fiber Reinforced Polymer (FRP) materials are a promising solution for strengthening reinforced concrete elements, offering advantages such as a high strength-to-weight ratio, corrosion resistance, and ease of application.

Carbon Fiber Reinforced Polymer (CFRP) material is a composite material that consists of carbon fiber or carbon fiber fabric as the reinforcing body, and resin, ceramics, metals, cement, carbon as the matrix. This article expresses the capacity of CFRP materials to enhance their bending resistance by conducting a literature review and developing component physical models.

Significant progresses have been made in the research on the flexural performance of reinforced concrete beams strengthened with CFRP materials. Oral Buyukozturk conducted many experiments to explain the phenomenon of brittle debonding failure in FRP material. By using a model-based approach, his study determined the impact of debonding on the performance and durability of FRP reinforcement [1]. Scholar Junwei Zhang conducted the flexural tests on five reinforced concrete beams that were strengthened with carbon fiber reinforced polymer (CFRP) sheets, which aimed to investigate the influences of span-depth ratio on flexural performance [2]. Wenxue Dong proposed the application of FRP materials in bridge engineering and identified the challenges associated with FRP composite materials. He also anticipated the main areas of development in this field [3]. Zekun Yang presented a mathematical technique to calculate the flexural bearing capacity of reinforced concrete short beams reinforced with externally bonded FRP sheets. Moreover, the calculation process incorporated the compressive stress-strain curve of Hognestad concrete, which includes a falling portion [4].

This paper aims to propose a technique for strengthening the bending capacity of CFRP materials and a straightforward formula for calculating the bending bearing capacity. These findings have practical significance for using CFRP to strengthen reinforced concrete beams.

2. CFRP materials' characteristics

Carbon Fiber Reinforced Polymer(CFRP) materials offer several advantages for strengthening beams and enhance their bending strength. Here are some key characteristics of CFRP materials.

2.1. High Strength-to-Weight Ratio

CFRP materials can provide significant strengthening effects without adding excessive weight to the structure, making them ideal for implementations where weight is a concern. CFRP materials use high-strength carbon fibers as reinforcing materials, which have much higher strength than traditional ones. CFRP materials use lightweight polymers as the matrix, usually with resins such as epoxy resin and polyimide, which have good adhesion and chemical corrosion resistance while also helping to reduce the weight of CFRP materials. The above conditions have created the high strength-to-weight ratio characteristics of CFRP materials.

2.2. Corrosion Resistance

Unlike traditional steel reinforcements, CFRP materials are highly resistant to corrosion. The basic components of CFRP like carbon fiber and polymer matrix are non-metallic and resistant to electrochemical reactions. Commonly used polymer matrices, such as epoxy resin and polyimide, have good chemical corrosion resistance and can effectively resist the erosion of acidic, alkaline, saline, and other media. CFRP material is a composite structure composed of multiple layers with high density and uniform structural characteristics, which can effectively block the penetration of corrosive media delay the aging and corrosion rate of the material. Ziye Pan further studied the aging control and corrosion resistance of FRP materials [5].

2.3. Elastic Change Ability

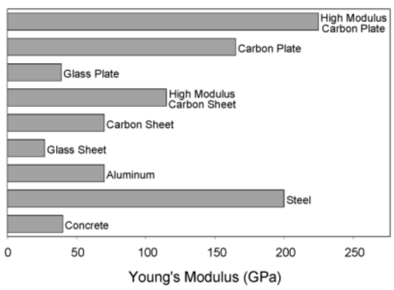

Figure 1. Elastic (Young 's) modulus [1]

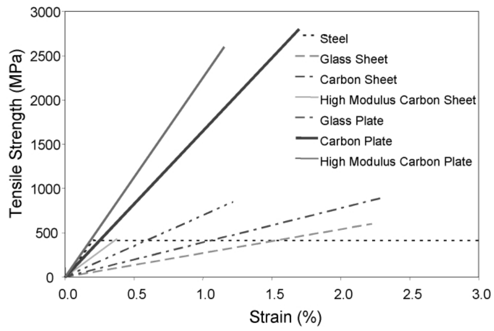

Figure 2. Stress-strain behavior [1]

From the two figures, it is clear that the Elastic modulus of CFRP material compositions are considerably less than that of steel. Figure 1 compares the elastic modulus of concrete, aluminum, and steel with those of several commercially available FRP composite systems, and Figure 2 shows a comparison of strength-strain behavior in tension [1]. Although the Young's modulus of FRP materials may be lower than that of metal materials, their high specific strength, corrosion resistance, design flexibility, and other advantages make them a high-quality material chosen to enhance bending performance. Especially in applications that require lightweight design, long-term durability, and excellent chemical performance, FRP can significantly improve the performance and service life of structural components.

3. The flexural performance of reinforced concrete beams

Reinforced concrete has many applications in engineering, among which beam components are the main ones. Beam components mainly bear bending moments and are typical bending resistant components. Therefore, reasonable design should be carried out in the design to prevent beams from bending failure or even brittle failure, causing economic losses and health and safety risks. Therefore, understanding the bending failure mode of beams is very helpful for structural design and later reinforcement.

For reinforced concrete beams, different reinforcement ratios, cross-sectional areas, and levels of concrete strength will have a significant impact on the flexural bearing capacity of the beam, with reinforcement playing a particularly important role. Taking a simply supported beam as an example, this issue can be addressed.

3.1. Under- and over-reinforced failure

In under-reinforced circumstances, the reinforcement ratio of the beam is too low. Before the concrete compression zone fails, the steel bars reach the yield stage in a short period of time, and the beam fails in a short period of time. This type of failure is similar to the brittle failure form of plain concrete.

In the over-reinforced term, the reinforcement ratio of the beam is too high, and the concrete in the compression zone of the reinforced concrete beam is damaged in a short period of time. This underutilization of the steel bars' tensile strength in the tension zone leads to brittle failure and is economically unreasonable.

3.2. Balanced failure

The reinforcement ratio is between under-reinforced failure and over-reinforced failure. The yield of the steel bars in the tensile zone initiates the failure of the beam, followed by the crushing of the concrete in the compressive zone. This failure fully utilizes the strength of the steel bars and concrete, and plastic deformation and crack development are obvious, which is ductile failure.

Over-reinforced and under-reinforced failures should be avoided in structural design, as they can cause rapid damage. Balanced failure is a normal form of failure, and its failure has good ductility [6]. So it can be a useful way to use FRP materials to enhance their bending resistance and ductility.

DOI: 10.54254/2755-2721/91/20241073

4. Strengthening method and mechanism

The flexural bearing capacity of reinforced concrete beams is mainly provided by the lower-tensile steel bars. When it undergoes bending failure, the lower concrete cracks and the tensile steel bars yield, these two characteristics provide a good idea to enhance the flexural capacity. CFRP cloth can be posted at the bottom of the concrete tensile zone to help the tensile steel bars bear the bending moment, delay and reduce concrete cracking, and enhance the ductility of reinforced concrete beams [7].

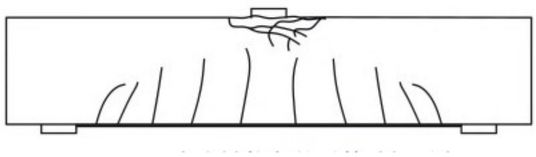

Figure 3. Installation method

From the Figure 3 it can be seen that the method to enhance the bending capacity of a beam is like adding steel bars to the compression zone of the beam. Therefore, the similar method can be used to derive the calculation formula for the bending bearing capacity of the beam cross-section.

4.1. Computational model

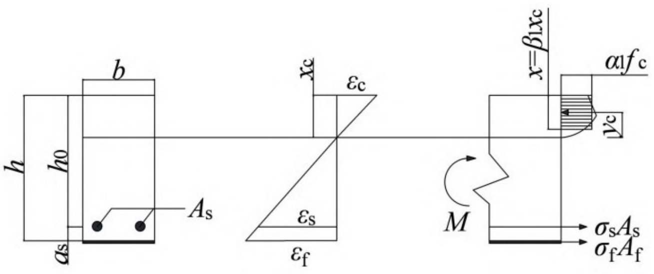

Figure 4. Model after posting CFRP cloth [4]

Figure 4 is the computational model of the beam after posting CFRP cloth, referring to Code for Design of Concrete Structures GB 50010-2010. To simplify the calculation, the stress graph of the concrete in the compression zone is replaced with an equivalent rectangular stress graph, and the rectangular stress graph coefficients α_1 and β_1 for the concrete in the compression zone. The following formula can be therefore obtained:

$$\alpha_1 f_c b x = k_1 f_c b x_c \tag{1}$$

$$x = 2(x_c - yc_c) = 2(1 - k2)x_C \tag{2}$$

$$\beta 1 = \frac{x}{xc} = 2(1 - k2) \tag{3}$$

$$\alpha_1 = \frac{k_1}{\beta_1} = \frac{k_1}{2(1 - k_2)} \tag{4}$$

where α_1 is the ratio of the stress value of the concrete rectangular stress in the compression zone to the design value of the concrete axial compressive strength. And β_1 is the ratio of the height of the compressed area in a rectangular stress diagram to the neutral axis.

4.2. Calculation formula

By converting Formula (1) and Formula (2), as well as knowing the design value of the tensile strength of CFRP material (σf), the calculation formula can be obtained for the flexural bearing capacity of reinforced concrete beams with CFRP cloth posted on them, as follows:

DOI: 10.54254/2755-2721/91/20241073

$$\alpha_1 f_c bx = \sigma_s A_s + \sigma_f A_f \tag{5}$$

$$M_u = \sigma_s A_s \alpha_d \left(h_0 - \frac{x}{2}\right) + \sigma_f A_f \alpha_d \left(h - \frac{x}{2}\right) \tag{6}$$

As the span-to-height ratio of the beam decreases, the strain distribution of the mid-span normal section becomes increasingly inconsistent with the plane section assumption, and the internal force arm gradually decreases. Therefore, it is necessary to introduce an internal force arm correction coefficient to modify the shallow beam formula that conforms to the assumption of a flat section. Referring to the Code for Design of Concrete Structures GB 50010-2010, it can be obtained that:

$$\alpha_d = 0.8 + 0.04 \frac{l_0}{h} \tag{7}$$

where l0 means short beam calculation span [4]. This process is similar to the calculation of the flexural bearing capacity of the normal section of a reinforced beam, and it also shares a similar failure mode, with problems of over-reinforcement and under-reinforcement failure. So, when strengthening the bending resistance of beams, these issues should also be considered.

4.3. Calculation instance

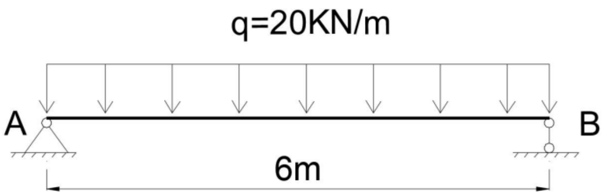

Figure 5. Force diagram

The cross-sectional dimensions of this reinforced concrete beam are b*h=250*500, the strength grade of concrete is C30, the environmental category is Class 1, and the steel bars are made of HRB400 grade steel bars. From the Design of Concrete Structures GB 50010-2010, it can be seen that σ_s =360N/mm^2, f_c =14.3N/mm^2, f_t =1.43N/mm^2, α_1=1.0, and As=1256mm^2.

When the load shown in the figure is applied, the tensile steel bars originally configured in the structure are not sufficient to provide enough bending capacity, so the CFRP cloth is posted to enhance its bending capacity. The following formula can be used:

$$M_u = \alpha 1 f_c bx \left(h_0 - \frac{x}{2}\right) \tag{8}$$

Through force analysis, it can be calculated that M=Mu=360KN*m, x=228mm, and the initial configuration of tensile steel bars is not sufficient to provide sufficient bending bearing capacity:

$$M_u > \sigma_s A_s \alpha_d \left(h_0 - \frac{x}{2}\right) \tag{9}$$

So it is necessary to post CFRP sheet to improve its bending resistance. The following formula can be used to determine at least how much bending bearing capacity CFRP fabric is required, and then determine the specifications and parameters of the CFRP fabric to be posted.

$$M_u - \sigma_s A_s \alpha_d \left(h_0 - \frac{x}{2}\right) = \sigma_f A_f \alpha_d \left(h - \frac{x}{2}\right) \tag{10}$$

5. Conclusions

This paper examines the failure modes of reinforced concrete beams and the performance characteristics of CFRP materials. It concludes that using CFRP reinforcement effectively improves the bending strength and failure extension of the beam, and analyzes the mechanism behind reinforcing the bending capacity of beams with CFRP reinforcement and derives a calculation formula to access the bending performance of beams. This has a reference value for the technique of reinforcing flexural components and the process of cost calculation. However, there are still certain shortcomings. Following the installation of CFRP bars, their failure mode has also changed, resulting in the emergence of failure-related issues. The method of posting FRP bars is still worth discussing, including the impact of temperature and other conditions on the installation processes. FRP materials have low elastic change ability, hence achieving improved results can be accomplished by applying pre-tension to the FRP reinforcement, effectively converting it into prestressed reinforcement.

The widespread implementation of CFRP materials will lead to a movement towards making structures lighter, which in turn helps to reduce energy consumption and carbon emissions, therefore promoting the sustainable development of the environment. Furthermore, a more profound comprehension of the properties of CFRP materials can equip engineers and designers with a wider range of innovative design choices, optimizing product performance and minimizing expenses.

References

[1] Buyukozturk O,Gunes O,Karaca E. Progress on understanding debonding problems in reinforced concrete and steel members strengthened using FRP composites[J].Construction and Building Materials, 2004, 18(1): 9-19.
[2] Zhang Junwei, Wang Tingyan. Experimental study on the flexural performance of reinforced concrete short beams reinforced with CFRP fabric [J]. Concrete, 2020, (09): 31-36.
[3] Dong Wenxue. Development and Application of FRP Composite Materials in Bridge Engineering[J]. Aging and Application of Composite Materials, 2024, 53(02): 86-89. DOI:10.16584/j.cnki.issn1671-5381.2024.02.019.
[4] Yang Zekun, Fang Sheng'en, Wu Yingxiong, et al. Formula for flexural bearing capacity of RC short beams reinforced with externally bonded FRP[J]. Journal of Nanchang University (Engineering Edition), 2023, 45(03): 254-260. DOI:10.13764/j.cnki.ncdg.2023.03.009.
[5] Pan Zi Ye .Research on aging control and corrosion resistance of FRP material type bridge tunnel structure [J] .Adhesive, 2021, 48 (12): 192-196
[6] Liu Lixin, Xie Lili, Sang Dayong. Experimental study on the flexural performance of reinforced concrete beams reinforced with prestressed carbon fiber cloth[J]. Building Structures, 2007, 37(S1): 298-300. DOI:10.19701/j.jzjg.2007.s1.096.
[7] Xue Weichen, Zheng Qiaowen, Yang Yu. Design and research on the flexural bearing capacity of FRP reinforced concrete beams [J]. Engineering mechanics, 2009, 26(01): 79-85

Proceedings of the 2nd International Conference on Functional Materials and Civil Engineering
DOI: 10.54254/2755-2721/91/20241072

Structural damage prediction based on Bayesian updating with Monte Carlo sampling

Jiahao Chen[1,4,*], Chenfei Lin[2], Zhuohang Yang[3]

[1]School of Civil Engineering South Central University, Changsha, Hunan Province, 410000, China
[2]International Union College Dalian Maritime University, Dalian, Liaoning Province, 116000, China
[3]School of Civil Engineering, Chongqing Jiaotong Universitychongqing, Chongqing, 400000, China

[4]8210212121@csu.edu.cn
*corresponding author

Abstract. A series of engineering accidents in recent years have caused people to worry about the safety of engineering structures. As buildings continue to age, engineering accidents are increasing, and it is necessary to monitor their health. Bayesian updating can determine the probability of damage to a structure by collecting a posteriori information, and can more accurately estimate the location and extent of damage, thereby predicting the risk of structural damage and repairing the damage in time, significantly improving engineering efficiency. This paper attempts to update the information of the simulated structure based on the Bayesian updating method to obtain a more accurate posterior distribution of the potentially damaged components to demonstrate the feasibility and superiority of the technique. This paper finds that Bayesian updating can be used in conjunction with modeling software such as SMsolver. By constructing a structural model with SMsolver and processing the data with Bayesian updating, it is possible to calculate the damage problems of the structure accurately. At the same time, this paper also uses Monte Carlo sampling technology in combination with the Bayesian updating method to explore the prediction effect of structural damage. Using Monte Carlo sampling methods, the failure probability and damage location of the structure can be effectively estimated under the condition of known prior information, thereby improving production efficiency and the accuracy of structural inspection.

Keywords: Bayesian updating, Bayesian principle, structural damage, Monte Carlo sampling.

1. Introduction

With China's reform and opening up at the end of the last century, the economy developed rapidly, and domestic infrastructure construction also ushered in rapid development. Many bridges, roads and high-rise buildings were quickly built and put into use in a short period. However, with the passage of time and the increase in traffic volume and vehicle weight requirements, China's existing steel structures are aging, and the degree of fatigue deterioration is also increasing. Therefore, methods for evaluating and updating the actual fatigue life of such structures are urgently needed.

The randomness of fatigue growth and the uncertainty of the load history of steel structures require regular and repeated inspections, which have become an important part of the bridge evaluation and management process. In this case, Bayesian updating derived from the Bayesian theorem can be well applied to assess and update the actual fatigue of the structure. Bayesian theory can be used to more effectively update fatigue reliability models using the results of NDI technology, improving the estimation of the remaining fatigue life and safety of existing steel bridge structures, allowing them to continue to be used while minimizing unnecessary repairs or re-installation [1].

In the long-term operation of structural facilities, the aging and fatigue of structures become inevitable problems over time. In order to ensure the safety and reliability of these structures during their life cycle, and to improve the efficiency of damage detection and maintenance, more advanced detection and evaluation methods are needed.

In 1998, Beck [2] and others first applied Bayesian theory to model updating in the field of civil engineering, proposing a basic framework for Bayesian updating. To solve the problem of integrating the posterior distribution of parameters, Beck and others introduced the Metropolis-Hastings (MH)-based Markov Chain Monte Carlo (MCMC) algorithm into Bayesian updating and used the shear model to prove the reliability of the method [3]. In this study, two structural models will be established using SM Solver, and the structure's posterior information and the structure's failure probability will be updated using the Bayesian update method and the Monte Carlo sampling method, respectively, to propose a more efficient structural damage prediction method.

This paper aims to predict and assess structural damage based on Bayesian updating and Monte Carlo sampling methods. This paper aims to explore the feasibility and superiority of these two methods in structural damage prediction and verify their effectiveness through specific experiments. To achieve this goal, this paper introduces the basic principles of Bayesian updating and Monte Carlo sampling and their applications in structural damage prediction, including specific calculation formulas and processes. Second, this paper verifies the application of Bayesian updating and Monte Carlo sampling in structural damage prediction through two specific experiments, and finally, this paper proposes future research directions and application prospects.

2. Basic methods

2.1. Bayesian updating method

Based on the principle of Bayesian, the new information about an object obtained through factual evidence or experiments is used as the likelihood (i.e., the probability of the event actually occurring and the probability of the event not occurring), and the original prior probability of the object is calculated through the Bayesian formula to obtain the posterior distribution of the object, thereby obtaining more reliable posterior information about the object [4]. This study established a model of a plane truss with possible damage using SM Solver. The lengths and stiffnesses of some members and supports were known, while the stiffnesses of the members with possible damage were unknown and assigned a possible prior distribution. The author used the actual deformation of the truss structure as new information to perform Bayesian updating on the model to obtain a more accurate stiffness distribution of the damaged members (see Experiment 1 for details).

In this study, the unknown stiffness of the damaged member is regarded as a random variable, and the true value of the structural deformation is used to update the prior probability density function of the parameters to obtain the posterior probability density function [5]. The basic formula is as follows:

$$P(B|A) = \frac{P(A|B)P(B)}{P(A)} = cP(A|B)P(B) \tag{1}$$

Where B is the vector of parameters to be updated, i.e. the result vector obtained after Monte Carlo sampling; A is the observed data, i.e. the true displacement of the structure; P(B) is the prior distribution of the damaged member, which is often regarded as a generalized unbiased uniform distribution in the absence of historical experience; the likelihood function P(A|B) is the conditional probability of

DOI: 10.54254/2755-2721/91/20241072

displacement A when B occurs; c is a normalization constant to ensure that the posterior probability density function is integrated to 1 [6]. P(B|A) is the posterior distribution probability of the stiffness of the damaged member that is desired to be obtained from the test results.

2.2. Monte Carlo sampling

Monte Carlo sampling is a computational method based on probability, statistical theory, and methods. It simulates the behavior of a random process or system through a large number of random samples to obtain the statistical characteristics or approximate solution of the process or system [7]. PMBOK uses Monte Carlo simulation as a technical means of quantitative risk analysis in project risk management. In engineering, Monte Carlo simulation is an effective risk analysis method, often used in engineering investment risk analysis and industrial system reliability and risk analysis [8]. With the advent of the information age, Monte Carlo sampling analysis of structural failure probability has gradually become the mainstream structural damage prediction method in engineering [9,10].

In order to demonstrate the efficiency and convenience of combining the Monte Carlo sampling method with the Bayesian updating method to calculate the failure probability of structures, the author established a statically determinate two-force beam model in the study, and the member area, material strength, and load on the structure (hereinafter referred to as the relevant parameters) all obeyed the corresponding distribution. The author used Excel to randomly sample the relevant parameters 10,000 times to calculate the failure probability of the model, and the results can be used to determine the damage probability of the structure (see Experiment 2 for details).

2.3. Introduction to the tool

SMSolver was developed by the Structural Mechanics Solver Development Group of the Department of Civil Engineering at Tsinghua University. It is a computer-aided analysis and calculation software (course) for teachers, students and engineers. The solver includes a series of problems involved in the classic structural mechanics courses, such as the geometric composition, statics, super statics, displacement, internal forces, influence lines, free vibration, elastic stability, and ultimate load of two-dimensional planar structures (systems). All of these problems are solved using accurate algorithms.

3. Experimental results and discussion

3.1. Test 1: Bayesian updating of a planar truss model

Use SM Solver to build the structural model: define the length unit in the model as meters (m), the unit of force as kilonewtons (KN), and the unit of member stiffness as kilonewtons multiplied by the square of meters (KN×m²); define the nodes of the structure, take the length of each cross-member as 15m; connect all nodes to form individual member units, and combine them into the final structure as shown in Figure 1. In this model, the researcher defines the prior information as follows: the stiffness data of the known intact members (as shown in Table 1) and the support locations; the prior information of the stiffness of the damaged members (members 3-4, i.e., element 3) obeys a uniform distribution U (0.90, 1.98).

Table 1. Related Rod Stiffness Tables

1-2	2-3	4-5	1-6	6-7	7-8
1.8	1.71	1.8	1.98	1.89	1.89
8-5	2-6	3-6	3-7	4-8	
1.98	1.62	1.53	1.539	1.62	

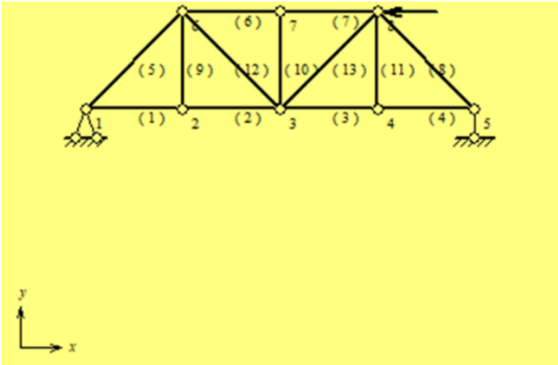

Figure 1. Diagram of the truss model

3.2. Test 1 process

After the truss model is built, the prior belief about the stiffness distribution of member 3 needs to be updated based on the actual deformation of the structure (in this experiment, the displacement at node 3, Δ, is used as the deformation parameter) when the structure is subjected to a load (the fact that occurs in Bayesian theory) The experimenter assumes that the upper limit of the single load applied is 100KN. The SMSolver was used to simulate the effects of various loading methods on the stress of each member of the structure and the overall stability of the structure. It was finally decided to apply a horizontal left lateral force of 100KN at node 8, as shown in Figure 2 (omitted here, does not affect the test results).

3.3. Calculate the deformation at node 3

SM Solver is used to simulate the displacement at node 3 when the load is applied according to uniform distribution under different stiffness values of element 3, as shown in Table 2. Table 2 shows partial results of uniformly distributed values. The tester gives the true displacement at node 3 as Δ_r=0.01287m, and the standard deviation of the test is σ=0.5.

Table 2. Values of element 3(partial)

EA	u -Horizontal displacement	v -Vertical displacement	θ-Corner
0.9	-0.01282895	0.00162577	-0.00042596
0.92	-0.01282895	0.00158048	-0.00042747
0.94	-0.01282895	0.00153712	-0.00042891
0.96	-0.01282895	0.00149556	-0.0004303
0.98	-0.01282895	0.0014557	-0.00043163
1.00	-0.01282895	0.00141744	-0.0004329
1.02	-0.01282895	0.00138067	-0.00043413
1.04	-0.01282895	0.00134532	-0.00043531
1.06	-0.01282895	0.0013113	-0.00043644
1.08	-0.01282895	0.00127855	-0.00043753
1.10	-0.01282895	0.00124698	-0.00043858
1.12	-0.01282895	0.00121654	-0.0004396
1.14	-0.01282895	0.00118717	-0.00044058

3.4. Calculation of displacement using the principle of virtual work

The axial force diagrams of the axial forces of each member when P = 1KN and when P = 100KN are shown in Table 3 and Table 4, respectively. The expression for calculating the displacement Δ at node 3 using the virtual work principle

$$\Delta_{ij}=\sum\int\frac{N\overline{N}}{EA}ds=\sum\frac{Nl\overline{N}}{EA} \tag{2}$$

DOI: 10.54254/2755-2721/91/20241072

Table 3. Axial force diagram of each rod when P is 1KN

Rod end 1				Rod end 2		
Unitary code	Axial force	Shearing force	Bending moment	Axial force	Shearing force	Bending moment
1	-0.75000000	0	0	-0.75000000	0	0
2	-0.75000000	0	0	-0.75000000	0	0
3	-0.25000000	0	0	-0.25000000	0	0
4	-0.25000000	0	0	-0.25000000	0	0
5	-0.35355339	0	0	-0.35355339	0	0
6	-0.50000000	0	0	-0.50000000	0	0
7	-0.50000000	0	0	-0.50000000	0	0
8	0.35355339	0	0	0.35355339	0	0
9	0.00000000	0	0	0.00000000	0	0
10	0.00000000	0	0	0.00000000	0	0
11	-0.00000000	0	0	-0.00000000	0	0
12	0.35355339	0	0	0.35355339	0	0
13	-0.35355339	0	0	-0.35355339	0	0

Table 4. Axial force diagram of each rod when P is 100KN

Rod end 1				Rod end 2		
Unitary code	Axial force	Shearing force	Bending moment	Axial force	Shearing force	Bending moment
1	-75.0000000	0	0	-75.0000000	0	0
2	-75.0000000	0	0	-75.0000000	0	0
3	-25.0000000	0	0	-25.0000000	0	0
4	-25.0000000	0	0	-25.0000000	0	0
5	-35.3553390	0	0	-35.3553390	0	0
6	-50.0000000	0	0	-50.0000000	0	0
7	-50.0000000	0	0	-50.0000000	0	0
8	35.3553390	0	0	35.3553390	0	0
9	0.00000000	0	0	0.00000000	0	0
10	0.00000000	0	0	0.00000000	0	0
11	0.00000000	0	0	0.00000000	0	0
12	35.3553390	0	0	35.3553390	0	0
13	-35.3553390	0	0	-35.3553390	0	0

The above data is multiplied by the virtual work principle to obtain the nodal 3 processing theory displacement formula:

$$\Delta = 0.01214 + \frac{93.75}{EA} \tag{3}$$

DOI: 10.54254/2755-2721/91/20241072

3.5. *Calculate the likelihood function and output the updated results*

The researcher integrated the above-mentioned data in Excel and updated it using Bayesian principles.

Table 5. Partial diagram of the update process

prior belief	Δ	Likelihood	Prior	likelihood*Prior	Post
0.9	0.0131817	0.6571716	0.925926	0.608492268	0.8328379
0.92	0.013159	0.6752955	0.925926	0.625273589	0.8558064
0.94	0.0131373	0.6917853	0.925926	0.640541954	0.876704
0.96	0.0131166	0.7067177	0.925926	0.654368269	0.895628
0.98	0.0130966	0.7201739	0.925926	0.666827712	0.9126811
1	0.0130775	0.7322375	0.925926	0.677997722	0.9279694
1.02	0.0130591	0.7429929	0.925926	0.687956397	0.9415998
1.04	0.0130414	0.7525237	0.925926	0.696781237	0.9536783
1.06	0.0130244	0.760912	0.925926	0.704548189	0.9643088

In Table 5, prior belief is the uniform distribution of the stiffness of element 3; Δ represents the theoretical displacement value of node 3 calculated by the principle of virtual work under the corresponding stiffness of element 3; likelihood is the likelihood function, that is P(A ∣ B), in the Bayesian formula, the difference between the theoretical displacement value and the true displacement value x=Δ-Δ_r, and the standard deviation σ=0.5 is substituted into the normal distribution error formula:

$$f_e(x) = \frac{1}{\sqrt{2\pi * \sigma}} e^{-\frac{1}{2}(\frac{x}{\sigma})^2} \tag{4}$$

The formula for calculating the likelihood function is:

$$L(Y|X) = \frac{1}{\sqrt{2\pi \times 0.5}} \times e^{\left(-\frac{1}{2}\times\left(\frac{12.14+\frac{93750}{X\times10^5}-12.87}{0.5}\right)^2\right)} \tag{5}$$

In the actual calculation, since the prior distribution is a uniform distribution ranging from 0.9 to 1.92, the probability of each value is:

$$P(X) = \frac{1}{1.92 - 1.91} \tag{6}$$

Normalize it and then calculate the posterior distribution.

Using the Bayesian formula, the above calculation results are used to calculate the posterior information under different stiffness distributions. The researchers plot the prior distribution and the updated results of the structure in the statistical charts shown in Figure 2 and Figure 3 , which can more intuitively show the effect of the Bayesian updating method on updating the structural damage information:

DOI: 10.54254/2755-2721/91/20241072

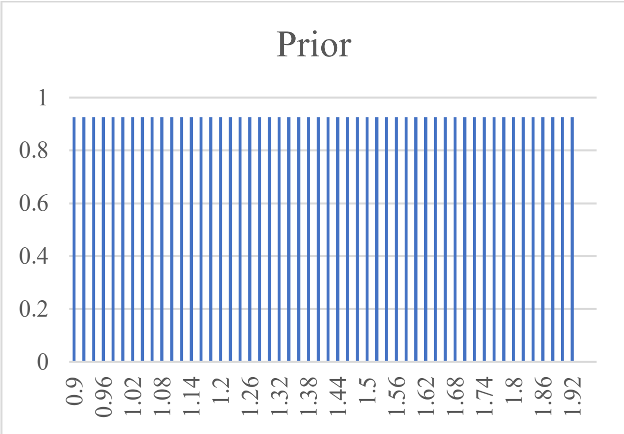

Figure 2. Prior probability distribution (uniform distribution) for static structural bars

Figure 2 shows the prior probability of a uniform distribution, which means that the probability of each possible value is equal when there is no observation data. The probability of each X value is:

$$P(X) = \frac{1}{1.92-0.91} \tag{7}$$

This means that the probability of each value is equal within the range of all possible initial stiffness values, and this uniform distribution assumption provides the basis for subsequent Bayesian updates.

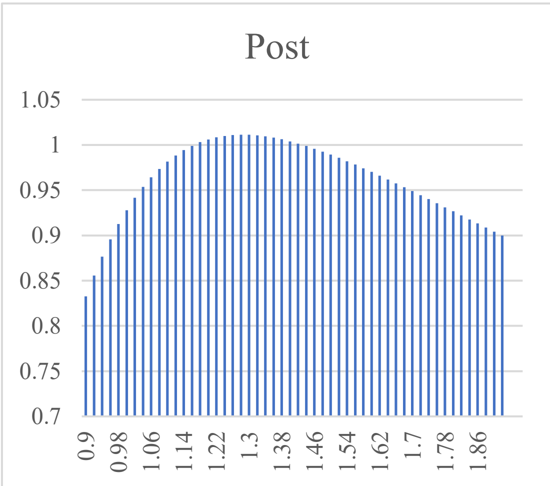

Figure 3. Posterior probability distributions for static structural bars

Figure 4 shows the posterior distribution (the likelihood function y = 0.5 mm has been calculated from the structural solver), which shows how the probability of each possible value changes under the influence of the observed data. The Bayesian update method dynamically adjusts the probability of each possible value by combining the prior distribution and the likelihood function of the observed data.

$$\text{Posterior} = \frac{P(X \mid Y)}{\sum P(X \mid Y)} \tag{8}$$

As can be seen from the figure, the posterior distribution has changed significantly from the prior distribution. In particular, the probability in the middle section (between 1.14 and 1.54) has increased significantly, while the probability at the two ends has decreased relatively. This shows that the initial stiffness value in the middle section is more likely to reflect the actual situation under the influence of the observed data. The Bayesian update makes the posterior distribution more reflective of the damage in the actual project by introducing the observed data into the calculation of the prior distribution.

In the figure on the right, the peak of the posterior probability density function appears around 1.34, indicating that the probability of an initial stiffness of 1.34 is highest after the observation data is incorporated. Through this redistribution of probability, the researchers can more accurately identify and assess possible damage in the truss structure.

The posterior distribution clearly shows the influence of the observation data on the probability distribution. The results show that the Bayesian updating method is highly effective and reliable in structural health monitoring. This not only verifies the theoretical feasibility of the method, but also provides a solid foundation for practical engineering applications.

4. Test 2: Monte Carlo sampling calculation of the failure probability of a statically determinate two-force beam

In order to explore the predictive effect of the Bayesian updating method on structural damage, this study established a static two-force beam model after clarifying the updating process in Experiment 1, and used the Monte Carlo sampling method to calculate its failure probability. To this end, the researchers set a series of conditions:

The load P (KN) conforms to the extreme value I-type distribution (α=0.3, u=20);

When the variables conform to the extreme value I-type distribution, the probability formula is satisfied:

$$F_X(x) = \exp\left[-e^{-\alpha(x-\mu)}\right] \tag{9}$$

$$f_X(x) = \alpha \exp\left[-\alpha(x-\mu) - e^{-\alpha(x-\mu)}\right] \tag{10}$$

The material strength (MPa) conforms to a lognormal distribution (λ=3.8, ξ=0.3);

When the variable conforms to a lognormal distribution, the probability formula is satisfied:

$$f(x) = \frac{1}{x\sigma\sqrt{2\pi}} e^{-\frac{(lnx-\mu)^2}{2\sigma^2}} \tag{11}$$

The cross-sectional areas A1 (15 cm2 to 20 cm2) and A2 (10 cm2 to 15 cm2) are uniformly distributed.

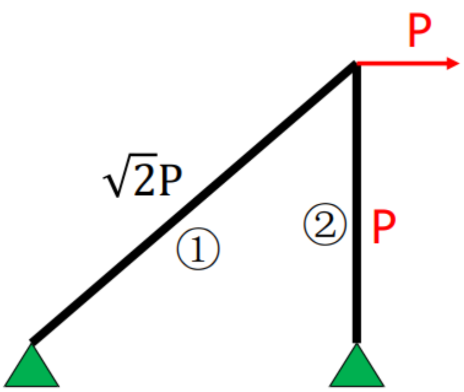

Figure 4. Static two-force rod model diagram

This model (Figure 4) has a strong randomness. The load, material strength, and cross-sectional area are randomly generated parameters based on known a priori information. As long as the stress on one member is greater than its material strength, the structure is considered to have failed. The approximate failure probability can be simulated by Monte Carlo sampling.

Using Excel, four columns of random numbers ranging from 0 to 1 are generated, with 11,000 rows each. According to the distribution types of load P, cross-sectional area A1 and A2, and material strength, the corresponding codes are written according to the formulas listed above, and applied to the four columns of random numbers to create 11,000 random values for the four indicators. It is determined whether the structure fails by comparing the relationship between the stress on the two members and the material strength. After 11,000 samples, the study gets the results shown in Table 6 and Table 7. Table 6 only selected a small portion of the 11000 data points, while Table 7 presents the calculation results of failure probability:

Table 6. Results of big data sampling (partial)

r1	P	r2	A1	r3	A2	r4		Fy	P/ √2/A1(Mpa)	P/A2(Mpa)	Fail 1?	Fail 2?
0.398	20.272	0.0926	15.463	0.245	11.224	0.148	-1.04	32.682	9.27	18.062	0	0
0.072	16.782	0.3647	16.823	0.962	14.81	0.026	-1.95	24.928	7.054	11.331	0	0
0.157	17.945	0.9772	19.886	0.302	11.51	0.94	1.553	71.223	6.381	15.59	0	0
0.2	18.41	0.1859	15.93	0.682	13.41	0.665	0.427	50.812	8.172	13.729	0	0
0.794	24.885	0.215	16.075	0.518	12.589	0.93	1.477	69.617	10.95	19.768	0	0
0.479	21.024	0.2237	16.119	0.572	12.862	0.447	-0.13	42.958	9.223	16.346	0	0
0.261	19.014	0.9532	19.766	0.843	14.214	0.022	-2.02	24.404	6.802	13.377	0	0
0.177	18.171	0.7023	18.511	0.881	14.403	0.938	1.535	70.84	6.941	12.616	0	0

Table 7. Results of big data sampling

total failure numbers	59
failure probability	0.005363636

According to the calculation results, we used the Monte Carlo sampling method to sample 11,000 times for this statically determinate two-force beam. The result was that the number of failures of member 1 was 1, the number of failures of member 2 was 58, and the total number of failures was 59. Therefore, the failure probability of this structure was 59/11,000, or 0.536%. This experiment shows that with certain prior information, the failure probability and damage location of the structure can be estimated using Monte Carlo sampling, thereby more accurately identifying and locating structural damage and greatly improving production efficiency.

5. Conclusion

This study explores the operational method of using Bayesian methods to update infrastructure information. During the study, SMsolver was used for modeling and Excel's probability statistics function was used to process the data. First, a truss model with possible damage was simulated, including the physical quantities of the material properties of the node elements and the stiffness of the elements,

DOI: 10.54254/2755-2721/91/20241072

as well as the probability distribution of the stiffness of the damaged members. SM Solver then performs the loading simulation for the most unfavorable loads to explore the loading scenarios that are most likely to result in damage to the members. Then, the internal forces and displacements under the most unfavorable load are obtained using the virtual work principle, and the posterior probability of stiffness corresponding to all stiffness possibilities is calculated using the Bayesian theorem to complete the update of the damaged member information.

This study established a statically determinate two-force beam model and used the Monte Carlo sampling method to explore the effectiveness of the Bayesian updating method in structural damage prediction with known a priori information. The experimental results show that the structure's failure probability and damage location can be estimated more accurately by random sampling of the load, material strength and cross-sectional area. This result shows that the Monte Carlo sampling method can be effectively applied to the estimation of the failure probability of the structure, which has important application value in practical engineering. It can improve production efficiency and ensure the structure's safety and reliability through accurate damage identification and location. This approach provides an effective technical tool for structural health monitoring and maintenance.

The research findings show that the Bayesian updating method can significantly improve the accuracy of structural damage assessment. Specifically, by dynamically correcting and improving the assessment results of the structural health status with the latest inspection data, the accuracy and reliability of the inspection can be improved, especially in dynamic systems. In addition, the Bayesian updating method can also be used to build risk assessment models to dynamically assess the risk level of structures and provide scientific decision support for managers. The study also shows that the use of Monte Carlo sampling in combination with the Bayesian updating method can more effectively calculate the probability of structural failure, providing a more efficient method for structural damage prediction.

In today's solid mechanics research, damage is mainly dealt with at the material point level, and in the constitutive law, it is formulated as a boundary value problem in continuum damage mechanics. On the other hand, damage to a specific structure is mainly observed at the structural level. Previously used detection methods for assessing the condition of structures or individual components have been widely used. In general, these methods are only used for qualitative state description rather than quantitative description. In summary, Bayesian updating combined with modeling software such as SMsolver can provide a solid theoretical and technical basis for developing the next generation of intelligent structural health monitoring systems, enabling real-time monitoring and dynamic assessment of infrastructure. By continuously adjusting and improving model parameters through Bayesian updating, the structural health status can be dynamically reflected, supporting scientific decision-making and providing a strong guarantee for the long-term safe operation of infrastructure. This research not only has important theoretical significance, but also provides practical solutions for engineering practice.

Authors Contribution

All the authors contributed equally and their names were listed in alphabetical order.

References

[1] Wang C S Hao L Fu B N 2012 Fatigue Reliability Updating Evaluation of Existing Steel Bridges Journal of Bridge Engineering 17(6) 955-965
[2] Katafygiotis L S Beck J L 1998 Updating models and their uncertainties II: Model identifiability Journal of Engineering Mechanics 124(4) 463-467
[3] Ji L Li Ping D Ji Ming L Journal of Shanghai Jiao Tong University 1-17[2024-06-18] https://doi.org/10.16183/j.cnki.jsjtu.2023.584
[4] Groen Frank J and E L 2003 Droguett Bayesian estimation of the variability of reliability measures Annual Reliability and Maintainability Symposium IEEE 2003
[5] Liao M Renaud G BombardieR Y 2020 Airframe digital twin technology adaptability assessment and technology demonstration Engineering Fracture Mechanics 225 106793

DOI: 10.54254/2755-2721/91/20241072

[6] Behmanesh I Moaveni B 2014 Bayesian FE model updating in the presence of modeling errors[C] Model Validation and Uncertainty Quantification Volume 3 Cham Springer International Publishing 119-133

[7] Press 2002 Mathematical Dictionary Volume 4 Beijing China Science and Technology 124(4) 463-467

[8] Yuan S 2023 Standardization by the public (20) 63-65

[9] Targoutzidis Antonis 2012 A Monte Carlo simulation for the assessment of Bayesian updating in dynamic systems Reliability Engineering & System Safety 100 125-132

[10] Xiao X Wang Z Y Li Q W 2022 Engineering Mechanics 39(S1) pp 336-341

Proceedings of the 2nd International Conference on Functional Materials and Civil Engineering
DOI: 10.54254/2755-2721/91/20241070

A novel solar-assisted air source heat pump system for urban renewal: Experimental test and numerical simulation

Michael Gan

Dulwich College Shanghai Pudong, Shanghai, China

michael.gan0907@hotmail.com

Abstract. Old residential communities require novel heating solutions to meet heating demands sustainably. In Southern China, current heating systems in old communities have high energy costs and lack sustainability. A potential solution, air source heat pumps (ASHP), have evaporators susceptible to frost accumulation and poor heating performance at low ambient temperatures. This study proposes a hybrid design that uses additional solar thermal energy to improve energy gains from the air source; the innovative serial coupling design increases the air-source temperature by engineering the evaporator of the ASHP as the load-side of the heat exchanger. The novel hybrid design aims to be efficient, cost-effective, and sustainable, satisfying urban redevelopment needs. A prototype of the novel hybrid solar-assisted ASHP system was constructed; various performance parameters were evaluated, and system operation in extreme climates was simulated in TRNSYS. Results indicated that the novel hybrid system had significantly superior heating performance, delivering a 70.1% improvement in heating rate compared to single-source ASHP under lower ambient temperatures (13°C). The novel hybrid system also had a high COP value between 5.7 and 6.3, significantly exceeding values of 2.3-3.5 for most air-conditioning units. It demonstrates consistent performance in all simulated climates. It is estimated that the novel hybrid system can save 1000 RMB in annual energy costs for an average Shanghai family and reduce Shanghai's CO_2 emissions by 4.7 million tons. The novel system addressed limitations of ASHP, optimizing performance while maintaining sustainability, offering a promising solution for urban renewal projects in China.

Keywords: air source heat pump, solar energy, coupling, urban renewal, environmental sustainability.

1. Introduction

Heating poses both challenges and opportunities for urban areas in relation to social and environmental sustainability. Under China's space heating policy, cities in Southern China do not have access to central heating. In the absence of central heating, the comfort of indoor environments in old neighborhoods awaiting urban renewal is poor. Residents are forced to rely on local electric heating, which is usually expensive, inadequate, and inefficient [1]. A recent survey by the author, of thirty residents randomly sampled from old Shikumen communities and public housing estates in downtown Shanghai indicated that there is a notable heating demand in Shanghai from November to the coming February. The use of environmentally sustainable heating methods is also found to be very limited (Figure 1). Major issues with current heating methods, included high energy costs, air-conditioning being too dry, and poor heating performance from appliances (Figure 2).

DOI: 10.54254/2755-2721/91/20241070

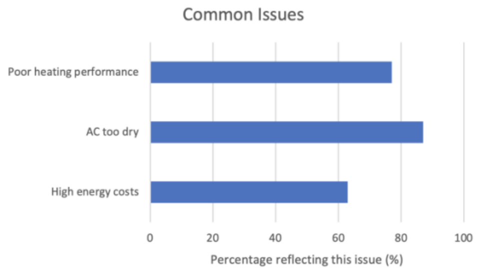

Figure 1. Heating methods used by Shanghai residents (results from the survey)

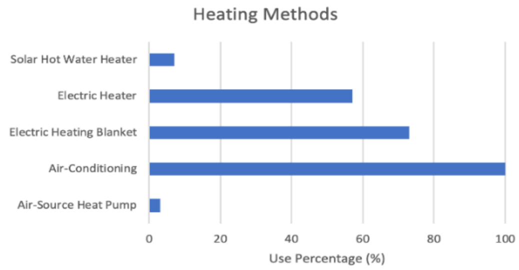

Figure 2. Common issues with heating methods reflected by residents (results from the survey)

Nie et al. [2] showed that the average indoor temperature in Shanghai during winter is around 17 °C, below the advised range of 20-21 °C for comfort; 91% of residents surveyed in their study often or occasionally felt cold indoors during winter.

The built environment is responsible for 37% of global CO_2 emissions; heating is a major source of energy consumption [3]. This has led the UN Environmental Program (UNEP) to recommend the development of "sustainable, zero-carbon and resilient" structures that are conscientious of their environmental footprint [4]. Transforming energy systems in urban areas has become crucial to strategies seeking to reduce carbon emissions in many countries. Heat pumps have been identified as a promising candidate in this sustainable revolution: they are 3-5 times more efficient than gas boilers and can offset 500 million tons of CO_2 emissions by 2030 [5]. Air source heat pumps (ASHP) that extract heat from the external air have been recognized for their low energy consumption and ease of installation in urban areas, making them attractive replacements for fossil-fuel based systems [6]. Heating takes up 68% of the energy use of an average Chinese household, so popularizing ASHP installation in large Chinese cities has the potential to improve efficiency and drastically reduce CO_2 emissions [7].

However, current ASHP systems face obstacles in becoming widely used. Being single-source heat pumps, ASHP lack versatility and stability. Cai et al. [8] suggested that a fundamental contradiction of ASHP is that their heating capacity is positively correlated to ambient temperature. This means their performance is suboptimal when heating demand is greatest during winter. Auxiliary heating is often required to meet heating demands, offsetting the environmental benefits of ASHP. Furthermore, Song et al. [9] noted that the outdoor coil of ASHP is susceptible to frost deposition in winter. Frost reduces the COP (coefficient of performance) as it obstructs airflow and increases thermal resistance between the evaporator and the air. It can also make the operation of the heat pump system unreliable and intermittent, rendering it unsuitable for domestic household usage [10]. This issue is especially pertinent in Shanghai, which is located in the heavy-frost region for 60% of its heating period [11].

Solar water heaters are commonly used in Southern China for heat supply. Despite being clean and efficient, they are also constrained by being single-sourced [12]. Jouhri and Dakar [13] noted that the efficacy of solar water heaters is restricted by the intermittent and unreliable nature of solar irradiation and heating demand. For instance, in Shanghai, irradiation is highest in May and lowest in December and January when heating demands are most pronounced [14].

This study aims to address the limitations of the above single-source systems by combining them in a solar thermal ASHP (ST-ASHP) that derives energy from two sustainable sources – air and solar irradiation. A serial indirect expansion design (IDX-ST-ASHP) is adopted where the solar collector's cycle is separated from the ASHP's cycle, and the refrigerant cycle of the solar collector interacts with that of the ASHP through a heat exchanger. Liu et al. [15] demonstrated that IDX-ST-ASHP exhibit enhanced performance in low-temperature conditions as the use of a secondary fluid optimizes heat transfer and reduces the risk of the refrigerant freezing or leaking.

Several experimental and modeling studies have been conducted on different IDX-ST-ASHP; however, most focus on parallel configurations where the solar thermal collector and ASHP are separately linked to the heat storage tank. Yerdesh et al. [16] found the solar collector refrigerant cycle

DOI: 10.54254/2755-2721/91/20241070

in parallel systems ineffective during winter, as the solar irradiation of 500w/m^2 did not allow the solar collector heat transmitter to heat the storage tank to sufficiently high temperatures. Hence, a major weakness of the parallel IDX-ST-ASHP systems is that they require a certain level of solar irradiation to produce a heating effect; when solar irradiation levels are low, the performance of the entire hybrid system is impacted. Furthermore, parallel configurations cannot increase air source temperature through coupling, so the issues of poor heating performance in low ambient temperatures and frost accumulation on evaporator coils facing ASHP are unaddressed.

This study proposes a novel hybrid IDX-ST-ASHP that adopts a serial configuration. In the novel serial configuration, coupling occurs in the heat exchanger. The source-side of the heat exchanger is the solar thermal collector, and the load-side is the ASHP evaporator. This allows energy from the solar thermal collector to improve the temperature of the ASHP air source. It is hypothesized that the hybrid design can deliver better heating performance over conventional single-source ASHP due to the synergistic effects of the two clean energy sources. The novel coupling design for the hybrid sources is anticipated to increase energy gains from the air source and reduce the risk of frost accumulation on the evaporator.

This study focuses on providing a compact, versatile, user-friendly heating solution that can be implemented in old buildings during regeneration. The large and complex systems tested by most current studies are incompatible with the requirements of urban renewal. For one, many historic structures enjoy protection status, so construction projects that are obtrusive to the building may be deemed inappropriate for conservation and thus not allowed. Even in non-protected structures, installing conventional heaters may be impossible due to structural constraints and budget overruns. The adaptable design of the novel hybrid system strives to optimize user experience, heating efficiency, and environmental sustainability, addressing the unique demands of the city’s elderly population as well as site constraints imposed by urban renewal.

2. Methods

2.1. Prototype Design and Construction

The basic design of the novel hybrid ST-ASHP system is shown in the diagram below (Figure 3). The main innovation of this prototype lies in the heat exchanger; the load-side of the heat exchanger simultaneously functions as the evaporator of the ASHP. The coupling design allows the solar thermal collector to increase the temperature of the air source, giving the ASHP better performance.

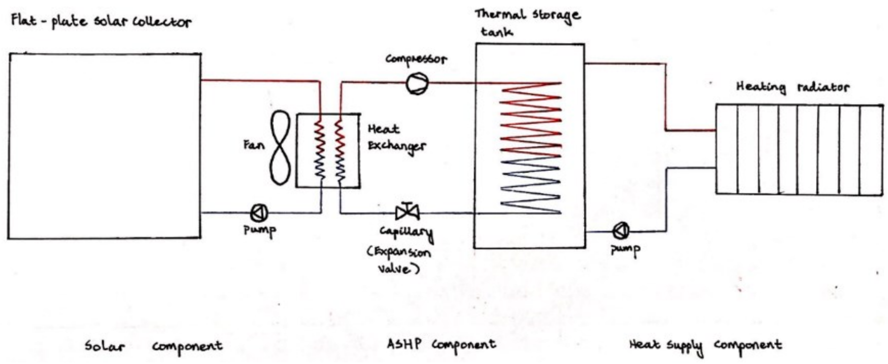

Figure 3. Schematic diagram of the novel solar-assisted ASHP (original sketch by author)

A prototype was constructed based on the above design (Figure 3). The novel hybrid system consists of three main parts: a solar thermal collector cycle which connects the solar thermal collector with the source-side of the heat exchanger; the ASHP component which contains the load-side of the heat exchanger (simultaneously posing as an evaporator), the compressor, and the condenser unit in the heat storage tank; finally, the radiator-heat storage tank cycle which connects the heat storage tank to the radiator (Figure 4 and Figure 5).

The characteristics of different components were considered in the design of the novel hybrid system. A flat-plate solar thermal collector was selected as it is cost-effective and can withstand high temperatures during the summer [17]. A fin-type heat exchanger with a counter-flow design was selected to maximize heat transfer efficiency. Counter flow heat exchangers have the inlet of the hot-side fluid corresponding with the outlet of the cold-side fluid. This allows the cold-side fluid to reach maximum temperature as it exits the heat exchanger, optimizing the efficiency of heat transfer. The tank acts as a thermal storage unit that mitigates the impact of fluctuating solar radiation throughout the day [18]. Additionally, it improves the hydronic flexibility of the heating system.

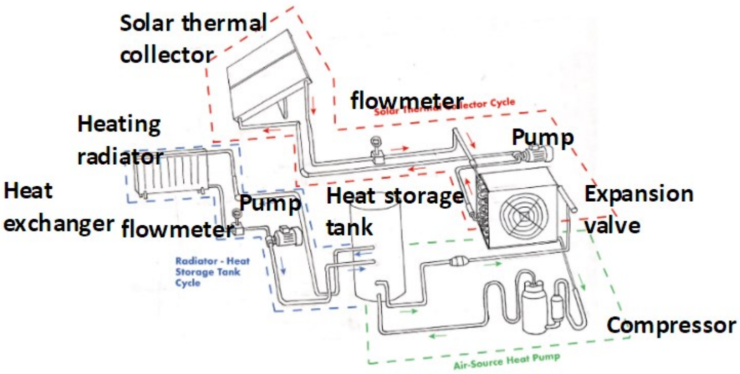

Figure 4. A simplified diagram by the author showing main components and the cycles and directions of flow in the novel hybrid ST-ASHP system

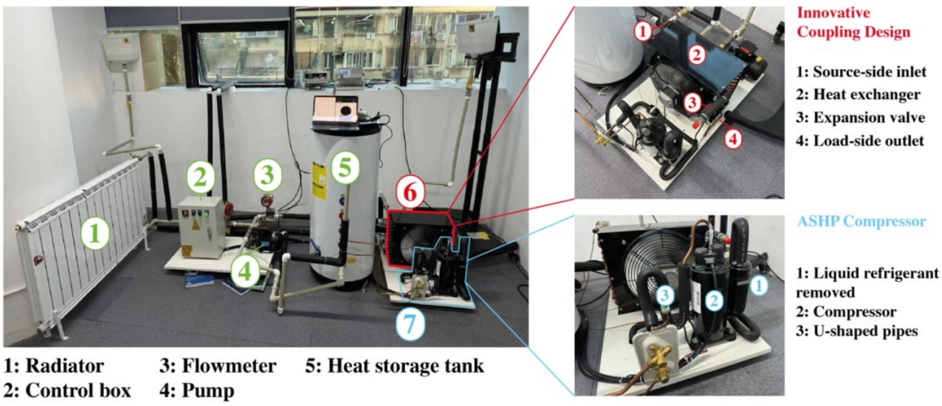

Figure 5. The indoor part of the prototype system, with the ASHP unit and the radiator-heat storage tank cycle. The solar collector is located on the balcony outside (photos by author)

2.2. Experimental Procedures

Experiments were conducted on the novel hybrid system prototype to evaluate its performance under different ambient temperatures and compare its performance in hybrid and non-hybrid modes. The procedures for these experiments are shown in the flowchart below (Figure 6).

DOI: 10.54254/2755-2721/91/20241070

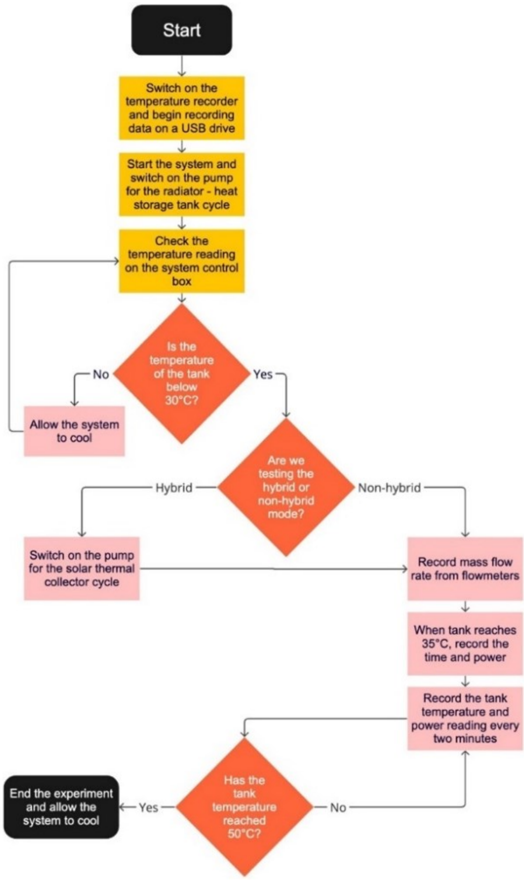

Figure 6. Flowchart showing the methodology and experiment procedures

2.3. *Monitoring Points and Calculation of Key Parameters*

Monitoring points in the prototype system was shown in Figure 7.

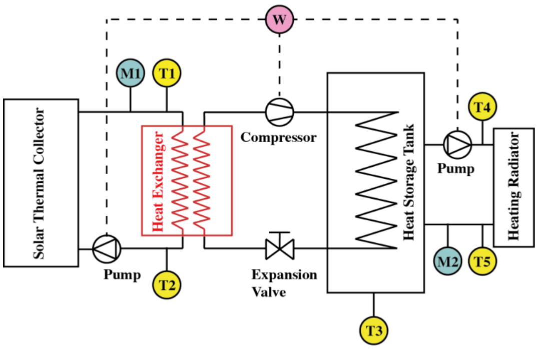

Figure 7. Monitoring points in the prototype system. Yellow indicates temperature recording points, turquoise indicates flowmeters, and pink indicates the power meter

Table 1 shows the measuring equipment used. Raw data from the multi-channel temperature recorder is recorded on a USB drive. This is combined with manually recorded power and tank temperature readings at intervals of two minutes. Initially, all the data collected is compiled into an Excel spreadsheet. Data is selected for the period of time as the tank temperature increases from 35 °C to 50 °C. This temperature range was determined for safety reasons; 50°C is also within the recommended temperature range for water used in a heating radiator. Thus, the prototype experiment is able to simulate the heating demands of residents, allowing an evaluation of the novel hybrid system's social viability.

DOI: 10.54254/2755-2721/91/20241070

Table 1. Measuring equipment used

Component type	Notes
Multi-Channel Temperature Recorder	Eight available recording channels; temperature data from the recorder can be stored on a USB drive
Digital Power Meter	Used to measure the instantaneous power of the system
Flowmeter	Used to measure the mass flow rate of water in the solar thermal collector cycle and the radiator cycle

Heating rate was calculated by plotting the tank temperature (T_3) against time and modeling a linear line of best fit. The gradient of the linear model gives the heating rate.

The COP of the system is also evaluated by calculating both the instantaneous and average COP of the system. COP measures the ratio of power output by a system to power input to a system. In this study, the COP value is referenced as an important benchmark for environmental sustainability. The method for COP calculation is detailed below (refer to Table 2 for nomenclature used in the equations).

Solar thermal collector energy output (per second):

$$Q_{solar} = m_1 c \left(T_1 - T_2\right) \tag{1}$$

Radiator energy output (per second)

$$Q_{rad} = m_2 c \left(T_4 - T_5\right) \tag{2}$$

Instantaneous COP:

$$\mathrm{COP_i} = \frac{Q_{rad}}{W} \tag{3}$$

Average COP:

$$\mathrm{COP_a} = \frac{\int Q_{rad}\, dt}{\int W\, dt} \tag{4}$$

Table 2. Nomenclature

Variable		Units
Q_{solar}	Power supplied by the solar thermal collector	W
Q_{rad}	Power of the radiator	W
$\mathrm{COP_i}$	Instantaneous COP	
$\mathrm{COP_a}$	Average COP	
m_1	Mass flow rate of the solar thermal collector cycle	kg/s
m_2	Mass flow rate of the radiator-heat storage tank cycle	kg/s
T_1	Temperature of the heat exchanger source-side inlet	°C
T_2	Temperature of the heat exchanger source-side outlet	°C
T_3	Temperature of the heat storage tank	°C
T_4	Temperature of the radiator inlet	°C
T_5	Temperature of the radiator outlet	°C
c	Specific heat capacity	J/kg°C
W	Power consumption of the system	W

The energy supplied by the solar thermal collector is calculated using temperature data from the outlet and inlet of the flat plate collector; from this, the contribution of the solar thermal collector cycle to the novel hybrid system can be found. Three sets of data were collected for different ambient temperatures. Throughout the process, comparisons between the non-hybrid and hybrid working modes of the system were measured to validate the efficacy and potential of the novel hybrid system. The hybrid mode involves all parts of the system, whereas the non-hybrid mode excludes the solar thermal collector cycle and reflects the performance of a single-source ASHP. Only sets where the hybrid and non-hybrid modes were tested under similar ambient temperatures were used to ensure the validity of the comparison.

2.4. TRNSYS Simulations

Two models were built in TRNSYS to simulate the hybrid and non-hybrid working modes of the heating systems (Figure 8, Figure 9). Simulations were run on the two systems constructed using climatic data from December 1 to December 31 for a total of 8736 hours. This time interval was selected as it roughly coincides with the experimental tests on the prototype system.

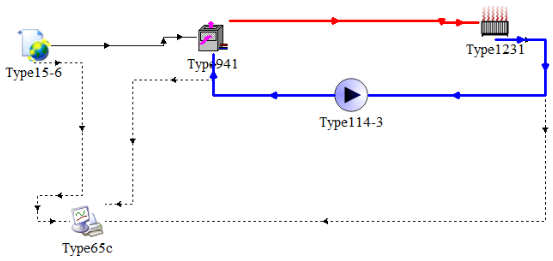

Figure 8. The non-hybrid system built for the TRNSYS simulation

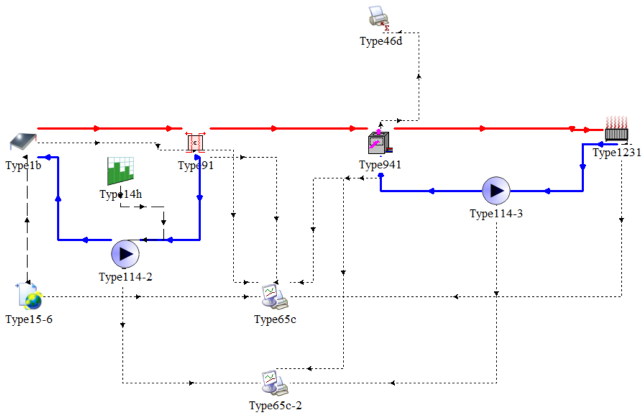

Figure 9. The hybrid system built for the TRNSYS simulation

For the purposes of the simulation, the system was simplified by removing the heat storage tank. Evaluating the inlet and outlet temperature of the radiator was prioritized so the intermediate stage of the heat storage tank could be removed without affecting the metrics investigated. A control function to the solar thermal collector cycle was added to regulate the system; under the forcing function, the solar thermal collector operates between 08:00 and 18:00 daily, ceasing to work during the night. This simulates anticipated usage patterns where the hybrid system operates during the day, storing the heat generated in the tank to be used during the night.

The novel coupling design was simulated using a heat exchanger that connects the temperature of the source-side liquid to the temperature of the inlet air to the evaporator of the ASHP. Realistically, the heat transfer at this stage would be much smaller than a direct exchange, so the heat exchanger effectiveness was adjusted to 0.1 to factor in the loss of thermal energy in our prototype.

DOI: 10.54254/2755-2721/91/20241070

3. Results

3.1. Overview of Experimental Data

Three sets of data were collected at different ambient temperatures. Each set includes data collected from testing the system in hybrid and non-hybrid modes at a particular ambient temperature.

Table 3. Overview of experiment results from the different sets collected

Set	Mode	Ambient Temperature (°C)	Rate of Temperature Increase (°C/s)	Average COP
1	Non-hybrid	13	0.001189	7.99
	Hybrid	13	0.002022	6.18
2	Non-hybrid	17	0.002878	7.11
	Hybrid	17	0.003615	6.32
3	Non-hybrid	20	0.003627	7.19
	Hybrid	20	0.004273	5.73

3.2. Heating Rate

The time taken for the heat storage tank temperature to increase from 35°C to 50°C and the rates of temperature increase (°C/s) for the different operating modes and ambient temperatures are given below:

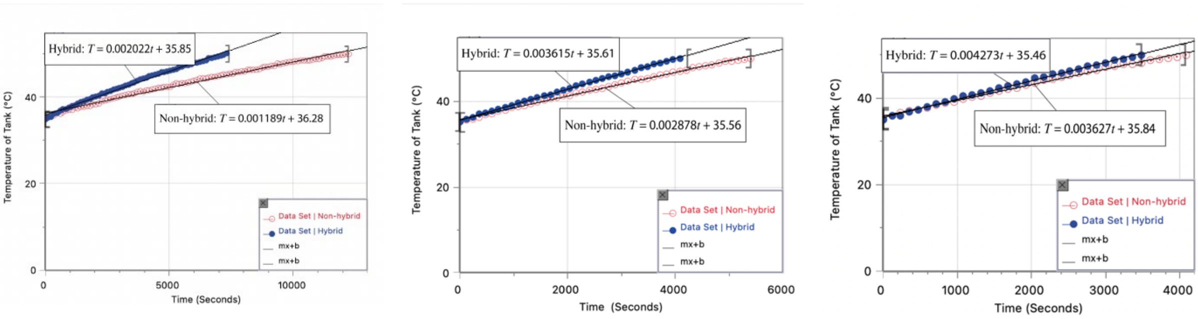

Figure 10. The heating rate achieved by the hybrid and non-hybrid systems at ambient temperatures of A: 13°C; B: 17°C; C: 20°C

At an ambient temperature of 13°C, the system took 7320 seconds in hybrid mode and 12240 seconds in non-hybrid mode for the temperature of the heat storage tank to increase from 35°C to 50°C. When the ambient temperature was 17°C, the system took 4080 seconds in hybrid mode and 5400 seconds in non-hybrid mode; at 20°C, it took 3480 and 4080 seconds respectively (Figure 10).

The corresponding rates of temperature increase were obtained from the gradients of the linear functions; a comparison of these rates is shown below:

As anticipated, as the ambient temperature decreases, the rate at which the system heats the heat storage tank decreases – the temperature of the ASHP's air source is lower, leading to less thermal energy obtained for the ASHP; hence, for the same change in temperature, a longer time is required. However, we notice that the system in hybrid mode can heat the water in the tank from 35°C to 50°C in less time than the system in non-hybrid mode under all ambient temperatures (Figure 11). The percentage improvement in the rate of temperature increase becomes more pronounced as the ambient temperature reduces: at 20°C, the rate was 17.8% higher in hybrid mode, increasing to 25.6% higher at an ambient temperature of 17°C, finally reaching a maximum value at 13°C, the lowest ambient temperature tested, with a significant 70.1% increase (Figure 12).

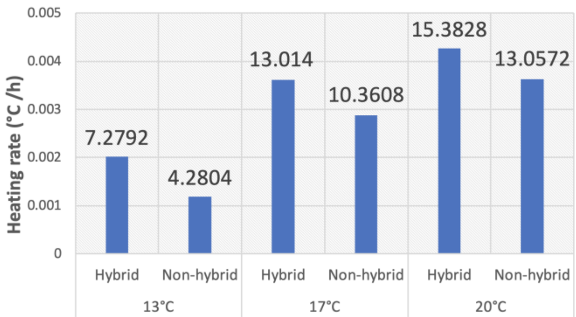

Figure 11. Comparison of the heating rates achieved by the hybrid and non-hybrid systems at different ambient temperatures (°C/h)

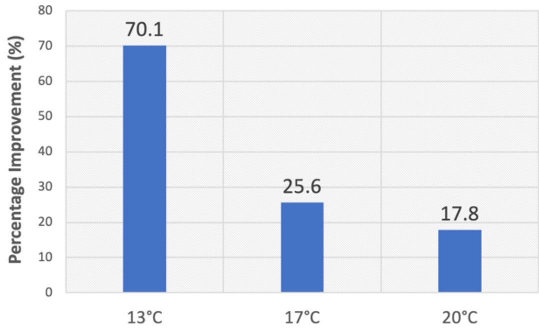

Figure 12. Percentage improvement of the hybrid system's heating rate over non-hybrid at different ambient temperatures

This is illustrated by the notable reduction of heating times at 13°C, where the system in hybrid mode was able to save 4920 seconds (82 minutes) compared to the system in non-hybrid mode. The hybrid system had superior heating performance under all ambient temperatures. These results exemplify the improved performance and efficiency generated by having a second energy source, validating and confirming the advantages of the unique coupling design adopted in the novel hybrid ST-ASHP system.

3.3. Impact of the Solar Thermal Collector

The amount of energy supplied by the solar thermal collector increased with ambient temperature. At 13°C, there were the most fluctuations in the energy supplied by the solar thermal collector per second, with most values ranging between 200J and 300J. At an ambient temperature of 17°C, most values ranged from 300J to 400J. At 20°C, all values were above 400J, with over half falling between 500J and 600J (Figure 13). This confirmed prior observations that the novel hybrid ST-ASHP system heats the heat storage tank more rapidly at higher ambient temperatures, as the solar thermal collector is able to supply more energy to the ASHP by heating the water to a higher temperature.

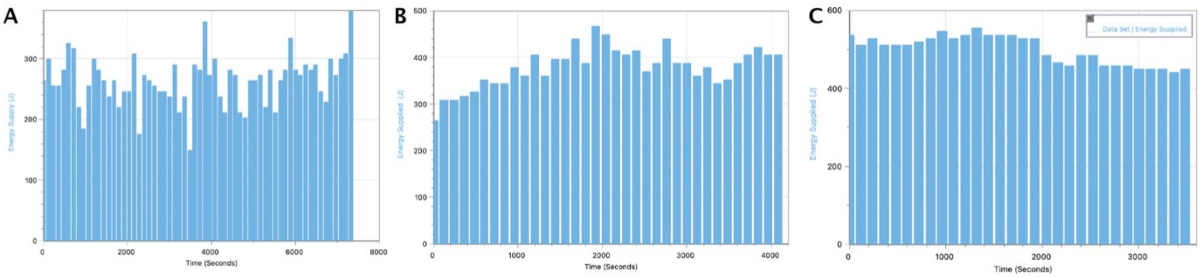

Figure 13. The energy supplied by the solar thermal collector of the hybrid system at ambient temperatures of A: 13°C; B: 17°C; C: 20°C

However, it appeared that the impact of the solar thermal collector is felt most strongly at lower ambient temperatures; although the solar thermal collector supplies less energy at these temperatures, it is responsible for differentiating the performance of the hybrid system from a single-source system by improving the heat gain at the evaporator of the ASHP. Furthermore, this additional thermal energy also serves an important role in reducing the risk of frost accumulation on the ASHP evaporator in the heat exchanger by increasing the surface temperature of the evaporator coils.

3.4. Instantaneous and Average COP of the System

The following graphs show how instantaneous COP varies for systems in non-hybrid and hybrid modes at the three ambient temperatures tested:

The instantaneous COP of the systems appear to exhibit increasing trends over time, illustrated more clearly at higher ambient temperatures. This is because the inlet temperature of the radiator increases more than the room temperature, so heat transfer from the radiator to the room is greater. At each ambient temperature, the instantaneous COP is slightly higher for non-hybrid mode compared to hybrid mode (Figure 14). This is to be expected as the hybrid system involved an additional pump for the solar thermal collector cycle.

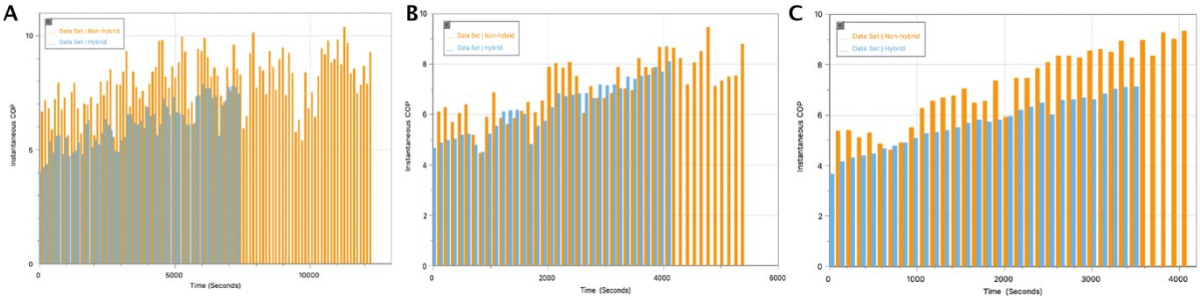

Figure 14. Instantaneous COP of the hybrid (blue) and non-hybrid (orange) systems at ambient temperatures of A: 13°C; B: 17°C; C: 20°C

The average COP values are calculated by taking the integral of power input and power output. The average COP also indicates that the non-hybrid system has a higher COP under all ambient temperatures tested. The average COP does not show a clear trend with ambient temperature; experiment results show that it falls between 5.5 and 6.5 when the system is in hybrid mode and between 7 and 8 when it is in non-hybrid mode (Figure 15). Nonetheless, the hybrid system was still able to achieve a high COP value (twice the 2.3-3.5 range for most air-conditioning units), and its superior heating performance compared to the single-source ASHP compensates for the lower COP value.

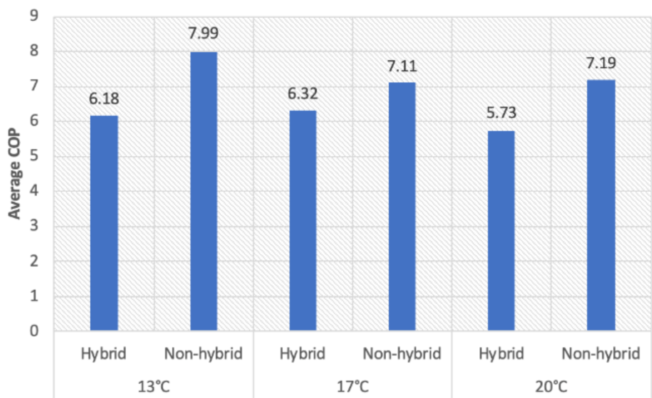

Figure 15. Average COP of the hybrid and non-hybrid systems at different ambient temperatures

3.5. TRNSYS Simulation Results

TRNSYS simulations were developed for the novel ST-ASHP system to evaluate its applicability in a range of climates. These simulations are based on the prototype system explored in section 2.2, with minor adjustments to ensure compatibility with the TRNSYS software. Two models were built in TRNSYS to simulate the hybrid and non-hybrid working modes of the heating system.

Four Chinese cities (Shanghai, Guilin, Beijing, and Shenyang) covering diverse geographical and climatic regions were selected for the simulation study to evaluate the applicability of the novel hybrid ST-ASHP system in a range of environments. Simulation results are given in Figures 16-19. See Table 4 and Table 5 for the keys of the TRNSYS simulation graphs:

DOI: 10.54254/2755-2721/91/20241070

Table 4. Key for all TRNSYS graphs for hybrid systems

Label	Color	Notes
T Ambient	Red	Ambient temperature, from the Meteonorm file for each city
T Source In	Blue	Temperature of the source-side inlet of the heat exchanger
T Source Out	Pink	Temperature of the source-side outlet of the heat exchanger
T Rad In	Orange	Temperature of the inlet of the radiator
T Rad Out	Green	Temperature of the outlet of the radiator

Table 5. Key for all TRNSYS graphs for non-hybrid systems

Label	Color	Notes
T Ambient	Red	Ambient temperature, from the Meteonorm file for each city
T Rad Inlet	Blue	Temperature of the inlet of the radiator
T Rad Outlet	Pink	Temperature of the outlet of the radiator

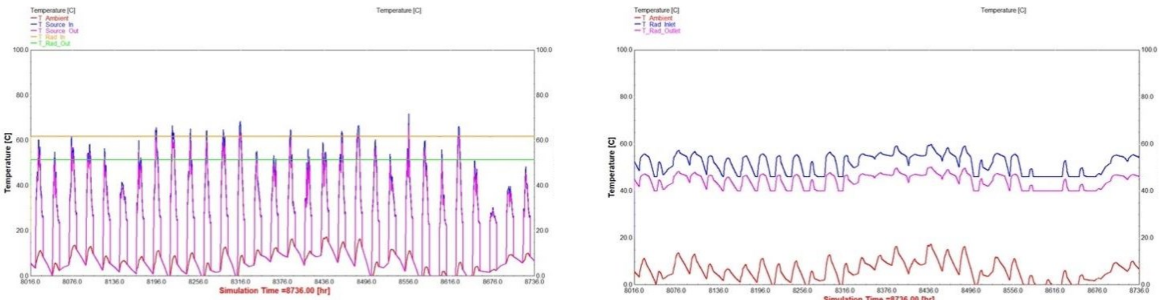

Figure 16. Simulation results of two models in Shanghai (left: hybrid, right: non-hybrid)

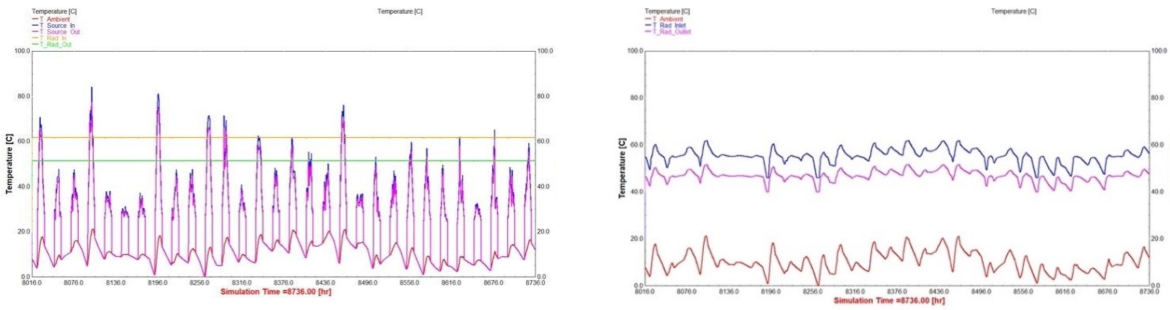

Figure 17. Simulation results of two models in Guilin (left: hybrid, right: non-hybrid)

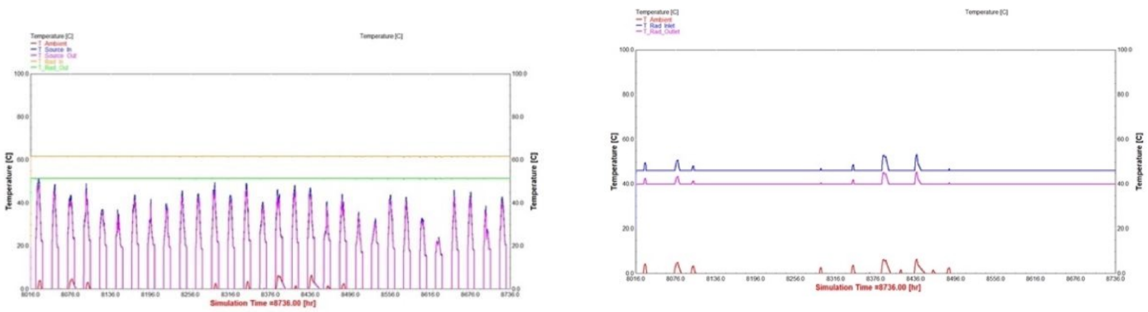

Figure 18. Simulation results of two models in Beijing (left: hybrid, right: non-hybrid)

DOI: 10.54254/2755-2721/91/20241070

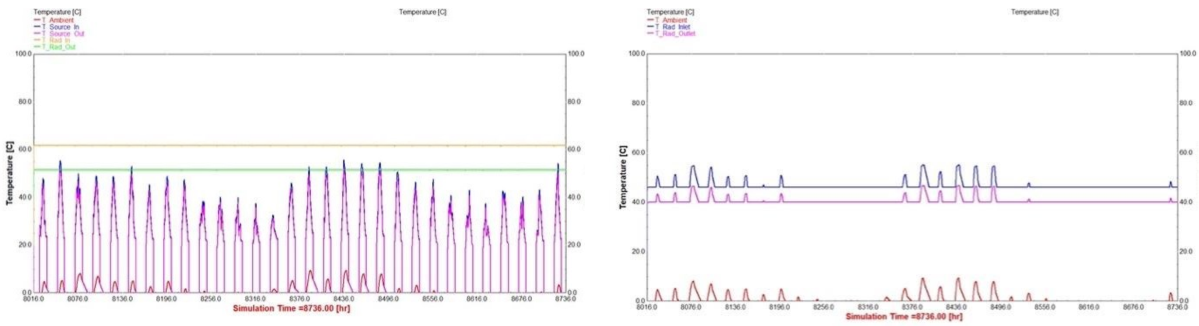

Figure 19. Simulation results of two models in Shenyang (left: hybrid, right: non-hybrid)

The hybrid system performs very consistently in all climatic conditions simulated, maintaining a radiator inlet temperature above 60°C and a radiator outlet temperature above 50°C; a temperature difference of 10°C between the inlet and outlet is sustained throughout. We notice that the temperature of the radiator inlet and outlet for the hybrid systems does not fluctuate over time and is unaffected by changes in the ambient temperature; this holds even in Beijing and Shenyang, where temperatures are sub-zero for significant periods of the simulation (Figure 18 and Figure 19).

In comparison, the temperature of the radiator inlet and outlet for the non-hybrid system fluctuates significantly with ambient temperature. Generally, the simulations above demonstrate that this relationship is positive, with increases in ambient temperature generally leading to higher inlet and outlet temperatures. However, as the changes in inlet temperature are largely mirrored by similar changes in outlet temperature, the temperature difference between the two for non-hybrid systems is still relatively stable between 5°C and 8°C. Shenyang and Beijing, with the lowest ambient temperatures, have the smallest temperature difference of slightly above 5°C, whereas Guilin, with the highest ambient temperature of the four cities simulated, had the greatest temperature difference of around 8°C (Figure 17, Figure 18, and Figure 19). Nonetheless, these are all smaller than the 10°C temperature difference maintained by the hybrid system. A greater temperature difference indicates a greater power output. Hence, the results of the simulation suggest that the hybrid system is able to perform consistently and reliably under a range of climatic conditions, achieve greater power output, and has the potential to be utilized in both Southern and Northern Chinese cities.

4. Discussion

4.1. Theoretical analysis

The experimental test of the prototype and TRNSYS simulations demonstrated that the innovative coupling design of the novel hybrid system optimizes ASHP performance. This is evidenced by the superior heating rate of the novel hybrid system over conventional single-source ASHP at all ambient temperatures tested, with especially pronounced improvements at low ambient temperatures. These results support the hypothesis, as they suggest that the additional solar thermal energy supplied to the air source in the heat exchanger was responsible for the improved heating performance of the novel hybrid system. Furthermore, the high COP values achieved by the novel hybrid system indicates its environmental sustainability.

The novel hybrid system effectively addressed the two major concerns associated with current single-source ASHP. It is able to enhance ASHP performance significantly in low ambient temperatures by virtue of its novel coupling design. The air source temperature is raised by supplementary thermal energy from the solar thermal collector, allowing the ASHP to extract more heat to transfer indoors. Additionally, the surface temperature of the ASHP evaporator on the load-side of the heat exchanger is also increased, reducing the risk of frost accumulation.

Compared to parallel configurations explored in previous studies, the innovative serial configuration adopted in the novel hybrid system effectively addresses the primary concern facing ASHP – low air source temperature. Aside from the versatility hybrid sources offer, this design maximizes the synergistic effects of the two sources by allowing the solar thermal collector to increase the air source temperature for the ASHP. In parallel systems, the ASHP is still negatively impacted by low air source temperature because the supplemental energy from the solar thermal collector is separately linked to the tank and cannot increase the air source temperature of the ASHP.

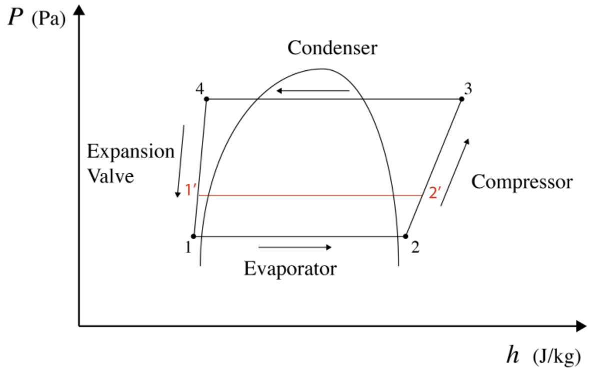

Figure 21. Pressure-enthalpy diagram for the ASHP. 1'-2' represents the evaporating pressure in the hybrid system

Theoretically, the substantial improvements in heating rate can be explained by analyzing a pressure-enthalpy diagram. The additional energy supplied by the solar thermal collector increases the evaporation pressure (Figure 21). This increases the density of the working fluid, meaning for the same rotational speed of the compressor and volumetric flow rate, the mass flow rate increases. Hence, more thermal energy is supplied, and the heating capacity of the ASHP increases. The comparative advantage of the hybrid system increases as the evaporation pressure reduces with ambient temperature; therefore, the increase in evaporation pressure is greater when the hybrid system is used in lower ambient temperatures, making its effects more obvious.

The performance of hybrid and non-hybrid systems could only be compared if they operated under the same ambient temperature to ensure a fair test. However, it was impossible to control the ambient temperature between experiments. Ultimately, multiple sets had to be collected, and those with similar ambient temperatures were selected for comparison. Other variables, like moisture, could not be controlled but may have an impact on the results. These inherent limitations of the experiment were addressed through simulations on TRNSYS that allowed a wide range of environmental factors to be controlled.

4.2. Socio-economic analysis

Estimations were made to evaluate the social impacts of the novel hybrid heat pump. Assuming that a household currently owns two air conditioning units with a 1000 W power rating each, the total energy cost is roughly 488 RMB. Using the 1:2 ratio between the COP of air conditioning units and the novel hybrid heat pump, we find that the novel hybrid heat pump can save 244 RMB per month, amounting to 976 RMB over the four-month heating period determined through the survey research.

Air conditioning units use an average of 1440 kWh of electricity over one heating period; again, as the novel hybrid system is twice as efficient, it only uses 720 kWh over this same period. Each kWh of electricity roughly corresponds to 0.82 kg of CO_2 emissions; hence, each family could reduce their carbon footprint by over 590 kg every winter. For the total of 8 million families in Shanghai, 47 million kg of CO_2 can be saved per year in CO_2 emissions from heating. While these calculations are preliminary and based off assumptions, they indicate the socio-economic viability of the novel hybrid heat pump.

DOI: 10.54254/2755-2721/91/20241070

5. Conclusions

In this study, an innovative hybrid solar-assisted air source heat pump was designed and constructed to address the limitations of singles-source air source heat pumps. The novel system was evaluated through prototype experimentation and numerical simulation. The main conclusions of the research are as follows:

1. The novel hybrid system was found to have superior heating performance compared to traditional non-hybrid air source heat pumps, with especially pronounced advantages in low ambient temperatures. At 13°C, it achieved a heating rate 70.1% higher than the non-hybrid system. This suggests the efficacy of the innovative coupling design that improved thermal energy gains from the air source for the novel hybrid system.
2. The novel hybrid system achieved high average COP ratings between 5.7 and 6.3, significantly higher than the 2.3-3.5 COP ratings for most air conditioning units. Hence, the novel hybrid system demonstrates its potential as a renewable and efficient heat method. Using the ratio between the COP ratings of the novel hybrid system and air conditioning units, rough estimates suggest that the novel hybrid system can save around 1000 RMB in energy costs for an average Shanghai family per year and reduce CO_2 emissions by up to 4.7 million tons if it sees widespread application
3. TRNSYS simulations indicate that the novel hybrid system enjoyed consistently high performance under a variety of ambient temperatures and climatic conditions; this offers a marked improvement over traditional single-source ASHP systems that see fluctuations in performance.

Although the study demonstrates the technological viability of the concept of a novel hybrid solar-assisted ASHP, there are certain limitations in the study that could be addressed in future work:

(1) For safety reasons, the temperature range of the storage tank can only be set to 35-50°C. Although this does not affect the conclusion, in real situation however, considering heat losses or heat efficiency of the entire system, the temperature range can be set to higher levels (for example 35-70 °C) in future research.

4. Second, the selection of the testing equipment and the design of the system is a little bulky at this stage. This is mainly due to local availability, cost, and experimental time pressure. With careful selection of system components, a more compact design can be achieved to improve installation flexibility. The specific installation of the prototype system in urban renewal contexts could be investigated through modelling with Sketchup and AutoCAD; general strategies can be developed for vernacular housing in Shanghai.
5. Future research could focus on further improving the COP of hybrid heating systems like the novel ST-ASHP; in particular, the solar thermal collector of the system may be designed to track the sun, thereby maximizing the thermal energy gains from solar irradiation.

Although further research is needed to optimize the system design, current research demonstrated clearly that the novel hybrid system is an efficient, cost-effective, and sustainable system for urban renewal.

References

[1] Hall, Casey. *Why Shanghai's oldest neighbourhood has to shiver each winter*. (2018, January 4). South China Morning Post. https://www.scmp.com/news/china/society/article/2126825/why-shanghais-oldest-neighbourhood-has-shiver-each-year-through

[2] Nie, Y., Bu, Z., & Yang, J. (2017). Discussion on heating strategies in winter of residential buildings in Shanghai aiming at ultra-low energy target. *Procedia Engineering*, *205*, 3130–3137.

[3] Environment, U. N. (2022, November 9). *2022 Global Status Report for Buildings and Construction*. UNEP - UN Environment Programme. https://www.unep.org/resources/publication/2022-global-status-report-buildings-and-construction

[4] *CO2 emissions from buildings and construction hit new high, leaving sector off track to decarbonize by 2050: UN*. (2022, November 9). UN Environment. http://www.unep.org/news-and-stories/press-release/co2-emissions-buildings-and-construction-hit-new-high-leaving-sector
[5] *Heat Pumps - Energy System*. IEA. https://www.iea.org/energy-system/buildings/heat-pumps
[6] Wang, X., Xia, L., Bales, C., Zhang, X., Copertaro, B., Pan, S., & Wu, J. (2020). A systematic review of recent air source heat pump (ASHP) systems assisted by solar thermal, photovoltaic and photovoltaic/thermal sources. *Renewable Energy*, *146*, 2472–2487. https://doi.org/10.1016/j.renene.2019.08.096
[7] *Research shows huge heat pump potential in china*. (n.d.). CLASP. Retrieved 23 December 2023, from https://www.clasp.ngo/updates/research-shows-huge-heat-pump-potential-in-china/
[8] https://doi.org/10.1016/j.proeng.2017.10.134
[9] Cai, J., Zhou, H., Xu, L., Shi, Z., Zhang, T., & Ji, J. (2022). Energy and exergy analysis of a novel solar-air composite source multi-functional heat pump. *Renewable Energy*, *185*, 32–46. https://doi.org/10.1016/j.renene.2021.12.033
[10] Song, M., Deng, S., Dang, C., Mao, N., & Wang, Z. (2018). Review on improvement for air source heat pump units during frosting and defrosting. *Applied Energy*, *211*, 1150–1170. https://doi.org/10.1016/j.apenergy.2017.12.022
[11] Patil, M. S., Seo, J.-H., & Lee, M.-Y. (2017). Heat transfer characteristics of the heat exchangers for refrigeration, air conditioning and heat pump systems under frosting, defrosting and dry/wet conditions—A review. *Applied Thermal Engineering*, *113*, 1071–1087. https://doi.org/10.1016/j.applthermaleng.2016.11.107
[12] Wen, B. (2018). Winter heating in Shanghai.*Mechanical and Electrical Information*, 546, 146-147.
[13] *Solar water heaters*. (n.d.). Energy.Gov. Retrieved 23 December 2023, from https://www.energy.gov/energysaver/solar-water-heaters
[14] Jouhri, M., Dhakar, P. (2019). A Review Study on Solar Water Heating Systems. *Journal of Emerging Technologies and Innovative Research*. https://www.researchgate.net/publication/345002100_A_Review_Study_on_Solar_Water_Heating_Systems
[15] Dong, S., Xu, T., & Chen, M. (2022). Solar radiation characteristics in shanghai. *Journal of Physics: Conference Series*, *2351*(1), 012016. https://doi.org/10.1088/1742-6596/2351/1/012016
[16] Liu, Y., Zhang, H., & Chen, H. (2020). Experimental study of an indirect-expansion heat pump system based on solar low-concentrating photovoltaic/thermal collectors. *Renewable Energy*, *157*, 718–730. https://doi.org/10.1016/j.renene.2020.05.090
[17] Yerdesh, Ye., Abdulina, Z., Aliuly, A., Belyayev, Ye., Mohanraj, M., & Kaltayev, A. (2020). Numerical simulation on solar collector and cascade heat pump combi water heating systems in Kazakhstan climates. *Renewable Energy*, *145*, 1222–1234. https://doi.org/10.1016/j.renene.2019.06.102
[18] Esfandeh, S., Hemmat Esfe, M., & Kamyab, M. H. (2022). Chapter 11—Applications of nanofluids in solar energy collectors focusing on solar stills. In H. M. Ali (Ed.), *Advances in Nanofluid Heat Transfer* (pp. 341–373). Elsevier. https://doi.org/10.1016/B978-0-323-88656-7.00010-6
[19] Yao, J., Chen, E., Dai, Y., & Huang, M. (2020). Theoretical analysis on efficiency factor of direct expansion PVT module for heat pump application. *Solar Energy*, *206*, 677–694. https://doi.org/10.1016/j.solener.2020.04.053

Proceedings of the 2nd International Conference on Functional Materials and Civil Engineering
DOI: 10.54254/2755-2721/91/20241074

Research on the application and prospects of variable reluctance inductive sensors

Yi'an Zhao

School of integrated Circuits,Shandong University, Jinan City, Shandong Province, 250101, China

202100400029@mail.sdu.edu.cn

Abstract. Variable reluctance inductive sensors are extensively utilized in the industrial field due to its unique working mechanism and good performance characteristics. Based on the working principle of Variable Reluctance Inductive Sensors, this paper reviews its development history, application in industrial automation and medical industry. Through the analysis of variable reluctance inductive sensors, variable reluctance inductive sensors have the advantages of high sensitivity, low cost and reliability which can support its wide application in precision measurement, position detection and motion control, but it is susceptible to the interference of the external magnetic field and the influence of the temperature which limits its development space and scope. However, the advancement of new materials, intelligent technologies and multi-mode integration has broadened the potential of future development of sensors and created more challenges for the development of variable reluctance inductive sensors. The update of new research conditions also provides a valuable reference of research and application in related fields

Keywords: Variable reluctance inductive sensors, reluctance effect, sensors, Inductive coil, position detection.

1. Introduction

As a kind of sensor, variable reluctance inductance sensor plays an important role in the field of industrial control and position detection because of its unique working mechanism and good performance characteristics. Its working principle is based on the magnetoresistive effect, and the position information of the object is determined by detecting the change of the magnetic circuit impedance. Variable reluctance inductance sensors are used in a wide range of applications, especially in the industrial sector, and are ideal for detection, process monitoring, control, positioning, motion, safety and fault diagnosis. With the advent of integrated circuits and microprocessors, inductive sensors have become more miniaturized and intelligent. This paper describes the working principle and development history of the variable reluctance inductance sensor, lists the common applications of the variable reluctance inductance sensor in the fields of liquid level monitoring, robot arm positioning system, flow monitoring, vehicle speed detection and magnetic medical equipment, and summarizes the advantages and disadvantages of the variable reluctance inductance sensor.

With the gradual reduction of feature size and the highly integrated circuit, the development of future sensors will follow four directions: miniaturization, flexibility, passive wireless, and sensor fusion. I hope this paper can provide some reference value for future readers.

2. Operating principle

The variable reluctance inductance sensor is mainly composed of an induction coil and one or more ferromagnetic moving chips, as shown in figure1. Its working principle is based on the magnetoresistive effect in electromagnetism, which describes the effect of changes in the magnetic field inside a substance on an electric current. This type of sensor is designed to convert object motion into a measurable change in resistance.

When an electric current passes through the induction coil, it creates a magnetic field, and the distribution of magnetic potential lines around the coil changes depending on the position of the sensing object and the material properties. A change in the position of a moving chip (for example, due to physical movement, vibration, or proximity) can affect the local distribution of the magnetic field, thereby altering the magnetic flux. These changes in the magnetic field cause the induced electromotive force (i.e. the voltage generated by electromagnetic induction) to change. By measuring inductance or reflected impedance, an electrical signal that is proportional to the distance or speed the object is moving can be obtained [1].

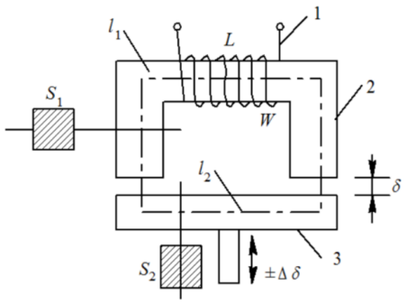

Figure 1. Variable reluctance inductance sensor schematic diagram

3. History of development

The history of sensor development dates back to the mid-19th century. As early as 1856, British physicist Sir William Thompson discovered that in general materials, the change in resistance is usually less than 5%, and this effect is later called "constant magnetoresistance". With the development of electronics, these early magnetoresistive concepts were translated into sensor technology for measurement and control. In the initial stages, such sensors are used in the industrial and military fields for basic position detection tasks.

After decades of development, the design and manufacture of modern variable reluctance inductance sensors have been significantly improved in terms of accuracy, stability and reliability [2]. Advances in materials science in particular have driven the development of these sensors, such as the use of new soft magnetic materials that can reduce hysteresis and improve response speed [3]. With the advent of integrated circuits and microprocessors, variable reluctance sensors have become more efficient and intelligent in data processing and transmission [4].

4. Application example

Variable reluctance inductance sensors are used in a wide range of applications, especially in the industrial sector, and are ideal for detection, process monitoring, control, positioning, motion, safety and fault diagnosis.

4.1. Level monitoring

Variable reluctance inductance sensors play a key role in liquid level monitoring, and their usefulness comes from their ability to accurately monitor the height change of liquid level. The use of variable reluctance inductance sensors in liquid level monitoring is based on the magnetoresistive effect, that is, when a conductor or semiconductor passes a current, its resistance value will change with the change of the magnetic field. The sensitive unit mainly consists of a reluctance inductor coil and its matching magnet system, and the magnet system is usually directly related to the level of the measured medium.

In specific applications, the sensor's sensitive unit usually consists of a coil made of one or more magnetic materials, whose inductance value is affected by the strength of the nearby magnetic field. The change in level causes the position of the buoy to change, and the buoy is fitted with a magnet that can move relative to the inductor coil. With the rise and fall of the liquid level, the up and down movement of the buoy will change the relative position of the magnet and the inductor coil, thus changing the magnetic flux density in the coil [5].

Since the magnetoresistance of an inductor coil is related to the magnetic flux density, a change in the liquid level actually causes a change in the magnetoresistance in the coil. A change in coil reluctance causes a change in the magnetic field generated by the current passing through the coil, so that the inductance value of the alternating current passing through the coil changes accordingly. This change in the inductance value can be detected by the circuit, for example, the coil can be used as a component of the RLC oscillation circuit, and the change in its inductance value will cause the resonant frequency of the circuit to change. The change in frequency can be easily detected by a frequency meter or other electronic measuring device and is ultimately converted into an electrical signal proportional to the level of the liquid level. These electrical signals are processed by data and can be used to automatically trigger the opening and closing of the pump or valve to control the discharge and filling of the liquid.

Such a system can not only ensure the automatic control of the liquid level in the storage tank, but also prevent the risk of overflow or dry burning, and is widely used in the liquid level control process in the chemical, water treatment and food and beverage industries. With this non-contact level measurement method, the variable reluctance inductance sensor ensures height measurement accuracy and system reliability, while reducing the need for maintenance and repair. The simple design of these sensors, which do not contain any moving parts, makes them ideal for level measurement, especially in situations where maintenance is critical or mechanical buoys are not appropriate. In addition, variable reluctance inductance sensors also have good environmental adaptability and long-term stability, which makes them widely used in liquid level monitoring. Commonly used instruments for liquid level detection are shown in figure2.

Figure 2. Liquid level detector

4.2. Positioning system of industrial robot arm

Multiple variable reluctance sensors are installed on the robot arm to accurately measure the joint position, as shown in figure3. As the robot arm moves, the ferromagnetic core in the joint moves in the induction coil, causing the magnetic circuit impedance to change accordingly. This change in impedance results in a change in the induced voltage in the coil, and this voltage signal is amplified, filtered, and converted analog-to-digital into the control system. The control system uses these data to calculate and adjust the movements of the robot arm to reach the predetermined working position and ensure the accuracy of the assembly or handling task [6]. In this process, the sensor's linear output range and accuracy are critical, as they affect the performance of the final control system.

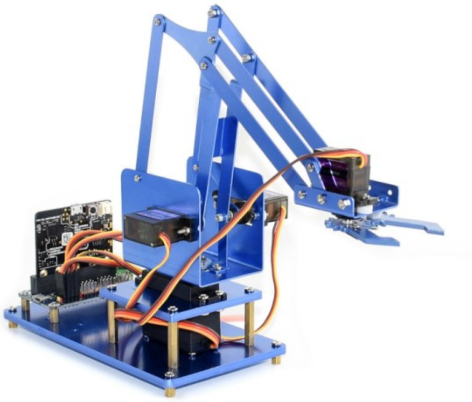

Figure 3. Robot arm

4.3. Flow monitoring

In flow control applications, variable reluctance inductance sensors can monitor and manage the flow of a variety of media, including liquids, gases and powders. Not only does it provide critical information about the magnitude, energy consumption, and efficiency flowing through the medium, but it also allows the overall flow output to be optimized by adjusting the inlet and outlet of the medium. The application of this sensor ensures the real-time adjustment and fine management of the flow control process, thus meeting the demand for accurate flow control in complex systems [7]. Common instruments for flow detection are shown in Figure 3.

Figure 4. Flow detector

4.4. Vehicle speed monitoring

The traditional speed monitoring equipment of vehicles is often interfered by the complicated environment such as road and wheel sliding. In contrast, the variable reluctance inductance sensor can measure the speed by detecting the rotation state of the gear or axle of the speed sensor, and the detection result is fed back to the vehicle control system. Therefore, the application of variable reluctance inductance sensors in automobile speed detection is often in the form of wheel speed sensors, as shown in figure4.

In variable reluctance inductance sensors, the sensing unit usually consists of a fixed reluctance inductor coil and a rotating gear or magnetic marker. This gear or magnetic marker is usually mounted on a wheel or drive shaft with periodic magnetic markers or teeth that affect the magnetic field passing through the sensitive unit environment. As the wheel rotates, magnetic markers or teeth pass at a fixed distance through a magneto-resistive inductive sensor fixed nearby. In this way, the local strength of the magnetic field changes with each rotation through a mark or tooth. As the magnetic field strength changes, the reluctance generated by the inductor coil also changes accordingly, thus affecting the inductance value through the inductor coil. With the change of wheel speed, the speed of the magnetic tooth through the induction coil also changes, resulting in a corresponding change in the frequency of the inductance value on the coil. These changes can produce an alternating voltage through the inductor coil, the frequency of which is proportional to the frequency of the magnetic mark or tooth passing through the coil (i.e. the rotational speed of the wheel). By measuring the frequency of this generated alternating voltage, the wheel speed of the vehicle can be determined very accurately, which is further converted to the vehicle's traveling speed [8]. In order to improve the availability of the signal, the original generated signal is usually conditioned, such as filtering and pulse shaping, so as to obtain a clearer and more accurate speed representation signal.

Variable reluctance inductance sensors use the reluctance effect to detect the speed of the wheel or related rotating parts, thereby indirectly measuring the speed of the car. This type of sensor is widely used in the speed measurement and control system of modern automobile because of its advantages such as no contact, high accuracy and fast response speed.

Figure 5. Wheel speed measuring sensor

4.5. Magnetic medical equipment

Magnetic medical devices include MRI(nuclear magnetic resonance imaging apparatus as shown in figure5), MRS(nuclear magnetic resonance spectrometer) and SQUID(superconducting quantum interferometer). Among these devices, the application of variable reluctance inductance sensors in magnetic medical devices is often based on their ability to accurately measure changes in the magnetic field and convert these changes into electrical signals.

In medical imaging devices such as magnetic resonance imaging (MRI), sensors can be used to monitor and calibrate the strength of highly uniform magnetic fields generated by the device. The sensitive unit in such applications is mainly composed of a magnetoresistive material, whose resistance value changes in response to small changes in the external magnetic field. Any change detected by the magnetoresistive inductance sensor indicates a deviation in the strength of the magnetic field. The magnetoresistive material inside the sensor will change its resistance value with the change of the magnetic field, and then the change of resistance value is sensed by the bridge circuit connected to it, and the voltage change of the bridge output is related to the change of the magnetic field strength. In this way, magnetic medical devices can monitor the strength and uniformity of the magnetic field in real time [9].

The resulting voltage signal can then be converted into a digital signal and processed by the algorithm inside the device to ensure that the magnetic field conditions required for the imaging process are met. This precise control is the key to high-quality magnetic resonance imaging.

Figure 6. MRI

5. Advantages and disadvantages

The variable reluctance inductance sensor provides non-contact measurement, which means there is no mechanical wear in the system. Thanks to its design based on the magnetoresistive effect, it can achieve very high measurement accuracy with good repeatability and response speed. In addition, their relatively simple design makes this class of sensors very reliable and easy to maintain, reducing maintenance costs.

However, the performance of these sensors is significantly affected by changes in temperature, which can alter the properties of magnetic materials, requiring the necessary temperature compensation. In addition, for non-ferromagnetic materials, the detection effectiveness of variable reluctance sensors is limited, because these materials have relatively little effect on the magnetic field. Therefore, they are usually designed for position measurements of ferromagnetic objects.

6. Conclusion

As a mature and reliable sensor technology, variable reluctance inductance sensors play a vital role in many modern industrial and scientific research fields. Although their performance in non-ferromagnetic material detection and high-temperature environments will be limited, these shortcomings are gradually being overcome through technological innovation and material improvement. In the course of future development, it can be foreseen that variable reluctance sensors will continue to maintain their core position and gain wider applications in the field of automation and intelligent systems.

Due to my limited ability and time, there are still many areas worth further research and improvement in this topic, including the failure to conduct parameter measurement and comparison experiment of variable reluctance inductance sensor, and the scope of application examples of variable reluctance inductance sensor is not wide. In the subsequent optimization, relevant experiments will be added to demonstrate the point of view, and discussions in amplitude measurement, thickness measurement, eddy current inspection and other aspects will be added.

References

[1] Du Y W .Resistive, Capacitive, Inductive, and Magnetic Sensor Technologies[M]. CRC Press: 2014-12-09.

[2] Chen H. Optimum operating conditions for inductive sensors[J]. Research and Exploration in Laboratory, 2016, 35(3):32-36, 55.

[3] Wu, Y., Xiao,L., Hou, S. Magnetoresistive/Superconducting Composite Magnetic Sensors: Principles and Developments[J]. Physics,2019,48(1):14-21.

[4] Yu, H. Research on signal processing methods for inductive displacement sensors [D]. Shanghai: Shanghai Jiao Tong University, 2014.

[5] Yang, Y. Accurate Level/Volume Monitoring System for Ships Based on Magnetostrictive Level Sensors[D]. Shanghai: Shanghai Maritime University, 2006.

[6] Zheng, X., Hu. Z, Ni, S. et al. Adaptive impedance control of a dual-arm surgical robot based on force synchronization[J]. Transducer and Microsystem Technologies, 2023, 42(4):95-98.

[7] Chen, W., Lin, J., Luo, X., et al. Application of various flow meters in tunnel drainage [J]. Yunnan Water Power, 2023, 39(2): 229-232.

DOI: 10.54254/2755-2721/91/20241074

[8] Huang, R., ITS Traffic Monitoring Based on Magnetoresistive Sensors and ZigBee Networks [D]. Nanjing University Of Posts And Telecommunications, 2012.
[9] Jiang, S., Zhang, P, Liu, J, et al. Research on robot drive and control sensing technology in nuclear magnetic resonance environment[J]. Journal of Basic Science and Engineering, 2012, 20(3):472-483.
[10] Melexis Co. Ltd. MLX90513 Inductive Sensor Chips[J]. Sensor World, 2023, 29(11):44.
[11] TURCK (Tianjin) Sensor Co. Ltd. General purpose inductive sensors[J]. Automation Panorama, 2013(3):8.
[12] Mociran B ,Gliga M .Optimization of an Inductive Displacement Transducer[J]. Sensors, 2023, 23(19).
[13] Yu. A T .On the Contribution of the Magnetoresistive Effect to Intrinsic Nonlinear Distortions of Induction Sensors[J].Bulletin of the Lebedev Physics Institute, 2022, 49(8): 257-260.
[14] Du Y W .Resistive, Capacitive, Inductive, and Magnetic Sensor Technologies[M]. CRC Press: 2014-12-09.
[15] Semiconductor Components Industries LLC; Patent Application Titled "Devices, Systems And Methods For Determining And Compensating For Offset Errors Arising In Inductive Sensors" Published Online (USPTO 20200064159) [J]. Electronics Newsweekly, 2020.
[16] Mociran B ,Gliga M .Optimization of an Inductive Displacement Transducer[J]. Sensors, 2023, 23(19).

Proceedings of the 2nd International Conference on Functional Materials and Civil Engineering
DOI: 10.54254/2755-2721/91/20241087

Behavior and design of earthquake-resistant concrete structures

Jiangning Bian

College of Engineering and Technology, China University of Geosciences Beijing, Beijing, China

15804816802@163.com

Abstract. Earthquakes, as one of the primary natural disasters, cause significant destruction to building structures. Historically, the collapse of buildings due to earthquakes has resulted in numerous casualties and economic losses. This paper, through a method of literature review, explores the mechanisms of damage to concrete structures under the action of an earthquake and presents the principles of earthquake-resistant design. It analyzes how factors such as the mechanical properties of structural materials, the form of the structure, the strength of connection nodes, and the conditions of the foundation affect structural damage. It proposes measures to enhance the seismic performance of concrete structures through ductility design, strength design, uniform design, and the strategy of multiple lines of defense. This study holds significant implications for the construction industry by offering a systematic set of earthquake-resistant design principles and strategies which can enhance the seismic resilience of existing and future structures, mitigating the damage caused by earthquakes. Moreover, for society at large, this research underscores the importance of reducing seismic disaster risks through scientific design, contributing to the protection of people's lives and property, and promoting sustainable societal development.

Keywords: earthquake-resistant, civil engineering,concrete structures, structure design.

1. Introduction

Earthquakes are one of the main natural disasters that cause destruction to the structure of buildings. Concrete structures are widely used in high-rise buildings and infrastructure due to their durability and cost-effectiveness. However, earthquake-induced ground motion can cause severe structural damage or even collapse, leading to casualties and economic losses. Therefore, it is crucial to design concrete structures that can resist seismic forces. This paper first introduces the mechanisms of damage to concrete structures during an earthquake, including flexural damage, shear damage, buckling damage, and connection failure. Subsequently, it outlines the basic principles of earthquake-resistant design, including ductility design, strength design, uniform design, and the strategy of multiple lines of defense, to ensure that the structure maintains overall stability and functionality during extreme seismic events. In the section on research progress, we have reviewed several recently published papers on the topic of earthquake-resistant concrete structures. For instance, Dindar et al. proposed new developments in the Earthquake Energy Demand Spectra in their study, offering a novel perspective on assessing the energy consumption of structures under seismic action [1]. Furthermore, Wu et al. conducted a performance-based seismic fragility analysis of RC frame structures, providing an empirical basis for seismic-resistant design [2]. These studies indicate that a deeper understanding and application of earthquake-resistant design principles are crucial for enhancing the seismic resilience of structures. This study holds significant academic significance and practical application value in the field of earthquake engineering. It not only enriches the theoretical foundation of seismic-resistant design for concrete structures but also provides engineers with practical design guidance and strategies. By thoroughly analyzing the impact of earthquakes on structures, this research offers a scientific basis for reducing seismic disaster risks and protecting people's lives and property. Furthermore, this study provides a reference for policymakers when formulating relevant building codes and disaster prevention and mitigation strategies, contributing to the promotion of sustainable societal development and the capacity to withstand natural disasters.

2. Fundamental principal

2.1. Mechanisms of Damage

The mechanisms of damage to concrete structure buildings under the action of an earthquake are multifaceted, involving factors such as the mechanical properties of structural materials, the form of the structure, the strength of connection nodes, and the conditions of the foundation. Firstly, flexural damage is one of the most common forms of damage, typically occurring at the yield points of beams and columns. When the bending stress exceeds the yield strength of the material, it can lead to significant plastic deformation or even fracture of the structure. Shear damage often occurs in shear walls or frame columns, where structural deformation under shear forces exceeds the shear strength of the material, potentially leading to local or global instability of the structure. Buckling damage may occur in slender columns or walls, and when subjected to compressive forces, if the pressure exceeds the critical value, the structure may buckle, leading to overall failure. Connection failure refers to the failure of connection points between components under the action of an earthquake, which can weaken the integrity and continuity of the structure and is one of the key factors leading to structural damage. Finally, foundation failure is caused by the instability of the foundation or uneven settlement, which can cause the superstructure to tilt, crack, or even collapse. To enhance the seismic performance of concrete structures, it is necessary to consider these mechanisms of damage comprehensively during the design phase and to adopt corresponding design measures.

2.2. Principles of Earthquake-Resistant Design

The fundamental principles of seismic design for concrete structure buildings involve ensuring that the structure can dissipate energy through plastic deformation instead of fracture, typically achieved through ductility design. All parts of the structure must have sufficient load-bearing capacity to withstand the maximum seismic forces that may encounter, according to the strength design. Moreover, uniform design prevents damage due to local weaknesses. The design strategy of multiple lines of defense means that even if parts of the structure fail, the remaining parts can still maintain its overall stability. Energy dissipation design involves specific dissipation elements to reduce the seismic energy transmitted to the upper parts of the structure.

3. Structure analysis

3.1. Structural layout in seismic design of various different concrete structures

The characteristic of a frame structure is its light self-weight, which is suitable for situations that require large interior spaces and flexible layouts. The reduction in overall weight can effectively decrease seismic forces. If designed properly, the seismic performance of frame structures is generally good, achieving high ductility. However, due to their lower lateral stiffness, the horizontal deformation during an earthquake is considerable, which can lead to damage to non-structural components. For taller structures, the excessive horizontal displacement can cause a significant P-Δ effect, exacerbating structural damage. Therefore, the height of frame structures should not be excessive.

Shear wall structures are characterized by their high lateral stiffness and strength, resulting in good overall spatial performance. However, because there are many walls and a heavier weight, the seismic forces are also greater, and the layout and use of the interior space are less flexible. Shear wall structures are more suitable for residential and hotel buildings, where there are many walls and a more uniform division, achieving a higher degree of unity between the load-bearing and protective structures.

In shear wall structures, to meet the needs of having large spaces such as shops on the ground floor, the first one or several floors are often changed to an internal frame structure or a frame shear wall structure, known as the bottom large space shear wall structure. This type of structure has poorer seismic performance, so its height must be limited.

Additionally, the seismic performance of the structure can be improved by setting up shear walls locally to form a 'shear-wall-frame' structure. The characteristics of the frame-shear wall structure are that they overcome the shortcomings of pure frame and pure shear wall structures to some extent, leveraging their respective strengths, with higher stiffness, lighter self-weight, a more flexible layout, and more uniform structural deformation. They have good seismic performance and are commonly used in office and hotel buildings.

In addition to the structures mentioned above, there are also tube structures, mega-frame structures, and suspension structures, among others."

3.2. Case design study

3.2.1 Structural Overview. In this case, the design principle of "strong columns and weak beams" is adopted, where seismic forces can come from any direction. However, in seismic design, it is generally only necessary and essential to perform seismic calculations for the two principal axes of the structure, which are the longitudinal and transverse directions [3].

The centerlines of beams and columns should ideally coincide to ensure direct force transfer and reduce the adverse effects caused by excessive eccentricity [4].

The frame-shear wall structure is depicted in figure 1. The seismic fortification intensity is 7 degrees, with a seismic resistance level of 3 for the frame component and a seismic resistance level of 2 for the shear wall component. The structure is situated on a Class I site, with a design basic seismic acceleration of 0.10 g, and is categorized in the first seismic group. Consequently, the design response spectrum characteristic period utilized is 0.65 seconds. The structural damping ratio is 0.05. The shear wall concrete grade is C50 [5].

Beam Cross-Section:250mm×550mm

Column Cross-Section:500mm×500mm

Wall Thickness:300mm

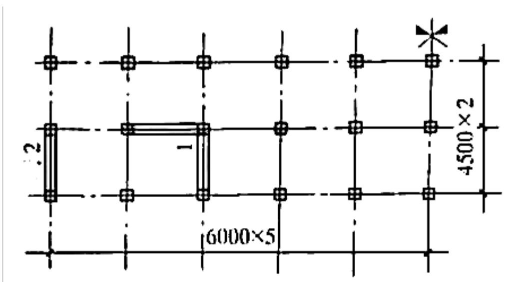

Figure 1. columns and shear wall lay out

3.2.2 Frame Stiffness Calculation. Moment of Inertia of a Beam Cross-Section can be depicted by

$$I_B = 1.2 \times \left(\frac{1}{12} \times 0.25 \times 0.55^3\right) = 0.004159m^4 \tag{1}$$

In the formula, the factor 1.2 accounts for the stiffness effect of the T-shaped cross-section [6].

The linear stiffness of the beam, where the modulus of elasticity is 2.6×10^7MPa, can be illustrated as

$$i_B = \frac{E_c I_B}{l} = 2.6 \times 10^7 \times 0.004159 \times \frac{1}{4.5} = 2.4030 \times 10^4 kN \cdot m \tag{2}$$

The lateral stiffness value of the framework's peripheral column D is

$$K = \frac{i_{B1}}{i_c}, \alpha = \frac{0.5 + K}{2 + K} \tag{3}$$

where K=0.8024, and α=0.4647

and the lateral stiffness value of the framework's interior column is

$$K = \frac{i_{B1} + i_{B2}}{i_C}, \alpha = \frac{0.5 + K}{2 + K} \tag{4}$$

where K=1.6048, and α=0.5839.

3.2.3 Shear Wall. The figure of the shear wall is as follows: Shear walls are primary structural elements in buildings designed to resist lateral loads, such as those from earthquakes or wind. Typically made of reinforced concrete, they possess high shear strength and stiffness. In the context of this paper, the characteristic of shear wall structures is their high lateral stiffness and strength, which provides excellent overall spatial performance for the building [7].

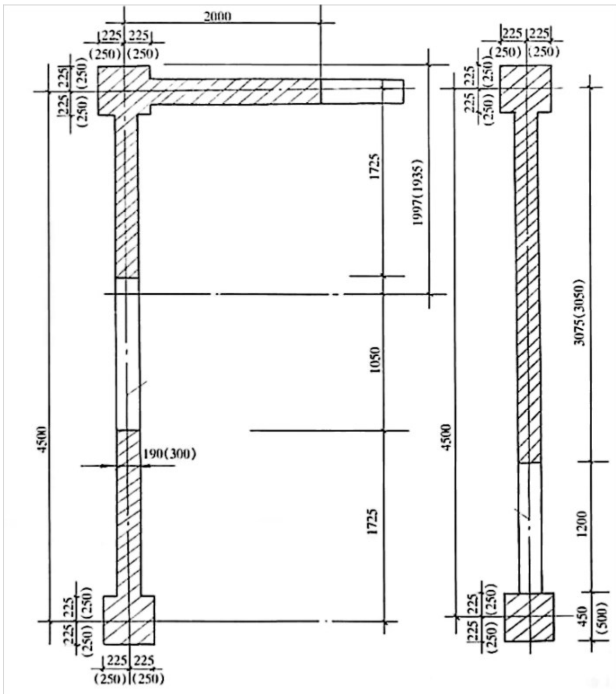

Figure 2. drawing of the shear wall

3.2.4 Seismic Verification principal. The horizontal seismic forces at each floor can be converted into an equivalent triangular distribution of horizontal forces. The principle of conversion is that the bending moment effect produced by the horizontal seismic forces F at each floor is equivalent to that produced by the triangular distribution of horizontal forces [8].

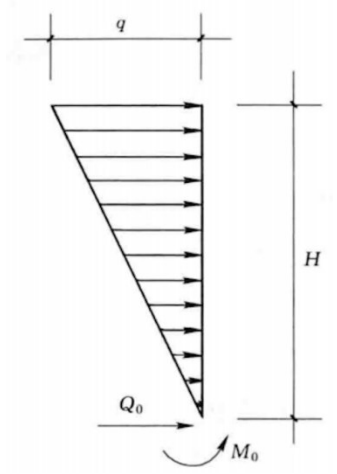

Figure 3. Force diagram

$$M_0 = \frac{qH}{2} \times \frac{2H}{3} = \sum F_i H_i = 109900kN \cdot m \tag{5}$$

$$q = \frac{3\sum F_i H_i}{H^2} = \frac{3 \times 109903}{39.8^2} = \frac{208.14kN}{m} \tag{6}$$

The total equivalent lateral seismic force can be calculated by

$$F_{EK} = \frac{1}{2} \times 208.14 \times 39.8 = 4141.99 \tag{7}$$

4. Conclusions

This paper analyzes the damage mechanisms of concrete structures subjected to seismic forces and presents a series of seismic-resistant design principles and strategies through structural case analyses. These design measures include ductility design for energy dissipation, strength design to ensure adequate load-bearing capacity, uniform design to avoid local weaknesses, and a multi-line defense strategy to maintain the overall stability of the structure. The application of these design principles can significantly enhance the seismic performance of concrete structures and reduce the damage caused by earthquakes. Future research should continue to explore new materials and technologies to further improve the seismic resistance and resilience of structures.

However, there are some limitations to this study. Firstly, the paper mainly focuses on theoretical analysis and the proposal of design principles, with relatively less validation in practical engineering applications. Secondly, there is insufficient exploration of the application of new materials and innovative technologies in seismic-resistant design. Future research should delve deeper into these aspects and conduct more experimental verification to ensure the practicality and effectiveness of the design principles.

Looking forward to the field, we anticipate further development and refinement of seismic-resistant design theories, especially in terms of the application of new materials, intelligent structural systems, and high-performance computing technologies. Moreover, interdisciplinary collaboration will help address the complex issues in seismic-resistant design from multiple perspectives, promoting innovation and development in this field.

References

[1] Ahmet Anıl Dindar, Cem Yalçın, Ercan Yüksel, Hasan Özkaynak, and Oral Buyukozturk, "Development of Earthquake Energy Demand Spectra," Earthquake Engineering Research Institute,Earthquake Spectra, Volume 31, No. 3, pages 1667–1689, August 2015; © 2015

[2] GB 50011-2010. "Code for Seismic Design of Buildings." China Architecture Industry Press, 2010.

[3] Krawinkler H., Fajfar P. Performance-Based Seismic Design Concepts and Principles. In: Proceedings of the 15th World Conference on Earthquake Engineering; 2012.
[4] Paulay, T., & Priestley, M. J. N. (1992). Seismic Design of Reinforced Concrete and Masonry Buildings. John Wiley & Sons.
[5] Nakano, T., & Sato, H. (2001). Development and application of a new seismic wall system in high-rise building structures. Journal of Structural and Construction Engineering, 48(1), 35-42.
[6] WU Qiao-yun, ZHU Hong-ping, Fan Jian. "Performance-based seismic fragility analysis of RC frame structures." Engineering Mechanics, 2012.
[7] Park, R., & Paulay, T. (1975). Reinforced concrete structures. Journal of the Structural Division, 101(ST7), 1589-1601
[8] Fajfar, P., & Fischinger, M. (1989). N2 - A method for non-linear seismic analysis of regular buildings. Earthquake Engineering and Structural Dynamics, 18(6), 557-563.

DOI: 10.54254/2755-2721/91/20241096

The function and the principle about how self-healing materials are used in metal wear condition

Jinlin Zhou

Shanghai Starriver Bilingual School, Shanghai, 201100, China

17317739180@163.com

Abstract. Due to the wide range of metals used in different industries, the increase in the service life of metals and metal materials has always been a more important research direction. Relevant research has proved that self-repairing materials in lubricants can help machines to repair themselves by utilizing self-modifying properties, thus restoring them to a better working condition. This paper mainly summarizes and analyzes the experimental materials by means of literature review, and discusses the working principle of such materials and the application of self-repairing materials in industrial production. The article also confirms through its analysis that during the operation of the machine, the composite lubricant reacts with the metal surface and forms a thin film, which results in a substitution reaction. In this way, the damaged metal is replenished by the composite material and the machine can return to normal operation. However, this method can only be applied to machines that work for a short period of time, and is not able to solve the problem of large areas of severely damaged machines, so the relevant materials to assist in the modification of the metal still need to be continuously developed and researched.

Keywords: Metallic self-repair, ITCS, Machine, Lubricate with catalyze. Chemical reaction.

1. Introduction

There are many forms of self-healing material, such as bio-mimetic, self-healing polymers and elastomers. Most of these materials were used as to self-repair plastic because the chemical bond that breaks between polymers and elements are much easier to repair. As for metal, due to the special bond-metallic bond-between atoms. It is hard for them to bond together without any other chemical reagents or catalyzer [1]. Also, damage for metal is really urgent, a small damage or crack might cause the machine and whole system to break down. For instance, a small crack from engine might cause the car to stop and stop functioning. It is extremely for driver especially when they are driving on the high way. However, there is a kind of materials, hydroxyl-silicate, that can help metal to self-repair without human constantly additions due to its similar function of self-healing [2]. There are two physical and chemical procedure in this process when hydroxyl-silicate is helping the metal to recover. Each step during the procedure does not only heal the metal, but also create a better condition for metal to exists. The physical procedure creates a condition for chemical reaction to exchange the metal from lubricate. This achieves the goal of effectively extend the machines' service life, and protecting it from further injuries that might occurred from severe conditions such as, collision between heavy objects. This paper mainly focus on the development for self material. The purpose is to use the self material in metal to improve the life of machine by using the physical and chemical reaction between the compound in lubricate and the metal.

DOI: 10.54254/2755-2721/91/20241096

This research can be cited in the manufacture and maintenance of machines, thus helping companies to improve the efficiency and life of their machines.

2. The mechanism of action about self-healing metallic material.

According to the substitution reaction that can happen between metals, the scientists designed a system for hydroxyl-silicate to exchange the metal from the broken machine.

There are three basic procedures that hydroxyl-silicate work. The first step is the hydroxyl-silicate will be mixed in lubricant and added between the metallic machine. The hydroxyl-silicate will not react with lubricant. Due to the comparative large size with the protrusions on the metal. Hydroxyl-silicate can effectively furnish the surface of the damaged metal. The second procedure is that hydroxyl-silicate can help to clean the surface, so there is a more smooth surface for hydroxyl-silicate to prepare for the next step [3].

Both the first and second step can be considered as a physical change.

The third procedure can be counted as a chemical reaction between hydroxyl-silicate and the damaged metal. When the hydroxyl-silicate reaches the surface of the damage metal and the first two steps occur, the large particle of hydroxyl-silicate will collide and rub with the protrusions. During this process, large amount of heat will be released in a small period of time and create a perfect condition for hydroxyl-silicate to form a replace reaction with the protrusion or the cracks. Therefore, the cracks will be fixed up, the protrusion will be cleaned, and the metal or the machine recover.

This kind of self-healing metallic material can be considered as chemical reaction.-

2.1. The classification of the film which created by the self-healing material

When the material in lubricate substitute with the metal, there will be films formed by the self-healing product and it is the basic condition for substitution. There are four types of them.

First kind of film is formed directly between the metal from the surface of the machine and the additive in the lubricant. This can form a chemical film which contains polar molecule. Since it is polar, it will be physically absorbed by the pair surface of the metal so it can achieve the purpose for protecting the metallic surfaces from damage. This kind of film can normally be formed by the active additive in the lubricant such as s, p, cl, b. It can form chemical compound like ferrous sulfide, ferric chloride . Second kind of film are formed by lots of small crystal balls [4]. As mentioned above, during procedure one and two, the protrusion and the additive will rub and collide to release large amount of heat. In the high temperature condition, the additive and the metal from metallic surface will form eutectic balls. The film which is formed by these eutectics can not only repair the metal but also fill the gaps between pits and eventually let the pair surface to be much smoother. The third kind of film is formed by the additive in the lubricant. The lubricant just deposits on the pair surface and form the film. For instance, by adding MoS2 or graphite which both of them have flat structure will deposits on the pair surface of the metal. Since the Van der waals's force is extremely low between different layers. It can also make the surface smoother [5]. The last film can help the metal to adapt the friction between other objects. This film is normally metallic. It will not tire but has a higher special density.

The first and second film are totally formed by chemical reaction. However, the third kind of film was actually quite different, it does not involve in any chemical procedure and the fourth film was formed by chemical and physical reaction.

2.2. The reason people choose to use film to help metal to repair

The metal that rubs against each other does not looks like what it is. Most people believe that the surfaces just rub without any other materials. However, even for the material that has not been deal with anything will have films to let them rub against each other. For instance, like oxidation film will exists if this machine has not been preserved well. Normally, this film can protect the metal from damage. However, the film will still be destroyed if the condition is too harsh and there is not enough time for the metal to form a new film. This is why the additive must not only help the metal to repair itself, but also create films.

3. In-situ tribochemical self-repair (ITCS) Working Principle

When people first discovered about that B, N, C, S can actually filtrate into some surface during friction [6]. People realized that metal can achieve similar effect, which is really similar to MRRs. In this way, the additive can filtrate into the metal through friction. After filtration, the additive can evoke response to form new structure or form new particle. For instance, Cu, Sn, Bi, Cr, W can all be used in this procedure as long as they are organic metal.

The possible material for the additive to achieve self-healing.

Nano-materials are be considered as the most important material. Nanoparticles OD-n is considered to be a type of ideal material for self-healing. During the first two steps of self-healing process, OD-n is able to produce Nanometals and metallic oxide can be used in the next to chemical process for self-repair.

There are two ways to achieve self repair and ITCS. The first way is to use soft repair. Soft repair can also be achieved in two ways. First, OD-n is a ball-like particle, so it can be used as a pom ball to fill between the pits. Just like the Second film and create a smooth surface for metal. Second, After the OD-n formed a film and is absorbed on the surface metal, it can achieve self-healing by adding the actual contact surface area of fictional duality and decreasing the imprinting force on the repairing surface. The second way is to use hard repair. OD-n can show its chemical activity, and let it self to form a reduction reaction by letting out the electron. Therefore, OD-n will turn into microcrystal. Due to the high temperature condition which was created when the additive rub against the pair surface, It can form a molten alloy film. This process required nanometal to react with OD-n, so it is important to choose nano CuO, PbO etc. These materials can effectively help OD-n to form a reduction reaction since they are easy to lose electron. As for the OD-n, people tend to choose Cu, silver, Pb, etc. Consider that they are wear resistant, these metals are good replacement for the damaged part. Therefore, the best additive should be n-CuS-MoS_2, n-Pb-MoS_2, etc.

4. The application for metallic self-healing material

4.1. Condition

The metallic self-healing material cannot use with new equipment or machines that require little time to maintain. It also needs the machine that is over run-in period. The reason that these three types of machines (the new machine, the machine that is not over run-in period and the machine that need little time to repair) cannot use is because these machines' surface does not need to be polish or grind. As for the machine or equipment that reach the condition for using the material, the lubricant can be added after the maintenance.

4.2. The perfect application for self-healing material

Cylinder in the engine can be considered as one of the machines that reaches the requirement for using the self-healing material. When the cylinder has not been hurt too much, the machine can be injected by the self-healing material directly into cylinder and turn off the engine. After the metal was injected by it, people need to open the engine per 10 second. In this way, it can make sure that self-healing materials are spread all over the engine. The surface of the cylinder can be identified as the Figure 1 [7]. Different density of the additive can cause different surface. When the temperature is around 200 degrees to 400 degrees, the additive can achieve its best effect. In the reality, when the first injection is finished, the second injection needs to be finished after the car has run over 400-600 kilometer. It can not only decrease the loss during working, but also help to replenish the material needed for self-healing.

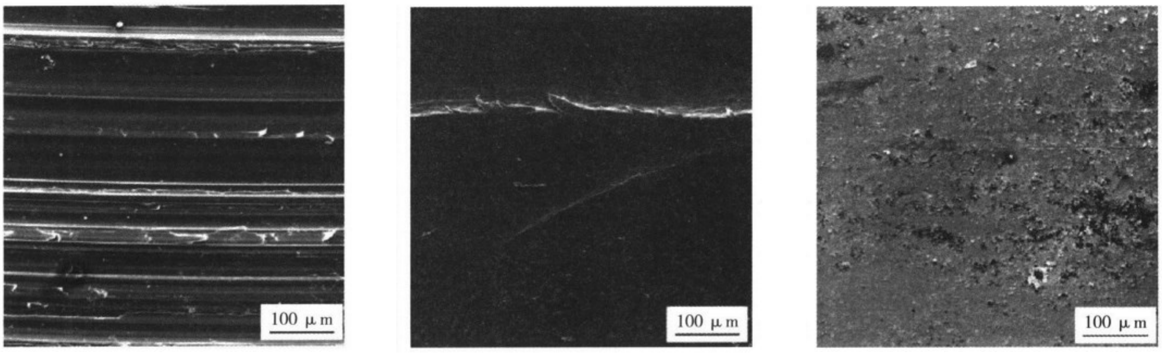

(a) concentration 0% (b) concentration 10% (c) concentration 20%

Figure 1. The effect of different concentration of magnesium hydroxysilicate on damaged surface [7]

4.3. Improvement for self-healing material

At the cylinder where 15-20cm to the top, the loss during working is quite obvious. Also, when the engine starts, the loss also reaches the maximum. When the temperature reaches 93.3 degrees, the loss decreases as temperature increases. Therefore, it is still important to track for the cylinder that has used this technology to find out what is the best condition to reach the best effect.

5. Conclusion

The paper focuses on the use of composites in lubricate to help the machine to self-repair. While the machine is in operation, the compound lubricate reacts with the metal surface and forms films, resulting in a substitution reaction. In this way, the damaged metal is replenished by the compound. However, there are still some pending issues with this approach. In some condition, if the surface of the machine is extensively and severely damaged, the compound can only help to repair part of the machine and cannot restore the machine to normal operation. In addition, this can only be applied to machines that work for short periods of time. Due to the heat generated and the conditions, the time required for composites to complete the process is not sufficient and hence not suitable for self-healing materials.

Due to time and resource reasons, this paper mainly discusses the topic in the form of theoretical analysis and review during the analysis, without involving specific experimental tests and within a certain range of literature references.

References

[1] Yang Y, Ding X, Urban MW. Chemical and physical aspects of self-healing materials[J]. Progress in Polymer ence, 2015: 34-59. DOI:10.1016/j.progpolymsci.2015.06.001.

[2] Qi XW, Jia ZN, Yang YL, Fan BL. Characterization and auto-restoration mechanism of nanoscale serpentine powder as lubricating oil additive under high temperature[J]. Tribology International, 2011. DOI:10.1016/j.triboint.2011.02.001.

[3] Rao X, Sheng C, Guo Z, et al. A review of online condition monitoring and maintenance strategy for cylinder liner-piston rings of diesel engines[J]. Mechanical Systems and Signal Processing, 2022, 165:108385.DOI:10.1016/j.ymssp.2021.108385.

[4] Yunxia Z L. Self-repairing properties of complex titanium grease containing hydroxyl silicate[J]. Tribology International, 2020, 149(1).

[5] Maximiano P, Duraes L, Simoes P. Intermolecular interactions in composites of organically-modified silica aerogels and polymers: A molecular simulation study[J]. Microporous and mesoporous materials: The offical journal of the International Zeolite Association, 2021(314-): 314. DOI:10.1016/j.micromeso.2020.110838.

[6] Yang Z, Fu Z, Yu G, et al. A self-repairing approach for the M-Lattice modular robotic system using digital hormone model[J]. Robotics & Autonomous Systems, 2017, 97: 1-15. DOI:10.1016/j.robot.2017.08.001.

[7] Ping-An Z. The Functional Characteristics and Applied Prospect of the Metallic Auto Restoration Materials[J]. China Surface Engineering, 2004.
[8] Thomas S, Birbilis N, Venkatraman M S, et al. Self-repairing oxides to protect zinc: Review, discussion and prospects[J]. Corrosion Science, 2013, 69(APR.): 11-22. DOI:10.1016/j.corsci.2013.01.011.

DOI: 10.54254/2755-2721/91/20241091

Study on UV-Curable Acrylic Clear Viscoelastic Materials with Grafted Structures

Junqi Liu

School of Advanced Soft Matter, South China University of Technology, Tianhe District, South China University of Technology, Duxing Building (Building No. 2) North Tower 102, Guangzhou, China

junqilius@outlook.com

Abstract. Flexible substrates are crucial for wearable electronic strain sensors, but achieving biocompatibility, low cost, and aesthetic appeal alongside good mechanical performance remains challenging. Acrylic-based clear viscoelastic films (CVFs) are gaining attention due to their excellent transparency and potential for enhanced mechanical properties. This study synthesized copolymers CVF1-4 with varying branch content using soft monomers 2-ethylhexyl acrylate (2-EHA), butyl acrylate (n-BA), and functional monomer acrylic acid (AA). Employing a "grafting-through" strategy, small molecule monomers, ATRP-synthesized oligomer pBA25, and photoinitiator 1,6-hexanediol diacrylate (HDDA) were in-situ polymerized under UV light to form transparent, flexible elastic films CVF1-4. Between -20 to 80 °C, CVF1-4 demonstrated excellent mechanical properties such as low modulus (in the kPa range), low glass transition temperature (below -20 °C), large deformation (500-600%), and high strain recovery rate (>95%). Among them, CVF3 with 15% branching showed a balanced comprehensive performance, exhibiting primarily elastic behavior at room temperature. Therefore, selecting appropriate molecular composition and grafting structure provides a simple and customizable solution for optimizing CVF properties.

Keywords: Clear viscoelastic materials, Grafting, Flexibility, Photocrosslinking.

1. Introduction

Wearable electronic devices are cutting-edge products in artificial intelligence for health monitoring, diagnosis, and portable electronics [1]. As core components, electronic sensors capture physiological signals and convert them into visual electronic signals, effectively detecting human activities. Ideal wearable electronics need excellent softness to adapt to muscle movements and avoid irreversible deformations like bending, wrinkling, or breaking during use. Since they are in direct contact with the skin, they must also have low biotoxicity and removability, sometimes requiring high transparency for aesthetic reasons. However, traditional electronic sensors based on metallic conductors and other inorganic materials struggle to combine these advantages.

Organic materials for flexible strain sensors are typically lightweight and aesthetically pleasing with adjustable mechanical properties. Thermosetting resins like polyolefin elastomers are widely used in the industry due to their low cost, aging resistance, and stability. Solvent-based production methods may include plasticizers, potentially releasing harmful substances like formaldehyde. To balance softness and toughness, achieving reversible large deformations within the normal use temperature range requires attention to the composition and structure of the polymers.

2. Research Status and Background

The clear viscoelastic film (CVF) is a flexible polymer with excellent optical properties, such as high light transmittance and low haze, without the need for additional additives. It has been applied as an adhesive for foldable smartphone screens [2]. CVF is essentially a viscoelastic material, where there is always a trade-off between elastic and viscous properties. For instance, increasing the strain recovery rate often negatively impacts the elongation at break. To enhance reversible recovery and various mechanical strengths, the main approach currently is to incorporate additional processing agents and plasticizers into the CVF network to improve cohesion. However, many additives are cytotoxic and may reduce transparency, thereby limiting the material's application [3].

Grafting methods can improve or customize polymer properties without using additives or altering chemical composition. This is achieved by chemically bonding macromolecular branches or functional side groups to the polymer backbone, producing products that exhibit characteristics of both the main chain and side chains [4]. By properly controlling the branch composition, various properties such as strength and ductility can be effectively improved. This effect is similar to adding plasticizers, but graft structures do not migrate or leach out over time, preventing surface contamination and supporting the requirements of "green chemistry" [5].

The monomer composition, including types and content, affects various properties of acrylic CVF. For example, Seung-Suk Baek et al. [6] found that the structure of acrylic monomers influences the rigidity of the polymer backbone. The larger the free volume of substituents such as side chains, the lower the cohesion of the polymer, resulting in a decrease in tensile strength and other elastic properties. Ju Hak Lee et al. [7] used UV curing to copolymerize EHA with MA, AA, and HEA, respectively, and found that polymers containing AA had higher peel strength; adding MA achieved instant strain recovery with nearly zero hysteresis loss; however, organic solvent ethanol negatively affected the mechanical and optical properties of the copolymers.

Molecular weight is also associated with the viscoelasticity of acrylic CVF. Jung-Hun Lee et al. [8] found that increasing molecular weight can enhance intermolecular interactions through chain entanglement, as evidenced by various thermally initiated acrylic copolymers with molecular weights ranging from 86 kDa to 108 kDa, showing significantly enhanced viscoelasticity. Raghunath P. Ingale et al. [9] used reversible addition–fragmentation chain transfer polymerization (RAFT) to obtain EHA emulsion-type polymers with molecular weights of 2×105, 7×105, 14×105, and 20×105 Da. Their shear strength positively correlated with molecular weight, while peel strength first increased and then decreased, with the highest peel strength observed in products with a molecular weight of 7×105 Da.

Crosslinking forms network structures between molecular chains, allowing a wide range of adjustments to material properties, making it possible to prepare CVF with varying performance from a single raw material. Based on the reaction conditions, crosslinking agents are divided into thermal crosslinking agents like isocyanates and UV crosslinking agents like 1,6-hexanediol diacrylate (HDDA).

More flexible and elastic acrylic graft polymers have been extensively studied in recent years. Andrew Goodwin et al. [10] used the "grafting through" method, first synthesizing structurally defined poly(methyl methacrylate) (PMMA) side chains through living anionic polymerization, and then using RAFT to randomly copolymerize them with n-BA, achieving a product with a fracture elongation of 170% and a strain recovery hysteresis of less than 15%. Anastasia Mpoukouvalas et al. [11] combined "ATRP" and "grafting through" to introduce short pBA side chains into a uniformly crosslinked HEA network, obtaining a structurally defined super soft elastic material with high flexibility and rebound after large deformation, and a storage modulus in the elastic region of less than 5 kPa.

From the preparation system perspective, acrylic CVF is mainly realized through a free radical polymerization mechanism, primarily including solution polymerization and bulk polymerization. Gang Li et al. [18] explored the effects of different processes on solvent-based acrylic CVF, finding that segmented polymerization products had the best overall performance and higher reaction conversion

DOI: 10.54254/2755-2721/91/20241091

rates compared to graft polymerization and one-shot feeding methods. Heeyeon Moon et al. [12] initiated and in-situ crosslinked under thermal, UV, and combined conditions, successfully conducting solvent-free bulk polymerization to directly obtain acrylic copolymer films. They showed that the combination of both methods favored a more systematic adjustment of crosslink density, resulting in products with balanced viscoelasticity and good optical transparency, providing a feasible approach to obtaining environmentally friendly acrylic CVF.

3. Research Design

The rise of wearable devices has driven research on CVF. Currently, most research on acrylic CVF focuses on linear copolymers, with less attention to the impact of grafting. To explore the relationship between branch number and performance, this study constructed a model of acrylic copolymers with short branches and grafting gradients, aiming to improve deformation degree while balancing reversible recovery performance and mechanical strength, thereby expanding the application of CVF in flexible optical materials. To maintain CVF's transparency and biocompatibility, only acrylic monomers were used as copolymer raw materials and crosslinking agents without adding other additives. By using the "grafting-through" strategy and ATRP, macromolecular monomers with controllable polymerization degree ($n = 25$) were synthesized and polymerized using a solvent-free UV method to reduce cost and environmental pollution. The study compared the differences in rheological properties, reversible recovery performance, and tensile properties of CVFs with different branch contents, analyzing the impact of network structure and branch number on performance, providing a reference for optimizing CVF performance.

3.1. Specific Plan

A series of grafted acrylic CVFs were designed to systematically study their properties. Soft monomers n-butyl acrylate (n-BA, Tg=-56°C) and 2-ethylhexyl acrylate (2-EHA, Tg=-70°C), and hard monomer acrylic acid (AA, Tg=106°C) were mainly selected, adjusting the content of the three to make the copolymer's Tg below room temperature. The functional monomer AA contains highly polar -COOH, which can increase cohesion; thus, AA content does not exceed 10 wt% to maintain softness. To study the effect of branch content on CVF performance, four gradients of 0%, 5%, 15%, and 30% were set, synthesizing CVF1 (linear control) and CVF2/3/4 (graft structure). Short-chain macromolecular monomer (pBA25, polymerization degree 25) was used for "grafting-through" in-situ polymerization to prepare random copolymers. The composition and structure of the products were analyzed using gel permeation chromatography (GPC), Fourier-transform infrared spectroscopy (FTIR), nuclear magnetic resonance hydrogen spectroscopy (1H-NMR), and tested for tensile strength, creep recovery, rheological properties, and glass transition temperature to comprehensively evaluate the viscoelasticity and flexibility of CVF.

3.2. Technical Route

The designed acrylic CVF is based on a free radical polymerization mechanism. The overall preparation route is shown in Figure 1. Firstly, ATRP is used to prepare macromolecular monomers with the required polymerization degree, which are then polymerized with other small monomers in bulk polymerization, initiated and crosslinked under UV conditions to directly prepare films.

3.3. Technical Route

The acrylic CVF designed in this paper is based on the free radical polymerization mechanism. The overall preparation route is shown in Figure 1. First, the macromolecular monomer with the required degree of polymerization is prepared using ATRP. Then, it is bulk polymerized with other small molecule monomers, initiated and cross-linked under UV conditions, and directly formed into a film.

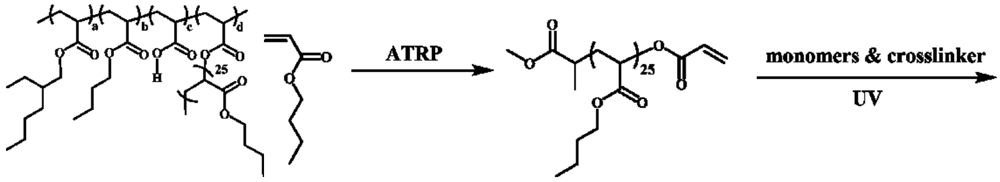

Figure 1. Technical Route

4. Preparation of Transparent Viscoelastic Body

(1)

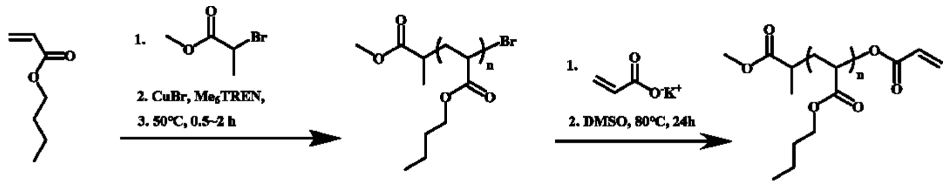

(2)

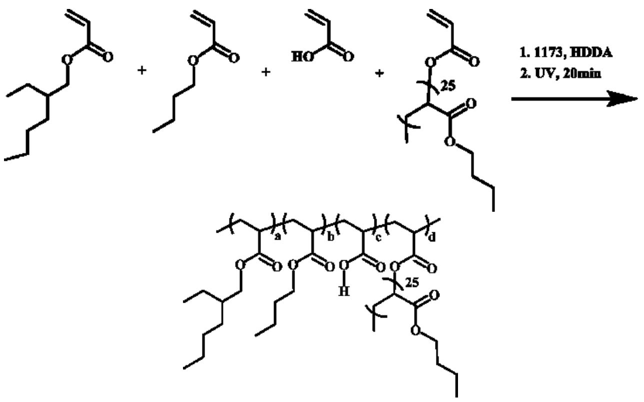

Figure 2. Preparation steps of acrylic viscoelastic body (a) synthesis of macromolecular monomer; (b) synthesis of graft copolymer

Dissolve the catalyst CuBr in purified BA according to the molar ratio [M]0:[I]0:[C]:[L]=25:1:0.05:0.05, add the initiator methyl 2-bromopropionate and Me6TREN, and rapidly inject into an anaerobic reaction system. Heat in a water bath to 50°C, stir at 200 rpm, and react for 20 minutes under nitrogen protection. After the reaction, add EAc to dissolve, filter three times through a sintered glass funnel and basic alumina, filter twice through petroleum ether, and rotary evaporate to obtain pBA25-Br. Dissolve pBA25-Br and potassium acrylate (molar ratio 3:1) in DMSO, stir for 24 hours in an 80°C oil bath for nucleophilic substitution reaction. Pour the product into ice water, stir, and layer, discard the upper aqueous phase, wash with KHCO3 solution to remove DMSO and potassium acrylate. Dissolve in DCM again, break the emulsion with NaCl aqueous solution, extract twice with DCM, dry and filter, and rotary evaporate to finally obtain pBA25.

Weigh the required monomers according to Table 4-3, add 1 g each of photoinitiator 1173 and crosslinker HDDA according to 0.1% of the mass of the acrylic copolymer backbone, and mix the prepolymer. Cut a suitably sized silicone frame and attach it to a 50μm thick silicone release film, clamp with an ultra-white glass plate, and then inject the above mixed liquid into the silicone frame, exhausting the air. Control the total energy of the photoreaction to 3000 mJ/cm², react under UV light with a power of 9.6 mW/cm² for 20 minutes to obtain the formed CVF gel film.

Table 1. Experimental Formulations

Ingredients	2-EHA(g)	n-BA(g)	AA(g)	pBA25 (g)
CVF_1	4.5	4.5	1	0
CVF_2	4.5	4.5	1	0.5
CVF_3	4.5	4.5	1	1.5
CVF_4	4.5	4.5	1	3

5. Experimental Results Analysis

This paper designs CVF1-4 with a gradient of short side chain mass fractions. The mass ratios of the comonomers are 2-EHA:n-BA:AA = 45:45:10:0, 45:45:10:5, 45:45:10:15, 45:45:10:30. The overall polymerized products are soft, transparent solid films similar in appearance, as shown in Figure 3.

Figure 3. Actual Product Image, from top to bottom: $CVF_{1\text{-}4}$

5.1. Gel Rate Analysis

The gel rate is expressed as the ratio of the remaining mass of CVF1-4 after swelling in a good solvent EA to the initial mass, reflecting the proportion of the cross-linked part. Physical cross-linking is mainly caused by hydrogen bonds between the carboxyl groups of AA and chain entanglement caused by intermolecular interactions; chemical cross-linking is derived from the stable network formed by the reaction with bifunctional HDDA. Table 2 shows that the gel rates of the four samples are all between 93% and 97%, indicating a good degree of cross-linking. Although the pBA25 content is different, due to the bridging effect of HDDA being superior to physical action, the difference in the degree of cross-linking is not significant. The gel rate of CVF4 is the lowest (93.48%), possibly due to a large number of short grafted polymers forming a brush structure, making chain cross-linking difficult. Because highly cross-linked copolymers are difficult to dissolve in solvents suitable for GPC, and the insoluble part exceeds 90%, GPC was not used to measure the molecular weight and distribution of $CVF_{1\text{-}4}$.

Table 2. Gel Rate of Grafted Transparent Viscoelastic Body

Sample	Gel Rate (%)
CVF_1	95.53
CVF_2	94.84
CVF_3	96.83
CVF_4	93.48

DOI: 10.54254/2755-2721/91/20241091

5.2. Structural Characterization

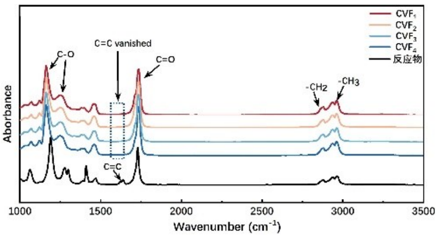

Figure 4. NMR spectra of the macromonomer.

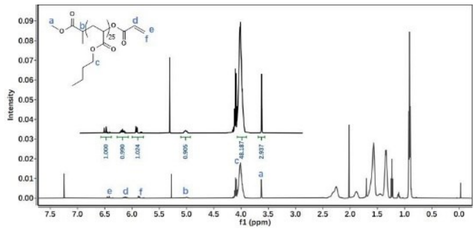

Figure 5. FTIR spectra of the acrylic copolymer and the reactive monomers.

To estimate the length of the grafted side chains, gel permeation chromatography (GPC) was first used to analyze the ATRP product pBA25-Br. The number average molecular weight was found to be 3512 Da, close to the theoretical value of 3385 Da; the weight average molecular weight was 4143 Da, with a polydispersity index of 1.180, indicating minimal chain transfer.

Nuclear magnetic resonance (NMR) spectroscopy revealed that peaks in the 2-2.5 ppm range correspond to the α-H of the carboxyl group in BA, peaks in the 1-2 ppm range are mainly from saturated aliphatic side chains, peaks in the 5.5-6.5 ppm range correspond to C=C double bonds after end group substitution, the peak at 5 ppm corresponds to the α-H of the initiator carboxyl group, the broad peak at 4.1 ppm is attributed to the α-H of the butyl group in BA, and the sharp peak at 3.6 ppm corresponds to -CH3 in the initiator. Combining integration area calculations, the yield of pBA25 was approximately 90.08%, with an absolute degree of polymerization of 24, indicating that the macromonomer was successfully synthesized via an active free radical method with a high yield. Fourier transform infrared spectroscopy (FTIR) analysis showed that the FTIR spectra of CVF1-4 exhibited absorption peaks of -CH3 and -CH2 (2860 cm-1, 2929 cm-1, 2959 cm-1), the carbonyl C=O absorption peak (1731 cm-1), and characteristic peaks of -C-O- (1170 cm-1 and 1250 cm-1). The characteristic peak of the C=C double bond (1636 cm-1) disappeared, indicating that the C=C bond participated in the free radical addition, and the final product no longer contained C=C bonds. In conclusion, the acrylic CVFs were successfully synthesized, conforming to the molecular structure characteristics of the copolymer P(AA-co-2-EHA-co-n-BA).

5.3. Rheological Properties

From the perspective of viscoelasticity analysis, increasing the viscosity of CVF leads to a reduction in elasticity. The viscosity of the polymer is related to the loss modulus (G"), while elasticity is related to the storage modulus (G'). When G" is greater than G', the loss factor (tan δ = G"/G') is greater than 1, indicating that viscosity is dominant, and the polymer will exhibit stress relaxation under external force, leading to energy dissipation and irreversible deformation when the external force is removed, which is unfavorable in practical applications.

Considering the operating temperature range of wearable electronics from -20°C to 80°C, this study tested the rheological behavior of four CVF samples from -50°C to 150°C, obtaining curves of storage modulus (G'), loss modulus (G"), and loss factor (tan δ) with temperature (see Figure 5 and Table 3). Figure 5(a) shows that the storage modulus of the four samples is large at low temperatures, rapidly decreases with increasing temperature, reaches its maximum at -50°C, approaches zero at room temperature, and then remains stable. The variation trend of the loss modulus with temperature is similar in Figure 5(b).

At -50°C, 25°C, and 150°C, the moduli of CVF1-4 decrease sequentially, with CVF1 having the highest modulus and CVF4 being the softest but with poorer mechanical performance. As the graft content increases, the polymer chains' mobility enhances, making chain relaxation or slippage easier. The moduli of CVF1-4 at 25°C are less than 100 kPa, and are nearly zero at high temperatures, but do not lead to a viscoplastic state, indicating good pressure-sensitive properties.

DOI: 10.54254/2755-2721/91/20241091

Figure 5(c) shows that the loss factor-temperature curves also exhibit a similar trend: tan δ rises sharply at -30°C and -20°C, then gradually decreases. At 25°C, tan δ is much less than 1, and even when heated to 150°C, the proportion of viscosity does not increase, because hydrogen bonding between -COOH groups hinders chain mobility, contributing more to elasticity. Therefore, CVF primarily exhibits elasticity at room temperature, with overall stable viscoelasticity within the operating temperature range. The glass transition temperature (Tg) is the most crucial parameter for determining the minimum operating temperature of CVF; polymers exhibit viscous liquid state below Tg. The peak of the tan δ-T curve in Figure 5(c) corresponds to Tg, showing that all curves have only one glass transition temperature peak without significant peak width change, indicating the formation of a random copolymer among the reactants. The Tg values of CVF1-4 are all below -20°C, being -22.60°C, -24.94°C, -25.69°C, and -29.39°C respectively. Considering the Tg values of the copolymer monomers AA, 2-EHA, and n-BA are 106°C, -70°C, and -56°C respectively, according to the Fox equation (5-1):

$$\frac{1}{T_g} = \frac{W_1}{T_{g1}} + \frac{W_2}{T_{g2}} + \frac{W_3}{T_{g3}} + \cdots \ldots \tag{5-1}$$

The Tg of the copolymer can be predicted, decreasing with increasing graft content because the increase in graft structure dilutes the hydrogen bonds between AA components, enhancing molecular chain mobility. Additionally, pBA25 used for grafting is a soft segment with a low Tg, leading to a significant overall Tg reduction, making the product softer.

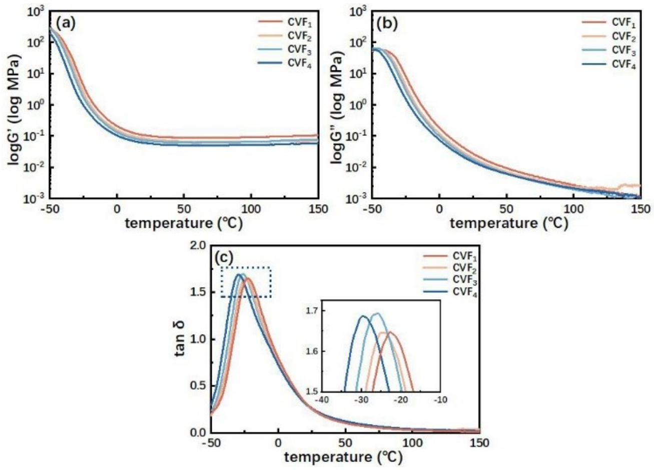

Figure 6. Temperature dependence of (a) storage modulus; (b) loss modulus; (c) loss factor of the grafted transparent viscoelastic body.

5.4. **Continuous Tensile Cycles**

Wearable electronics undergo significant bending and folding during use; therefore, their flexible substrates need to possess good reversible strain recovery to avoid buckling or wrinkling caused by residual strain. To characterize this performance of the acrylic CVF, this study examines the stress-strain relationship of the material during loading-unloading applications through continuous tensile cycles.

Overall, the room temperature cyclic process of four CVFs with different numbers of side chains exhibited reproducibility, as the curves obtained from ten consecutive experiments showed no significant differences. The maximum stress (stressmax) did not decrease at the maximum strain, and the stress at the initial strain point was almost at the original zero point, indicating that the prepared CVFs possess excellent recovery performance.

Figures 6(a), (b), and (c) respectively show the stress-strain curves of the four samples during the first, fifth, and tenth cycles. From these figures, it can be seen that with the increase in side chain content, the peak stress of the samples decreases sequentially. CVF1 has the highest peak stress, reaching 0.161 MPa, followed by CVF2 and CVF3 at 0.121 MPa and 0.0917 MPa, respectively. CVF4 has the lowest peak stress among the four, at 0.0675 MPa. As the number of short side chains composed of the soft

DOI: 10.54254/2755-2721/91/20241091

monomer BA increases, the Tg decreases, the material becomes softer, and its ability to resist stress diminishes.

In this study, the initial strain (Ɛn+1) at which stress begins to develop in the (n+1)th cycle is used as the residual strain for the nth cycle, according to equation (4-2).

$$R_n = \frac{300\% - \varepsilon^{n+1}}{300\%} \times 100\% \tag{5-2}$$

The strain recovery rates (R) for CVF1-4 during the first, fifth, and ninth cycles are shown in Table 3. CVF1-4 rarely exhibited yielding behavior, with strain recovery rates close to 100%. CVF1-4 nearly fully recovered in each loading-unloading cycle, with minimal irreversible breakage of weak bonds. Even after continuous cycling, the strain recovery rate only slightly decreased after nine cycles. For example, in CVF3, this value decreased from 95.46% to 95.05%, further demonstrating that CVF1-4 exhibit good elasticity within the testing range.

It was also found that CVFs, being viscoelastic materials, exhibit significant hysteresis behavior, with distinct differences between the loading and unloading stress-strain curves. This is due to energy dissipation caused by molecular chain friction during stretching, as well as hydrogen bonds and intermolecular forces within the CVFs. The hysteresis rate (H) reflects the sample's ability to recover elasticity and is related to the contribution of viscoelasticity: the greater the elasticity, the lower the hysteresis rate. CVF1 has the lowest hysteresis rate due to its fewer short side chains and higher density of intermolecular interactions and hydrogen bonds, demonstrating greater elasticity. The hysteresis rates of CVF2 and CVF3 are slightly higher and similar to each other, while CVF4 has the highest hysteresis rate, indicating a greater proportion of viscosity. As the number of cycles increases, the hysteresis rate of all samples decreases. Covalent bond breakage may occur in the initial cycle, but subsequent cycles mainly dissipate energy through hydrogen bonds or polar groups. This process is slow, and the properties tend to stabilize in subsequent cycles.

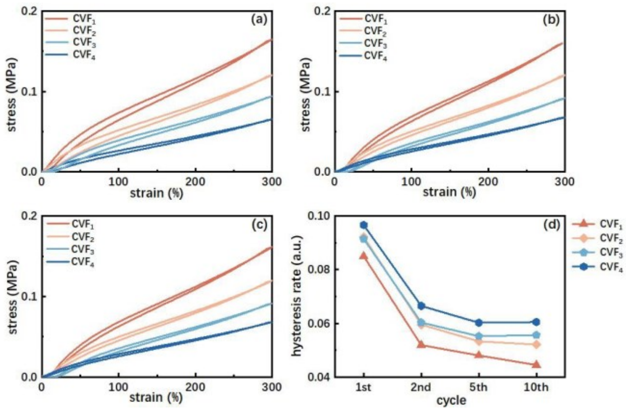

Figure 7. Grafted Transparent Viscoelastic Material (a) First Tensile Cycle (b) Fifth Tensile Cycle (c) Tenth Tensile Cycle (d) Hysteresis Rate

Table 3. Experimental Formulations

Sample	$stress_{max}$ (MPa)	R_1 (%)	R_5 (%)	R_9 (%)	H_1 (a.u.)	H_2 (a.u.)	H_5 (a.u.)	H_{10} (a.u.)
CVF_1	0.161	98.11	97.90	97.83	0.0850	0.0519	0.0480	0.0445
CVF_2	0.121	97.83	97.77	97.70	0.0922	0.0595	0.0533	0.0521
CVF_3	0.0917	95.46	95.39	95.05	0.0915	0.0603	0.0552	0.0556
CVF_4	0.0675	98.30	98.04	97.90	0.0966	0.0665	0.0602	0.0605

5.5. Research Summary

A series of grafted acrylic CVFs were successfully prepared through "grafting-through" and UV-initiated crosslinking. The products CVF1-4 consist of acrylic monomers, with short side chain structures imparting flexibility and viscosity. 2-EHA (Tg = -70 °C) and n-BA (Tg = -56 °C) provide primary flexibility, while the functional monomer AA (Tg = 106 °C) creates high-density hydrogen bonds. The addition of the crosslinking agent HDDA results in a gel rate of 93-97%, further enhancing the mechanical properties and stability of the samples.

To investigate the effect of grafting on viscoelastic properties, short side chains of pBA25 were introduced into the CVF backbone in mass fractions of 0%, 5%, 15%, and 30%, yielding four products: CVF1-4. At room temperature, their moduli are in the kPa range, with glass transition temperatures below -20 °C, and deformations reaching 500-600%, with nearly 100% reversible strain recovery. The products exhibit stable viscoelasticity within the -20~80 °C range, showing more elasticity at 25 °C. An increase in grafting quantity leads to softer CVFs, a decrease in glass transition temperature (from -22.60 °C to -29.39 °C), a maximum fracture strain of 572.442%, and a shear creep of 51.76%. However, the samples' Young's modulus, storage modulus, and loss modulus decrease at the same temperature, and the hysteresis rate of reversible tensile cycles increases, indicating that more side chains reduce elastic performance.

In summary, CVF3, with a moderate graft content, exhibits the best performance among the four samples, showing good and balanced viscoelasticity within the operational temperature range.

6. Conclusion

High-transparency acrylic CVFs with clear short grafted structures and high-density crosslinked networks were successfully synthesized based on the free radical reaction mechanism. The random copolymer products CVF1-4 exhibit a single, low glass transition temperature, making them suitable for a wide temperature range. As viscoelastic materials, they possess good and enduring stable mechanical properties, capable of multiple deformation and recovery cycles, and rarely exhibit irreversible damage under large deformations.

Due to different graft content ratios and similar gel rates, CVF1-4 display unique mechanical properties. Overall, as the short side chains of pBA25 increase, the density of functional carboxyl groups capable of forming hydrogen bonds decreases, making the acrylic CVFs softer. Although they can undergo greater deformations, their ability to recover reversible strain declines, and they struggle to resist significant stress.

In this study, the modulus decrease caused by increased side chains seems highly influenced by the copolymer composition, varying with different circumstances, and requires further research. For example, although pBA25 as a side chain structure expands the molecular chain volume and can dilute intermolecular hydrogen bonds and other forces, reducing cohesive forces by lowering crosslinking density, CVF3, containing 15% side chains, shows the highest fracture stress and initial adhesion, possibly due to its slightly higher gel rate compared to the other three, having a more significant effect in these aspects than crosslinking density. Additionally, the overall performance difference between CVF1 without grafting and CVF2 with 5% side chains is minimal, possibly because the BA monomer itself has shorter and smaller side chain groups, which are less effective in reducing chain entanglement and friction caused by hydrogen bonds compared to copolymer monomers like 2-EHA with larger side groups [13]. BA homopolymers are more prone to entanglement than BA-EHA copolymers of the same molecular weight. Adding more BA monomers might reduce the mobility of polymer chains, but no definitive studies have yet clarified the relationship between the two.

An ideal CVF should have high fracture strength to avoid potential damage in practical applications and a large fracture elongation to accommodate significant deformations during folding. Therefore, to achieve CVFs with excellent comprehensive performance, an appropriate molecular composition and structure should be selected to balance its mechanical properties, such as viscosity and elasticity, ultimately enabling applications in flexible sensors.

References

[1] Qian Xin, Su Meng, Li Fengyu, et al. Advances in Research on Flexible Wearable Electronic Sensors [J]. Journal of the Chinese Chemical Society, 2016, 74(07): 565-575.

[2] Jin Bin, Zhang Peng, Xia Jianhui. Study of Acrylic Optical Transparent Viscoelastic Materials for Flexible Displays [J]. Adhesion, 2022, 49(06): 1-6.

[3] Czech Z. Synthesis and cross-linking of acrylic PSA systems[J]. Journal of Adhesion Science and Technology: The International Journal of Theoredtical and Basic Aspects of Adhesion Science and Its Applications in All Areas of Technology,2007,21(7):625-635.

[4] Mitchell M, Erfan D, N A K, et al. Sticky Architecture: Encoding Pressure Sensitive Adhesion in Polymer Networks. [J]. ACS central science,2023,9(2):197-205.

[5] Sylwia D ,Francesca L ,Adam G , et al. Toward Green Atom Transfer Radical Polymerization: Current Status and Future Challenges. [J]. Advanced science (Weinheim, Baden-Wurttemberg, Germany),2022,9(19):e2106076-e2106076.

[6] Baek S, Jang S, Hwang S. Preparation and adhesion performance of clear acrylic pressure sensitive adhesives: effects of substituent structure of acrylate monomer[J]. International Journal of Adhesion and Adhesives,2016,64:72-77.

[7] Lee H J, Myung H M, Baek J M, et al. Effects of monomer functionality on physical properties of 2-ethylhexyl acrylate based stretchable pressure sensitive adhesives[J]. Polymer Testing,2019,76:305-311.

[8] Lee J, Lee T, Shim K, et al. Molecular weight and crosslinking on the adhesion performance and flexibility of acrylic PSAs[J]. Journal of Adhesion Science and Technology, 2016, 30(21): 2316-2328.

[9] Ingale P R, Jagtap N R, Adivarekar V R. Effect of Molecular Weight on Performance Properties of Pressure-Sensitive Adhesive of Poly (2-ethylhexyl acrylate) Synthesized by RAFT-Mediated Miniemulsion Polymerization[J]. The Journal of Adhesion,2016,92(3):236-256.

[10] Wang W, Lu W, Goodwin A, et al.Recent advances in thermoplastic elastomers from living polymerizations: Macromolecular architectures and supramolecular chemistry[J].Progress in Polymer Science,2019,95:1-31.

[11] Anastasia M, Wenwen L, Robert G, et al. Soft Elastomers via Introduction of Poly (butyl acrylate) “Diluent” to Poly (hydroxyethyl acrylate)-Based Gel Networks[J]. ACS Macro Letters, 2013, 2(1):23-26.

[12] Heeyeon M, Kihoon J, Jin M K, et al.Solvent-free Deposition of Ultrathin Copolymer Films with Tunable Viscoelasticity for the Application to Pressure Sensitive Adhesives.[J].ACS applied materials interfaces,2018,10(38):32668-32677.

[13] Dongdong W, Jiapeng L, Fushi L, et al. Solvent-free and biodegradable pressure-sensitive adhesive based on chlorosulfonated Poly (propylene carbonate) [J]. Polymer, 2023, 286: 126418-126418.

DOI: 10.54254/2755-2721/91/20240953

The future of flying: Explore more energy-efficient airplane wings

Albert Liu

Singapore International School Hong Kong, Hong Kong, China

18600048006@vip.163.com

Abstract. In recent years, there has been a substantial rise in the popularity of air travel, bringing with it a surge in the consumption of jet fuel, a nonrenewable resource responsible for 2.4% of global carbon emissions. As air travel continues to gain prevalence, the anticipation of a significant increase in carbon emissions and a subsequent surge in jet fuel costs looms large. Maintaining affordability in air travel while mitigating carbon emissions necessitates a focus on maximizing airfoil efficiency. This study investigates how airplane wing design affects the aerodynamic performance of aircraft, with a specific focus on the impact of wing angle of attack, wing length, and winglets. In this research, this study use Computational Fluid Dynamics software to simulate and analyze the aerodynamic forces acting upon an aircraft to deduce its drag and lift coefficients. Employing diverse fluid dynamics formulas, the research calculates the aerodynamic performance of various aircraft airfoil designs, aiming to identify the optimal design. The envisioned optimal configuration is likely to feature an elongated wing, a 20° angle of attack, and suitable winglets stalled, strategically incorporated to enhance overall efficiency in air travel.

Keywords: Aerodynamics, Force Analysis, Computational Fluid Dynamics, Aircraft Wing Design, Winglet

1. Introduction

1.1. Background

Airplanes stand out as the most efficient and also safest way of travel in the modern world. This is because of its remarkable speed which allows this study to cover extensive distances within a few hours. Accidents are also infrequent with only 5 fatal accidents among 32.2 million flights in 2022 [1]. Each aircraft has a pair of huge wings, which could generate enough lift to help the airplane overcome gravity. However, the large size of the wings also creates a large drag force, which greatly increases the consumption of fuel. So how to design airplane wings that could provide needed lift force but also have less drag force is an essential research topic. The airplane wing usually adopts the airfoil design, and the basic cross-section of an airfoil is shown in Figure 2. Hence, the airfoil wing's design is essential for an aircraft's performance. Increasing the lift and decreasing the drag can dramatically increase an aircraft's fuel efficiency, reducing carbon emissions and making air travel more affordable. This is important because most modern aircraft run on kerosene which is a non-renewable resource. Meanwhile, air travel makes up 2.4% of the global CO_2 emissions [2]. By increasing the efficiency, not only can the amount

DOI: 10.54254/2755-2721/91/20240953

of CO2 emitted in the air be reduced, but this study can also make airplanes have better efficiency. As this study anticipate the proliferation of supersonic airplanes in the near future, capable of speeds exceeding 330 meters per second, the importance of efficiency becomes even more pronounced. Increased efficiency plays a vital role in mitigating resistance on the aircraft, especially at such high speeds. The broader impact of enhancing efficiency extends beyond mere travel convenience; it opens up air travel accessibility to a wider demographic, making it affordable for many individuals worldwide. Simultaneously, it contributes to maintaining a healthier environment for all life on Earth. Therefore, the pursuit of increased efficiency in air travel emerges as a key imperative for both social and environmental considerations.

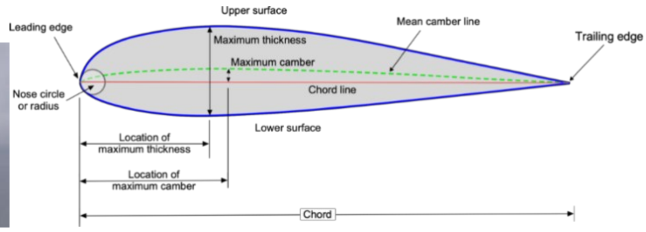

Figure 1. Boeing 747 Airplane [3]. **Figure 2.** Aircraft Airfoil Structure [4]

1.2. Literature Review

Many investigations on the aerodynamic performance of aircraft wings have been done. For example, in the paper "Proverse Yaw Characteristics of a Powered Blended Wing Body Aircraft of a Novel Design and Manufacture". The author used model aircraft and conducted flights to collect valuable data. The investigation involved testing various stabilizers and flaps to assess their impact on the aerodynamic behavior of the aircraft. In another paper titled "Development of a Rotor with Improved Aerodynamics to Propel a Quadcopter". the author delved into the influence of altering rotor shape on the aerodynamic performance of a quadcopter rotor. Utilizing 3D-printed rotors, the author conducted systematic tests on dedicated test stands to evaluate their performance. Additionally, this research scrutinized the effects of integrating winglets into the rotor design, providing insights into how such modifications can impact overall aerodynamics. In the study titled "Wing Design", the authors author explored the impact of altering the position, shape, and angle of attack of wings on aerodynamic performance. The paper delved into the effects of various wing configurations, including high-wing, mid-wing, low-wing, and parasol wings. Additionally, the author discussed crucial parameters such as aspect ratios and taper ratios, shedding light on their influence. In a parallel investigation, the paper titled "Aerodynamic Design Optimization Studies of a Blended-Wing-Body Aircraft"[9] focused on the effects of wing design for a blended wing-body aircraft. Utilizing Computational Fluid Dynamics (CFD), the study examined the implications of different wing designs and investigated the influence of changing speeds on these designs. The research contributes valuable insights into optimizing the aerodynamic performance of blended wing body aircraft through meticulous design considerations and CFD analysis.

1.3. This study

In this study, this study explores the impact of altering some key parameters—specifically, wing angle of attack, wing length, and the incorporation of winglets—on the drag and lift characteristics of a fixed-wing aircraft. The wing length is defined as the distance between the front and the back of the wing, while the angle of attack represents the angle formed by the airfoil and the direction of the freestream flow. Additionally, the study investigates the aerodynamic effects of winglets, small wings positioned at the wing's end, designed to enhance the aircraft's lift generation capabilities. My hypotheses are as follows: wing angle of attack, wing length, and winglet could have great effects on the aerodynamic performance of the airplane, and increasing the angle of attack will result in elevated levels of both lift and drag. Moreover, augmenting the wing length is anticipated to enhance lift with minimal impact on overall aerodynamic performance. Lastly, the addition of a winglet is hypothesized to marginally increase drag but significantly boost lift by mitigating turbulence along the wing's edge. This hypothesis is grounded in the expectation that the winglet will contribute to reducing turbulence, thereby positively influencing lift generation.

2. Methodology

In this section, this study introduces the governing equations that dictate fluid motions, providing insights into the underlying mechanisms governing the aerodynamic performance of aircraft. This discussion not only serves to elucidate the intricacies of aerodynamics but also offers a rationale for its utility in minimizing drag. The same set of equations is subsequently employed as a fundamental tool in the simulation phase to model and analyze the dynamic behavior of fluid motion. Consequently, it becomes imperative to illustrate the derivation and application of these equations within the simulation framework, highlighting their crucial role in understanding and predicting the aerodynamic characteristics of fixed-wing aircrafts.

2.1. General Approach to Research on Fluid Dynamics

The two most common research approaches to investigate the aerodynamic performance of an aircraft: Wind Tunnel Experiments and Computational Fluid Dynamics (CFD) Simulation. In CFD, computer software is used to calculate the performance of an aircraft model through simulation. In this study, Solidworks is used for the 3D modeling and CFD simulations of the model. Wind Tunnel Experiments, on the other hand, use a miniature model inside of a real wind tunnel which represents the real conditions of an actual flight. CFD is generally more accessible and cost- effective to conduct, however, it is quite limited and can only simulate phenomena to a certain extent. Wind Tunnel Experiments demand extensive preparation and involve the use of more costly equipment compared to CFD simulations. For this study, this study has chosen to employ CFD over Wind Tunnel Experiments due to its ease of setup, repeatability, and the absence of a need for advanced equipment.

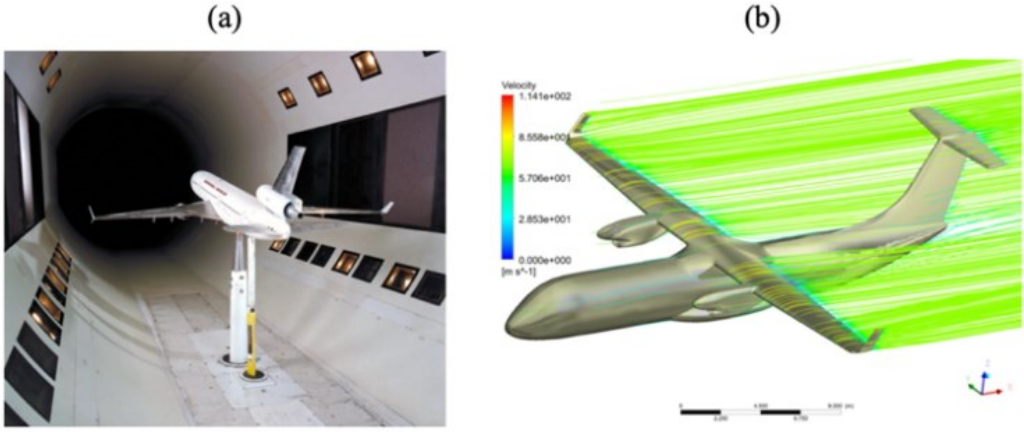

Figure 3. (a) NASA wind tunnel with the scale model of the MD-11 wide-body airliner [10], and (b) CFD simulation [11]

2.2. Principles of Fluid Dynamics

- **Mass conservations.**

The mass conservation states that for an arbitrary control volume, the net rate of mass increase within the volume is equal to the net mass flux into the volume. For example, in the infinitesimal control volume as shown in Figure 4, the rate of mass increase is $\frac{\partial(\rho dxdydz)}{\partial t}$. The net mass flux into the volume in the x-direction is calculated by subtracting the outflow rate from the inflow rate,

$$\rho v_x dydz - (\rho v_x dydz) + \frac{\partial(\rho v_x dydz)}{\partial x} dx = -\frac{\partial(\rho v_x)}{\partial x} dxdydz \tag{1}$$

And similarly, the net mass flux into the volume in *y*- and *z*- directions are:

$$y \text{ direction: } -\frac{\partial(\rho v_y)}{\partial y}\mathrm{d}x\mathrm{d}y\mathrm{d}z \tag{2}$$

$$z \text{ direction: } -\frac{\partial(\rho v_z)}{\partial z}\mathrm{d}x\mathrm{d}y\mathrm{d}z \tag{3}$$

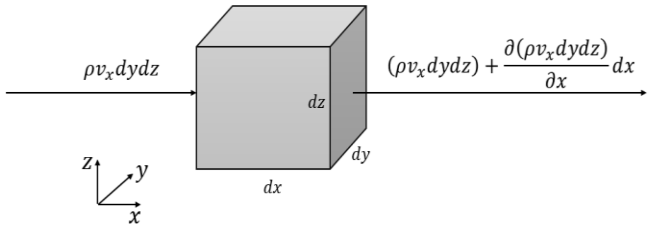

Figure 4. Taking *x* Direction as an Example Showing Mass Conservation in the Infinitesimal Control Volume

Summing the net mass fluxes into the volume in three directions (Equations 1-3) yields the total net mass fluxes, which equals to the rate of mass increase in the control volume,

$$-\frac{\partial(\rho v_x)}{\partial x}dxdydz - \frac{\partial(\rho v_y)}{\partial y}dxdydz - \frac{\partial(\rho v_z)}{\partial z}dxdydz = \frac{\partial\rho}{\partial t}dxdydz \tag{4}$$

By eliminating the term $dxdydz$, it simplifies to

$$-\left[\frac{\partial(\rho v_x)}{\partial x} + \frac{\partial(\rho v_y)}{\partial y} + \frac{\partial(\rho v_z)}{\partial z}\right] = \frac{\partial\rho}{\partial t} \tag{5}$$

For the general incompressible fluid flow, which is the case of my study, the fluid density is a constant value, i.e., $\rho = const$. Consequently, the rate of mass increase $\frac{\partial\rho}{\partial t} = 0$. This condition allows the expression of mass conservation as,

$$\frac{\partial v_x}{\partial x} + \frac{\partial v_y}{\partial y} + \frac{\partial v_z}{\partial z} = 0 \tag{6}$$

- **Momentum conservation**

The law of momentum conservation, an extension of Newton's 2nd Law, can be derived by expanding the equation of continuity in conjunction with the Newton's 2nd law. Given its vector nature, it can be decomposed into forces on each of the three dimensions. In general, the anticipated forces, including viscosity, pressure, and gravity, can be expressed in the following equations:

$$\mathrm{F} = \mathrm{ma} \tag{7}$$

$$x \text{ direction: } \rho\left(\frac{\partial v_x}{\partial t} + v_x\frac{\partial v_x}{\partial x} + v_y\frac{\partial v_x}{\partial y} + v_z\frac{\partial v_x}{\partial z}\right) = \mu\left[\frac{\partial^2 v_x}{\partial x^2} + \frac{\partial^2 v_x}{\partial y^2} + \frac{\partial^2 v_x}{\partial z^2}\right] - \frac{\partial p}{\partial x} \tag{8}$$

$$y \text{ direction: } \rho\left(\frac{\partial v_y}{\partial t} + v_x\frac{\partial v_y}{\partial x} + v_y\frac{\partial v_y}{\partial y} + v_z\frac{\partial v_y}{\partial z}\right) = \mu\left[\frac{\partial^2 v_y}{\partial x^2} + \frac{\partial^2 v_y}{\partial y^2} + \frac{\partial^2 v_y}{\partial z^2}\right] - \frac{\partial p}{\partial y} + \rho g_y \tag{9}$$

$$z \text{ direction: } \rho\left(\frac{\partial v_z}{\partial t} + v_x\frac{\partial v_z}{\partial x} + v_y\frac{\partial v_z}{\partial y} + v_z\frac{\partial v_z}{\partial z}\right) = \mu\left[\frac{\partial^2 v_z}{\partial x^2} + \frac{\partial^2 v_z}{\partial y^2} + \frac{\partial^2 v_z}{\partial z^2}\right] - \frac{\partial p}{\partial z} \tag{10}$$

- **Bernoulli Principle**

$$P_1 + \frac{1}{2}\rho v_1^2 + \rho g h_1 \& = P_2 + \frac{1}{2}\rho v_2^2 + \rho g h_2 \#(11)$$

Bernoulli's principle states that an increase in the speed of a fluid occurs simultaneously with a decrease in pressure or a decrease in the fluid's potential energy. The principle is named after Daniel Bernoulli, a Swiss mathematician, who published it in 1738 in his book Hydrodynamics. This principle holds significant importance in the field of aircrafts. It serves as the foundational concept enabling aircraft to generate lift, a crucial factor in achieving flight.

2.3. Force Analysis

The primary forces that are acted upon an aircraft are drag, lift, gravity, and thrust. Drag is a force that pushes the aircraft in a direction opposing to the direction of motion. Drag poses a detrimental impact on the aerodynamic performance of an aircraft and should be minimized whenever possible. Trust pushes the aircraft forward and acts in the opposite direction of drag. Gravity is the force that attracts all objects with mass toward each other, pulling the aircraft toward the ground due to Earth's gravitational attraction. Lift generated by the Bernoulli effect, acts in the upward direction, countering the force of gravity. Lift counters gravity and should be maximized for improving the aerodynamic performance.

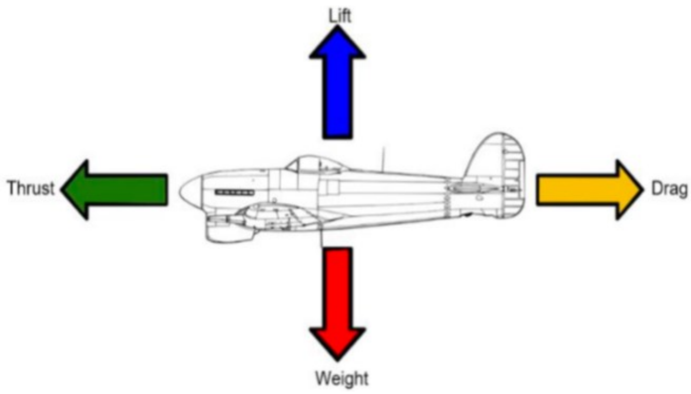

Figure 5. Forces Acted Upon an Aircraft.

The Drag and Lift coefficients are formulas that are used to quantify an object's capacity to generate drag and lift forces. The reason why drag coefficient and lift coefficient instead of drag and lift are used is because there are many factors affecting the amount of drag generated by an object. However, the significance of an object's capacity to generate drag or lift would be more important when considering its impact on aerodynamic performance.

The Drag Coefficient is defined as:

$$c_d = \frac{2F_d}{\rho u^2 A} \quad (12)$$

The lift coefficient is defined as:

$$c_l = \frac{2F_l}{\rho u^2 A} \quad (13)$$

Here C_d is the Drag coefficient, C_l is the lift coefficient. F_d is Drag(N). F_l is lift(N). u is speed(m/s). ρ is the the fluid density(kg/m^2). A is the reference area(m^2).

DOI: 10.54254/2755-2721/91/20240953

2.4. *Utilized Software*
SolidWorks is a 3D CAD design software developed by Dassault Systèmes. Widely employed for various design applications, it serves as a robust tool for individuals designing a range of objects and structures. SolidWorks enables this study to design model airplanes and simulate their performance in flight. The flow simulation tool allows this study to simulate an aircraft in the air and obtain information on the various forces acting upon it.

3. Results and Discussion
In this section, this study first elucidates the methodologies employed for aircraft model development, simulation procedures, and finally the presentation of investigation results.

3.1. *Model Development:*
To conduct the simulation and analysis, this study needs to create aircraft models. Firstly, this study creates a sketch of the aircraft body as shown in Figure 6. This study only makes half of a cross section because, the sketch can then be extended into a full body using the rotation tool.

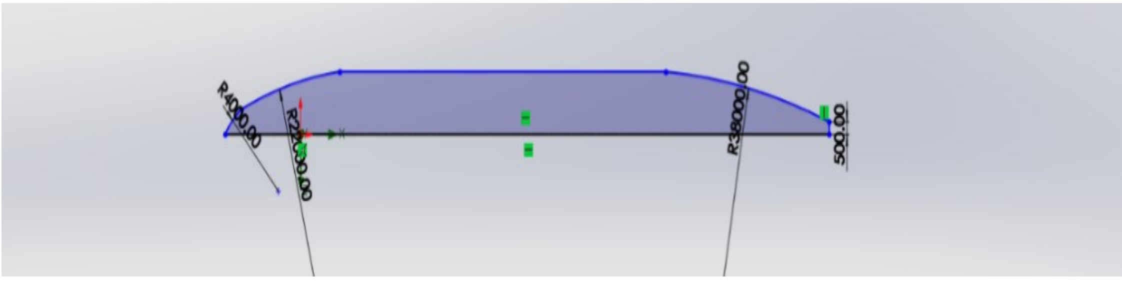

Figure 6. The Cross-section of an Airplane Body.

Next, this study initiates the airfoil design process by sketching the airfoil on the side of the aircraft body, as depicted in Figure 7. Utilizing the extrude tool, this study transforms the sketch into a three-dimensional object. Employing the symmetry tool, this study generates an identical copy of the airfoil on the opposite side of the aircraft body. Subsequently, this study replicates the procedure on the rear section of the plane, incorporating a smaller wing to craft rudders. The tail fin is then fashioned, featuring a single wing positioned above the rear of the aircraft, as illustrated in Figure 7.

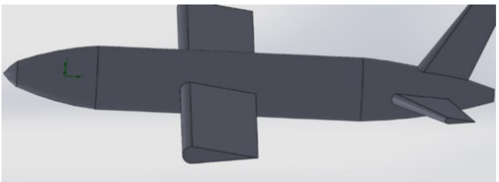

Figure 7. Aircraft Body with Wing.

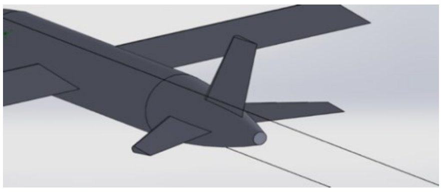

Figure 8. An Airplane Tail Fin

3.2. *General Simulation Procedure*
I first need to open the Solidworks flow simulation page to run simulations. Then this study uses the wizard tool and create a CFD flow simulation and apply custom settings. After that, the simulation page opens, this study can rename the simulation and give it a description as shown in Figure 9. This study then clicks "continue" and select the units. This study selects the SI units because it is the one this study am most familiar with and click "continue".

DOI: 10.54254/2755-2721/91/20240953

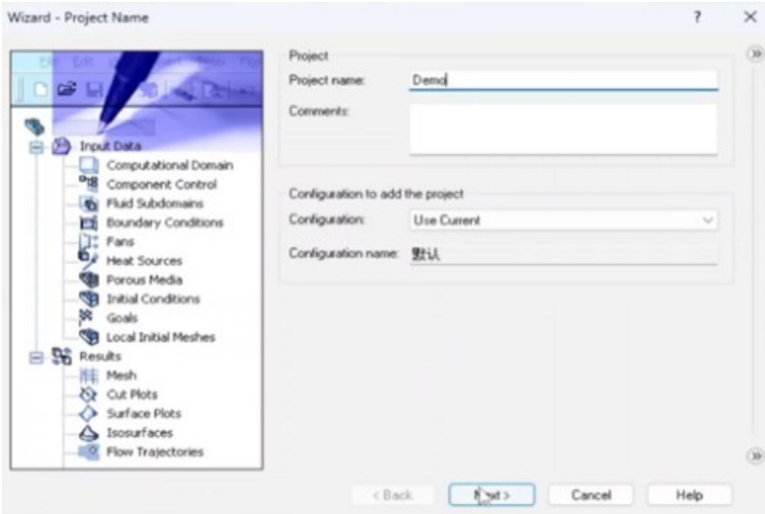

Figure 9. The Simulation Page

For the next step, this study chose the simulation type as external flow simulation mode as depicted in Figure 10 and proceed by selecting “continue”. In external flow simulation mode, the fluid is simulated to interact with the external surfaces of the object rather than within its internal spaces. In this research, this study employs the external flow simulation mode at default settings.

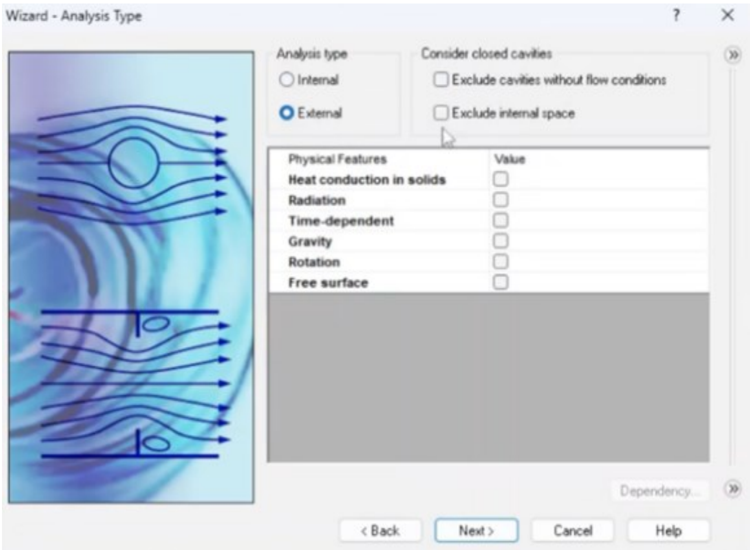

Figure 10. Picking the External Flow Simulation Mode

I proceed by clicking the plus sign next to “gases” and selecting air, as illustrated in figure 11. It's noteworthy that the default air setting in SolidWorks represents atmospheric pressure at sea level on Earth.

DOI: 10.54254/2755-2721/91/20240953

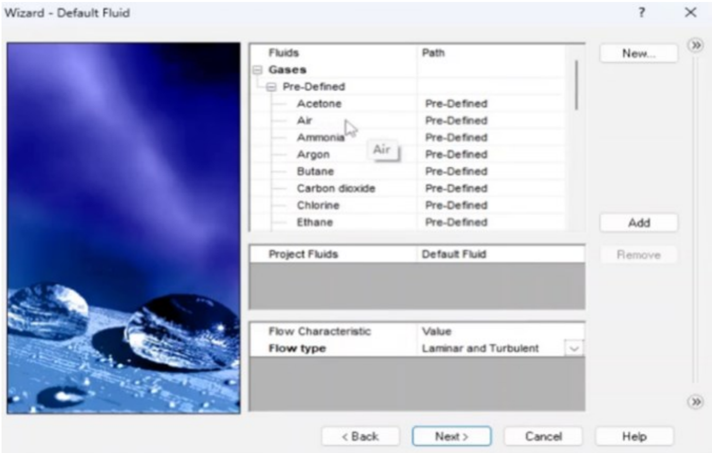

Figure 11. Picking Air as the Simulation Fluid.

On the initial environment conditions page, this study need to set the speed to 100 m/s which is my experimental velocity, as demonstrated in figure 12. Opting for a velocity of 100 m/s is a good speed is considered suitable for experimentation as it effectively simulates realistic flight conditions for an aircraft while maintaining a reasonable simulation time. This study then clicks complete, finalize the setup and prepare to commence the simulation.

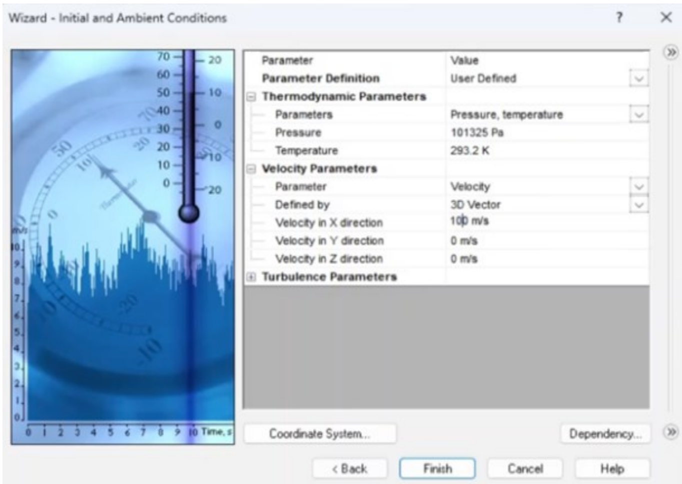

Figure 12. Setting the Speed

After that, this study defines the boundary conditions by selecting all the faces on the plane and switch the boundary type to “real wall” as shown in Figure 13 “Real wall” is a condition that simulates if the object was a solid object in real life with no microscopic bumps on its surface.

DOI: 10.54254/2755-2721/91/20240953

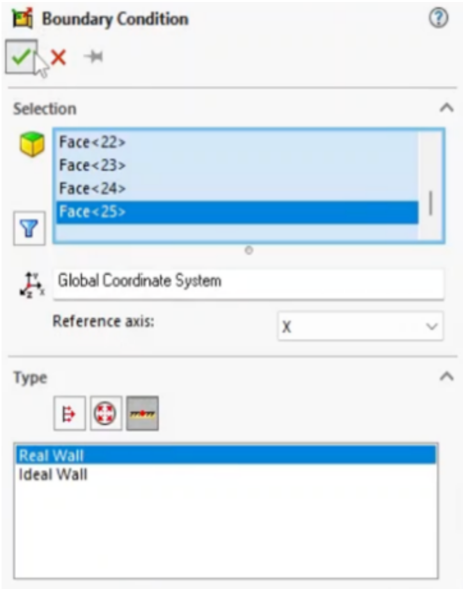

Figure 13. Defining Boundary Conditions

Figure 14. Computational Domain Settings

After that, this study set the computational domain. to the values 450 m, -150 m for X direction, 6 0m, -60 m for Y direction, and 40 m, -40 m for Z direction. This is a reasonable range for conducting simulations as this study want to analyze the flow around the airplane, so this study needs enough space for the flow to be fully developed.

Now this study inserts the simulation global goals. This study selects the drag and lift as shown in figure 15. This study needs to set these goals because this study needs to get these data in order to calculate drag coefficient and lift coefficient which are important in calculating aerodynamic efficiency.

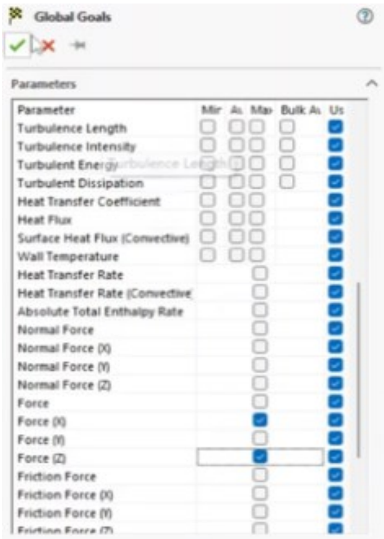

Figure 15. Picking the Global Goals

Aside from global goals, this study also needs to set the algebra goals. This study inserts the drag coefficient and lift coefficient goals as shown by figure 16.

DOI: 10.54254/2755-2721/91/20240953

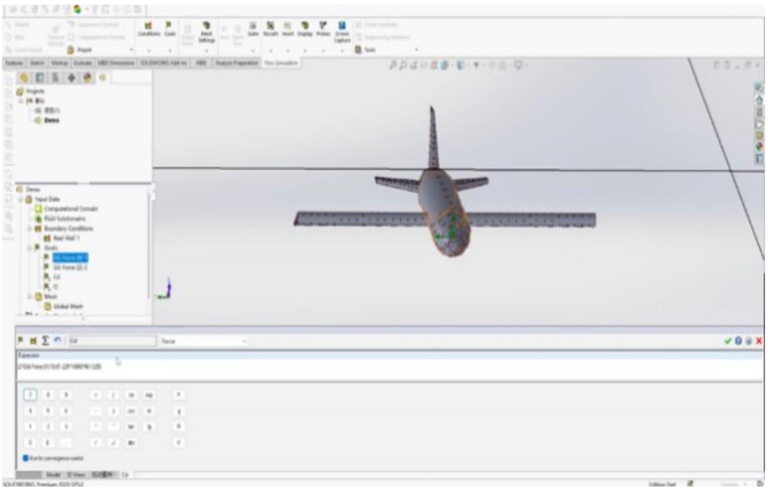

Figure 16. Inserting the Lift Coefficient Formula

To conclude the process, this study set the mesh as shown by Figure 17, the mesh is responsible for making the computer understand how precise the calculations need to be.

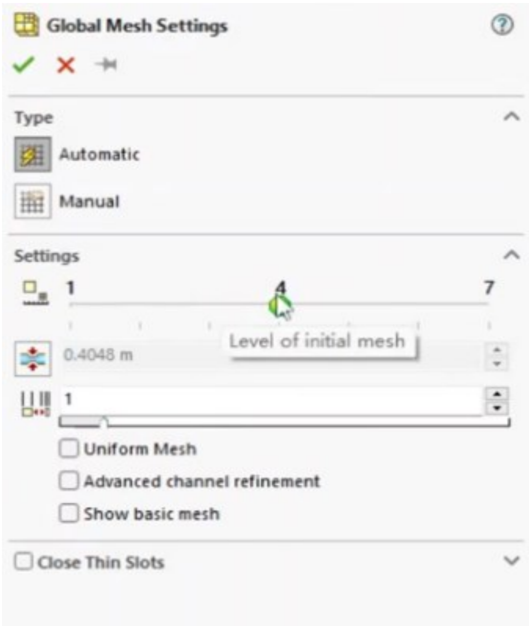

Figure 17. Changing the Global Mesh Settings

3.3. Effect of Modifying Aircraft Angle of Attack

Angle of attack is the angle between the chord line of the wing of a fixed-wing aircraft and the oncoming air for a fixed-wing aircraft. Modifying the angle of attack of an aircraft wing will have a significant impact on aerodynamic performance, making this parameter very crucial for aerodynamic performance. The aircraft with different wing angles are shown in Figure 18.

DOI: 10.54254/2755-2721/91/20240953

Figure 18. Test Aircrafts with Different Angle of Attack, with the angle of attack from 0, 5, 10, 15, 20,25 degrees.

After conducting experiments, it can be concluded that by increasing the angle of attack, the drag coefficient and lift coefficient both increases as shown in figures 19 and 20. When the Angle of attack was 0, the drag coefficient was 0.92 and the lift coefficient was 0.04. After the angle of attack is increased to 25°, the drag coefficient was 1.83 and the lift coefficient is 2.49.

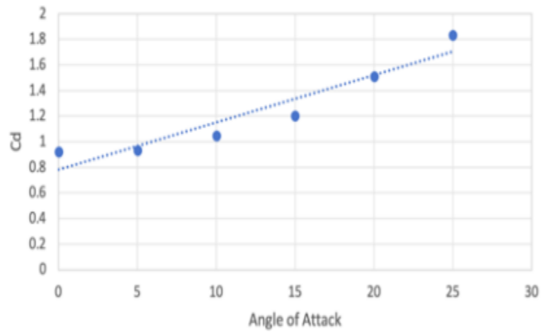

Figure 19. Drag Coefficient with Respect to Angle of Attack

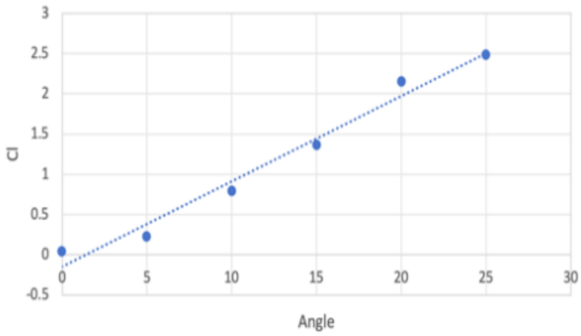

Figure 20. Lift Coefficient with Respect to Angle of Attack.

Using the pressure and velocity contours of the aircraft shown by Figures 21 and 22, this study can further understand how varying angles of attack influence aerodynamic performance. These contours offer a cross section of the aircraft to help this study understand what are the intensity of forces that occur inside of the aircraft. This unique perspective aids in comprehending the effects of different factors on aerodynamic efficiency and offers guidance on optimizing these factors for enhanced performance.

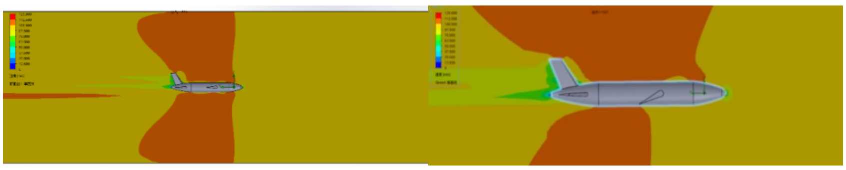

Figure 21. Velocity Contours for Angle of Attack

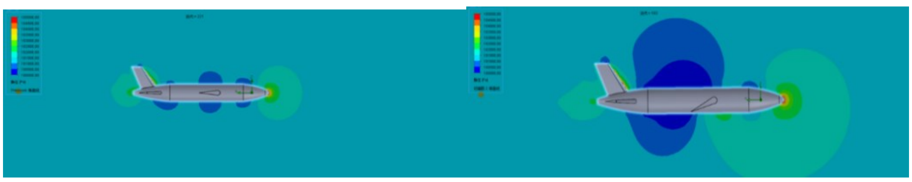

Figure 22. Pressure Contours for Angle of Attack

DOI: 10.54254/2755-2721/91/20240953

In an ideal situation, there should be as little pressure on the top of the plane as possible and as much pressure on the bottom of the plane as possible. This will make the lift the strongest because the pressure on the bottom of the plane would push the aircraft up which generates lift. As shown in the figures above, the pressure on top of the aircraft decreased as the angle of attack increased. However, same trend applies to the bottom of the aircraft as well. There was a significant decrease in pressure on the bottom of the aircraft when the angle of attack was 25°. Thus, the aircraft with the best aerodynamic efficiency is the aircraft with 20° angle of attack. This shows that the optimum angle of attack for aerodynamic efficiency is 20°.

To balance out the drag and lift, the Cl/Cd ratio must be calculated. After calculating the ration, this study discovered that the Cl/Cd ratio is highest at a 20° angle as shown by figure 3.18. At, 0°, the Cl/Cd ratio is 0.04. After increasing the angle of attack, the Cl/Cd ratio peaked at 1.42 when the angle of attack was 20°. After that, the Cl/Cd ratio decreased to 1.36 when the angle of attack increased to 25°. This means that the aircraft will have the highest aerodynamic performance when the aircraft wing is at a 20° angle of attack since the drag is balanced with the lift.

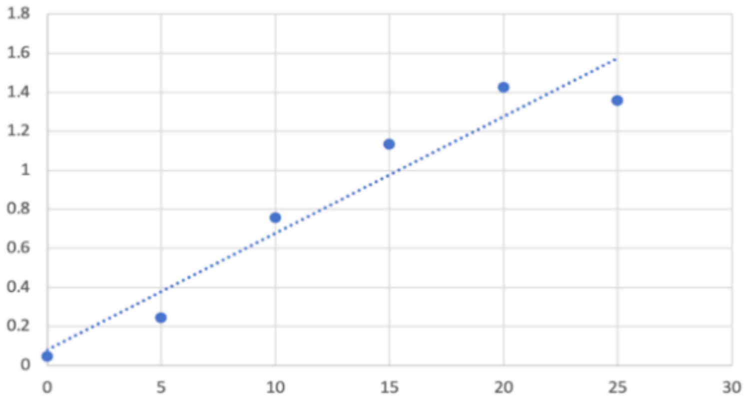

Figure 23. Cl/Cd Graph for Angle of Attack

3.4. Effect of Wing Length

The angle of attack of a wing is not the sole factor affecting wing performance. Another crucial factor is the wing length. In this context, wing length is defined as the distance between the front and back of an airfoil. Figure 24 shows my test aircrafts with different wing length. The pictures are arranged in an increasing order with the plane with the lowest wing length on the top and the highest on the bottom. The angle of attack is kept constant at 20° which had the highest aerodynamic performance as shown by the previous section.

Figure 24. Test Aircrafts with Different Wing Length.

After conducting experiments, this study has discovered that increasing wing length generally increases the lift while decreasing the drag. As shown in Figure 25, the Aerodynamic performance, which is the lift coefficient divided by the drag coefficient, has an increasing trend. The optimal aerodynamic performance was observed when the wing length reached its maximum, implying that the aircraft's aerodynamic efficiency is at its best when the wing length is longer.

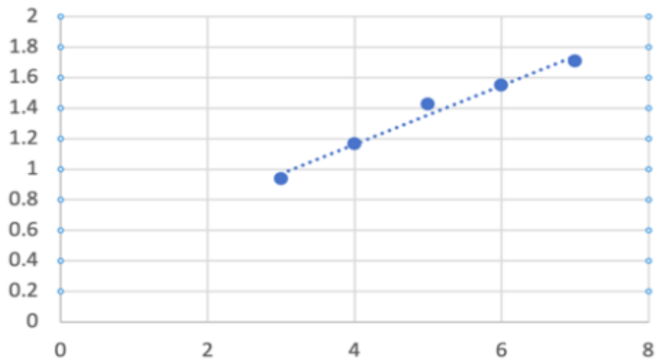

Figure 25. Cl/Cd Graph for Wing Length

As mentioned above, an aircraft more pressure below the aircraft and less above to increase aerodynamic efficiency. As shown by figure 26 and figure 27, the aircrafts all have a similar amount pressure on top of the plane. However, the plane with the highest pressure is the one with 7m wing length. This further reinforces that increasing wing length would increase lift.

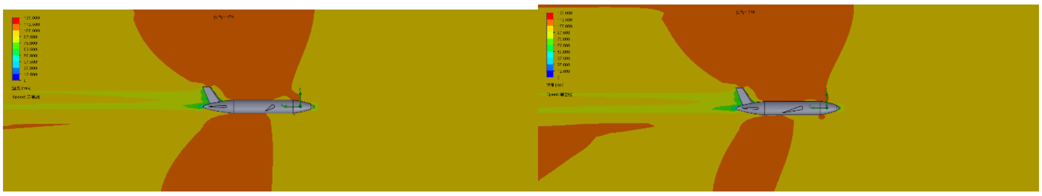

Figure 26. Aircrafts with Different Wing Length

Below are the pressure Contours for Wing Length:

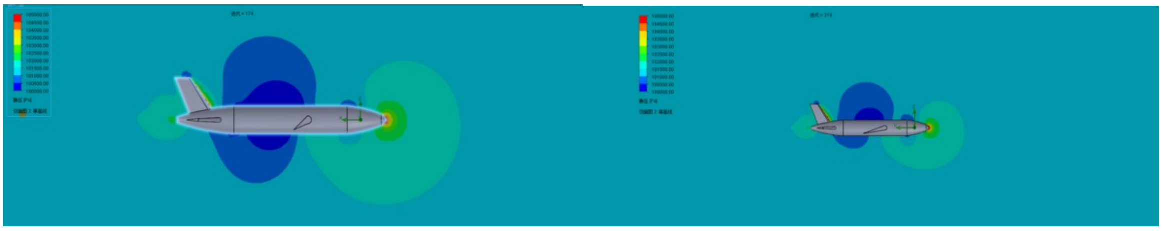

Figure 27. Pressure Contours for Wing Length

3.5. Effect of Winglets

Winglets are tiny wings that are added on the edge of a wing to increase lift. Winglets were inspired by nature when birds like eagles have tiny curves at the end of their wings. In the aerospace industry, many commercial aircraft companies incorporate winglets at the tips of wings to improve aerodynamic performance, a practice illustrated shown in figure 28.

Figure 28. Eagle and Airplane Winglets

DOI: 10.54254/2755-2721/91/20240953

To understand the impacts of adding winglets to aircraft airfoils. This study then added winglets to my test aircraft in Solidworks and ran simulations. This study also conducted studies on changing the angle of the winglets to see the effects. After conducting experiments and calculations, this study discovered the lift-to-drag coefficient ratio was 1.13 before adding winglets and increased to 1.38 adding winglets. This shows that adding winglets does assist in improving aerodynamic performance. This study then wanted to conduct simulations on the effect on changing the winglet angle on the aerodynamic performance of an aircraft. This study took the same aircraft that this study used to get the previous results and changed the angle. As shown in figure 29, the first aircraft had a 40° winglet angle, the second had a 30° winglet angle, and the third had 20° winglet angle.

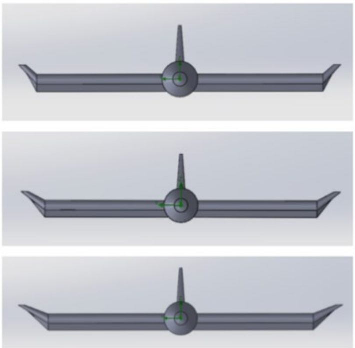

Figure 29. Test Aircrafts with Winglet.

After conducting experiments, the velocity and pressure contours of the different test aircrafts with winglets were once again obtained to give more insights on the effects of winglets on aerodynamic performance.

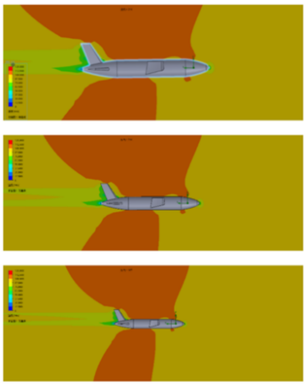

Figure 30. Velocity Contour for Airplanes with Different Winglet Angles

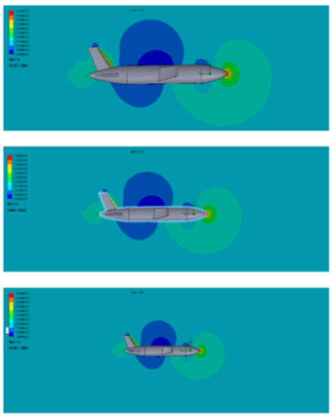

Figure 31. Pressure Contour for Airplanes with Different Winglet Angles

As depicted in figure 30 and figure 31, there is no significant difference between the velocity and pressure contours of the aircrafts with different winglet angles. This implies that winglet angle of aircraft can be modified in various ways without significantly impacting its efficiency.

This observation is further supported by the absence of a discernible trend in the Cl/Cd ratio. The negligible difference in the aerodynamic performance of these aircrafts suggests that any trend is too inconsequential to draw meaningful conclusions. As illustrated by figure 32, at 40° winglet angle which is the highest point, the aerodynamic performance was 0.722 while at 30° winglet angle which is the lowest point, the aerodynamic performance was 0.696. This difference is too insignificant to gain any value from and thus it can be concluded that modifying winglet angle has no significant impact on aerodynamic performance.

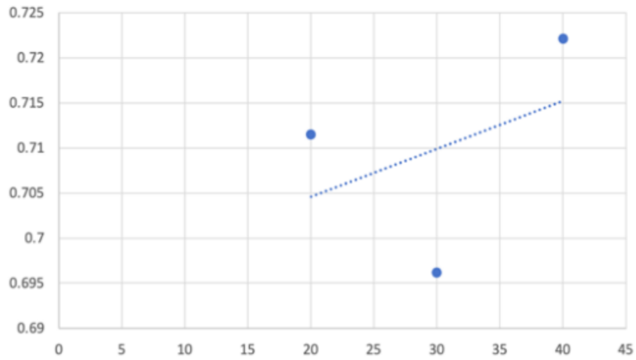

Figure 32. The ratio Cl/Cd with Respect to the Winglet Angle

4. Conclusion & Future Work

4.1. Conclusion

In this study, this study uses the CFD approach to investigate how the airplane wing design affects the aerodynamic performance of the airplane. Three parameters are investigated: the wing angle of attack, the wing length, and the winglets. The results indicate that, for the current airplane model, the optimal aerodynamic performance of an aircraft is achieved when the angle of attack is set at 20°. Furthermore, for the current airplane model, the experiment suggests that the most effective wing length for enhancing aerodynamic performance is 7m. Additionally, the study demonstrates that incorporating winglets contributes to improved aerodynamic performance, but the angle of the winglets has minimal impact on the overall efficiency. These findings hold significant implications for society, as aircraft designers can leverage this knowledge to maximize fuel efficiency and payload capacity.

4.2. Future work

I will persist in exploring factors that will affect aerodynamic performance like wing shape. Additionally, this study will create swept wings and delta wings to see their performance in the air. This study also wishes to test many models in different airspeeds to see what different airfoil designs might suit different scenarios. Moreover, my curiosity extends to understanding why high-speed aircraft, such as jets and space shuttles, seldom incorporate winglets. This inquiry stems from the hypothesis that fast-moving aircraft require exceedingly low drag for optimal flight, and the potential drag generated by winglets may influence their limited use in such applications.

References

[1] Timperley, Jocelyn. “Should We Give up Flying for the Sake of the Climate?” BBC, BBC, 19 Feb. 2020, www.bbc.com/future/article/20200218-climate-change-how-to-cut-your-carbon-emissions-when-flying.
[2] Admin, and Admin. “Lift and Drag Force.” Mech4study, 17 Apr. 2019, www.mech4study.com/fluid-mechanics/lift-and-drag-force.html/. Accessed 21 Jan. 2024.
[3] Dynamic Flight. “Airfoils in General.” Www.dynamicflight.com, 6 Nov. 2017, www.dynamicflight.com/aerodynamics/airfoils/. Accessed 20 Jan. 2024.
[4] Wikipedia Contributors. “Drag Coefficient.” Wikipedia, Wikimedia Foundation, 5 Oct. 2019, en.wikipedia.org/wiki/Drag_coefficient.
[5] Australian Aviation. “Virgin Australia Adding Split Scimitar Winglets to Five Boeing 737-800s.” Australian Aviation, 9 Aug. 2019, australianaviation.com.au/2019/08/virgin-australia-adding-split-scimitar-winglets-to-five-boeing-737-800s/. Accessed 21 Jan. 2024.
[6] Wikipedia. “File:Haliaeetus Leucocephalus7 (Softeis).Jpg - Wikipedia.” Wikipedia.org, Oct. 2006, en.m.wikipedia.org/wiki/File:Haliaeetus_leucocephalus7_%28softeis%29.jpg. Accessed 21 Jan. 2024.

[7] Vance, James E, and Walter James Boyne. "Airplane | Definition, Types, Mechanics, & Facts." Encyclopædia Britannica, 23 Jan. 2019, www.britannica.com/technology/airplane.
[8] Lyu, Z., & Martins, J. R. (2014). Aerodynamic design optimization studies of a blended-wing-body aircraft. Journal of Aircraft, 51(5), 1604-1617.

DOI: 10.54254/2755-2721/91/20241111

The innovative application of phase change materials in heat storage products: warmer pads

Zhengjing Li

Merchant Marine College, Shanghai Maritime University, Shanghai, China

lizhengjing@stu.shmtu.edu.cn

Abstract. As the issue of energy shortage becomes increasingly severe, energy storage technology has gradually attracted global attention, with the application of phase change materials (PCMs) being particularly widespread. This paper focuses on a common daily product: the warmer pad, and investigates the selection and ratio of suitable PCMs to achieve a recyclable heat storage solution. The study first outlines the research background, significance, and methods, then summarizes the basic principles of phase change and the role of differential scanning calorimetry (DSC) in the study of phase change heat storage. Finally, the properties of PCMs with different proportions were tested, and the DSC curves were analyzed. The results showed that the phase change material mixture with a ratio of paraffin: OBC: expanded graphite = 77:20:3 exhibits excellent performance in heat storage, with a thermal conductivity of 0.547 W/m·K, a phase change latent heat of 150 J/g, and a phase change temperature of 41.9°C. The warmer pad achieved a surface temperature close to 40°C and a heat release duration of nearly one hour. This study aims to promote the industry's transformation towards sustainable development and provide a reference for research in the field of daily-use products with phase change heat storage.

Keywords: Phase Change Materials, Applied Research, Warmer Pad, Differential Scanning Calorimeter.

1. Introduction

1.1. Research Background

The issue of global energy scarcity is becoming increasingly prominent, primarily due to the over-exploitation and consumption of fossil fuels. With the introduction of China's goals for ‘carbon peak and carbon neutrality’ and the construction of a new energy system, the development of new and renewable clean energy sources has become crucial. However, clean energy sources such as solar and wind power exhibit intermittency and discontinuity, leading to mismatched supply and demand in both time and space. Therefore, the development of energy storage technologies is becoming increasingly important. Thermal energy storage is a vital component of this, playing a significant role in the utilization of renewable energy. Heat storage materials typically come in two forms: chemical and physical. Chemical heat storage materials utilize chemical reactions or dissolution heat to store thermal energy, which can easily cause environmental pollution. Physical heat storage materials are divided into sensible heat and phase change types. Sensible heat storage materials store heat by increasing the temperature of the conductive medium, making it difficult to control temperature changes, resulting in lower heat capacity and larger volume. In contrast, phase change materials offer higher energy density, more stable temperatures, lower energy consumption, and longer service life. Consequently, phase change materials are gradually gaining attention in the field of heat storage [1]. As summarized by Wang et al [2], phase change thermal storage technology has been widely applied in building energy conservation, such as in air conditioning in summer and heating in winter. Jie et al [3] studied the application of phase change materials in shell-and-tube heat exchangers, demonstrating high energy storage efficiency. Tang [4] posits that the application of phase change technology in solar thermal storage systems can effectively improve energy utilization efficiency.

As people's living standards improve and their pursuit of a comfortable life intensifies, phase change materials also show a very broad prospect in daily life applications. Zhi [5] used a binary mixture of stearic acid and disodium hydrogen phosphate dodecahydrate as the phase change material for a heat storage pad. The heating temperature was around 55°C, with a heating time for up to 160 minutes. The final temperature during heat release was around 26°C, and the heat release time generally exceeded 500 minutes. Bin [6] developed a phase change heat storage electric floor heating system using paraffin and expanded graphite. After mixing the phase change material with concrete, the surface average temperature during heat storage was 1.35°C lower than that of ordinary concrete, and the heating time was extended by 1 hour and 41 minutes. During heat release, the surface average temperature was 1.49°C lower than that of ordinary concrete, and the cooling time was extended by 1 hour and 52 minutes. Meng et al [7] summarized the use of temperature-regulating clothing with phase change materials, which can be applied for medical cooling, heat protection, diving, polar exploration, and infrared camouflage.

Therefore, phase change warmer pads capable of heat storage and release hold significant research value. As a heating product, warmer pads have consistently been the top choice for individuals in winter or low-temperature settings. The market demand for these products is on the rise, as illustrated in Figure 1. However, widespread issues with currently available warmer pads, such as the risk of burns, the potential for liquid expansion, and environmental concerns, have prompted a shift in market expectations beyond basic heating functionality. There is an increased focus on the products' eco-friendliness, sustainability, and health safety. Phase change warmer pads can meet these market requirements by leveraging their recyclability, non-polluting nature, and safety features.

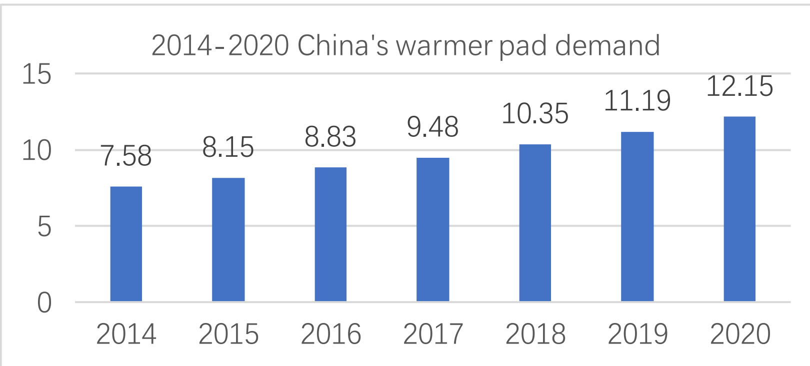

Figure 1. 2014-2020 China's warmer pad demand (in billions of pads).

1.2. Research Purpose and Significance

The core purpose of this study is to design a novel recyclable green warmer pad using phase change materials, aiming for a cycle of use that is pollution-free and safe. This study seeks to provide an efficient heat storage solution for warmer pads, reducing environmental impact while meeting the demands of modern society for high-efficiency, comfortable, and environmentally friendly heating products. This approach is intended to promote the industry's transformation towards sustainable development.

DOI: 10.54254/2755-2721/91/20241111

1.3. Research Methods

This research endeavor incorporates a variety of methodological approaches, including theoretical analysis, empirical experimentation, and comparative evaluation. The theoretical analysis involved an exhaustive examination of pertinent literature and patent documentation, providing a comprehensive understanding of the internal mechanisms and performance criteria of warmer pads. This analysis laid the groundwork for conceptualizing a phase change material-based warmer pad framework. Subsequently, the empirical experimental method was pivotal in validating theoretical postulates and refining design parameters. A spectrum of materials was scrutinized through ratio experimentation, employing analytical instruments such as DSC and thermographic cameras to ascertain key thermal properties, including phase transition temperatures, latent heat, thermal conductivities, and surface temperature profiles. Furthermore, the comparative method was extensively utilized to juxtapose the performance of the prototype phase-change warmer pad against conventional warmer pads and analogous commercial products. This comparative analysis was instrumental in discerning areas for performance enhancement and ensuring the competitiveness of the proposed warmer pad design.

2. Experimental Principles and Methods

2.1. Basic Principles of Phase Change Materials

2.1.1. Thermodynamic Principles of Phase Change Processes

The basic principle of phase change materials is predicated on their capacity to absorb or release substantial quantities of latent heat during transitions between different phase states. As the material undergoes a phase transition from solid to liquid, it absorbs heat (melting), and when it reverts from liquid to solid, it emits heat (solidification). Given that this transition involves merely the transfer of energy without an accompanying change in temperature, it holds substantial applicability and broad scope for future applications within the realms of thermal energy storage and temperature regulation. The latent heat of fusion for phase change materials, which is the heat absorbed or released during the phase transition, as in equation (1),

$$\Delta H = T \cdot \Delta S \tag{1}$$

where ΔH represents the latent heat, T denotes the temperature of phase change, and ΔS signifies the change in entropy during the phase change process.

2.1.2. Classification and Characteristics of Phase Change Materials

Phase change materials can be differentiated based on the phase transition type into solid-solid, solid-gas, solid-liquid, and liquid-gas transitions. Solid-solid transitions primarily consist of materials such as polyols, while solid-liquid transitions encompass crystalline hydrates, metals and alloys, alkanes, and alcohols. When classified by material composition, PCMs are divided into organic, inorganic, and composite categories. The organic category includes paraffin waxes, fatty acids, polyols, etc.; the inorganic category comprises crystalline hydrates, molten salts, metals and alloys, etc and the composite category consists of mixtures of organic-organic, organic-inorganic, and inorganic-inorganic combinations. According to the temperature range, they are further categorized into low-, medium-, and high-temperature phase changes [8].

PCMs have the ability to absorb or release substantial latent heat during phase transitions. This feature enables warmer pads to deliver a stable output of thermal energy over an extended period without the need for additional energy input. Furthermore, by adjusting the proportions and selecting appropriate materials, the phase change temperature of PCM can be customized. This customization allows warmer pads to cater more effectively to the diverse requirements of various users and application settings, thus facilitating temperature regulation. Additionally, PCMs are associated with minimal environmental pollution and offer an extended lifespan.

2.2. Experimental Materials

As shown in Table 1, the experimental materials selected include paraffin wax, OBC, foaming agent, expanded graphite, and SEBS.

Table 1. Experimental materials and their characteristics.

Material	Characteristics
Paraffin wax	Existing studies are abundant, the cost is relatively low, and the phase change temperature is suitable for warmer pads.
OBC	It serves as a supporting matrix to prevent paraffin leakage and enhance heat-induced flexibility[1].
Foaming agent	Fill spaces.
Expanded graphite	Utilizing a porous structure to match paraffin and enhance the thermal conductivity coefficient [9].
SEBS	Enhance shape retention, prevent leakage, and increase heat-induced flexibility.

Paraffin wax is produced by Donglin Plastics Business Department in Zhangmutou, Dongguan City, with a latent heat of 220.5 J/g, OBC is manufactured by Dow Chemical Company in the United States (Model 9530, characterized by a density of 0.887 g/cm³ and a melt flow rate of 190℃/2.16 kg). The foaming agent is produced by Hongzhi Network Information Technology Co., Ltd., and 80-mesh expanded graphite is produced by Qingdao Jintao Graphite Co., Ltd.

2.3. Differential Scanning Calorimetry

2.3.1. Principles of Operation and Experimental Procedure of DSC

DSC is a high-precision thermal analysis technique capable of accurately measuring the heat flow changes of materials during phase transitions. It measures the relationship between the heat flow rate of the sample and the reference material as a function of temperature or time, from which the phase change latent heat and the onset temperature of the material can be calculated [10]. DSC is characterized by programmable temperature control, simplicity, speed, minimal human factor influence, and good repeatability [11]. The sample and the reference material are placed in fixed positions in a common heating or cooling environment. When the sample undergoes a phase transition, such as melting or crystallization, it absorbs or releases heat, causing a temperature change in the sample container. The DSC instrument maintains temperature consistency between the sample and the reference material by controlling the heating or cooling rate. If the sample requires additional heat to maintain isothermal conditions (such as during melting), the instrument provides additional energy, the input of which is the DSC signal. The DSC curve is a graph of the heat flow as a function of temperature or time during the experiment.

Before performing DSC testing, first, weigh 5 to 10 mg of the sample using a precision electronic balance and seal it in a crucible, as shown in Figure 2. Then place the crucible into the DSC equipment for testing. Set an appropriate temperature range according to the characteristics of the sample and heat or cool at a constant rate. During the cooling phase, after reaching the preset lowest temperature, maintain an isothermal period of 2 to 5 minutes to ensure the sample is completely solidified. Then, heat to the highest temperature at the specified rate to complete the test. After the test is finished, the cooling or heating curve of the sample, phase change temperature, and latent heat value can be obtained through analysis software. Throughout the measurement process, liquid nitrogen is used as a refrigerant, while nitrogen gas serves as a protective gas and purge gas.

DOI: 10.54254/2755-2721/91/20241111

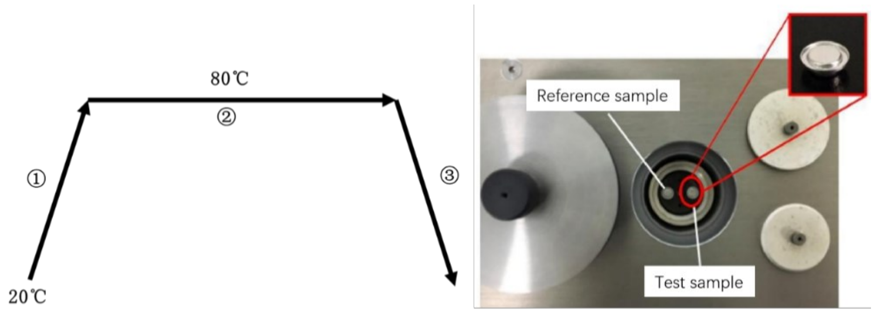

(a) (b)

Figure 2.(a)①Melting: The solid turns into a liquid, causing the temperature to rise.;②Isothermal: 2 minutes.; ③Solidification: The liquid turns into a solid, causing the temperature to fall. (b)The positions of the reference and test samples in the Differential Scanning Calorimeter [12].

2.3.2. Application of DSC in the Study of Phase Change Materials

DSC serves a crucial role in the research of phase change materials. As a high-precision thermal analysis technology, DSC is capable of measuring the heat flow changes associated with temperature during the heating or cooling of materials. These measurements help scholars both domestically and internationally to better understand phase change materials, delve deeper into their thermal properties, and act as a vital link between fundamental research and practical applications. In this experiment, DSC is utilized for the identification of phase change temperatures, the measurement of the latent heat of phase transitions, and the optimization of material compositions.

2.4. Experimental Equipment

The primary equipment utilized in the experiment includes a DSC and a thermal conductivity analyzer, as shown in Figure 3. The DSC, manufactured by NETZSCH Instruments GmbH, model DSC200F3, is primarily used for measuring the temperature and latent heat of phase change materials. The thermal constant analyzer, produced by the Swedish Hot Disk company, model TPS500s, is mainly employed for determining the thermal conductivity coefficient of phase change materials. Additional auxiliary equipment is listed in Table 2.

(a) (b)

Figure 3. (a)differential scanning calorimeter (b)thermal conductivity analyzer.

DOI: 10.54254/2755-2721/91/20241111

Table 2. Experimental instrument information

Instrument	Manufacturer	Model	Precision
Precision electronic balance	Shanghai fangrui instruments co., ltd.	Fa2004	±0.1 mg
Digital temperature controlled water bath	Shanghai lichen bangxi instrument technology co., ltd.	Hh-4	0.1 °c
Thermocouple	Agilent Technologies	-	0.05 °C
Thermal conductivity analyzer	Swedish hot disk	Tps 500 s	0.01 °c
Differential scanning calorimeter	Netzsch instruments gmbh	DSC200f3	-
Vacuum drying oven	Shanghai qiao yue electronics co., ltd.	Dzf-6020	-
Beakers, Glass Rods, etc	Tmall Online Shopping Platform	-	-

3. Research

3.1. Warmer Pad Structural Design

The text of your paper should be formatted as follows: The overall structure, as shown in Figure 4, includes a Flexible soft shell, PCM, Isolated layer, Heating sheet, Circuit, Charging port, and Wire. In terms of energy supply, as depicted in Figure **5**, a lithium battery is chosen for its high energy density and stable power supply characteristics, serving as the storage and release device for electrical energy. Additionally, a temperature control circuit and heating sheet are integrated to ensure that the warmer pad provides a uniform and stable heat output during use.

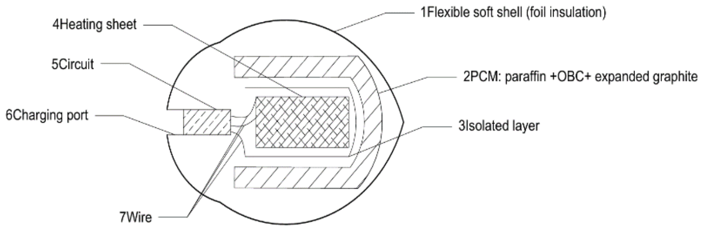

Figure 4. The overall design of the warmer pad.

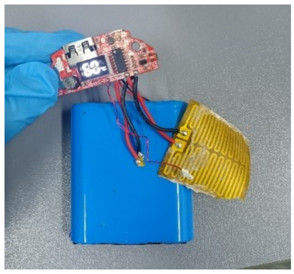

Figure 5. Circuit, heating element, and lithium battery.

3.2. Experimental Content

3.2.1. Comparison of DSC Curves for Phase Change Materials with Different Proportions

Three sets of experiments were conducted in total. The first set utilized a mixture of paraffin wax, OBC, and a foaming agent. Experiments were performed with mixture ratios of 66:33:1 and 65:27:6.7 for paraffin, OBC, and foaming agent, respectively. A meticulous analysis of the DSC curves, as depicted in Figure 6, revealed that an increase in the proportion of the foaming agent led to an expansion in the temperature range of the beginning and end of the phase transition. This suggests that the foaming agent facilitates better integration between paraffin and OBC. Nevertheless, due to a decrease in the overall quantity of paraffin, there was a reduction in the latent heat.

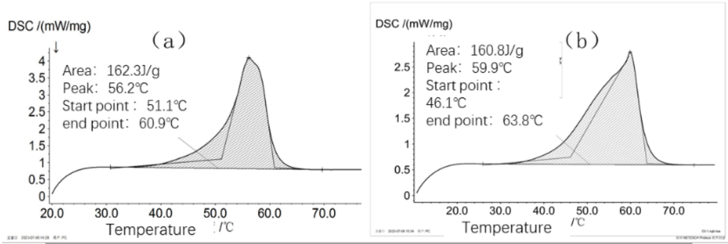

	paraffin wax (%)	OBC (%)	Foaming Agent (%)
(a)	66	33	1
(b)	65	27	6.7

Figure 6. The ratio of phase change materials consisting of paraffin wax, OBC, and foaming agent, as well as the DSC test results.

The second set of experiments involved a composite of paraffin wax, OBC, and expanded graphite. These were tested using DSC with mixture ratios of 77:20:3 and 65:30:5 for paraffin, OBC, and expanded graphite, respectively, as depicted in Figure 7. Studies show that incorporating expanded graphite results in a substantial decrease in latent heat, accompanied by variations in the temperature range of the phase transition. The difference in temperature between the initiation and termination of the phase change also widened, signifying a more extensive and gentle phase transition process[13]. This effect may arise from the thermal interaction between the expanded graphite and the phase change material, as well as the distribution of expanded graphite throughout the PCM matrix [14]. An excess of expanded graphite could lead to a drastic reduction in the phase change latent heat, whereas an insufficient amount might not deliver the anticipated improvement in thermal conductivity. The thermal conductivity of the material with the ratio of paraffin to OBC to expanded graphite at 77:20:3 was determined to be $0.547\ W/(m \cdot K)$.

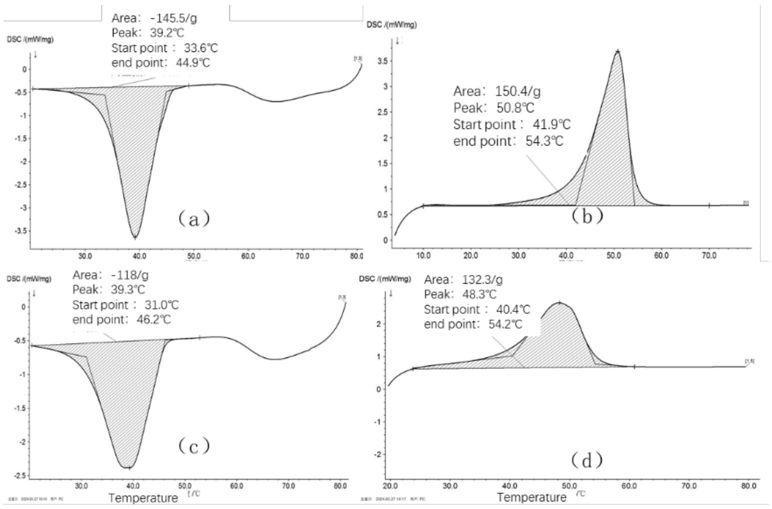

	Paraffin wax (%)	OBC (%)	Expanded graphite (%)
(a) 、 (b)	77	20	3
(c) 、 (d)	65	30	5

Figure 7. Phase change materials: ratio of paraffin, OBC, and expanded graphite and DSC test results.

The third set of experiments involved a composite of paraffin wax, SEBS, and expanded graphite. SEBS effectively reduces the leakage rate and has excellent sealing performance [15]. The ratio chosen was 77:20:3 for paraffin, SEBS, and expanded graphite, respectively. However, under the conditions of a 160°C high-temperature oil bath, the composite material failed to fully melt into a liquid during the experiment, as depicted in Figure 8. This observation suggests potential issues with compatibility and thermal stability among paraffin, SEBS, and expanded graphite, which may be attributed to poor miscibility between SEBS and paraffin, or the thermal stability of expanded graphite at elevated temperatures. To resolve this issue, future studies could utilize additional characterization methods, such as Fourier Transform Infrared Spectroscopy (FTIR), Thermogravimetric Analysis (TGA), and Scanning Electron Microscopy (SEM), to delve deeper into the thermal performance and microstructure of the materials [16].

(a) (b)

Figure 8. (a)Paraffin in a molten state; (b)Non-molten state after the addition of SEBS and expanded graphite.

3.3. Thermal Flow Analysis

During the melting process, materials absorb heat, leading to an endothermic peak on the heat flow curve; conversely, during the solidification process, materials release heat, manifesting as an exothermic peak. As the temperature increases during melting, the PCM absorbs heat, and an endothermic peak emerges on the DSC curve, with its peak position aligning with the material's melting point. The area under the endothermic peak expands as melting continues until the material is entirely in a liquid state. The heat flow variation during this phase, represented by the area under the curve, directly reflects the material's latent heat of fusion, indicating the energy required for the transition from solid to liquid. The rate of phase change influences the DSC curve's morphology. In DSC testing, the rate of phase change dictates the speed of heat exchange, subsequently affecting the shape and characteristics of the heat flow curve. When the phase change rate is rapid, heat is quickly absorbed or released, resulting in a sharp peak with a large area on the DSC curve. Conversely, a slower phase change rate leads to a more gradual heat exchange, resulting in a broader and flatter peak on the DSC curve. An increase in the cooling rate results in a broader and flatter shape, potentially due to altered crystallization behavior from rapid cooling, which disperses the heat release process [17].

3.4. Performance Testing

Tests can be conducted using an infrared thermal imager and thermocouples to evaluate the performance of the warmer pad. As depicted in Figure 9, the infrared imager demonstrates that with an ambient temperature of 26°C, the surface of the warmer pad can essentially achieve 40°C, offering users a warm and comfortable heating effect without causing high-temperature burns. Furthermore, this level of temperature performance can last for almost one hour, showcasing the warmer pad's outstanding thermal sustainability.

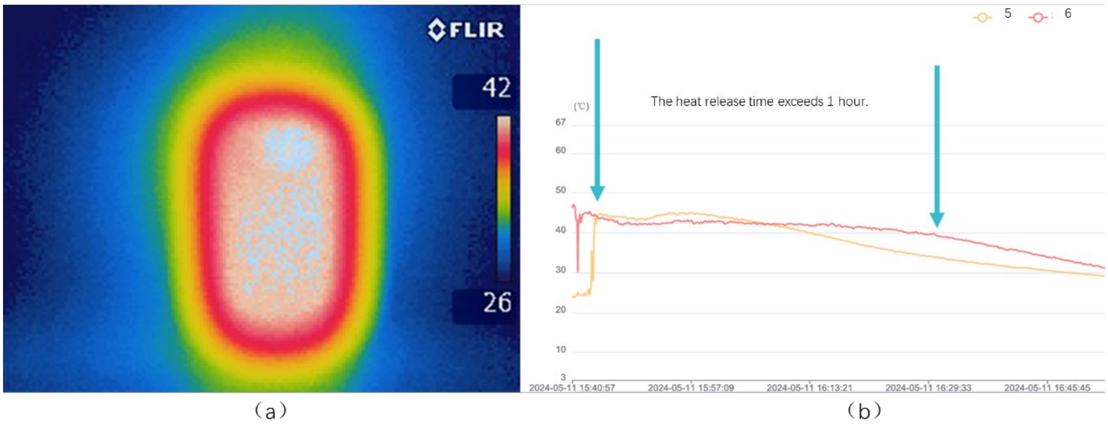

Figure 9. (a)Infrared imager for measuring surface temperature (b)Thermocouple for testing the temperature variation curve on the surface of the warmer pad.

4. Conclusions

Through the research, the following conclusions have been drawn:

- Selection and proportioning of phase change materials: the selection and proportioning of phase change materials for the warmer pad were determined after extensive analysis. The precision of the equipment affected the accurate measurement of the foaming agent dosage in the first group. The third group, which included SEBS, did not exhibit a liquid state, while expanded graphite was found to enhance the thermal conductivity. Therefore, the second group's composition of paraffin wax, OBC, and expanded graphite was chosen as the phase change materials. Based on DSC and thermal conductivity analyses, the selected ratio of paraffin to OBC to expanded graphite was 77:20:3. this composition not only has a considerable thermal conductivity coefficient of 0.547 $w/(m \cdot k)$ but also possesses a suitable and stable latent heat of phase change of 150 j/g and a phase change temperature of 41.9°c. These characteristics are crucial for the performance of the warmer pad.
- Performance testing of the warmer pad: using an infrared thermal imager and thermocouples for assessment, the warmer pad was shown to maintain a surface temperature of 40°c and provide heat for approximately one hour, demonstrating its superior performance.

In the future, the development of phase change warmer pads will be expanded to advance alongside technological innovations and growing consumer awareness. With the integration of nanotechnology and artificial intelligence, these products will become more intelligent and exhibit enhanced thermal performance. Furthermore, as environmental and energy-saving consciousness strengthens, phase change warmer pads are anticipated to find widespread applications in fields such as healthcare, outdoor sports, and daily warmth. Through continuous technological innovation and market adaptation, these products are poised to become essential tools for energy conservation, emission reduction, and improving quality of life, contributing to the realization of a green, intelligent, and healthy lifestyle.

References

[1] Bei L, Dao L, and Liang Y 2017 “Research Progress on Thermal Storage Materials with Composite Phase Change.” Journal of Refrigeration 38(4): 36–43.
[2] Biao H, Hui W, Zhen Z, and Qi L 2024 “Preparation and performance of ammonium aluminum sulfate dodecahydrate-sodium sulfate decahydrate eutectic composite phase change materials.” New Chemical Materials. doi:10.19817/j.cnki.issn1006-3536.2024.10.035.
[3] Bin W 2024 “Study on the application of phase change thermal storage electric floor heating.” Lanzhou Jiaotong University. doi:10.27205/d.cnki.gltec.2023.001865.

[4] Di W and Bo C 2024 "Application analysis of phase change heat storage technology in building energy saving." Housing and Real Estate (14): 123–5.
[5] En C, Da L, Sheng Y, and Xin L 2024 "Preparation and Performance Study of PP/SEBS/HDPE Composite Materials." Materials And Application 46(8): 20–3. doi:10.20143/j.1671-1602.2024.08.020.
[6] Feng, Tianping, Xuelai Zhang, and Jun Ji 2024 "Preparation and Properties of Gel-Type Low-Temperature Phase Change Materials." Journal of Energy Storage 90: 111644. doi:10.1016/j.est.2024.111644.
[7] Jin T 2023 "Overview of Thermal Storage Technology for Solar Energy System." Nonferrous Metals Engineering & Research 44(6): 26–9.
[8] Li, Jie, Wenchao Duan, Zian Peng, Yuehao Chen, Huilan Chen, Qi Peng, Shuguang Liao, Xiaoqin Sun, and Changwei Jiang 2024 "An Experimental and Numerical Study on the Energy Storage and Release Performance of Shell and Tube Heat Exchangers with Phase Change Material for the Data Center." Applied Thermal Engineering 255: 123966. doi:10.1016/j.applthermaleng.2024.123966.
[9] Lin, Xiangwei, Xuelai Zhang, Jun Ji, Lu Liu, Yifan Wu, Mai Yang, Dingyu Lu, and Huifan Zheng 2021 "Development of Flexible Form-Stable Phase Change Material with Enhanced Electrical Resistance for Thermal Management." Journal of Cleaner Production 311: 127517. doi:10.1016/j.jclepro.2021.127517.
[10] Lin, Xiangwei, Xuelai Zhang, Lu Liu, Jiyuan Liang, and Wei Liu 2022 "Polymer/Expanded Graphite-Based Flexible Phase Change Material with High Thermal Conductivity for Battery Thermal Management." Journal of Cleaner Production 331: 130014. doi:10.1016/j.jclepro.2021.130014.
[11] Meng D, Xin H, Gao L, Ya G, and Mei W 2024 "Research progress of phase change materials in the field of temperature regulating clothing." Wool textile journal 52(1): 122–7. doi:10.19333/j.mfkj.20231004306.
[12] Peng L, Chao W, Xing L, Shu S, and Ai Z 2024 "Preparation of Foaming Masterbatches Based on Low-Temperature Machinable SEBS and Micro-foaming Thermoplastic Elastomers." China Plastics Industry 52(3): 27–33.
[13] Shu L, Gang W, Yi L, Li Z, and Li M 2024 "Research on Differential Scanning Calorimetry Method for the Determination of Melting Point of Paraffin Wax." Petroleum Processing and Petrochemicals. 55(5): 165–71.
[14] Xiao S, Wei L, Xiu L, Yan L, and Yu W 2019 "Influence factors and testing techniques for differential scanning calorimetry." Analytical instrumentation (4): 74–9.
[15] Yi Y, Jing P, Zhi C, Yu D, Yang W, and Nan L 2024 "The study on the preparation and performance of the N-E/DHPD/EG composite phase change materials." Journal of Functional Materials.https://kns.cnki.net/KCMS/detail/detail.aspx?dbcode=CAPJ&dbname=CAPJLAST&filename=GNCL2024060300D (June 13, 2024).
[16] Zambrano, Pablo, Marcela Manrique-Moreno, Karla Petit, José R. Colina, Malgorzata Jemiola-Rzeminska, Mario Suwalsky, and Kazimierz Strzalka 2024 "Differential Scanning Calorimetry in Drug-Membrane Interactions." Biochemical and Biophysical Research Communications 709: 149806. doi:10.1016/j.bbrc.2024.149806.
[17] Zhi C 2007 "Research and the development of phase-change product." Beijing University of Technology. https://kns.cnki.net/KCMS/detail/detail.aspx?dbcode=CMFD&dbname=CMFD2007&filename=2007189487.nh (July 22, 2024).